Universitat Autònoma de Barcelona

Biocompatible Ti-based metallic glasses and nanocomposite materials

Doctoral Thesis presented by:

Anna Hynowska

Supervised by:

Maria Dolors Baró Mariné

Eva Pellicer Vilà

Jordi Sort Viñas

Departament de Física, Facultat de Ciències

Bellaterra, September 2014

La Prof. Mª Dolors Baró Mariné, la Dra. Eva Pellicer Vilà i el Dr. Jordi Sort Viñas, directors de la tesi doctoral duta a terme per Anna Hynowska i que porta per títol "Biocompatible Ti-based metallic glasses and nanocomposite materials",

FAN CONSTAR:

Que l'aportació de la doctoranda al treball que es presenta ha estat fonamental tant pel que fa al disseny experimental com pel que fa a la realització dels experiments, incloent-hi la síntesi de les mostres i llur caracterització, l'anàlisi de les dades i la discussió i elaboració dels resultats presentats.

I per a que consti, a petició de la interessada i als efectes oportuns, ho signen a:

Bellaterra, 1 de setembre de 2014

Mª DOLORS BARÓ MARINÉ EVA PELLICER VILÀ JORDI SORT VIÑAS

Acknowledgement

First and foremost, I would like to express my sincere gratitude to my supervisors Prof. Maria Dolors Baró, Dr. Eva Pellicer and Dr. Jordi Sort, for their guidance, support, patience and their advices on both personal and professional levels for my development. I am greatly honored to have had my PhD under such an excellent supervising.

Besides my advisors, I am indebted to all co-authors of the articles I have published so far. A special acknowledgement goes to Dr. Jordina Fornell and Dr. Pau Solsona who shared their knowledge and experiences in the field of metallic glassy and nanocomposite materials. I would also like to thank Prof. Santiago Suriñach for his fruitful advices and help in all aspects.

I am grateful to my many colleagues from the group "Física de Materials II" for their help and friendship: Jordina, Pau, Aïda, Alberto, Sergio, Marta, Enric, Miquel, Irati, Jin, Alberto, Roger. Also, many thanks to Pablo, Patxi and Alex from the other Department, who were such a great friends and helped me a lot either on the scientific or non-scientific matters.

A special note of thanks goes to Estefania Boix-Lopez and Marion Limo; without their advice this PhD would not have been possible.

It gives me great pleasure to acknowledge the support and help coming from the people from the Microscopy Service, especially Emma Rossinyol and Onofre Castells for their permanent assistance in TEM and SEM experiments, as well as the people from X-ray Diffraction and Chemical Analysis Services at UAB.

It was a great opportunity to participate in the European Research Academic-Industrial Initial Training Network on "Innovative Biocompatible Titanium-based Structures for Orthopaedics" funded by the European Commission under the FP7 – 'People' Programme. The project was realized under the framework of Marie Curie ITN Action. It gave me the possibility to meet greatest specialists in this field. My genuine thanks also go to Prof. Jürgen Eckert, Prof. Marianna Calin and Dr. Annett Gebert from IFW Dresden in Germany, for the possibility to carry out my research in their institution during my BioTiNet secondment.

Thanks to the people from BioTiNet. I spent an amazing time with all BioTiNet fellows during all internal meetings of BioTiNet. Matthias, Julio, Yaofeng, Ajit, Mathew, Natalia, Kadir, Somayeh, Mehdi, Ganna, Martina, Bartek, Simon, Edi, Sasan, Florina, and Ile – THANKS for advices and friendships we made during BioTiNet time life.

Thanks to my friends (Olka & Krzysztof K., Ala M., Klaudia L. & S., Daria & Hubert M, Natalia P., Karolina Sz., Juan A., Joanna L.) and flat mates, who made my stay in Barcelona unforgettable.

Dziękuję przyjaciołom z Polski, mojej rodzinie, a w szczególności rodzicom za Waszą bezwarunkową miłość. Bez waszego wsparcia nie zrealizowałabym tego wszystkiego!! Dziękuję!

Table of Contents

Preface

The contents of this Thesis have been organized in different Chapters as follows:

- **Chapter 1.** An overview of biomaterials for orthopedic applications, synthethic strategies toward metallic glasses, metallic glass composites and nanocrystalline materials, and a description of their most relevant properties, is presented.
- **Chapter 2**. The main goals of the Thesis are highlighted in this Chapter.
- **Chapter 3**. It provides a brief description of the working conditions for the techniques used in the synthesis and the structural, mechanical, biological and electrochemical characterization of the samples.
- **Chapter 4**. It presents the results and their discussion as a compilation of articles. A brief summary is included before each article.
- **Chapter 5.** It points out the main conclusions of the doctoral Thesis.
- **Chapter 6**. Future perspectives are briefly outlined in this Chapter.

List of Figure

List of Tables

List of Abbreviations, Acronyms and Symbols

A	*Number of potential sites for heterogeneous/homogenous nucleation*	*FFR*	***F**ast **F**ourier **R**econstruction*
AFM	***A**tomic **F**orce **M**icroscopy*	*FFT*	***F**ast **F**ourier **T**ransformation*
ASTM	***A**merican **S**tandard **T**est **M**ethod*	*FVM*	***F**ree **V**olume **M**odel*
b_a	*Anodic Tafel slope*	*G*	*Shear modulus*
b_c	*Cathodic Tafel slope*	*GFA*	***G**lass **F**orming **A**bility*
bcc	*Body-centered cubic*	*GIXRD*	***G**lazing **I**ncident **X**-**r**ay **D**iffraction*
BMG	***B**ulk **M**etallic **G**lass*	ΔG^*	*Gibbs free energy*
BSE	***B**ack **S**cattered **E**lectrons*	ΔG^*_{het}	*Gibbs free energy for heterogeneous nucleation*
c_f	*Structural defect concentration*	Δg_v	*Difference in Gibbs free energy between the unit volume of the solid and the liquid*
C_p	*Heat capacity*	*H*	*Hardness*
D	*Fragility index*	*hcp*	*Hexagonal closed-packed*
DSC	***D**ifferencial **S**canning **C**alorimetry*	*HR-TEM*	***H**igh **R**esolution **T**ransmission **E**lectron **M**icroscopy*
E	*Electrode potencial*	I_v	*Steady-state nucleation rate*
E_a	*Activation energy of crystallization*	*j*	*Current density*
ECM	***E**xtracellular **O**rganic **M**atrix*	j_{corr}	*Corrosion current density*
E_{corr}	*Corrosion potential*	*K*	*Bulk modulus*
E_{OCP}	***O**pen **C**ircuit **P**otential*	k_B	*Boltzmann constant*
E_r	*Reduced Young's modulus*	*k*	*Reaction rate*
FCC	***F**ace **C**entered **C**ubic*	*LRO*	***L**ong–**R**ange **O**rder*

MA	***M**aster **A**lloy*	ΔT_{xg}	*Supercooled liquid region*
MAUD	***M**aterials **A**nalysis **U**sing **D**iffraction*	T_x	*Crystallization temperature*
MG	***M**etallic **G**lass*	u	*Velocity through which atoms come from the liquid to the crystal-liquid boundary*
MSC	***M**ulti-**S**tep **C**rystallization*	*UT*	***U**ltrasonic **M**easurement*
MRO	***M**edium–**R**ange **O**rder*	ν	*Poisson's ratio*
n	*Avrami exponent*	*WAXS*	***W**ide **A**ngel **X**-Ray **S**pectroscopy*
NC	***N**ano**c**rystalline*	*XRD*	***X**-**R**ay **D**iffraction*
R	*Gas universal constant*	α	*Transfer constant*
r^*	*Critical radius*	γ	*Interfacial free energy between the solid and the liquid*
R_P	*Polarization resistance*	ε	*Strain*
R_c	*Critical cooling rate*	η	*Viscocity*
RT	***R**oom **T**emperature*	η_a	*Anodic overpotential*
SAED	***S**elected **A**rea **E**lectron **D**iffraction*	η_c	*Cathodic overpotential*
SAXS	***S**mall **A**ngel **X**-**R**ay **S**pectroscopy*	τ	*Incubation time for crystallization*
SE	***S**econdary **E**lectron*	λ	*Wavelength*
SEM	***S**canning **E**lectron **M**icroscopy*	σ	*Stress*
SRO	***S**hort–**R**ange **O**rder*	σ_y	*Yield stress*
T_a	*Annealing temperature*	φ	*Heating rate*
T_g	*Glass transition temperature*	$<D>$	*Average coherently diffraction length*
T_m	*Melting temperature*	$<\varepsilon^2>^{1/2}$	*Microstrain*
TTT	***T**ime-**T**emperature-**T**ransformation*		
T_{rg}	*Reduced glass transition temperature*		
T_{VF}	*Vogel-Fulcher temperature*		

ABSTRACT

This Thesis covers the synthesis and overall characterization of Ti-based glassy alloys and nanostructured materials. Several Ti-based nanostructured alloys with nominal composition, Ti-44.3Nb-8.7Zr12.3Ta, Ti-31.0Fe-9.0Sn, $Ti_{40}Zr_{20}Hf_{20}Fe_{20}$, $Ti_{45}Zr_{15}Pd_{35-x}Si_5Nb_x$ (x = 0, 5%), and Ti-based bulk metallic glass (BMG), $Ti_{40}Zr_{10}Cu_{38}Pd_{12}$, were investigated. These materials were chosen due to their potential applications as orthopedic implants. The first part of the study focused on the synthesis and characterization of these alloys by paying special attention to the correlation triangle microstructure-mechanical behaviour-biocompatibility. The second part was devoted to ion-irradiation treatment of the BMG material as a means to modify the surface properties and therefore increase its biomechanical compatibility.

All samples were produced by arc melting and subsequenct suction casting. The in-depth thermal and structural characterization of above-mentioned samples was carried out by means of differencial scanning calorymetry (DSC) and x-ray diffraction (XRD), together with scanning and transmission electron miscroscopies (SEM, TEM). Subsequently, the samples were subjected to mechanical (nanoindentation, acoustic measurement), electrochemical (potentiodynamic polarization tests) and biological (cytotoxicity, cell morphology, adhesion and differentiation) analysis.

It is shown that Ti-Nb-Zr-Ta nanostructured alloy is appealing because of its low Young's modulus (E_r = 71 GPa), whereas the Ti-Fe-Sn system is interesting because of its large hardness (H = 8.9 GPa). Meanwhile Ti-Zr-Pd-Si-Nb alloy possesses relatively low Young's modulus (E_r = 85 GPa) and high hardness (H = 10.4 GPa). The lowering of Young's modulus and the increase in hardness was achieved through proper combination of β-stabilizer elements (Nb, Ta, Fe and Pd) alloyed with Ti. Partial replacement of Pd by Nb is a convenient strategy to decrease the Young's modulus (almost a drop of 30% in E_r was observed) of the Ti-Zr-Pd-Si system, and to reduce costs. On the other hand, a microstructure consisting of a mixture of nanophases gives rise to large hardness values, as is the case of Ti-Zr-Pd-Si-(Nb) and Ti-Zr-Hf-Fe alloys. Additionally, all studied alloys exhibit better wear resistance than that of commercially used Ti-6Al-4V. None of the studied materials showed extensive corrosion damage when tested electrochemically, although pitting was observed in $Ti_{40}Zr_{10}Cu_{38}Pd_{12}$ BMG. The biological assays demonstrated that either preosteoblast mouse or human cells adhered very well to the surface of the studied

alloys and were able to differentiate into osteoblasts. This is due, to some extent, to the presence of safe (i.e., non-toxic) elements in alloys' composition.

In this Thesis, it is also demonstrated that for sufficiently low ion fluencies and low incident energies, the glassy structure of the as-cast $Ti_{40}Zr_{10}Cu_{38}Pd_{12}$ BMG is preserved after irradiation at room temperature (RT). Conversely, the same mild irradiation conditions applied at a temperature close to T_g (620 K) induce partial nanocrystallization at the surface of the material. As a consequence, the changes in mechanical properties observed after irradiation at RT (reduction of hardness and Young's modulus, presumably due to the increase of the free volume concentration) are opposite to those observed after temperature-assisted ion irradiation processes. Namely, an enhancement is observed after high-temperature irradiation of the Ti-based glassy alloy. Hence, these results indicate that, by tuning both the sample temperature and the irradiation conditions, the properties of the resulting material can be controlled in order to meet specific technological demands, such as mechanical performance.

RESUM

Aquesta Tesi comprèn la síntesi i caracterització d'aliatges de base Ti amorfs i nanoestructurats. Així, s'han estudiat diversos aliatges amb composició Ti-44.3Nb-8.7Zr12.3Ta, Ti-31.0Fe-9.0Sn, $Ti_{40}Zr_{20}Hf_{20}Fe_{20}$, $Ti_{45}Zr_{15}Pd_{35-x}Si_5Nb_x$ (x = 0, 5%) com a exemples d'aliatges de base Ti nanoestructurats, i el vidre amorf massís $Ti_{40}Zr_{10}Cu_{38}Pd_{12}$. Aquests materials es van escollir tenint en compte les seves potencials aplicacions com a implants ortopèdics. La primera part d'aquesta Tesi va consistir en la síntesi i caracterització d'aquests aliatges bo i fent especial èmfasi en les correlacions existents en el triangle microestructura – comportament mecànic – biocompatibilitat. En la segona part es van dur a terme tractaments d'irradiació amb feixos d'ions del vidre amorf com a estratègia per modificar les seves propietats superficials i, de retruc, incrementar-ne la compatibilitat biomecànica.

Totes les mostres es van sintetitzar per fusió d'arc i posterior emmotllament. Es va dur a terme una caracterització exhaustiva de tipus tèrmic i estructural de les mostres anteriorment mencionades mitjançant calorimetria diferencial d'escombrat (DSC), difracció de raigs X (XRD) i microscòpia electrònica de rastreig i transmissió (SEM, TEM). Tot seguit, els materials es van caracteritzar mecànicament (nanoindentació, mesures acústiques), electroquímicament (assaigs de polarització potenciodinàmica) i biològicament (toxicitat, morfologia, adhesió i diferenciació cel•lular).

S'ha vist que l'aliatge nanoestructurat Ti-Nb-Zr-Ta és interessant pel seu baix mòdul de Young (Er = 71 GPa), mentre que el sistema Ti-Fe-Sn destaca per la seva elevada duresa (H = 8.9 GPa). Ensems, l'aliatge Ti-Zr-Pd-Si-Nb posseeix un mòdul de Young relativament baix (Er = 85 GPa) i una duresa elevada (H = 10.4 GPa). En general, quan s'alien amb el Ti elements estabilitzadors tipus β (Nb, Ta, Fe i Pd), combinats d'una forma adient, s'aconsegueix reduir del mòdul de Young del material i, al mateix temps, incrementar-ne la duresa. La substitució parcial de Pd per Nb és una estratègia eficaç per disminuir el mòdul elàstic (es va observar una davallada de fins a un 30% en el valor de Er) del sistema Ti-Zr-Pd-Si i, simultàniament, reduir-ne el cost. D'altra banda, s'obtenen valors elevats de duresa, com és el cas dels aliatges Ti-Zr-Pd-Si-(Nb) i Ti-Zr-Hf-Fe, quan s'aconsegueix tenir una microestructura formada per una mescla de nanofases. Val a dir que tots els aliatges estudiats presenten una resistència al desgast superior a la de l'aliatge d'ús comercial Ti-6Al-4V. Així mateix, no s'ha observat un deteriorament significatiu dels materials en els

estudis de corrosió electroquímica, malgrat que es va detectar atac per picadura en el vidre amorf massís $Ti_{40}Zr_{10}Cu_{38}Pd_{12}$. Els assajos biològics van demostrar que tant les cèl•lules preosteoblast de ratolí com humanes s'adhereixen molt bé sobre la superfícies dels aliatges i que són capaces de diferenciar-se en osteoblasts, en part com a conseqüència de la presència d'elements no tòxics en la seva composició.

En aquesta Tesi també es demostra que per a fluències d'ions i energies incidents suficientment baixes, es preserva el caràcter amorf del vidre massís $Ti_{40}Zr_{10}Cu_{38}Pd_{12}$ després de la irradiació a temperatura ambient. En canvi, quan aquestes condicions d'irradiació s'apliquen a una temperatura propera a Tg (620 K), s'indueix una nanocristal•lització parcial a la superfície del material. Això fa que ocorrin canvis en les propietats mecàniques que són totalment oposats dels observats a temperatura ambient (reducció de la duresa i del mòdul de Young probablement a causa de l'increment de concentració del volum lliure). En particular, després del tractament amb feixos d'ions a alta temperatura, s'observa un increment tant de la duresa com del mòdul de Young. Els resultats indiquen, per tant, que bo i modulant tant la temperatura de la mostra com les condicions d'irradació, poden controlar-se les propietats del material resultant per tal de satisfer demandes tecnològiques específiques, com ara de tipus mecànic.

Introduction

1.1 Biomaterials for orthopedic applications

Due to the faster population aging, a concern related to the development of suitable materials for bone replacement is continuously arising [1, 2]. More than 50 million fractures occur worldwide every year, most from accidents, falls and activity-related injuries and most occurring primarily in the under-65 population. Annually, more than eight million fracture repair procedures (open and closed reduction with and without fixation, internal fixation without reduction, application of external fixator, etc.) are performed globally, most often on the radius/ulna, wrist/hand, tibia/fibula and ankle/foot. It is reported that world-wide sales of orthopedic implants alone in 2003 represented a most of €6.4 billion, while the orthoworld's, orthopedic industry report states that in 2012 the worldwide orthopedic product sales reached €31.6 billion [3, 4]. In this scenario, the aim of current investigations is to develop orthopedic implants that can stand for longer periods of time or even the entire lifetime without failure or need for a revision surgery [5].

1.1.1 Currently used materials and their limitations

Permanent implant alloys are typically divided into three types of materials systems: stainless steels, cobalt-chromium-molybdenum based alloys and titanium alloys, whose main features are described below [6]:

- **Austenitic stainless steel** – the most commonly employed steel alloys are 316 and 316L grades [3]. These alloys exhibit good strength and ductility. Amongst both types, the 316L one is preferred by the American Standard Test Method (ASTM) for implant fabrications due to the presence of lesser carbon amount. In 316L, the probability of chromium carbide precipitation decreases and consequently intergranular corrosion can be avoided. Yet, studies on retrieved implants show that more than 90% of failure in 316L implants occur because of pitting and crevice corrosion attack [7]. The surgical grade 316L implants unavoidably corrode in the human body and release Fe, Cr and Ni ions which are prone to cause allergy and induce carcinogenicity [8].

- **Cobalt-chromium-molybdenum** – these alloys are being used in orthopedic implants due to their hardness, strength and resistance to corrosion and wear. There are two different types of Co-Cr-Mo materials currently in use: cast (low carbon), and wrought (high carbon) alloys [9, 10]. Each variety has a different microstructure and, in turn, different properties which make them best suited to meet a specific design or function. For instance, the cast Co-Cr-Mo alloys show lower ductility compared to the wrought Co-Cr-Mo alloys [11]. Moreover, for the orthopedic implant applications requiring high corrosion fatigue strength, cast Co-Cr-Mo alloy is less suitable than the wrought products [12]. However, these alloys have also some disadvantages. Namely, immerse studies conducted in simulated body fluids (e.g. Hank's salt solution), have shown that cobalt dissolves from the surface and is released to the solution, leaving simultaneously the remaining surface rich in molybdenum oxide (Mo^{+4}, Mo^{+5} and Mo^{+6}). This effect is not accepted by the body fluids and causes inflammatory reaction in the system [13].

1.1.2 Titanium and its alloys

Currently, titanium and its alloys are extensively applied in the biomedical field as implants and devices. Particularly appealing are Ti alloys, which replace hard tissues and cardiac and cardiovascular valves [14]. Its uniqueness comes from their outstanding physical and mechanical properties, such as low density, relatively low Young's modulus, good fatigue strength, formability and machinability [15, 16]. In addition, they exhibit excellent resistance to most environments and superior biocompatibility that derives from the existence of a natural protective oxide layer, consisting mainly of TiO_2 [2]. For all these reasons, Ti and its alloys have become the materials of choice for bone replacement and fixation.

One of the most common applications of titanium and its alloys are artificial hip joints consisting of an articulating bearing (femoral head and cup) (Figure 1). Moreover, they are often used in knee joint replacements, which consist of a femoral component, tibial component, and patella, as well as in dental implants [17–19]. Most of the dental implants inserted are based on the osseointegration concept that allows dental implants to blend with bone. In order to get an answer for the excellent properties of Ti and its alloys, one has to look into their structural characteristics. Titanium can exist in two allotropic forms. At low temperatures atoms are

disposed forming a hexagonal closed–packed (hcp) crystal lattice, which is commonly referred to as α-phase, while above 883 °C atoms are arranged in a body–centered cubic (bcc) crystal structure, known as β-phase [20]. The α-to-β transformation temperature, $T_{\alpha-\beta}$, in Ti alloys can either increase or decrease depending on the alloying elements [20]. Elements such as Al or O tend to stabilize the α-phase by increasing $T_{\alpha-\beta}$ and are termed α-stabilizers. Conversely, other elements stabilize the β-phase (e.g., V, Nb, Fe) by decreasing $T_{\alpha-\beta}$. Some elements, like Sn or Zr, behave as neutral solutes and have little effect on the transformation temperature, acting instead as strengtheners.

In general, addition of β-stabilizer alloying elements causes a lowering of the Young's modulus, an improvement of the alloy formability and an enhancement of the corrosion resistance [21]. This makes β-Ti alloys better suited for biomedical applications than α-Ti alloys. It has been shown that Nb, Zr, Ta, Sn or Fe are suitable alloying elements to reduce the Young's modulus of β-Ti without compromising the strength. These elements are non-toxic and can thus be safely used for implant applications [22].

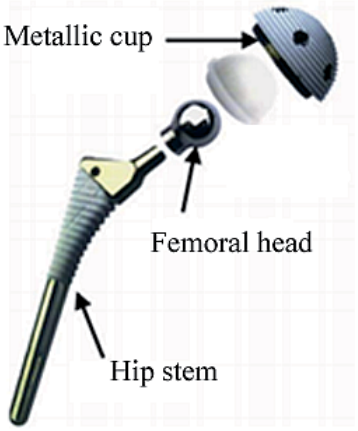

Figure 1: *Schematic diagram of an artificial hip joint [1].*

1.2 General requirements of biomedical implants

1.2.1 The bone - implant interface

The research field of bone tissue engineering encompasses the development of functional biomaterials for damaged hard tissue replacements (these include bones, teeth and cartilages). An appropriate combination of the following three key elements:

(a) cells

(b) a scaffold or carrier material (implants)

(c) bone stimulating molecules (e.g. growth factors)

is crucial for the bone to heal, sustain and improve bone tissue functions [23–25]. According to medical terminology, bone tissue is a living organ defined as a natural complex composed of an organic matrix fortified by an inorganic calcium phosphate (CaP) phase [26, 27]. The extracellular organic matrix (ECM) of bone consists of 90% collagenous proteins and 10% non-collagenous proteins. Carbonate rich hydroxyapatite is considered to be the most opulent mineral phase in human bone [28]. This calcified matrix is a scaffold for bone cells (osteoblasts, osteoclasts and osteocytes) helping in bone maintenance and organization (Figure 2). Bone remodeling mechanism relies on removing bone from one region and forming it in another place, and this is the function of the osteoclasts and osteoblasts, respectively [29]. Osteoclasts are bone-resorbing cells, while osteoblasts are bone-forming cells. Finally, osteoblasts transform into osteocytes, and those mature cells further form bone to some degree, which is important for maintaining the strength and health of the bone matrix. A balance between bone production and bone resorption is necessary for remodeling and renewing the skeleton [30].

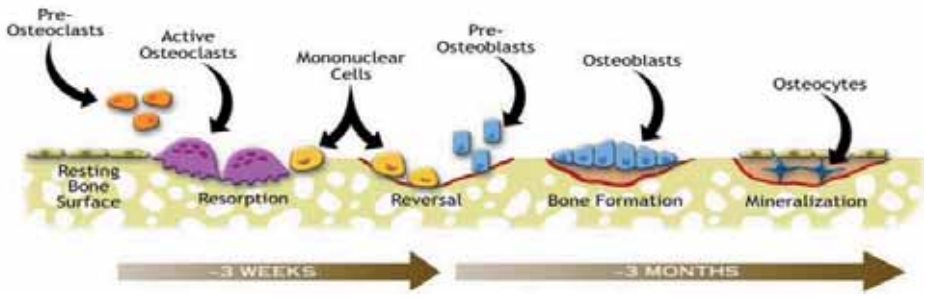

Figure 2: *Bone remodeling cycle [31].*

The substitution of the damaged hard tissues with artificial replacements is deeply related with the region in which the implant is to be inserted and the functions that can potentially provide. Therefore requirements of a given biomaterial will differ.

For implant fixation in bones, two methods are currently employed: (i) bone cement fixation and (ii) cementless implantation. The direct cementless anchoring of the prosthesis to the bone through osseointegration is recently the most frequently applied. However, the cementless prostheses require an optimal surface structure and composition to enable good osseointegration between the implant and the bone. Thus, it is desirable to design implants with structures and shapes that may enhance cellular activity and direct bone apposition (osseointegration). For example, Buser et al. evaluated the influence of different surface characteristics on bone integration in the case of titanium implants [32]. The highest extent of bone-to-implant contact was observed in etched surfaces produced by blasting or etching. Meanwhile Simmons [33] stated that initial matrix mineralization leading to osseointegration occurred more rapidly on porous-surfaced implants. Also, Yang et al. showed that osteoblast-like cells grew more rapidly into the pores and formed the extracellular matrix faster [34]. These results suggest that rough surfaces and porous coatings promote osseointegration. Surface roughness can be classified according to the scale of the irregularities at the material surface: (i) macroroughness refers to irregularities already visible at naked eye (from 100 μm to millimeters or more in size); (ii) microroughness refers to irregularities between 100 nm – 1 μm; (iii) nanoroughness refers to irregularities with sizes less than 100 nm [35]. Macroroughness seems to be favorable, because the relatively large irregularities may mechanically enhance the anchorage of the implant to the surrounding bone tissue. Simultaneously, the irregularities are too large to be felt by the cells (i.e. the cells can have enough space to spread on the irregularities or between them). Thus, macroroughness usually does not hinder cell adhesion and spreading.

Besides osseointegration, there are other issues which should be considered to increase the lifetime of a potential implant. These are the biocompatibility, the mechanical properties of the implant (e.g. hardness and Young's modulus) and its corrosion resistance in body fluids.

1.2.2 Biocompatibility

Strictly speaking, the biocompatibility of bone replacement materials is associated with osteoblast behavior in contact with the implant and, specifically, to their adhesion and spreading onto the implant surface [36]. This behavior affects the osteoblast's capacity to proliferate and to

differentiate themselves upon contact with the implant. Those processes are crucial for the establishment of a mechanically solid interface with complete fusion between the implant surface and bone tissue without any intermediate fibrous tissue layer. The materials used as implants are expected to be highly non-toxic; therefore elements such as Al, V, Ni, Co have to be avoided [37, 38]. For the cells to divide, previous spreading on the growth substrate is required. In addition, cells can even experience anoikis, i.e. a specific type of apoptosis caused by adhesion deprivation [39]. Cell spreading stimulates cell proliferation by at least two mechanisms, i.e. biochemical and mechanical pathways [40]. Biochemical mechanism is seen as a complex process mediated by transmembrane proteins called integrins, which cluster to form focal adhesions. The mechanical mechanism is related with changes in the tension of the actin cytoskeleton [41]. The actin fibers are tied to the structural components of the adhesion sides, also called the membrane cytoskeleton. It is still under question the correlation of the switching between the proliferation and differentiation programs and the maturation status of the adhesion plaques. Zaidel-Bar et al. systemized the cell–matrix adhesion structures into the following three types: less mature *focal complexes*, which drive cell spreading and migration, more mature *focal adhesions*, mediating robust adhesion of the cell to the extracellular matrix, and the most mature structures called *fibrillar adhesions*, which are involved in matrix remodeling [42]. Cytotoxicity can be measured indirectly, that is, culturing cells in the presence of a solution that has been previously in contact with a specific material, or directly, growing the cells on top of the material [43]. The success of a biomaterial is mainly dependent on the reaction of the human body to the implant, and this measures the biocompatibility of a material [44].

1.2.3 Mechanical properties

It is well known that orthopedic implants are subjected to loads during their life cycle after their insertion into the body. The most important mechanical properties that help to decide the type of material to be used as orthopedic implant are hardness, Young's modulus, yield strength, wear resistance, elastic recovery and resilience [45]. Herein we provide a brief definition of each property:

- **Hardness**: is the measure of how resistant a solid material is to various kinds of permanent shape change when a force is applied. This property can be evaluated by different techniques like scratch hardness, indentation hardness and rebound hardness. Hardness and also strength are measures of material's resistance to localized plastic deformation.

- **Young's modulus**: also called tensile modulus or elastic modulus, it is a measure of the stiffness of a material in the elastic regime.
- **Yield strength**: is the stress at which a material begins to deform plastically. Prior to the yield point the material will deform elastically and will return to its original shape when the applied stress is removed. Once the yield point is passed, some fraction of the deformation will be permanent and non-reversible.
- **Elastic recovery**: is a period of slight rebound in a material after a load has been removed.
- **Resilience**: is the ability of a material to absorb energy when it is deformed elastically, and release that energy upon unloading.

Implant fracture due to mechanical failure is related to the concept of biomechanical incompatibility. Ideally, the material employed to replace the bone should have similar mechanical properties to that of bone. For instance, the bone Young's modulus varies in the range from 4 to 30 GPa depending on the bone type and direction of measurement [46, 47]. Pronounced stress transfer between the implant and bone can cause resorption and subsequent implant loosening. This biomechanical mismatch, known as stress-shielding effect, can result in the death of the bone cells and occurs when the stiffness (or the Young's modulus) of the implant is much higher than that of the bone [48, 49].

Additionally, wear resistance also plays a crucial role when considering the mechanical behavior of an implant. Wear always occurs in the articulation of artificial joints as a result of the mixed lubrication regime. For example, the movement of an artificial hip joint produces billions of microscopic particles that are rubbed off during motions [50, 51]. These particles are trapped inside the tissues of the joint capsule and may lead to unwanted foreign body reactions. Therefore, the search for materials with high wear resistance attracts a lot of scientific interest, especially for load-bearing implants.

1.2.4 Corrosion resistance

A large number of chemical reactions in a human body are performed to maintain the viability of the system. When a metallic implant is inserted into the body, it gets exposed to the body fluid system and to the products of these reactions (e.g. chloride ions and proteins). It is well known that these products are potentially dangerous for metals and the immunity of the implant greatly depends on the constituent elements of the metallic implant. Broadly speaking, all metallic

implants electrochemically undergo some degree of corrosion [52]. Some alloys like stainless steel may corrode faster, while other metals like platinum or gold are tremendously corrosion resistant [53–55]. During the corrosion process, oxidation–reduction reactions take place, in which the metallic components of the alloy are oxidized to their ionic forms and the dissolved oxygen is reduced to hydroxide ions [5]. Two physico-chemical factors control the corrosion of the metal implant, i.e., (i) the strength of the thermodynamic driving forces, which provoke corrosion (oxidation/reduction reactions), and (ii) the existence of physical barriers such as surface oxide layers which slow down the kinetics of corrosion [56–57]. There are some additional factors which influence the corrosion process (e.g. pH) [58]. The effect of pH on the oxidation state of a given element when it is exposed to natural water is given by Pourbaix diagrams (Figure 3). This is a potential versus pH diagram (E_H-pH diagram) which predicts possible stable (equilibrium) phase of an aqueous electrochemical system. A simplified Pourbaix diagram provides the regions of "immunity", "corrosion" and "passivity" and can therefore predict the stability of a particular metal in specific conditions (environment). Hence, the *immunity* stands for the intact form of the metal; the *corrosion* shows the general attack and *passivation* occurs when the metal forms a stable coating of an oxide or another salt on its surface. Several techniques have been employed to investigate the corrosion behavior of implant materials in the laboratory. In order to replicate the real environment of the body fluids, the *in vivo* method can be applied to test the implant; however this method hinders the possibility to monitor the electrochemical processes and, in turn, investigate the degradation mechanism. Therefore the *in vitro* testing is the preferred method for the monitoring of the degradation processes and the development of new implant materials [59]. *In vitro* corrosion studies on orthopedic biomaterials are carried out in solutions that mimic body fluids (e.g. Hank's or Ringer's solutions) [59–61]. All are inorganic salt solutions that approximate the inorganic constituents in body solutions. They are isotonic solutions with the same salt concentration as cells and blood. Isotonic solutions are commonly used as intravenously infused fluids in hospitalized patients [60].

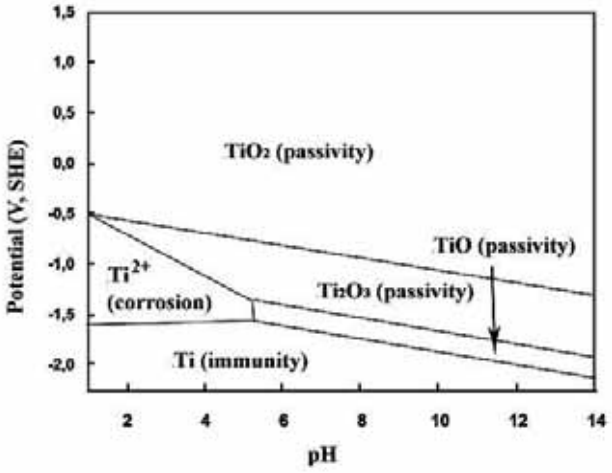

***Figure 3**: The Pourbaix diagram for titanium [62].*

The *in vitro* testing of the corrosion performance of a metallic implant can be evaluated electrochemically by potentiodynamic polarization methods. In this way, several relevant parameters like the open circuit potential (E_{OCP}), corrosion potential (E_{corr}), corrosion current density (j_{corr}) and polarization resistance (R_P) can be determined by Tafel analysis of the potentiodynamic polarization curves.

- *Tafel extrapolation*

The Tafel extrapolation method can be used to assess the corrosion rate of a metal when metallic dissolution is under activation control [63]. The most common application is for metals immersed in de-aerated acid solutions for which the anodic reaction for a bivalent metal is:

$$M \rightarrow M^{2+} + 2e^- \qquad \text{(Eq. 1.1)}$$

and the cathodic reaction is:

$$2H^+ + 2e^- \rightarrow H_2 \qquad \text{(Eq. 1.2)}$$

The semi-logarithmic plot in Figure 4 is not linear near the open-circuit potential (i.e. near zero overpotential). This is because the other half-cell reaction is still appreciable and contributes to the total current. However, at sufficiently high overpotentials, the contribution of the reverse reaction becomes negligible. In this linear Tafel region, the straight lines shown in Figure 4, can be extrapolated back to zero overpotential (i.e., back to E_0) to give the open-circuit exchange current density j_0.

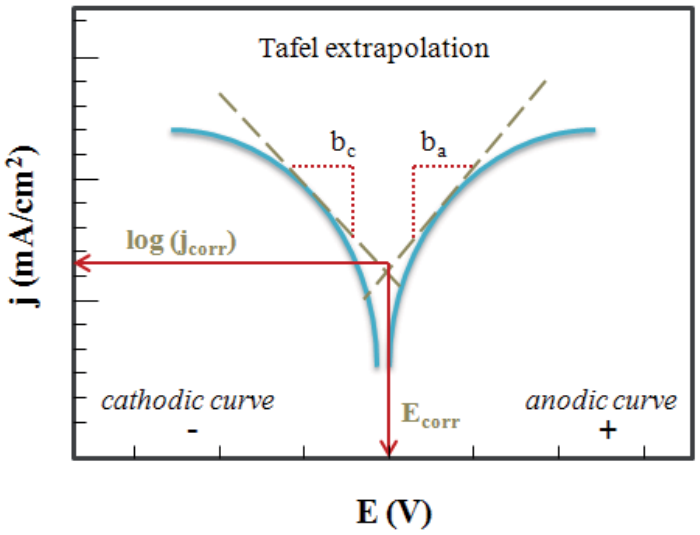

***Figure 4**: Semilogarithmic representation of polarization curves for corrosion under activation control (Tafel behavior).*

The well-known Tafel equation follows from the Butler-Volmer equation:

$$j_{net} = j_0[e^{\frac{\alpha nF(E-E_0)}{RT}} - e^{\frac{-(1-\alpha)nF(E-E_0)}{RT}}] \quad \text{(Eq. 1.3)}$$

At sufficiently high overpotentials, the rate of the reverse reaction becomes negligible so that Eq. 1.3 can be written as:

$$j_{net} = j_0[e^{\frac{\alpha nF(E-E_0)}{RT}}] \quad \text{(Eq. 1.4)}$$

or simply as:

$$j = j_0[e^{\frac{\alpha nF(E-E_0)}{RT}}] \quad \text{(Eq. 1.5)}$$

Taking logarithms in Eq. 1.5:

$$\log j = \log j_0 + \frac{\alpha nF(E-E_0)}{2.303 \cdot RT} \quad \text{(Eq. 1.6)}$$

Thus, a plot *log* $|j|$ vs. the overpotential (E-E_0) (or log $|j|$ vs. the electrode potential E) gives a straight line, as shown in Figure 4. From Eq. 1.6 when $E = E_0$, then $j = j_0$. Thus, the Tafel region can be extrapolated back to $E = E_0$ to give the exchange current density j_0, as shown in Figure 4.

Equation 1.6 can also be written as:

$$\eta_a = b_a \log \frac{j}{j_0} \quad \text{(Eq. 1.7a)}$$

Which is one form of the Tafel equation, where η_a is the anodic overpotential and b_a is the anodic Tafel slope given by:

$$b_a = \frac{2.303 \cdot RT}{\alpha n F} \quad \text{(Eq. 1.7b)}$$

Similar considerations also hold for the cathodic branch of the polarization curve. For the cathodic direction, when the back reaction (now the anodic reaction) becomes negligible, Eq. 1.3 produces a cathodic Tafel region which can also be extrapolated back to $E = E_0$ to give the exchange current density j_0, as also shown in Figure 4. Moreover Eq. 1.3 leads to:

$$\eta_c = b_c \log \frac{j}{j_0} \quad \text{(Eq. 1.8a)}$$

Where η_c is the cathodic overpotential and b_c is the cathodic Tafel slope

$$b_c = -\frac{2.303 \cdot RT}{(1-\alpha) n F} \quad \text{(Eq. 1.8b)}$$

From Figure 4, it can be easily seen that cathodic Tafel slopes have negative signs and the anodic Tafel slopes have positive signs. Tafel slopes have the units of volts or millivolts per decade of current density. The Tafel slope is always defined as $dE/d \log |j|$. If a well-defined Tafel region exists, as in Figure 4, the anodic and cathodic Tafel regions can be extrapolated back to zero overpotential. The intersection of the anodic and cathodic Tafel slopes gives the corrosion potential E_{corr} and the corrosion current density j_{corr} as indicated in Figure 4. Linear Tafel regions are usually observed for potentials 59 – 120 mV away from the open-circuit potential.

$$R_P = 2.303 \frac{b_a b_c}{b_a + b_c} \left(\frac{1}{j_{corr}}\right) \quad \text{(Eq. 1.9)}$$

If the Tafel slopes are known, one can calculate a qualitative parameter which is related to corrosion resistance, the so-called polarization resistance from the equation above.

- *Passive layer and pitting*

The presence of a passive layer on the surface of the majority of metallic implants (e.g. Ti), reduces the risk of corrosion. Besides the eventual formation of a passive layer, the type of alloying elements also influences the corrosion resistance. Different factors contribute to the corrosion performance of orthopedic materials: metallurgical factors (e.g. surface microstructure,

oxide structure and composition), mechanical factors (e.g. stress or relative motion) and electrolyte variables (e.g., pH, proteins and enzymes) [64].

A material intended for implant applications should be free from toxic and allergenic elements and should not be extensively affected by either generalized or localized (pitting) corrosion. For this purpose, interest is laid on designing suitable alloy compositions, microstructures (and crystallite sizes) that make the material immune in a body fluid environment.

1.3 Structural considerations

1.3.1 Metallic glasses (MGs)

By definition, a metallic glass (MG) is vitrified liquid obtained from the melt upon rapid cooling. MG form when the melt does not have enough time to crystallize upon cooling. MGs generally exhibit a glass transition, although, there are some exceptions (e.g. bulk $Nd_{70}Fe_{20}Al_{10}$ with 7 mm in diameter [65, 66] or some ribbon shape alloys). From the structural viewpoint, glassy materials are considered as amorphous solids that do not possess long–range crystallographic order (periodicity) (Figure 5a). This means that their constituent atoms are not arranged in an order (regular or periodic) manner in the three dimensions. Conversely, a crystalline solid exhibits a long–range order (LRO) structure (Figure 5b). Compared with conventional crystalline materials, metallic glasses possess neither grain- nor phase- boundaries [67].

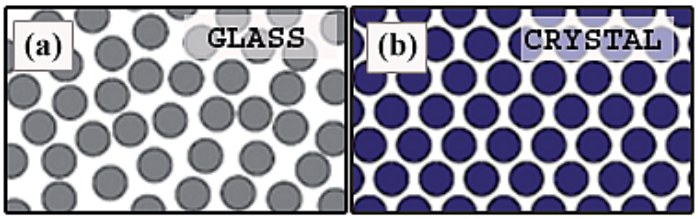

Figure 5: *Sketch presenting the structural arrangement of atoms in (a) glass and (b) crystal.*

Evidence for amorphicity is experimentally obtained from the presence of broad halos in the corresponding X-ray diffractograms (XRD) (Figure 6a). Also, differential scanning calorimetry (DSC) can help to prove the amorphous character of a given material (Figure 6b). Nevertheless, the most accurate technique is the high-resolution transmission electron microscopy (HR-TEM), by which one can observe the typical "salt – pepper" pattern (Figure 6c) and a broad diffuse halo ring in the selected area electron diffraction (SAED) pattern (inset Figure 6c).

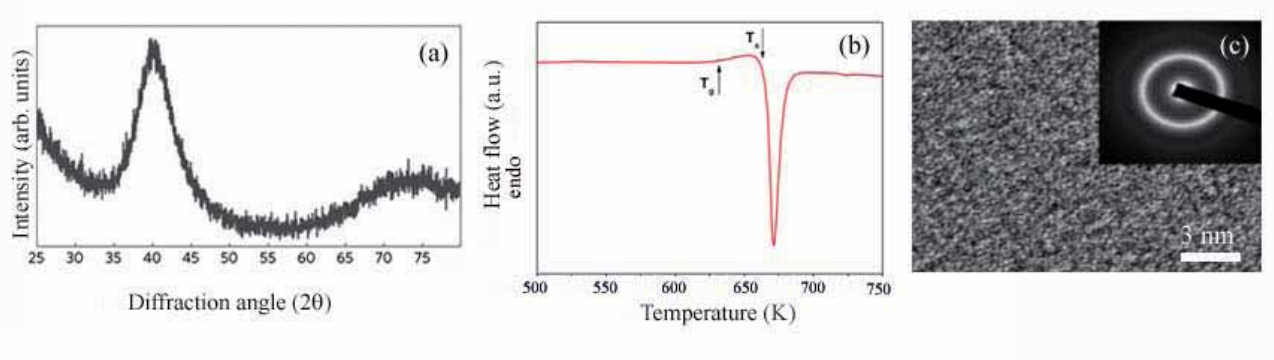

Figure 6: Typical (a) XRD pattern, (b) DSC curve [68] and (c) TEM black-white image, together with the SAED pattern of a metallic glass material [69].

The history of amorphous materials dates back to 1960', when Pol Duwez synthesized for the first time Au-25%Si alloy in a glassy state, by quenching the liquid at a very high cooling rate (10^6 K/s) [70, 71]. Since then, a large number of alloys of different compositions have been prepared as MGs. MGs exhibit outstanding physical, chemical, and mechanical properties, making them unique, and their extraordinariness stems from the "disordered" atomic arrangement.

1.3.1.1 The formation of glass structure

Basically, a liquid can solidify as a crystal or form a glass. Some considerations can be made regarding the difference between crystal and glass formation on the basis of the temperature dependence of the volume, viscosity and specific heat (Figure 7).

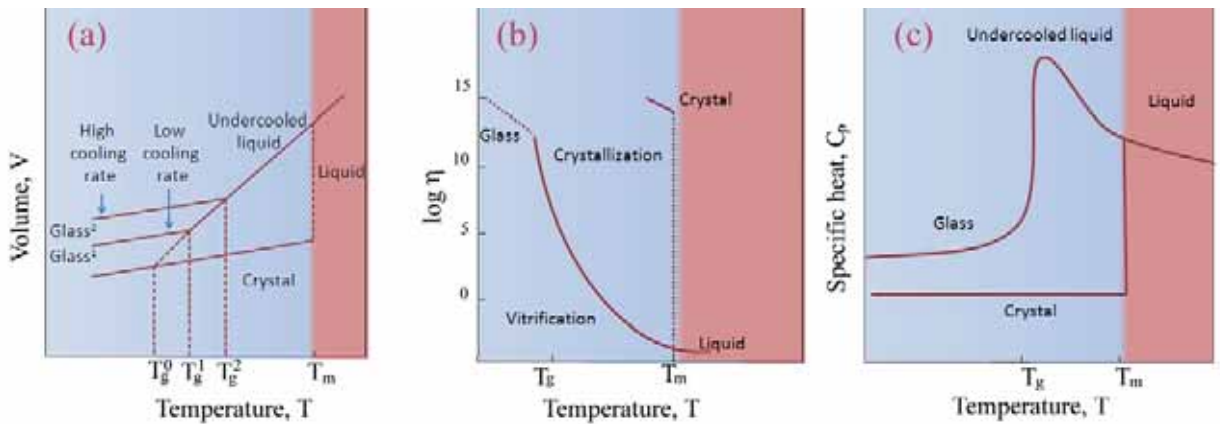

Figure 7: Variation of (a) volume, (b) viscosity and (c) specific heat with temperature for crystal and glass formation.

Generally speaking, for a liquid to undergo crystallization, undercooling below the equilibrium crystallization temperature is required. However, this is not sufficient to guarantee that crystallization takes place. There is an energy threshold that the liquid molecules have to overcome in order to be able to form the first crystals from the liquid. Therefore, the degree of undercooling plays a crucial role in the whole amorphization process. Besides, there are other factors which influence the amorphization process: viscosity of the liquid, interfacial energy between the melt and the crystal, the cooling rate and the existence of heterogeneous sites.

Figure 7a depicts how the volume decreases with the decrease of temperature for glass and crystal liquids. In case of glass forming liquids, the volume continuously decreases even in the undercooled region. Simultaneously, the viscosity increases until reaches very high values. At this point, the liquid gets "frozen-in", and this is defined as a glass (Figure 7b). The temperature at which the viscosity of the undercooled liquid reaches values of 10^{12} Pa·s is believed to be the glass transition temperature, T_g (Figure 7b) [72]. Actually, the exact glass transition temperature when this phenomenon occurs is not clearly defined, but is rather a function of the experimental conditions. For example, Nieh and co-workers stated that the slower cooling rate, the lower is the value of the glass transition temperature [73] (Figure 7a). In addition, Kauzmann found out that there is a temperature interval, in which the liquid becomes a glass. This range is called "glass transformation interval" [74].

Figure 7c shows that the specific heat increases with decreasing temperature until it reaches the T_m. From here glass and crystal can be distinguished by the difference in specific heat. A pronounced drop of specific heat, C_p, is observed below T_g for glasses. This is due to the fewer degrees of freedom existing in the "frozen" configuration of the metallic glass.

1.3.1.2 The concept of crystallization

- *Nucleation and growth of crystal*

The knowledge of crystallization process of glass forming alloys is of great importance in order to improve the glass forming ability. Crystallization consists of two processes: *nucleation* and *growth*. *Nucleation* is an initial stage of crystallization that relies on the formation of primary phase made of new small-size nuclei entirely from the liquid (often consisting of only a few hundred atoms). On the other hand, *growth* is a major stage of crystallization, which involves the increase in size of these nuclei leading to the disappearance of the primary phase.

- *Classical nucleation theory*

There are two types of nucleation: *homogeneous* and *heterogeneous*, which are distinguished according to the nucleation sites on the surface. The *homogeneous* type refers to the uniform distribution of the nuclei of the new phase throughout the primary (former) phase, whereas the *heterogeneous* nucleation is formed on preferential nucleation sites (e.g. insoluble impurities, container surface, grain boundaries, dislocations, etc.).

The classical nucleation theory [75–78] is explained by the equation:

$$\Delta G = -\frac{4\pi}{3} r^3 \Delta g_v + 4\pi r^2 \gamma \qquad \text{(Eq.1.10)}$$

Where Δg_v is the difference in Gibbs free energy between the unit volume of the solid and the liquid, and γ refers to the interfacial free energy between the solid and the liquid.

Basically, nucleation is favored when ΔG has a negative value. It is postulated that the free energy difference of a nucleus consists of a negative term for the volume of the nucleus, $-\frac{4\pi}{3} r^3 \Delta g_v$, and a positive term that accounts for the interfacial area between the nucleus and the liquid, $4\pi r^2 \gamma$, (Eq.1.10). This is only valid for spherical nucleus with radius r.
As a consequence, a nucleus with r higher than the critical radius r^* will decrease its energy by increasing r (i.e. by growing) (Figure 8). The free energy barrier for nucleation is given by [79, 80]:

$$\Delta G^* = \frac{16}{3}\pi \frac{\gamma^3}{(\Delta g_v)^2} \qquad \text{(Eq.1.11)}$$

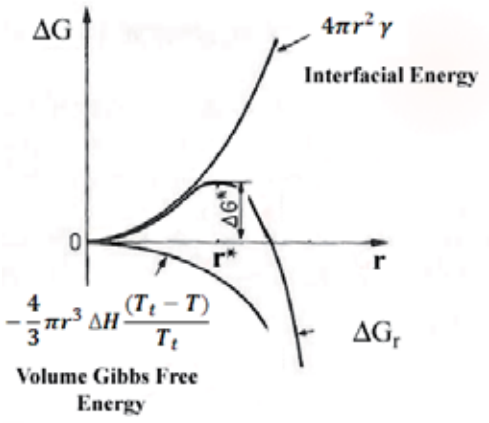

Figure 8: *Free energy change, ΔG, accompanying the formation of a spherical particle of a new phase as a function of radius, r.*

In case of heterogeneous nucleation, critical nucleus may appear at much smaller undercooling. Compared to ΔG^* (Eq. 1.11) the thermodynamic barrier to heterogeneous nucleation, ΔG^*_{het}, is reduced by a factor, the so-called wetting function:

$$f(\theta) = \frac{(2+cos\theta)(1-cos\theta)^2}{4} \quad \text{(Eq.1.12)}$$

The free energy, ΔG^*, of the critical nucleus can be regarded as the activation energy for nucleation in an Arrhenius equation for the steady–state nucleation rate, I_v [76]:

$$I_v = Ae^{\frac{-\Delta G*}{k_B T}} \quad \text{(Eq.1.13)}$$

The kinetic prefactor, *A*, accounts for the number of potential sites for heterogeneous or homogenous nucleation, as well as the temperature dependence of the mobility in the liquid, while k_B is the Boltzmann constant. Above the liquidus temperature, the liquid is thermodynamically stable and therefore no crystals can be created, thus the nucleation rate is equal to zero. As the liquid is undercooled below the liquidus temperature, the thermodynamic driving force for crystallization increases, i.e., Δg_v, becomes more negative. This leads to a reduction of the nucleation barrier, ΔG^*, and hence the nucleation rate increases. However, close to the glass transition (T_g), the nucleation rate decreases again as the mobility in the liquid decreases rapidly with lowering temperature. Assuming that the relevant mobility for nucleation is proportional to the fluidity of the liquid, the temperature dependence of the kinetic prefactor can be described by the Vogel-Fulcher equation for viscosity, $A\,(T) = A'/\eta\,(T)$ with:

$$\mathrm{A}' = \frac{N k_B T}{3\pi r_{at}^3}\pi \quad \text{(Eq.1.14)}$$

Where *N* is the number of potential nucleation sites and *r* is the atomic radius, then:

$$\eta = \eta_\infty \exp\left(\frac{DT_{VF}}{T-T_{VF}}\right) \quad \text{(Eq.1.15)}$$

where η_∞ is the high temperature limit of the viscosity, *D* is the fragility index, and T_{VF} is the Vogel-Fulcher temperature [81].

- *Crystals growth*

As aforementioned, crystal growth is a series of processes ascribed to an aggregation of atoms onto the surface of a crystal, causing an increase in crystal size. A velocity through which atoms come from the liquid to the crystal-liquid boundary is expressed by factor *u*:

$$u\,(T) = \frac{k}{\eta}\left(1 - \exp\left(\frac{-\Delta g_v}{k_B T}\right)\right) \quad \text{(Eq.1.16)}$$

Following the Johnson-Mehl-Avrami transformation kinetics, the fraction of transformed phase, x, in time, t, is given by:

$$x \sim \frac{\pi I(T) u(T)^3 t^4}{3} \qquad \text{(Eq.1.17)}$$

- *TTT diagrams*

The concept of the temperature dependence of transformation kinetics can be easily explained by the time–temperature–transformation diagram (TTT–diagram) (Figure 9). The C-shaped transformation curve is a useful tool to foresee the time necessary to initiate a formation of the stable (crystalline) solid state (*X*-axis) in a specified temperature (*Y*-axis). The "nose" of the TTT curve determines the higher transformation rates at intermediate temperatures and the lower ones at higher temperatures. It is possible to determine the critical cooling rate, R_c, using a TTT curve to prevent from crystallization. In approximate terms, R_c is given by the slope of the tangent that passes through the melting point at $t = 0$ [82–84].

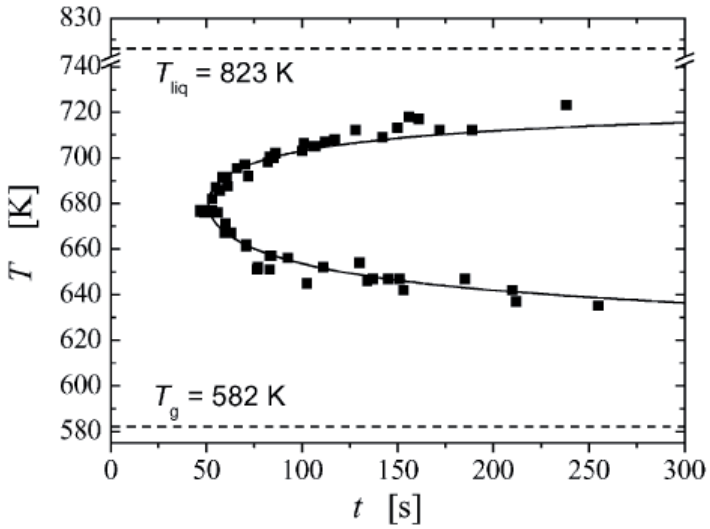

Figure 9: *Schematic time – temperature – transformation (TTT) diagram for $Pd_{40}Cu_{30}Ni_{10}P_{20}$ metallic glasses [82].*

1.3.1.3 Glass forming ability

It is commonly believed that a glass is not in a thermodynamically stable state (equilibrium), and that the thermodynamic principles are essentially applied only to systems in equilibrium. Yet, some considerations can be made especially for the system in undercooled liquid regime. For

understanding the fundamentals of glass formation to further design bulk metallic glasses (BMGs), knowledge about glass forming ability (GFA) is essential. The concept of GFA of a liquid is based on the critical cooling rate. This is the minimum cooling rate that allows the melt to be kept in amorphous state without any crystal precipitates upon quenching (solidification). Generally, GFA should be higher for smaller R_c. Nevertheless, R_c is not practically used for a precise assessment of GFA. There are other criteria much more convenient to determine GFA for different MGs. These criteria are associated with the characteristic temperature in DSC analysis. At present, the reduced glass transition temperature T_{rg} (glass transition temperature over liquidus temperature T_l) and the supercooled liquid region ΔT_{xg} (the temperature difference between the onset crystallization temperature T_x and the glass transition temperature T_g) are very often applicable. Turnbull [76] concluded that the reduced temperature, T_{rg}, must be close to 2/3 to obtain the amorphous state on the basis of the relationship between the nucleation ratios of crystals in amorphous state and the temperature, together with viscosity. According to Lu [85] the reduced glass transition temperature T_{rg} shows a better correlation with the GFA than that given by T_g/T_m for BMG (T_m: melting point). Nevertheless, both ΔT_{xg} and T_g/T_m show a good correlation with GFA. The larger ΔT_{xg}, the poorer glass formers. Finally, Inoue put forward three empirical rules according to which an alloy should tend to become amorphous [86]:

(a) The alloy should contain at least three elements;
(b) Difference in atomic size ratios should be higher than about 12% among the three main constituent elements;
(c) The heat of mixing among (major) constituent elements should be negative.

1.3.1.4 Structure of metallic glasses

The structure of metallic glasses combines two features that make these materials particularly interesting: *the packing fraction* is as high as in most crystalline phases, and they exhibit *liquid-like disorder* in atomic coordination. Several models have been suggested for the atomic packing system of metallic glasses like Bernal's [87], Polk's [88] and Gaskell's [89]. Nevertheless, the Miracle's concept has been found the most adequate until now [90–92]. Miracle described BMGs using a new sphere-packing scheme, i.e. a dense packing of atomic clusters composed of solute and solvent atoms. This model shows only three topologically different solutes with well-defined and predictable sizes relative to the solvent atoms. Besides, this model contains defects that also influence the structure of metallic glasses. It is also possible to foresee the number of solute

atoms in the first coordination shell of solvent atoms. This model allows predicting metallic glasses for a large number of alloys featuring both simple and complex compositions. Figure 10 schematically illustrates a cluster (group of atoms) consisting of a primary solute α, surrounded by the solvent atoms Ω. Besides, two topological distinct solutes can be located in the cluster and this is related with the geometry of the atomic system: the secondary β solute atoms that occupy cluster-octahedral interstices and the tertiary γ solute that occupies cluster-tetrahedral interstices (arrow in Figure 10b). In this model, the adjacent clusters share solvent atoms in common faces, edges or vertices so that neighboring clusters overlap in the first coordination shell leading to medium range order (MRO) and dense packing in three-dimensional spaces. From all the above, the structure of metallic glass is considered as a dense packing of overlapping atomic clusters and so those models allow us to understand metallic glass properties from a structural point of view.

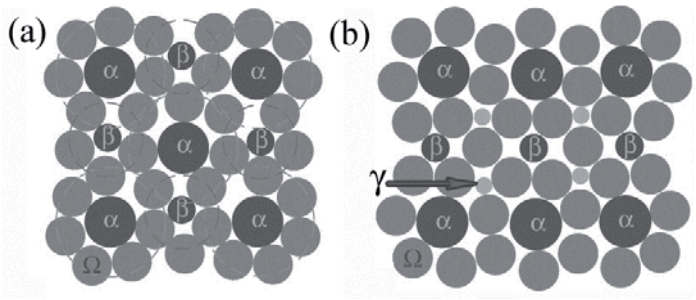

Figure 10: *Schematic two-dimensional representation of a denser cluster-packing structure of clusters in (a) (100) plane and (b) (110) [92].*

- *Free volume*

The free volume is another concept for a structural understanding of the glass state. The term free volume was originally established by Cohen and Turnbull for liquids [76–77] and later the concept was applied to metallic glasses by Spaepen [93]. The free volume model (FVM) refers to the atomic mobility of amorphous solids taking into account the free volume available for the atoms. The probability for the atom to be surrounded by a free volume threshold (v^*) is termed structural defect concentration, c_f [77]. When anisothermal heating is performed, the initial concentration, $c_{f,0}$, is shifted to the quasi-equilibrium defect concentration, $c_{f,e}$. The approach of the amorphous solid to the quasi-equilibrium defect concentration is called structural relaxation. The sample can be heated up to higher temperature, and then the defect concentration decrease until the equilibrium is reached. There are several methods by which the annihilation of free volume can be experimentally determined: *in situ* synchrotron diffraction, combination of density

measurements with DSC and positron annihilation spectroscopy [94–95]. Some limitations restricted the original Spaepen's FVM. Diffusion in metallic glasses was initially assumed to occur through atom jumps; however, molecular dynamics simulations revealed that diffusion is a more collective and diffusive process, where chain action occurs at many atoms linearly connected [96–97]. The free volume, apart from the diffusive process, can be also ascribed to the basis for deformation in metallic glasses at the atomic level. Plastic deformation of metallic glasses occurs by localized groups of atoms, often referred as "flow defects" or "shear transformation zone". When deformation takes place, the created shear bands locally nucleate in regions where the deformation-induced creation of free volume cannot be fully compensated by thermal diffusive relaxation [89], resulting in an excess of free volume junctions where the viscosity significantly reduces, resulting in localized strain softening.

1.3.2 From amorphous to nanocrystalline materials – synthetic strategies

Apart from their outstanding properties, MGs face some drawbacks. The main limitation is their tendency to undergo plastic deformation in narrow regions called shear bands. This leads to limited plasticity and ultimately causes failure. In addition, this evidently brittle manner occurs in any loading condition and limits the use of MGs in many applications. Recently, several synthetic routes have been suggested in order to overcome this drawback. One of the routes stems from the fact that plasticity in MGs can be increased by forming a two-phase microstructure consisting of a metallic glass matrix reinforced with a nano/micro-sized crystalline second phase. As a result, the rapid propagation of shear bands can effectively be hindered. There are two ways to embed a crystalline phase in an amorphous metallic matrix: (ii) *ex situ* formation of composites and (ii) *in situ* formation of composites (Figure 11). In *ex situ* composites, reinforcements are added to the melt during composite fabrication. In *in situ* composites, reinforcements are formed within the matrix during the composite fabrication, for example as a result of heterogeneous crystallization.

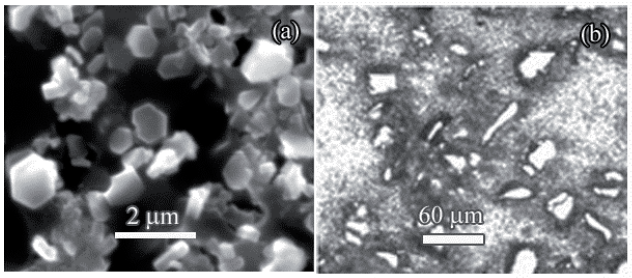

Figure 11: *SEM image of (a) in situ Al-4Cu-TiB_2 composites and (b) ex situ AA7075-Al-SiC composites formation [94].*

- *Ex situ composites*

Cytron et al. and Vaidya et al. [98–100] showed that *ex situ* composites could be achieved by adding ceramic particles or fibers to metallic glass ribbons produced by the melt spinning technique [101]. On the other hand, Li and co-workers investigated Mg-based BMG matrix composites, reinforced with SiC particles [102], and observed that compressive fracture strength of the reinforced composites reached about 963 MPa, a factor of 1.2 higher than for $Mg_{65}Cu_{20}Ag_5Gd_{10}$ monolithic glass. Later on, a novel Zr-based bulk metallic glass composite was fabricated using stainless steel capillaries as the reinforcement. Large plasticity (14%) was achieved in the composite with a reinforcement volume fraction of 38% [103]. The mechanical properties of metallic glass composites were improved because of the existence of additional phases, which promoted the formation of multiple shear bands during deformation, thus enhancing the overall macroscopic plasticity of the composite [104].

- *In situ composites*

In principle, two different ways are pursued to achieve a precipitated phase from the melt on cooling. On the one hand, the chemical composition of the melt itself can play a key role, as established by Kühn et al. [105], Hays et al. [106], and He et al. [107], who demonstrated that the mechanical properties of metallic glasses can be enhanced when nano or micrometer-sized crystals phases are embedded in the glassy matrix. Alternatively, a high melting point element can be added to the glass forming composition. In this case, nano/micro scale precipitates (dendrites embedded in a nanostructured matrix) in a glassy matrix can be typically obtained by rapid solidification techniques upon varying the casting conditions rather than the alloy composition. They are designed with the aim to combine the high strength of the nanostructured phase with the high plasticity of a ductile phase. Following these procedures, it is possible to obtain a microstructure composed of either micro- or nanometer-sized crystalline, quasi-crystalline or non-crystalline phases embedded in an amorphous matrix.

Besides the amorphous/nanostructured matrix composite material, other microstructures can also be achieved (by means of annealing of BMGs). With increasing annealing temperature, the glass may experience structural relaxation, phase separation, and then crystallization. With this approach one can improve the properties of BMGs, which is sometimes not feasible by *in situ* crystallization from the melt.

DSC is a commonly applied method to study the crystallization behavior of MGs. This method enables the identification of the characteristic temperatures in which the glassy phase transforms to the crystalline state, and sometimes it also allows determining the supercooled liquid region or even transformations from metastable phases to other metastable phase or equilibrium phases. In Figure 12 a typical DSC curve, with the aforementioned transitions indicated, is shown (in this case a glass transition, T_g, and crystallization events, T_{x1} and T_{x2}, are depicted). T_g is identified by a change in the slope of the base line and, although crystallization does not occur below Tg, the glass undergoes structural relaxation. Crystallization is indicated by one or various exothermic peaks, depending on the number of stages in which crystallization takes place, and generally occurs at temperatures above T_x. The resulting structure depends on the annealing time and temperature, as well as on the constituent elements of the system.

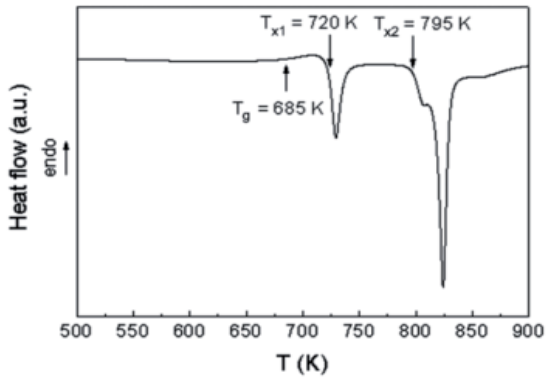

Figure 12: *Typical DSC curve of a metallic glass material [108].*

In general, annealing of MGs allows obtaining one of the following three different states: (a) relaxed glass, (b) phase separation and (c) crystallization.

- *Structural relaxation*

MGs are in a non-equilibrium state. When the MG is isothermally annealed at a temperature below T_g, the structure initially relaxes towards a more stable state. This process is defined as structural relaxation. Structural relaxation takes place through the glass structure annihilation of "defects" or reduction of its free energy by undergoing some recombination of defects or rearrangements through short-range ordering (SRO), respectively.

Structural relaxation in metallic glasses mainly exists in two regimes: low temperature (T_g -200 K < T_a < T_g -100 K) or high temperature ($T_a \geq T_g$ -100 K), where T_a is the annealing temperature.

However, some exceptions (e.g. binary glassy ribbons of Pd-Si, Fe-B and Zr-Cu alloys) with T_g just above room temperature exist.

In some cases, structural relaxation leads to a significant change in the physical and mechanical properties of BMGs. Generally, relaxed glasses exhibit decreased specific heat, reduced diffusivity, reduced magnetic anisotropy, increased elastic constants (by about 7%), increased mechanical hardness, significantly increased viscosity and, in some cases, loss of ductility. Relaxation can also change electrical resistivity, Currie temperature, enthalpy, superconductivity, density and several other structure-sensitive properties. The structural relaxation in metallic glasses can be analyzed by several techniques. The most frequently used are DSC and electrical resistivity measurements. For instance, structural relaxation in DSC cruves is revealed by an exothermic peak (loss of enthalpy).

- *Crystallization*

Following structural relaxation, metallic glasses are heated until they reach the crystallization temperature and then start to crystallize. The crystallization temperature is identified by the exothermic peak in the DSC curve. T_x and T_g depend on the heating rate given in the DSC scan. The faster is the heating rate, the higher these temperatures values. The exothermic peak reflects the heat released from the crystalline phase formation. If the DSC curve exhibits at least two steps transformation, the crystallization is called multi-step crystallization (MSC). Crystallization reactions can be classified into polymorphous, eutectic and primary crystallization reactions. The crystallization phenomenon can be schematically explained by the hypothetical free energy diagram (Figure 13).

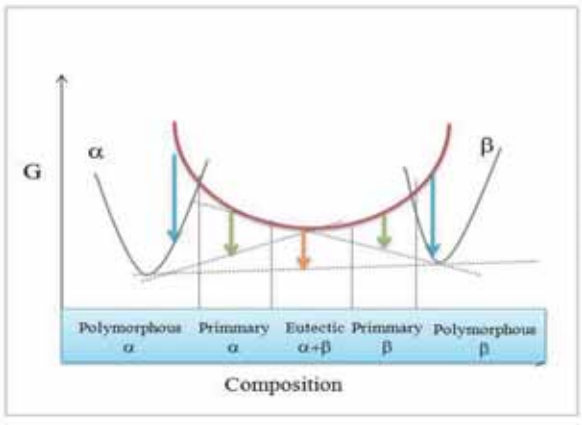

***Figure 13**: Hypothetical free energy diagram.*

- *Activation energy for crystallization*

The activation energy of crystallization (E_a) is interpreted as the potential energy barrier that the glass has to overcome in order to transform into the crystalline phase [109]. There are two ways to measure the crystallization energy: (i) by isochronal or (ii) by isothermal calorimetric processes. The activation energy of a given transformation in an isochronal process can be derived from Kissinger equation:

$$-\frac{E_a}{RT} = C + \ln\frac{\varphi}{T^2} \qquad \text{(Eq.1.18)}$$

Where φ is the heating rate, R is the gas universal constant and T is the peak temperature. Kissinger method assumes that the temperature depends on the reaction rate. The activation energy calculated by this method relies on the temperature dependence of the nucleation and growth rates and on any transient events [110].

Activation energy can also be determined by Johnson-Mehl-Avrami analysis (JMA) [111], which sets the mechanism of isothermal solid-state phase transformations [111, 112]. The reaction rate together with parameters regulating the nucleation rate and /or the growth morphology can be estimated using the formula:

$$x = 1 - \exp\{[k(t-\tau)^n)\} \qquad \text{(Eq.1.19)}$$

Where x is the transformed volume fraction, k is the reaction rate, t is the time, τ is the incubation time till crystallization sets in and n is the Avrami exponent. n is used to describe the transformation mechanisms, such as the nucleation and growth behavior [113].

- *Polymorphous crystallization*

In this mode of transformation, the glassy phase will transfer into a single crystalline phase without changing the composition. The polymorphous crystallization will occur only in composition ranges where the glass phase had formed at a composition corresponding to either a stable or metastable crystalline solid solution or an intermetallic phase. During polymorphous crystallization, the growth of crystals is linear with time and the growth rate has an Arrhenius dependence on temperature. The polymorphous crystallization is schematically presented in Figure 13 and pictured in Figure 14a.

- *Eutectic crystallization*

In this type of crystallization, the glassy phase transforms simultaneously into two (or more) crystalline phases by a discontinuous reaction. Eutectic crystallization can occur in the whole concentration range between two stable or metastable phases. Like polymorphous crystallization, the eutectic crystallization is a discontinuous reaction; the overall composition of the crystal and the glass are the same. The composition of the glass matrix remains unchanged until the glass-crystal interface sweeps past it. For such reactions, the crystal growth rate is independent of time until hard impingement with another crystal occurs. The eutectic reaction is indicated in Figure 13 and the image of a typical eutectic structure is shown in Figure 14b.

- *Primary crystallization*

This mode of crystallization is the main transformation mode observed in metallic glasses. It consists of a supersaturated solid solution first formed from the glass phase; consequently, the remaining glassy matrix will be enriched in solvent atoms until it will further transform (later on at higher temperature) by one of the mechanisms described above. The morphology of the primary crystalline phase depends on composition and ranges from a spherical to a highly dendritic structure. Primary crystallization is indicated in Figure 13 and a TEM image of this type of crystallization is shown in Figure 14c.

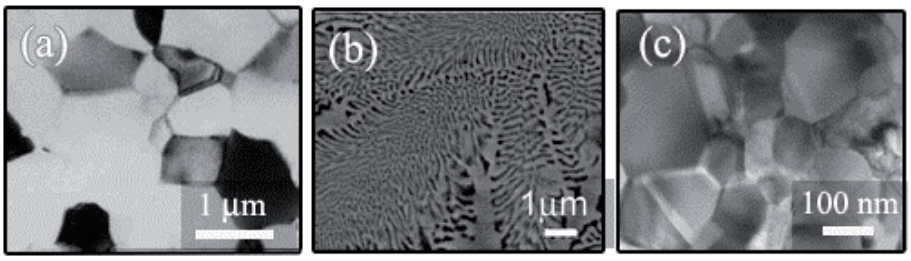

Figure 14: *TEM micrographs showing (a) polymorphous crystallization [114], (b) eutectic crystallization and (c) primary crystallization [115].*

Apart from BMG and the above-mentioned alternatives, there is also another class of materials exhibiting large plasticity (composition/structure dependence issue). Liu and co-workers considered the formation of nanostructured materials with bimodal grain size [116] in which fine grains could provide high strength, whereas coarse grains can enable strain hardening to enhance ductility. The next section will provide detailed insights into the research area of nanostructured (or nanocrystalline) materials.

1.3.3 Nanocrystalline (NC) materials

Nanocrystalline materials (NC) are single or multiphase polycrystalline solids with characteristic grain sizes of a few nanometers (< 100 nm). Owing to their extremely small crystallite dimensions (typically 1 - 100 nm), they are structurally characterized by a large volume fraction of interfaces. This results in an enhancement of various properties i.e. increased strength/hardness, improved toughness, reduced elastic modulus and ductility, enhanced diffusivity, higher specific heat, enhanced thermal expansion coefficient, and superior soft magnetic properties in comparison with conventional coarse-grained materials. NCs can be prepared in several ways: inert gas condensation, mechanical alloying, electrodeposition, crystallization from amorphous material, severe plastic deformation, cryomilling plasma synthesis, chemical vapor deposition, sputtering, physical vapor deposition and spark erosion [117].

1.3.3.1 Classification

According to Siegel [118] NC materials are classified as follows: (i) one-dimensional (1D) filamentary structures, (ii) two-dimensional (2D) layered or lamellar structures, and (iii) three-dimensional (3D) equiaxed grain nanostructured materials.

1.3.3.2 Microstructure

Figure 15 illustrates the typical structure of a NC material, which is made of two components: small crystallites (grey color) and interfacial components (brown color). The small crystallites exhibit long-range order and possess different crystallographic orientations, whereas the interfacial components create the intercrystalline network which varies locally. A NC material is characterized by a high amount of interfaces because the major fraction of atoms is actually located at the interface. The volume fraction of those interfaces may be calculated as $3\Delta/d$ (where Δ is the average interface thickness and d is the average grain diameter) [119]. The most important structural parameter of nanocrystalline single-phase alloys and pure metals is the grain size. Therefore, it is of utmost importance to accurately determinate the grain size. It is possible to meet this purpose on a basis of direct (imaging) and indirect (scattering) techniques. Multiphase nanocrystalline alloys can show different morphologies. For instance, a microstructure of equiaxed grains of different phases can be formed by crystallization of an

amorphous alloy [117] or by mechanical alloying [120], and a eutectic microstructure with lamellae width of nanometers may be also obtained by rapid quenching technique [107].

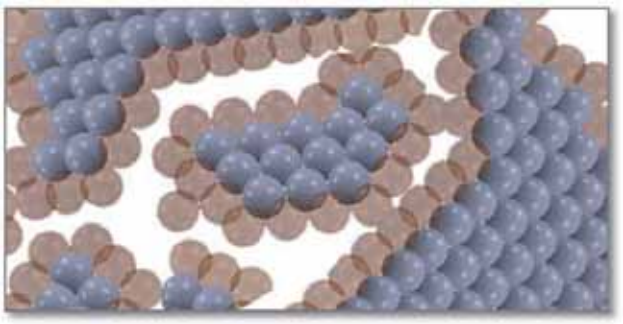

Figure 15: *Atomic structure of a two-dimensional nanocrystalline material [121].*

The structure of the crystallites and the atomic structure at the grain boundaries in NC materials is more or less the same as in their coarse-grained counterparts. Siegel [118] observed this similarity based on evidences from XRD, extended X-ray absorption fine structure (EXAFS), Mössbauer spectroscopy, Raman spectroscopy, HR-TEM and computer simulations. So, one can assume a boundary of a few atomic distances thick. However, it is safe to assume that the number of grain-boundary ledges is reduced in NC materials. The reorientation/rotation of the nanosized boundaries is also significantly enhanced in comparison with conventional boundaries [122]. HR-TEM shows that NC materials consist of small crystallites of different crystallographic orientation separated by grain boundaries. Even though not frequently reported, the grains contain a variety of crystalline defects such as dislocations, twin boundaries, multiple twins, and stacking faults. Lattice distortions in the crystallites may occur eiconfither in NC materials or in coarse-grained materials. It is now well established that the solid solubility of elements is usually higher in the nanocrystalline state than in the coarse-grained condition. This change in solid solubility can lead to changes in lattice parameters. Furthermore, a significant change in the vacancies concentration can also affect the lattice parameters. It has also been noted that NC materials have large mean square lattice strains, which increase systematically with decreasing grain size. This strain appears to depend on the thermal and mechanical history of the specimen, suggesting that at least part of the strain is not intrinsic to the nanocrystalline state.

1.4 Mechanical properties of MGs, MG-composites and NC materials

The mechanical properties of materials play an essential role when considering their applications (e.g. orthopedics). For this reason, a large number of studies have been carried out in this

research field. This section provides a comparison of the mechanical behavior of MGs, MG-nanocomposite materials and their crystalline counterparts.

- **MGs**

As aforementioned, the defining characteristics of MGs are their lack of crystallinity, and associated lack of microstructural features such as grains and phase boundaries. These features influence the outstanding mechanical properties of MGs. Remarkably, they exhibit high strength [123], relatively high yield strength in tension and compression [124] and their elastic modulus can be 30 % lower than the crystalline counterparts. Besides, the elastic strain limit of MGs can even exceed 2% prior to failure (under tensile or compressive conditions). This value is much higher (10 times) than that found in conventional metallic alloys. The elastic energy, which is represented by the surface area under the curve in the elastic region in a stress-strain curve, can be up to 30 times larger in MGs than in crystalline materials. However, MGs tend to fail soon after yielding with limited plastic deformation. At different temperature ranges the mechanism of deformation can differ.

- *Deformation mechanisms*

Two basic modes of deformation can be distinguished in metallic glasses: *homogeneous* and *inhomogeneous* flow.

The homogeneous flow occurs at low stresses and high temperatures ($T > 0.7T_g$). This process is related to the existence of viscous flow in which plastic strain is distributed continuously (not necessarily equally) between different volume elements within the material. That is, each volume element of the specimen contributes to the strain [125]. On the contrary, at temperatures well below the glass transition ($T < 0.7T_g$) and at high stresses, MGs undergo inhomogeneous deformation by concentrating severe plastic strain into nanoscale shear bands [126–128]. It is worthy noticing that MGs exhibit the phenomenon called “strain softening”. That is, an increase in strain makes the material softer and allows the material to be deformed at lower strain and higher rates. Shear band formation or shear localization in MGs has been considered a direct consequence of strain softening. In contrast, crystalline materials undergo “strain hardening”. With increasing the strain, the material becomes harder and therefore it is difficult to further deform it. Some theoretical models have been put forth to explain the inhomogeneous deformation in MGs. It is widely known that the shear banding of MGs occurs as a consequence

of formations and self-organizations of flow events. These plastic flows in MGs (a result of an excess free volume) may lead to a drop in viscosity. These phenomena can be ascribed to a series of discrete atomic jumps in the glass, at sites where the excess free volume is large enough. In fact, this process occurs via diffusion [93]. A more iterative approach was proposed by Argon [129–130], which states that plastic flow can be localized in a shear band in which the strain rate has been perturbed due to creation of free volume. A second hypothesis suggests that local adiabatic heating occurs in shear bands, which leads to a decrease in viscosity [128, 131]. This adiabatic heading could lead to a significant increase in the temperature to a level above T_g or even to the melting point of the alloy. Experimental evidence is available for both, the increase in free volume and rise in temperature, in shear bands during deformation.

- *Features of metallic glasses under deformation*

As can be observed in Figure 16 (b), MGs usually exhibit strain softening behavior. Nevertheless, it has been found that some ductile MGs examples show work hardening (Figure 16 (a)). This recently developed "ductile metallic glasses" exhibit high-strength (between 1272 and 1830 GPa) and a significantly improved ductility (the total true strain can reach up to 170% for binary $Pd_{81}Si_{19}$ alloy [129]). After the yield point, the stress level continues to increase, indicating a "workhardening-like" behavior [132–134]. This phenomenon is common for most BMGs exhibiting intrinsically enhanced ductility.

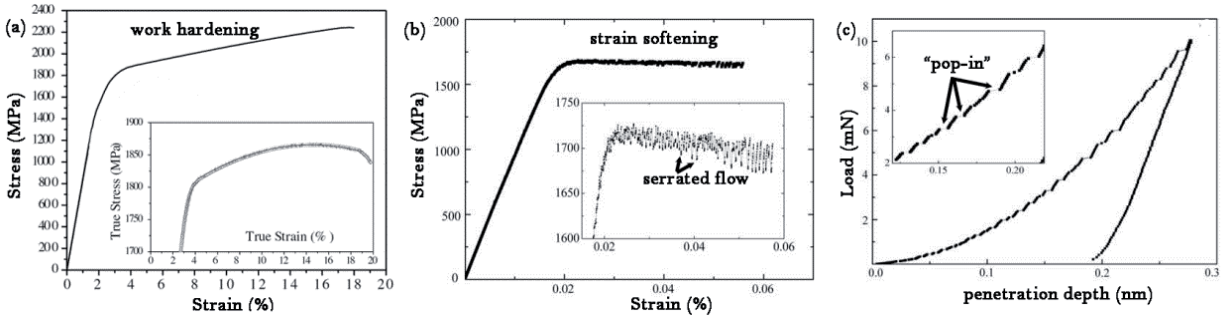

***Figure 16**: (a) Stress-strain compression curve of a $Cu_{47.5}Zr_{47.5}Al_5$ showing a highly "work-hardenable" metallic glass [135]; (b) Stress–strain curve of the $Ti_{40}Zr_{25}Ni_8Cu_9Be_{18}$ BMG alloy [136]. The inset shows the occurrence of serrated flow along with a progressive mechanical softening after yielding; (c) load-displacement nanoindentation curve of the $Ti_{40}Zr_{25}Ni_8Cu_9Be_{18}$ BMG alloy. The insets show the central parts of the loading curves, where some pop-ins can be easily distinguished [136].*

Figure 16 (b) depicts typical compressive strain-stress curve for BMG. Schuh et al. [137] have examined the mechanism of local increase in the free volume or evolution of structural order in

the glass. When shear bands form and propagate a sudden drop in load is noticed in the stress–strain plot. The surrounding material recovers elastically and arrests the shear-band propagation.

When this process gets repeated, we obtain a serrated flow. The free volume within the shear band increases during deformation, thereby decreasing its density and hence the resistance to deformation [137].

Serrated flow is also observed during nanoindentation, but only at slow loading rates. At this time, the activation of each individual shear band and the consequent sudden rise in load is known as a "pop-in" event (Figure 16 (c)). A single shear band can rapidly accommodate the deformation at slow loading rates. However, when the loading rate is high, there is not enough time to accommodate the strain and multiple shear bands operate at the same time resulting in a smooth load-displacement curve.

- **MG-composites**

In metallic glass composites, a second phase is introduced in the amorphous matrix with two main goals: promoting shear band initiation and branching (to distribute the plastic strain more broadly to avoid the catastrophic localization) and hindering shear band propagation. Since the main features of MG-composites have been explained in the previous section (Section 1.3.2), only some examples are given here. The second phase can exist in many types, shapes (particles or dendrites) and different sizes (from atomic clusters to micrometer-sized). For instance, the size can be in some way controlled by adjusting the solidification parameters (e.g. cooling rate). Sun et al. [138] developed a new processing technique to transform the dendritic morphology of the crystalline phase into spherical particles. The alloy with the spherical particles showed higher ductility (12% plastic strain) than the one with the dendritic morphology (8.8% plastic strain). Another example of increased plasticity (from 1.6% to 14.1%) was observed when 10% of niobium was added to $Cu_{60}Hf_{25}Ti_{15}$ BMG [139]. Additionally, the plasticity can be increased when nanocrystals or phase separation is generated during deformation process. Deformation-induced nanocrystallization is a phenomenon in which a secondary phase is precipitated during deformation within the initial glassy phase. In some cases, crystallization induced during compression test was considered to be correlated with the relatively low stability of the supercooled liquid phase and the high transformation rate of the primary precipitation phase. Other works suggest that the origin of plasticity is closely related to the SRO/ MRO existing in the glassy phase [140] and other authors attributed the large plasticity to the *in situ*

nanocrystallization produced by plastic flow within the shear bands [134, 140–141]. Ideally, the site of the generated crystals should be a bit larger and of the order of the shear band widths (i.e., tens of nm).

- **NC materials**

NC materials exhibit superior properties compared with conventional coarse-grained materials. This is attributed to the very fine grain sizes and consequently high density of interfaces in NCs. The grain size has significant influence on the yield strength. The relationship between yield stress, σ_y, and grain size d is given by the Hall-Petch equation [142]:

$$\sigma_y = \sigma_0 + kd^{-1/2} \qquad \text{(Eq. 1.20)}$$

where σ_0 is the lattice friction stress to move individual dislocations and k is a material dependent constant. Yield strength of vast majority of alloys increases with decreasing the grain size. However, the decrease of flow stress with decreasing grain size below 10 nm, initially identified by Chokshi et al. [142] in the nanocrystalline regime, was also found and confirmed by molecular dynamics calculations in face centered cubic (FCC) metals. This phenomenon is called inverse Hall-Petch reaction, and it is attributed to the growing role of grain-boundary sliding [142].

In grain-boundary strengthening, the grain boundaries act as pinning points impeding further dislocation propagation. Since the lattice structure of adjacent grains differs in orientation, it requires more energy for a dislocation to change direction and move into the adjacent grain. The grain boundary is also much more disordered than the innert parts of the grains, which also prevents the dislocations from moving in a continuous slip plane. Impeding this dislocation movement will hinder the onset of plasticity and hence will increase the yield strength of the material.

It is well known that grain size has a strong effect not only on yield strength but also on ductility and toughness of conventional grain size (> 1μm) materials. Grains can make crack propagation more difficult and therefore increase the apparent fracture toughness in conventional grain size materials. Nevertheless, some NC materials show reduced ductility - sometimes brittle behavior. This is presumably due to the inability of dislocation generation and limited motion at these nanometer grain sizes. Furthermore, nanocrystalline metals are characterized by a low work-hardening rate, which is a direct consequence of the low density of dislocations encountered after plastic deformation. This low work hardening rate leads to tensile instability and low tensile ductility. However, NC materials can show some ductility at room temperature if the plastic

deformation mechanism is not based on the dislocation generation and motion (for example, by deformation induced by grain boundary sliding). Dislocation activity occurs in the larger grains while the smaller grains provide the strengthening. Furthermore, it has also been shown that the ductility of a NC material is enhanced by increasing significantly the density of growth twins by annealing [143].

Different mechanisms have been proposed to account for the plastic deformation in NC materials. The most relevant are described below [144]:

- **Pile-up break down**: As the grain size is decreased, the number of dislocations piled up against grain boundary tends to progressively increase, at a fixed stress level, since this number is a function of the applied stress and of the distance to the source. At the same time, an increased stress level is needed to generate the same number of dislocations at the pile-up to accommodate plastic flow. However, at a critical grain size, we can no longer use the concept of pile-up to explain the plastic flow and alternative deformation mechanisms are activated. This is related to the inverse Hall-Petch regime.
- **Grain-boundary sliding**: Under an applied shear stress, one layer of grains slides with respect to the other, producing a shear strain in the process. Plastic deformation takes place by virtue of the top layer of grains translating to one direction with respect to the bottom layer of grains.
- **Core and mantle model**: The model is based on dislocation generation at or adjacent to grain boundaries and on the formation of work-hardened grain boundary layers. The existence of grain-boundary ledges with spacing of 10 - 100 nm provides an ample supply of nucleation sites of dislocations that, upon emission into the grains, cross-slip and multiply, creating a work hardened layer close to the grain boundaries. As the grain size is reduced, the ratio between volume fractions of the mantle and core increases, providing an increase in yield stress. Beyond a critical grain size, the ledges can no longer operate and do not promote plastic deformation in the nanocrystalline regime.
- **Shear band formation**: For grain sizes smaller than d < 300 nm shear band development is often observed to occur immediately after the onset of plastic deformation. This has been correlated to changes in strain hardening behavior at those grain sizes; since the ability to work harden by the increase in dislocation density is lost.
- **Mechanical twinning**: Mechanical twinning (occurence of planar defecs) and slip (linear defects) can be considered as competing processes. In FCC metals and alloys, the

twinning stress is directly related to the stacking fault energy. The decrease in grain size is expected to render deformation twinning more difficult. At least, this is what conventional materials science predicts in the micrometer regime [122]. Although mechanisms for deformation twinning in nanocrystalline metals remain controversial, some preliminary assessments indicate that: (a) the conventional nucleation mechanism breaks down in the nanoscale; (b) there are local stress concentrations (triple points, etc.) that raise the stress significantly, propitiating twinning; (c) the partial dislocation separation increases at the nanoscale domain, aiding twinning.

Grain boundary dislocation creation and annihilation: When the grain size is reduced to the NC regime, the mean free path of dislocations generated at grain-boundary sources is severely limited. Rather than cross slipping and generating work hardening, these dislocations can run freely until they meet the opposing grain boundary, which acts as a sink. Thus, the dislocation density remains low throughout the plastic deformation process, and work hardening is not significant. Dislocations, which were generated at one grain boundary, run unimpeded until they encounter the opposing grain boundary. Grain boundary ledges are responsible for generation of plastic flow in the conventional coarse-grain crystalline regime. However, as the grain size falls below 20 nm, the grain boundaries will become virtually free of ledges, and intrinsic and extrinsic grain-boundary dislocations have to be pushed out into the grains. Another significant difference is that the mean free path of dislocations is limited by the grains size, and therefore dislocation reactions, cross slip, and other mechanisms of dislocation multiplication are effectively prohibited. All these mechanisms may play a role under specific internal (grain size, composition) or external (temperature, strain rate, stress state) parameters.

1.5 Corrosion behavior of MGs, MG-composites and NC materials

An increasing number of investigations are currently focusing on the corrosion of crystalline, nanocrystalline and amorphous materials. It is well known that the corrosion processes are comparatively different between them. Amorphous alloys usually exhibit superior corrosion resistance than their crystalline counterparts [145] due to the lack of grain boundaries or second-phase precipitates, which could act as local electrochemically-active sites. On the contrary, crystalline alloys have a number of defects like grain boundaries, dislocations, second-phase precipitates, which make them more prone to corrosion. Although amorphous materials are usually chemically homogeneous, the presence of heterogeneities during casting cannot be often completely avoided, especially in commercial production. Some examples involve gas pockets

formed by entrapment of gas bubbles during production [146], small crystallites formed due to the presence of oxygen in the melt [147], or the gradient of MRO in the cross-section of a rod sample [148]. These heterogeneities or their interface with the glassy matrix can act as nucleation sites for pit initiation, and subsequently promote the corrosion. In general, the corrosion behavior of a particular system basically depends on the alloying elements and their relative amount, so fixed rules cannot be simply extracted. It is difficult to predict the corrosion behavior of NC materials in advance. Some authors have pointed out that NC materials exhibit enhanced corrosion resistance compared with their coarse-grained counterparts [150]. Grain size reduction in NC materials has been shown to considerably improve the corrosion performance for a wide range of electrochemical conditions. Many of these studies indicate that this is mainly due to the elimination of the localized attack at grain boundaries, which is one of the most detrimental mechanisms of degradation in polycrystalline materials. Several explanations have been put forward to explain this effect, including: (i) the solute dilution effect by grain size refinement; (ii) crystallographic texture changes with decreasing grain size and (iii) grain size-dependent passive layer formation [150]. In contrast, results obtained by other researchers have shown that NC materials possess higher rates of dissolution and corrosion [151–152].

1.6 Interest of Ti-based BMGs and NC materials

- *Interest of Ti-based BMGs*

Ti-based metallic glassy materials have been the focus of much study owing to the superior properties compared with crystalline counterparts. Ti-based MGs are promising as a new family of lightweight materials (implants) due to their relatively low-cost, low density, high specific strength, large compressive strength and relatively low Young's modulus and good corrosion resistance [136, 153]. A large number of studies have been performed in order to understand the amorphization process in Ti-based alloys since this typically increases the strength and corrosion resistance. First Ti-based MG alloys date back to 1977 [154], and were obtained by rapidly solidified Ti-M (M = transition metal) [155] (e.g.Ti-Ni-Cu [156] and Ti-Ni-Cu-Al [157]). The formation of MGs in bulk shape was limited by their poor glass forming ability, thus only fully glassy ribbons were produced. The breakthrough came in 1994, when Ti-based BMGs were first reported for the Ti-Zr-Ni-Be system by Peker and Johnson [158]. Up to now, several families of multicomponent Ti-based BMGs, such as Ti-Cu-Ni-Si-B [159] and Ti-Cu-Ni-Sn-Be-Zr [160], have been designed and characterized. Ti-based BMGs have been produced in the form of rods with maximum diameters up to 6-14 mm [161, 162]. Nevertheless, those dimensions are only

valid for metallic glasses with Be. For Be-free BMGs, the maximum diameter achieved is limited to 5 mm. Recently, several new Ti-based BMGs without toxic elements (e.g. Ti-Zr-Cu-Pd-(Sn) system) have been designed and fabricated by Inoue and co-workers [163]. The high glass forming ability of these BMGs enables the fabrication of rod-shape samples with diameters up to 6 mm. As previously mentioned, one of the drawbacks of BMGs that restricts their usage in various fields is that they typically exhibit limited plasticity at room temperature. In order to foster the applicability of BMGs as structural materials, the study of the mechanical behavior of BMGs is of paramount importance. It should be noted that, in spite of their interesting properties, some aspects of the mechanical behavior of BMGs have not been systematically addressed yet. In particular, the deformation mechanisms of metallic glasses have not been entirely explored. Very recently, some attempts have been pursued with the aim to obtain high strength and large plasticity Ti-based alloys [164].

- *Interest of Ti-based NC materials*

Ti-based NC materials with grain sizes lower than 100 nm can be prepared by a number of different techniques (ball milling and subsequent hot pressing, severe plastic deformation, suction casting, etc.) [122]. The grain size, morphology and composition can be controlled by tuning the processing parameters [117]. New Ti-based alloys with low Young's modulus (to ensure good mechanical compatibility with bone) and free from non-biocompatible elements (e.g., Al, V, Ni, or Co), are currently required for the next generation of metallic implant materials. Currently, a number of multi-component Ti-based alloys showing a nanocrystalline structure and not containing highly-toxic elements (Be, Ni, Al, V, Co, Cr, etc.), such as Ti–50Ta [165], Ti–Sn–Nb [166], Ti–Mo–Nb [167], Ti–Mo–Zr–Fe, Ti–Nb–Ta–Zr [168] and Ti–Fe–Sn [169], are of keen interest for the biomedical field. These alloys constitute the so-called "second generation" biomaterials [5, 170].

1.7 Surface modification of bulk metallic glasses (BMGs)

Traditionally, surface treatment processes have pursued one or several of the following goals: controlling friction and wear, improving corrosion resistance, promoting the change of a mechanical/physical property such as conductivity or reflectivity, altering dimensions and/or final appearance (e.g. color, luster) and, eventually, reducing costs [171]. The surface treatments can be classified into two main categories: treatments that involve covering the surface of a given material with a coating layer and treatments aimed at altering the surface itself, either modifying

the entire surface or only some specific regions of the surface (i.e., patterning). In the first case, one can distinguish between organic (paints, laminates, lubricants, or floor toppings) and inorganic coatings (electrodeposited and electroless coatings, conversion coatings, thermal sprayings, hot dippings or furnace fusings). Within the second category, different beam types (flame, induction, laser or electron beams) can be used, for example, to harden the surface of a material, while heavy diffusion processes like carburizing or nitriding can be applied to enhance its tribological performance. Likewise, mechanical and electrochemical polishing can be utilized to reduce surface roughness. In any case, the ultimate objective of the aforementioned treatments is to improve the functionality and/or service life of the material conceived for a given technological application.

Ion irradiation treatments are being used to alter the surface of certain materials in a uniform manner, through the creation of structural disorder and/or the modification of their properties. In recent years, several works have reported on the effects of ion irradiation on the near-surface morphology of different types of materials. Changes in roughness or porosity have been induced in metals and oxides by employing high energy (≈ MeV) incident ions (N, O or noble gases), sufficiently high fluences (typically > 1×10^{17} ions/cm^2) or directly using heavy ions (e.g., Bi^+) [172–177]. For instance, amorphous sponge-like germanium foams with tunable porosity and nanopore network geometries have been obtained by varying the ion energy, fluence, angle of incidence and target temperature [177]. Conversely, shrinking of pre-existing pores in the near-surface of amorphous metals has been accomplished by low-energy Ar^+ irradiation [178]. Moreover, in some cases, embedded nanofibers or nanowires have also been fabricated using appropriate ion irradiation conditions [179–180].

As explained in the previous sections BMGs suffer from limited room temperature macroscopic plasticity, compared to polycrystalline metals, due to formation and rapid propagation of a few shear bands [181]. The plasticity in these materials can be improved by promoting the nucleation and branching of multiple shear bands or by hindering their propagation. Stress in BMGs has been reported to enhance the atomic mobility (i.e., increasing the amount of free volume) [182–183], eventually also leading to post-synthesis nanocrystallization, if the applied stress is sufficiently high [184–185]. Ion bombardment of crystalline materials can introduce large amounts of structural defects at the surface, eventually leading to amorphization and subsequent worsening of the mechanical properties [186–189]. This process, which usually takes place when the material is subject to high ion fluences and/or irradiation with heavy incident ions, has to be taken into account in materials for structural applications, for example in nuclear reactors.

Contrary to crystalline alloys, BMGs can experience radically different microstructural surface effects depending on the ion irradiation conditions. While an increase of the free volume concentration, with the concomitant decrease of hardness, has been observed after ion irradiation at low fluences with low-energy incoming ions [190–192], partial nanocrystallization can occur for sufficiently high fluences and high incident ion energies [193–198]. In this case, an increase of hardness and plasticity is usually reported. Energetic and thermodynamic considerations to establish which irradiation conditions can either promote increase of free volume or nanocrystallization have been recently reported [199].

Goals of the Thesis

Taking into account the literature background and current needs within the field of biomaterials for orthopedic applications, the objectives of this Thesis can be briefly summarized as:

1. Synthesis of new Ti-based materials by arc melting and subsequent copper mold casting, that show an adequate combination of non-toxic alloying elements so that (a) either nanostructured or fully amorphous specimens are obtained, and (b) the resulting mechanical properties are relevant to the field.

2. In-depth characterization of the newly produced Ti-based samples in terms of microstructure, mechanical and corrosion behavior, and biocompatibility, by paying special attention to the correlations existing among these material properties.

3. To demonstrate the biocompatibility of the Ti-based materials by *in vitro* studies (i.e., cell culturing).

4. To devise and apply ion irradiation treatments to bulk metallic glasses as a means to alter their surface characteristics and to further explore the effect of such changes on the mechanical performance of the material.

Experimental Details

In this chapter, a brief explanation of the fabrication and main characterization techniques used throughout this Thesis is provided. Special emphasis is laid on the working conditions.

3.1 Sample preparation

The samples were obtained by arc melting and subsequent copper mold casting. This production route involves basically two steps: the production of a master alloy (MA) and its casting into rods. Some BMGs were further subjected to ion irradiation treatment in order to induce structural changes at surface level.

- **Arc melting**

An electric arc furnace is a system that heats charged material using an electric arc. The basic set-up is made of an electric arc copper crucible (right panel Figure 17 a), a furnace consisting of a shell with a roof on top (right panel Figure 17 b), and a retractable tungsten electrode entering the furnace (right panel Figure17 c). This electrode allows the formation of an electric arc between the material and the electrode. On contact, electrical power is transformed into heat as arcing takes place between the electrodes and the solid feedstock. The material is heated both by current passing through the charge and by the radiant energy evolved by the arc [147].

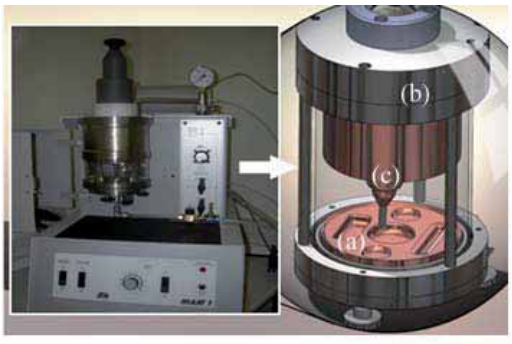

Figure 17: *Left: Picture of the arc melting device used [200]. Right: Schematic representation showing (a) – copper crucible, (b) – shells with a roof on top, and (c) – retractable tungsten electrode.*

- *Working conditions:*

MAs were prepared by arc melting of a mixture of high purity elements (99.9%) under a titanium-gettered argon atmosphere. The MAs were re-melted at least six times with successive inversions of the sample in order to ensure a homogeneous melt. Ingots of Ti-44.3Nb-8.7Zr-

12.3Ta (wt. %), Ti-31.0Fe-9.0Sn (wt. %), $Ti_{40}Zr_{20}Hf_{20}Fe_{20}$ (at. %), $Zr_{55}Cu_{28}Al_{10}Ni_7$ (at. %) and $Ti_{40}Zr_{10}Cu_{38}Pd_{12}$ (at. %) alloys were fabricated at Universitat Autònoma de Barcelona (UAB), while MAs of $Ti_{45}Zr_{15}Pd_{35}Si_5$ (at. %) and $Ti_{45}Zr_{15}Pd_{30}Si_5Nb_5$ (at. %) alloys were prepared at UAB and Leibniz-Institut für Festkörper-und Werkstoffforschung (IFW-Dresden).

- **Casting into rods – Cu mold casting**

Pieces of MA were introduced in a crucible (copper) and melted. Afterwards, the melt was sucked into a copper mold. The insertion into the Cu mold occurs by the application of a negative pressure at one end of a mobile copper mold (suction casting). Optimization of the casting parameters is of outmost importance in order to obtain fully amorphous samples. Chamber atmosphere is selected depending on the reactivity of the alloy with it [201].

- *Working conditions:*

Castings for the Ti-44.3Nb-8.7Zr-12.3Ta (wt. %), Ti-31.0Fe-9.0Sn (wt. %), $Ti_{40}Zr_{20}Hf_{20}Fe_{20}$ (at. %), $Zr_{55}Cu_{28}Al_{10}Ni_7$ (at. %) and $Ti_{40}Zr_{10}Cu_{38}Pd_{12}$ (at. %) alloys were done using MAM-1 device at UAB, while the $Ti_{45}Zr_{15}Pd_{35}Si_5$ (at. %) and $Ti_{45}Zr_{15}Pd_{30}Si_5Nb_5$ (at. %) alloys were prepared at UAB and IFW-Dresden. Rods with different diameter were obtained (see Table 1).

Table 1. *Dimensions of the metallic rod-shaped alloys.*

Composition	Ti-44.3Nb-8.7Zr-12.3Ta, $Ti_{40}Zr_{20}Hf_{20}Fe_{20}$, $Zr_{55}Cu_{28}Al_{10}Ni_7$, $Ti_{40}Zr_{10}Cu_{38}Pd_{12}$	Ti-31.0Fe-9.0Sn, $Ti_{45}Zr_{15}Pd_{30}Si_5Nb_5$, $Ti_{45}Zr_{15}Pd_{35}Si_5$
Rod diameter/ length (mm)	*2/ 35*	*3/ 35*
Casting conditions	*Working atmosphere: inert (Ar)* *Injection temperature: between 1250-2000˚C* *Ejection pressure: <1atm (~0.6 atm)*	

- **Surface treatment by ion irradiation**

Through this surface treatment, materials are subjected to high ion fluences and/or irradiation with heavy incident ions. Crystalline materials and BMGs can experience radically different microstructural surface effects depending on the ion irradiation conditions. Fundamentals of the treatment can be found in Section1.7/ Chapter 1. Monte – Carlo simulations were performed to reveal the appropriate ion dose and ion energy to induce the desired collisional surface damages.

- *Working conditions:*

The polished BMGs were irradiated with Ar ions using two consecutive irradiation processes (first one at 200 keV followed by another one at 75 keV) aimed at obtaining a significant and homogeneous radiation damage within the upper 100 nm from the surface. To avoid irradiation-induced overheating of the sample, the holder was water-cooled in the irradiations carried out at room temperature (RT). The aforementioned two-step irradiation processes were performed both at RT (on the as-cast alloys) and at T = 620 K, which is close to their glass transition ($T_{g,Ti\text{-}based}$ = 685 K, $T_{g,Zr\text{-}based}$ = 702 K, i.e., T ≈ 0.9T_g). For the high-temperature irradiation processes the samples were heated and cooled at 40 K/min and kept at T = 620 K for 1h (the two-step irradiation process, which lasted slightly less than 1h, was performed during the holding temperature segment).

3.2 Characterization techniques

This section gives a brief overview of the different techniques used for the thermal, structural, and mechanical characterization as well as the corrosion and biocompatibility assessment of nanostructured alloys and BMGs. DSC was used to study the thermal stability and crystallization processes. Morphological and structural characteristics of the materials were analyzed by means of SEM, TEM and XRD. Nanoindentation was used to determine relevant mechanical parameters of the samples. Furthermore, elastic constants were carefully determined using ultrasonic testing. Corrosion behavior characterization was conducted by electrochemical means using potentiodynamic polarization curves.

3.2.1 Thermal characterization

3.2.1.1 Differential scanning calorimetry (DSC)

DSC has been used to study the thermal stability and the crystallization kinetics of several materials. This technique looks at how a material's heat capacity, C_p, changes with temperature. A sample of known mass is heated or cooled and the changes in its heat capacity are tracked as changes in the heat flow. This allows the detection of transitions such as melting, glass transitions, phase changes, and curing.

This technique aims to maintain the sample and the reference material at the same temperature at any time during the experiment, by compensating independently the supplies of power to the sample and reference. The power needed to the bridge circuit in balance is proportional to the change in heat capacity or enthalpy. The integral of power over the time of the total event gives the energy difference between sample and reference, which corresponds to the enthalpy difference of the process.

- *Working conditions:*

DSC experiments were performed on a DSC-7 (Perkin Elmer) apparatus. The mass of sample was in the range of 10-30 mg for all specimens. The discs were placed in graphite crucibles in order to avoid any reaction between the sample and the crucible. In the reference cell, similar graphite crucibles were used. A heating rate of 40 K/min was applied. For the high-temperature irradiation processes, the $Zr_{55}Cu_{28}Al_{10}Ni_7$ and $Ti_{40}Zr_{10}Cu_{38}Pd_{12}$ samples were heated and cooled at 40 K/min and kept at T = 620 K for 1h (the two-step irradiation process, which lasted slightly less than 1h, was performed during the holding temperature segment).

3.2.2 Structural and morphological analysis techniques

3.2.2.1 Scanning electron microscopy (SEM)

The SEM uses a focused electron beam to produce images by means of scanning the surface of a sample. From the interaction between the electron beam and the sample, information about both, topography and composition can be obtained. The main signals produces by the SEM are secondary electrons (SE), back-scattered electrons (BSE) and characteristics X-rays. Secondary and backscattered electrons are separated according to their energies (Figure 18).

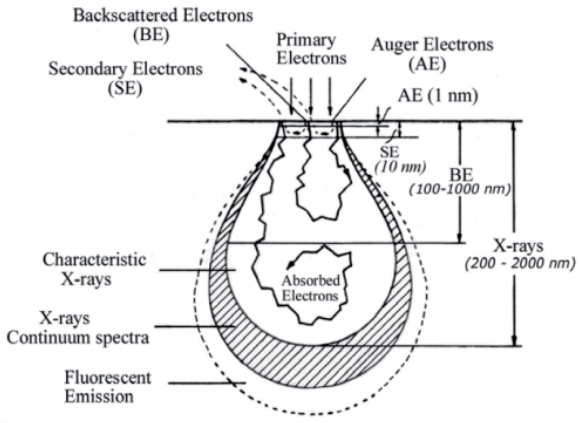

Figure 18: *Types of electrons and radiation generated after the interaction between the primary electron beam and the sample.*

- *Working conditions:*

Our observations were carried out using HR-SEM Zeiss Merlin and HR-SEM Gemini 1530 (Zeiss) microscopes, located at the Servei de Microscòpia of UAB and at IFW Dresden, respectively. The former is equipped with energy dispersive X-ray (EDX) analysis data acquisition system (INCA). Prior to observation, the following metallurgical specimen preparation procedures were applied:

(a) The samples were embedded in a conducting epoxy resin.
(b) Specimens were subsequently grinded to remove the resin and polished until mirror-like finish.

3.2.2.2 Transmission electron microscopy (TEM)

TEMs are capable of imaging at a significantly higher resolution than light microscopes. This enables the observation of small objects not visible on a light microscope. In a conventional TEM, a thin specimen is irradiated with an electron beam of uniform current density. If the penetration depth of the electrons is larger than the thickness of the sample they can go through it. The transmitted electrons are then focused onto a fluorescent screen. TEM exploits three different interactions of electron beam-specimen; unscattered electrons (transmitted beam), elastically scattered electrons (diffracted beam) and inelastically scattered electrons.

- *Working conditions:*

Prior to TEM observation, the samples were mechanically pre-thinned down to 80 μm. Mechanical dimpling at the centre of the sample reduced the thickness to around 20 μm and further thinning of the disks were carried out by ion beam milling at an incident angle of 5˚ with a beam energy of 4 keV. This process consists of bombarding the specimen with energetic ions in order to sputter the material, while usually rotated, until it is thin enough to be observed by TEM. The controlling parameters are the ion energy, the angle of incidence, the attack from the top and/or backside of the specimen and the time (Table 2). TEM images with SAED patterns were carried out on a 200 kV JEOL-JEM-2011, located at the Servei de Microscòpia of UAB. Fast

Fourier Transformation (FFT)/Fast Fourier Reconstruction (FFR), together with phase identification, were performed using Gatan Digital Micrograph software.

Table 2. *Control parameters used for ion milling.*

Ions	Argon
Energy	4 kV
Incident angle	5º
Attack	Bottom and top
Time	~ 5 – 10 h

3.2.2.3 X-ray diffraction (XRD)

XRD technique allows identifying the structural features (phases, crystal size, strain, etc.) of a specimen based on the scattered intensity of an X-ray beam hitting a sample as a function of incident X-ray and scattered angle, polarization, and wavelength or energy. If one assumes that the incident x-ray beam is perfectly collimated and monochromatic (with a single wavelength λ) and makes an incident angle, θ, with respect to the reticular planes of the crystal, it can be demonstrated that the following condition is fulfilled:

$$n\lambda = 2d\ sin\theta \qquad \text{(Eq. 3.1)}$$

where *n* is the reflection order and *d* is the interplanar distance of one family of crystallographic planes. This condition, known as the Bragg's law, is schematically represented in Figure 19 and it can be used to determine the angular positions of the XRD peaks diffracted by each family of planes.

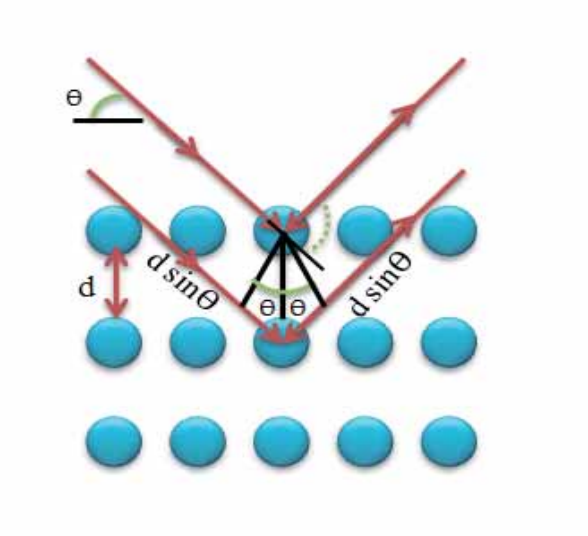

***Figure 19**: Schematic description of Bragg's Diffraction Law.*

The Bragg's law assumes the crystal is ideal without structural defects. This condition, however, is never fulfilled completely.

- **XRD pattern fitting. Rietveld method**

The overall microstructural parameters, such as lattice cell parameters (a), crystallite sizes (<D>, average coherently diffracting domain sizes), microstrains ($<\varepsilon^2>^{1/2}$, atomic level deformations), can be precisely evaluated by fitting the full XRD patterns using the "Materials Analysis Using Diffraction" (MAUD) Rietveld refinement program [202–203]. The Rietveld method uses a least square approach to refine a theoretical line profile until it matches the measured pattern. MAUD fits the XRD profiles deconvoluting the "pure" material profile from the instrumental broadening. Besides conventional XRD, there are other XRD techniques known (e.g. GIXRD, WAXS/SAXS), which allows different types of measurements.

- **Grazing incidence X-ray diffraction (GIXRD)**

In GIXRD, a limited penetration depth of the X-rays around the critical angle for total external reflection at smooth surfaces is exploited [204]. In this configuration the incident angle is fixed to

a low value (between 0˚ and 5˚) and the detector is rotated on a goniometer circle. Different depths of the sample can be investigated by varying the incidence angle. In addition, GIXRD has been used in clarifying the crystal structure of thin films, outmost surfaces treated by ion or laser irradiation, and nanoparticles with small diffracting volume. For instance, X-ray diffraction measurements of "thin" (1 – 1000 nm) films using conventional θ/2θ scanning methods generally produce a week signal from the film and an intense signal from the substrate. One of the ways to avoid intense signal from the substrate and get stronger signal from the film itself or the surface is to perform grazing angle of incidence.

- **Wide/Small angle X-ray scattering (WAXS/SAXS)**

Wide-Angle X-ray Scattering (WAXS) technique is typically used to determine the crystalline structure of polymers. The Bragg peaks scattered to wide angles (i.e., caused by sub-nanometer sized structures) are analyzed. Compared to Small-Angle X-ray Scattering (SAXS), in WAXS the distance from sample to the detector is shorter and thus diffraction maxima at larger angles are observed. In SAXS, the scattering at very low angles (0.1º-10º) is recorded. The synchrotron SAXS/WAXS gives flexibility to change/modify the sample stage. *In situ* measurements can therefore be performed to investigate dynamic structural changes of the samples. Structural changes occurring temperature variation, stress-strain variation, voltage application, etc., can be studied in real time at the SAXS/WAXS station.

- *Working conditions:*

Conventional X-ray diffractograms have been recorded on a Philips X'Pert Diffractometer in Bragg-Brentano geometry using CuK_α radiation (note that both wavelengths $\lambda(K_{\alpha1})$ = 1.5406 Å and $\lambda(K_{\alpha2})$ = 1.5443 Å have been used in an intensity proportion of $I(K_{\alpha2})/I(K_{\alpha1})$ = 0.5) in the 30˚-110˚2θ range (0.03˚step size, and 10 s holding time).

$Ti_{40}Zr_{10}Cu_{38}Pd_{12}$ and $Zr_{55}Cu_{28}Al_{10}Ni_7$ samples were structurally characterized by GIXRD, WAXS and SAXS. GIXRD patterns were acquired on an X'pert PRO MRD PANalytical X-ray diffractometer using CuK_α radiation with an incidence angle of the X-ray beam of 1º. WAXS/SAXS measurements were performed at BL11 – NCD beamline at ALBA Synchrotron Light Facility using an incident wavelength of 0.9999 Å.

3.2.3 Mechanical testing

3.2.3.1 Ultrasonic testing (UT): Pulse-echo technique

Contrary to most spectroscopy techniques that use electromagnetic waves in analysis (IR, UV, etc.), UT uses high frequency sound waves (higher than 20 kHz). It is a pulse-echo technique based on signal pulse propagation through a material (in the form of waves). The pulse is reflected at the opposite wall of the cell producing an echo, and travel time (t) can be directly related to the distance that the signal traveled (d). When such a wave propagates in a material it forces particles to oscillate. They oscillate around their positions with frequency equal to that of the ultrasonic wave, v, and can be calculated by $v = 2d/t$. The oscillation can be parallel to the direction of propagation, so that the sound wave generates a compressional wave. If the movement is perpendicular to the direction of propagation, a shear wave is generated. To determine the elastic constants (Young's modulus, E, and Poisson's ratio, v, bulk modulus, K and shear modulus, G), the velocity of the longitudinal (also known as compressional) and transverse waves (shear wave) has to be measured.

- *Working conditions:*

Samples of 2 and 3 mm in diameter and about 1-2 mm in length were prepared for the experiments. Prior to measurements, the rods were polished to perfect orthogonal geometry. Their densities were determined by the Archimedes method and the sample dimensions were measured with a digital caliper. A normal incidence shear wave transducer (V222-BB-RM from Olympus) with a frequency of 20 MHz was used to generate transverse waves. The longitudinal waves were produced with a Delay line transducer (V208-RM from Olympus) also with a frequency of 20 MHz. The transducers were employed with a panametric pulser-receiver (5072 PR from Olympus) and a digital oscilloscope. The pulser produces an electrical pulse to excite a transducer that converts the electrical input to mechanical energy creating an ultrasonic wave. Finally, the transversal and longitudinal signals were recorded and treated using a home-made Labview program. Subsequently, the elastic constants were automatically calculated.

3.2.3.2 Nanoindentation

Nanoindentation is an indentation test in which the length scale of the penetration is measured in nanometers rather than microns or millimeters and the applied load is in the order of μN and mN

rather than N as the conventional hardness measurements. Nanoindentation is considered as a depth-sensing indentation technique, since the penetration depth is continuously monitored as a function of the load during the test. This technique allows calculating hardness (H) and reduced elastic modulus (E_r) values using the Oliver and Pharr's method [205–206].

- *Working conditions:*

Nanoindentation experiments were carried out with an UMIS nanoindenter from Fischer-Cripps laboratories (Figure 20). All experiments were performed at room temperature, in load control mode using a Berkovich indenter tip. Prior to nanoindentation, the samples were carefully polished to a mirror-like appearance using diamond paste. The maximum applied loads ranged from 3 to 250 mN and a holding segment of 20 s was added in all the measurements. Thermal drift was always kept below ± 0.05 nm/s. At least 45 indentations for each loading condition were performed to verify the accuracy of the indentation data. The setup is equipped with an optical microscope which allows selecting the area of indentation and further observing the array of indentations if they are sufficiently large.

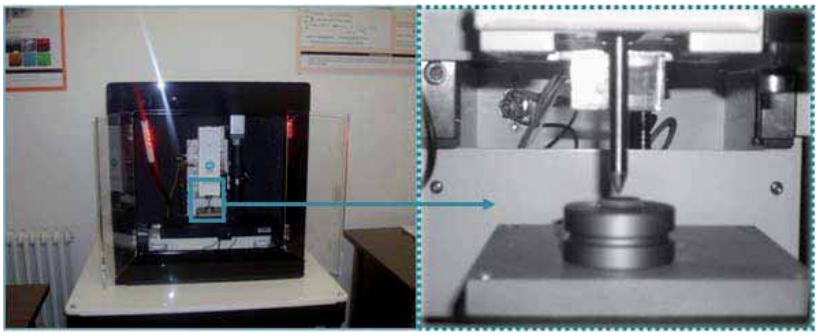

***Figure 20**: Left: Picture of a UMIS nanoindente equipment. Right: A zoomed picture of the Berkovich tip.*

3.2.4 Corrosion test: potentiodynamic polarization method

The fundamentals of the potentiodynamic polarization method are described in Section 1.2.4/Chapter 1

- *Working conditions:*

The corrosion tests were performed using a typical three-electrode cell connected to an Autolab potentiostat/ galvanostat (Figure 21). The reference electrode consisted of a double junction Ag | AgCl electrode filled with 3M KCl inner solution and 1 M NaCl interchangeable outer solution (E(SHE)= +0.210V). A platinum foil acted as the counter electrode. Once the sample (working electrode) was introduced in the electrolyte, the E_{OCP} was considered to be stabilized when fluctuations were smaller than 10 mV/h, which was typically achieved after 30 min. Afterwards, the potential was scanned from a value below E_{OCP} toward more positive values. All parameters are listed in Table 3.

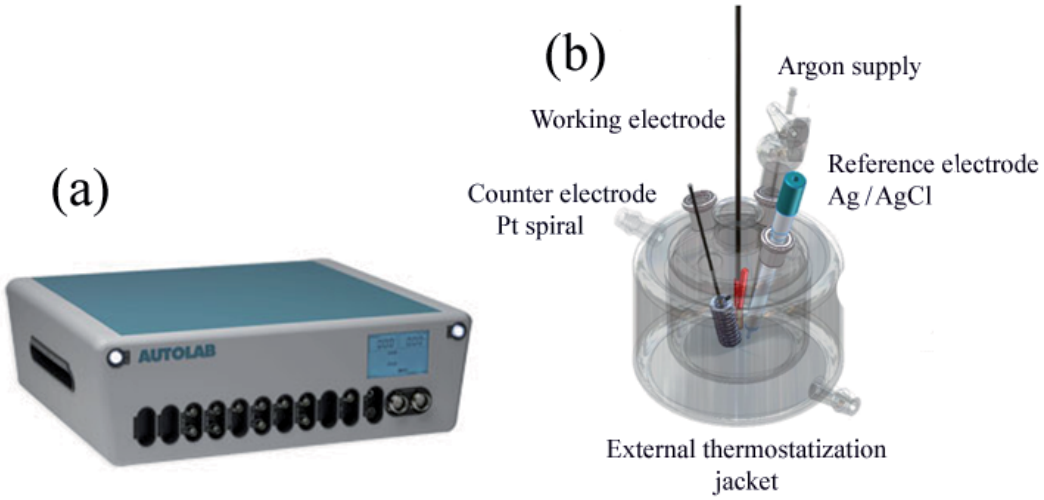

Figure 21: *(a) Picture of potentiostat/galvanostat (Autolab PGSTAT-320N); (b) sketch of the typical three-electrode cell configuration.*

Table 3. Corrosion tests parameters.

	(a) Ti-44.3Nb-8.7Zr12.3Ta (b) Ti-31.0Fe-9.0Sn	(c) $Ti_{40}Zr_{20}Hf_{20}Fe_{20}$	(d) $Ti_{40}Zr_{10}Cu_{38}Pd_{12}$	(e) $Zr_{55}Cu_{28}Al_{10}Ni_7$
Electrolyte	Hank's solution (HBSS)		5 wt.% NaCl	
Temperature	37 ± 1 ºC			RT
Scanned potential	$-300 < E_{OCP} < 400$ mV	-500 < E_{OCP} < 1500 mV	$-300 < E_{OCP} < 300$ mV	
Scan rate	0.1 mV/s	0.5 mV/s	0.1 mV/s	
Exposed area	(a) 0.031 cm^2 (b) 0.071 cm^2	0.31 cm^2		

3.2.5 Biological analysis

To determine the biocompatibility of a given material, some biological parameters have to be taken into account. This section sums up the different biological parameters studied. Two different cell lines, depending on the alloy, were used. MC3T3-E1 mouse preosteoblast cells were used for $Ti_{40}Zr_{20}Hf_{20}Fe_{20}$ alloy and Saos-2 human osteosarcoma cells were used for $Ti_{45}Zr_{15}Pd_{35}Si_5$ and $Ti_{45}Zr_{15}Pd_{30}Si_5Nb_5$ alloys (Table 4).

Cells were cultured in a specific medium supplemented with foetal bovine serum and maintained in an incubator at 37 ºC in a 5% CO_2 atmosphere. Cell culture medium was replaced twice a week with an equal volume of fresh medium.

Cytotoxicity:

Cytotoxicity was evaluated by detecting the activity of intracellular esterases using the Live/Dead Viability/Cytotoxicity kit for mammalian cells (Invitrogen). The principle of the method is that live cells are distinguished by the presence of esterase activity, determined by the enzymatic conversion of the virtually nonfluorescent cell-permeant calcein AM to the intensely fluorescent calcein (green). Ethidium homodimer enter cells with damaged membranes and links to nucleic acids, producing a bright red fluorescence in the nuclei of dead cells.

Morphology:

Alloy samples with cells attached on the surface were processed to be visualized by SEM. Briefly, cells were fixed with paraformaldehyde, dehydratated in series of ethanol and dried with hexametyl disilazane.

Adhesion:

Cell adhesion test consists in determining the presence, by immunodetection, of focal contacts, the sites where the cell adheres to the substrate. Phalloidin was used to visualize actin filaments that end in the focal contacts, whereas an antibody against vinculin was used to detect the focal contacts. Vinculin is a protein involved in focal contacts. Samples evaluation was done in a confocal laser scanning microscope.

Table 4. *Type of biological tests performed on the indicated alloys.*

Sample	Cell viability assay	SEM analysis of cells	Cell adhesion analysis	Cell differentiation assay
Ti-44.3Nb-8.7Zr12.3Ta	-	-	-	-
Ti-31.0Fe-9.0Sn	-	-	-	-
$Ti_{40}Zr_{20}Hf_{20}Fe_{20}$	X	X	X	X
$Ti_{40}Zr_{10}Cu_{38}Pd_{12}$	X	X	X	X
$Zr_{55}Cu_{28}Al_{10}Ni_{7}$	-	-	-	-
$Ti_{45}Zr_{15}Pd_{30}Si_{5}Nb_{5}$	X	X	X	-
$Ti_{45}Zr_{15}Pd_{35}Si_{5}$	X	X	X	-

Differentiation:

Preosteoblasts and undifferentiated osteoblasts are able to differentiate over time in culture. Differentiation was studied though the detection of calcium deposits, a sign of extracellular matrix mineralization, using Alizarin Red S staining. Secreted calcium deposits were detected by Alizarin Red S, which is a specific red histochemistry staining for calcium.

Results and Discussion: Compilation of Articles

In the following, the results derived from the Thesis work are presented as a compilation of the three articles approved to be included as constituents of the Thesis (4.1, 4.2 and 4.3). In addition, complementary information on the work done (manuscript 4.4) is also presented. A brief summary is included before each article. A thorough discussion of the results can be found in the articles themselves.

4.1. **Hynowska, A**.; Pellicer, E.; Fornell, J.; González, S.; Van Steenberge, N.; Suriñach, S.; Gebert, A.; Calin, M.; Eckert, J.; Baró, M.D.; Sort, J. Nanostructured β-phase Ti-31.0Fe-9.0Sn and sub-μm structured Ti-39.3Nb-13.3Zr-10.7Ta alloys for biomedical applications: Microstructure benefits on the mechanical and corrosion performances. *Mat. Sci. Eng. C* 32, **2012**, 2418–2425.

4.2. **Hynowska, A**.; Blanquer, A.; Pellicer, E.; Fornell, J.; Suriñach, S.; Baró, M.D.; González, S.; Ibáñez, E.; Barrios, L.; Nogués, C.; Sort, J. Novel Ti–Zr–Hf–Fe Nanostructured Alloy for Biomedical Applications. *Materials* 6, **2013**, 4930–4945.

4.3. Menéndez, E.; **Hynowska, A**.; Fornell, J.; Suriñach, S.; Montserrat, J.; Temst, K.; Vantomme, A.; Baró, M.D.; García–Lecina, E.; Pellicer, E.; Sort, J. Influence of the irradiation temperature on the surface structure and physical/chemical properties of Ar ion-irradiated bulk metallic glasses. *J. Alloys Compd.* 610, **2014**, 118–125

4.4. Hynowska, A.; Blanquer, A.; Pellicer, E.; Fornell, J.; Suriñach, S.; Baró, M.D.; Gebert, A.; Calin, M.; Eckert, J.; Nogués, C.; Ibáñez, E.; Barrios, L.; Sort, J. Nanostructured Ti-Zr-Pd-Si-(Nb) bulk metallic composites: novel biocompatible materials with superior mechanical strength and elastic recovery. *J. Biomed. Mater. Res. B*, **2014** (submitted).

4.1. Nanostructured β-phase Ti-31.0Fe-9.0Sn and sub-μm structured Ti-39.3Nb-13.3Zr-10.7Ta alloys for biomedical applications: Microstructure benefits on the mechanical and corrosion performances

In this article, an in-depth comparative study of the microstructure, mechanical properties and corrosion behavior in a physiological environment of two different nanostructured β-type Ti-based alloys (i.e., Ti-31.0Fe-9.0Sn and Ti-44.3Nb-8.7Zr-12.3Ta, wt.%), as well as the widely used commercial Ti-6Al-4V alloy, is reported.

These alloys were synthesized by arc melting, and subsequent Cu mold suction casting techniques. Ti-44.3Nb-8.7Zr-12.3Ta and Ti-31.0Fe-9.0Sn samples were cast in the form of rods of 2.5 mm and 3 mm in diameter, respectively.

Regarding the microstructure, the XRD pattern of the Ti-39.3Nb-13.3Zr-10.7Ta alloy only shows a few Bragg's peaks corresponding to the β-phase. This phase is distributed forming micrometer-sized regions of slightly different contrast and composition according to SEM-EDX analysis. This indicates that both regions consist of β-phase with different amounts of dissolved Zr, Ta and Nb. Additionally, TEM images show the presence of several sub-μm grains within the micometer-sized regions, together with the occurrence of different types of dislocations. On the contrary, a composite-like morphology is observed in the Ti-31.0Fe-9.0Sn alloy, consisting of micrometer-sized bright dendrites composed of hexagonal Ti_3Sn phase and dark dendrites of β-Ti. The latter is also one of the phases of the nanoeutectic matrix, while bcc-TiFe is the other phase in the eutectic matrix.

The dissimilar microstructures observed in the newly developed alloys have profound effects on the resulting physico-chemical properties, namely the mechanical behavior and the corrosion resistance in a bodily fluid. Nanoindentation experiments reveal that the Ti-31.0Fe-9.0Sn rods exhibit very large hardness (H ≈ 9 GPa) and high Young's modulus. Conversely, the Ti-39.3Nb-13.3Zr-10.7Ta alloy is mechanically softer (but still maintains a reasonable hardness, H, higher than for the well-known "TiOsteum" alloy, i.e. Ti-35Nb-7Zr-5Ta) and is particularly interesting because of its rather low Young's modulus (E ≈ 71 GPa). Both alloys show larger H/E ratios (i.e., better wear resistance) than commercial Ti-6Al-4V. From the point of view of biocorrosion, neither of the new alloys show potential breakdown within the explored potential window (up to 0.4 V). Both the corrosion potential, E_{corr}, and the corrosion current density, j_{corr}, values exhibited

by the Ti-39.3Nb-13.3Zr-10.7Ta alloy are similar to those of commercial Ti-6Al-4V, whereas a shift in E_{corr} towards more negative values and increased j_{corr} values are observed for Ti-31.0Fe-9.0Sn, probably due to its smaller average crystallite size. In any case, the surfaces exposed to the bodily fluid do not become particularly damaged. For all these properties, the β-type alloys investigated here are found to be better in many aspects than the commercial Ti-6Al-4V. In addition, due to the absence of toxic elements, these materials are well suited for a variety of biomedical purposes.

Nanostructured β-phase Ti-31.0Fe-9.0Sn and sub-μm structured Ti-39.3Nb-13.3Zr-10.7Ta alloys for biomedical applications: Microstructure benefits on the mechanical and corrosion performances

Anna Hynowska [a,*], Eva Pellicer [a,*], Jordina Fornell [a], Sergio González [a], Nele van Steenberge [b], Santiago Suriñach [a], Annett Gebert [c], Mariana Calin [c], Jürgen Eckert [c, d], Maria Dolors Baró [a], Jordi Sort [e,*]

[a]Departament de Física, Facultat de Ciències, Universitat Autònoma de Barcelona, E-08193 Bellaterra, Spain

[b]OCAS N.V., Pres. J.F. Kennedylaan 3, BE-9060 Zelzate, Belgium

[c]IFW Dresden, Institute for Complex Materials, PO Box 270116, D-01171 Dresden, Germany

[d]TU Dresden, Institute of Materials Science, D-01062 Dresden, Germany

[e]Institució Catalana de Recerca i Estudis Avançats (ICREA) and Departament de Física, Universitat Autònoma de Barcelona, E-08193 Bellaterra, Spain.

*Corresponding authors at: Departament de Física, Facultat de Ciències, Universitat Autònoma de Barcelona, E-08193 Bellaterra, Spain. Tel.: + 3493 5811401, fax: +34935812155.
E-mail addresses: anna.hynowska@campus.uab.cat (A Hynowska); eva.pellicer.icn@uab.cat (E. Pellicer); jordi.sort@uab.cat (J. Sort).

Abstract

Nanostructured Ti-31.0Fe-9.0Sn and Ti-39.3Nb-13.3Zr-10.7Ta (wt.%) β-type alloys, exhibiting different microstructures and dissimilar mechanical properties, have been prepared by copper mold casting. The microstructure, mechanical behavior and corrosion resistance, in simulated body fluid, of both alloys have been investigated and compared to those of commercial Ti-6Al-4V. Nanoindentation experiments reveal that the Ti-31.0Fe-9.0Sn rods exhibit very large hardness (H ≈ 9 GPa) and high Young's modulus. Conversely, the Ti-39.3Nb-13.3Zr-10.7Ta alloy is mechanically softer but it is interesting for biomedical application because of its rather low Young's modulus (E ≈ 71 GPa). Concerning the corrosion performance, Ti-35Nb-7Zr-5Ta shows a corrosion behavior comparable to Ti-Al6-V4, with no potential breakdown up to 0.4 V vs. Ag|AgCl. On the contrary, the Ti-31.0Fe-9.0Sn alloy exhibits a more anodic corrosion potential, but the value is still less negative than for pure elemental Fe and Ti. From all these properties and because of the absence of toxic elements in the compositions, the Ti-39.3Nb-13.3Zr-10.7Ta and Ti-31.0Fe-9.0Sn alloys are attractive for use as metallic biomaterials.

Keywords: Ti-based alloys; Microstructure; Mechanical properties; Corrosion behavior

1. Introduction

Research in the field of biomaterials (e.g., metallic alloys, polymers, ceramics or composites), suitable for permanent or biodegradable implants, has become a highly active field during the last decades, encouraged by the increase in the quality and longevity of life that the use of these materials can provide [1]. Traditionally, 316L austenitic stainless steel and Co-Cr alloys have been employed as metallic orthopedic implants. However, these materials suffer from the drawback that they exhibit an exceedingly large Young's modulus, E, and can be cytotoxic [2,3]. For this reason, new types of alloys, usually based on Ti, have been developed during recent years. These novel alloys exhibit a combination of excellent properties, such as low density (around 4-5 g cm^{-3}), relatively low E ranging from 50 to 110 GPa [4], high corrosion resistance [5] and good biocompatibility [3].

From a mechanical viewpoint, the strength of Ti-based alloys is close to that of 316L steel, whereas its density is 55% lower, thus resulting in a specific strength (strength normalized to density) much higher than that of conventional metallic implants [3]. Mechanical compatibility between the implant and the surrounding tissue is also of great importance. Namely, pronounced stress transfer between the implant and bone can cause resorption and subsequent implant loosening. This biomechanical mismatch, known as stress-shielding effect can result in the death of the bone cells and occurs when the stiffness (or the Young's modulus) of the implant is much higher than that of bone (E_{bone} ranges between 3 and 20 GPa) [6,7]. For this reason, Ti-based alloys with rather low E values are of keen interest for biomedical applications. Indeed, the Young's modulus of stainless steel and Co-Cr are 210 GPa and 240 GPa, respectively, thus more than twice the value of Ti-based alloys [3]. Additionally, suitable materials for implants are expected to be non-toxic and should not cause any inflammatory or allergic reaction in the human body [8]. In this sense, Ti is highly biocompatible, due in part to the formation of a thin passive oxide layer (2-3 nm) at the surface of the alloy, which protects the implant against reaction with bodily fluids.

Amongst Ti-based alloys, Ti-6Al-4V has become a widely used material in many technological applications, including the aerospace and automotive sectors, because it offers a combination of high strength, light weight, good formability and high corrosion resistance. Because of these outstanding properties as well as its cost-effectiveness, this alloy has also found applications in medical devices and as biomaterial for orthopedic implants [3]. Nevertheless, Ti-6Al-4V contains toxic elements (Al, V), which are released into the human body after long-term implantation and can eventually cause serious health problems, such as peripheral neuropathy, osteomalacia or Alzheimer [9-11].

Titanium can exist in two allotropic forms. At low temperatures atoms are disposed forming a hexagonal closed packed (hcp) crystal lattice, which is commonly referred to as α–phase, while above 883°C atoms are arranged in a body centered cubic (bcc) crystal structure, known as β–phase. The α-to-β transformation temperature, $T_{\alpha-\beta}$, in Ti alloys can either increase or decrease depending on the alloying elements. Elements such as Al or O tend to stabilize the α–phase by increasing $T_{\alpha-\beta}$ and are the so-called α-stabilizers.

Conversely, other elements stabilize the β–phase (e.g., V, Nb, Fe, etc.). Some elements, like Sn or Zr, behave as neutral solutes and have little effect on the transformation temperature, acting instead as strengtheners [3]. The Ti-6Al-4V alloy consists of a large fraction of hcp α–phase mixed with a small volume fraction of bcc β–phase [12]. In general, addition of β-stabilizing alloying elements causes a lowering of the Young's modulus, an improvement of the alloy formability and an enhancement of the corrosion resistance [9]. This makes β-Ti alloys better for biomedical applications than α–Ti alloys. It has been shown that Nb, Zr, Ta, Sn or Fe are suitable alloying elements that can be introduced in the alloy composition to reduce the Young's modulus of bcc Ti without decreasing the strength [13]. These elements are non-toxic and can thus be used for implant applications [14]. Amongst the β-type Ti alloys, the Ti-Nb-Zr and Ti-Nb-Zr-Ta families stand out from the rest because of their rather low E value [12,15]. In particular, the Ti-35Nb-7Zr-5Ta (wt.%) alloy (also known as "TiOsteum") exhibits a Young's modulus of 55 GPa, the lowest reported to date for Ti-based biocompatible materials [16]. However, usually the hardness, H, of β-type alloys is not particularly high and attempts have been made to increase it, for instance by adding elements with strengthening potential (e.g., Fe) [17], tuning the oxygen content [16], or engineering suitable microstructures with high strength [18,19].

The strength of metallic alloys not only depends on the crystallographic phases composing the microstructure but also on the size of the crystals and the presence of structural defects [20]. Nanocrystalline metals exhibit larger hardness and quite often better corrosion and wear resistance than coarse-grained ones [21]. Combination of large hardness with low Young's modulus (i.e., high H/E ratio) is indicative of good wear resistance [22]. This is an important parameter since orthopaedic implants are expected to suffer from abrasion with bone and hard tissues and the formation of wear debris can result in inflammatory reactions [23]. However, nanocrystalline alloys sometimes exhibit limited plasticity at room temperature. To increase it, micrometer-sized particles composed of a softer phase are sometimes embedded in the nanostructured harder matrix, forming a bimodal microstructure [18,19,24,25]. In this sense, the formation of β-Ti/TiFe composites consisting of β-Ti micrometer-sized dendrites embedded in a nanoeutectic matrix has been reported to result in optimum mechanical properties [26]. Addition of Sn to this system has been shown to further enhance its strength [27,28].

In this work, we investigate the mechanical properties and corrosion resistance, in simulated body fluid, of two nanostructured β-phase alloys with dissimilar microstructure and mechanical properties (i.e., Ti-31.0Fe-9.0Sn and Ti-44.3Nb-8.7Zr-12.3Ta), and compare them with commercial Ti-6Al-4V. These compositions were selected for several reasons. First, the Ti-Nb-Zr-Ta system is known to exhibit rather low Young's modulus (i.e., good biomechanical compatibility with bone) but moderate hardness, whereas the Ti-Fe-Sn system shows high yield strength but also exceedingly high Young's modulus, which could eventually lead to stress shielding effects. A material combining low Young's modulus with high strength would be ideally suited for biomedical implants. With this aim, we produced an alloy from the Ti-Nb-Zr-Ta system with larger Nb and Ta percentages than those in "TiOsteum" (the alloy composition of the Ti-Nb-Zr-Ta system showing the lowest Young's modulus), since both Nb and Ta should favor an increase of hardness and plasticity. In fact, although the properties of TiOsteum have been extensively investigated, those of other Ti-Nb-Zr-Ta alloys have been largely overlooked. On the other hand, Ti-31.0Fe-9.0Sn has been also investigated in some detail because of its interesting ultra-fine grained microstructure [27,28]. However, the mechanical properties of this alloy have been mainly investigated only by means of macroscopic compression experiments but not with nanoindentation. Here, we make use of the same nanoindentation experimental setup and the same experimental load-unload conditions to investigate both alloy families, with the aim of allowing for a better comparison of the mechanical behaviour between the different materials. In particular, nanoindentation experiments reveal that the Ti-31.0Fe-9.0Sn cast rods exhibit very large hardness (H ≈ 8 GPa) and relatively high Young's modulus. Conversely, the Ti-39.3Nb-13.3Zr-10.7Ta alloy is interesting because of its rather low Young's modulus (E ≈ 71GPa), thus favoring its biomechanical compatibility with bone, while exhibiting reasonable hardness, higher than that of the "TiOsteum" alloy. Remarkably, both alloys show larger H/E ratios (i.e., better wear resistance) than commercial Ti-6Al-4V. Concerning the corrosion behavior, neither Ti-39.3Nb-13.3Zr-10.7Ta nor Ti-31.0Fe-9.0Sn show passivity breakdown. The Ti-39.3Nb-13.3Zr-10.7Ta system shows comparable corrosion potential to Ti-6Al-4V, whereas the Ti-31.0Fe-9.0Sn alloy exhibits more anodic corrosion potential values. From all these properties and because of the absence of toxic elements in their compositions, the Ti-39.3Nb-13.3Zr-10.7Ta and Ti-31.0Fe-9.0Sn alloys are appealing for their use as metallic biomaterials.

2. Materials and methods

Cylindrical rods of 2 and 3 mm in diameter with compositions Ti-39.3Nb-13.3Zr-10.7Ta and Ti-31.0Fe-9.0Sn (wt. %), respectively, were prepared by Cu-mold suction casting. The master alloys were obtained from a mixture of high-purity elements (> 99.99 wt. %) by arc-melting in a Ti-gettered high purity Ar atmosphere on a water-cooled Cu hearth. The samples were structurally characterized by X-ray diffraction (XRD), using a Philips X'Pert diffractometer with monochromatic Cu K_α radiation. The patterns were analyzed by means of a full-pattern fitting procedure (Rietveld method) with the Microstructural Analysis Using Diffraction (MAUD) computer software [29,30]. An EVO-Zeiss scanning electron microscope (SEM), equipped with an energy dispersive x-ray spectrometer (EDX, Link ISIS-200) was used for microstructure observation and compositional analyses. Transmission electron microscopy (TEM) imaging was also performed, using a Jeol-JEM 2011 system operated at 200 kV.

Nanoindentation experiments were carried out on the as-cast samples using a UMIS equipment from Fischer-Cripps laboratories, with a Berkovich pyramidal-shaped indenter tip applying a maximum load of 250 mN. A load holding period of 20 s was added before unloading and the thermal drift was always kept below ±0.05 nms^{-1}. At least 50 indentations on each sample were performed to verify the accuracy of the indentation data. Prior to the nanoindentation tests the specimens were carefully polished to mirror-like appearance using diamond paste. The method of Oliver and Pharr was used to determine the hardness and the reduced Young's modulus [31,32]. Proper corrections for the contact area (calibrated with a fused quartz specimen), the instrument compliance, and the initial penetration depth were applied. The hardness was obtained from the ratio between the maximum load, P_{Max}, and the contact area of the indent, A, i.e.:

$$H = \frac{P_{Max}}{A} \quad (1)$$

From the initial unloading slope, the contact stiffness, S, was determined as follows:

$$S = \frac{dP}{dh} \quad (2)$$

where P and h denote the applied load and the penetration depth during nanoindentation, respectively. The elastic modulus was then evaluated based on its relationship with the contact area, A, and the contact stiffness:

$$S = \beta \frac{2}{\sqrt{\pi}} E_r \sqrt{A} \quad (3)$$

Here, β is a constant that depends on the geometry of the indenter (β= 1.034 for a Berkovich indenter) [33] and E_r is the so-called reduced Young's modulus, defined as:

$$\frac{1}{E_r} = \frac{1-\nu^2}{E} + \frac{1-\nu_i^2}{E_i} \quad (4)$$

The reduced modulus takes into account the elastic displacements that occur in both the specimen, with Young's modulus E and Poisson's ratio ν, and the diamond indenter, with elastic constants E_i = 1140 GPa and ν_i= 0.07. Finally, the elastic/plastic indentation energies were also calculated. The total mechanical work done by the indenter during loading, U_{tot}, was calculated from the area enclosed between the loading indentation segment and the displacement axis. This energy is defined as the sum of the elastic, U_{el}, and plastic, U_{pl}, energies:

$$U_{tot} = U_{el} + U_{pl} \quad (5)$$

The values of U_{el} were obtained from the area enclosed between the unloading segments and the displacement axis [34]. The elastic recovery was evaluated as the ratio between the elastic and the total (plastic + elastic) energies during nanoindentation, U_{el}/U_{tot}.

The corrosion behavior of the as-cast samples was investigated by electrochemical polarization measurements using a PGSTAT120 Autolab potentiostat/galvanostat (Ecochemie). Prior to the measurements, slices from the Ti-31.0Fe-9.0Sn and Ti-39.3Nb-13.3Zr-10.7Ta rods were cut and carefully ground with emery paper (SiC) down to grit 4000 and further polished with 6 μm diamond suspension. Subsequently, the samples were degreased in acetone and finally cleaned with distilled water. Electrochemical corrosion experiments were performed in naturally aerated simulated physiological Hank's balanced salt solution (HBSS) at 37.5ºC. The composition of the HBSS solution was: 8.0 g dm^{-3} NaCl + 0.4 g dm^{-3} KCl + 0.04788 g dm^{-3} Na_2HPO_4 + 0.06 g dm^{-3} KH_2PO_4 + 0.185 g dm^{-3} $CaCl_2 \cdot 2H_2O$ + 0.09767 g dm^{-3} $MgSO_4$ + 0.35 g dm^{-3} $NaHCO_3$ + 1.0 g dm^{-3} D-glucose. A typical three-electrode cell configuration was used. The reference electrode consisted of a double junction Ag | AgCl electrode filled with 3 M KCl inner solution and 1 M NaCl interchangeable outer solution (E(SHE)= +0.210 V). A platinum foil acted as the counter electrode. Before each polarization scan, the sample was immersed in the electrolyte and left for at least 2 h for stabilization until variations of the potential became smaller than 0.01 Vh^{-1}. The stabilized value was considered to be the open-circuit potential (OCP). Afterwards, the potential

was swept toward the anodic direction starting from 300 mV below to the OCP at a scan rate of 0.1 mV s^{-1}. The corrosion current density (j_{corr}) values were determined using the Tafel extrapolation method [35]. The polarization resistance, R_p, was used to determine the resistance of the alloys against corrosion [36]. The values of R_p were determined as:

$$R_p = \left(\frac{\Delta E}{\Delta i} \right)_{\Delta E \to 0} \quad (6)$$

where ΔE is the variation of the applied potential around the corrosion potential and Δi is the resulting polarization current. If the Tafel slopes (anodic slope, b_a, and cathodic slope, b_c) are known, the corrosion current, i_{corr}, can be calculated using the Stern-Geary equation [35,36]:

$$i_{corr} = 2.303 \frac{b_a b_c}{b_a + b_c} \left(\frac{1}{R_p} \right) \quad (7)$$

The mechanical properties and the corrosion behavior ofthe nanostructured Ti-31.0Fe-9.0Sn and Ti-39.3Nb-13.3Zr-10.7Ta alloys were compared with those of commercial Ti–6Al–4V [37].

3. Results and discussion

3.1. Microstructure

SEM images (backscattered electrons) of the Ti-39.3Nb-13.3Zr-10.7Ta and Ti-31.0Fe-9.0Sn as-cast alloys are shown in Fig. 1(a) and (b), respectively. The Ti-39.3Nb-13.3Zr-10.7Ta sample is composed of dark and light grey regions of a few micrometers in lateral size.

TEM images (shown as insets) reveal the presence of several sub-μm grains within the micrometer-sized regions, together with the occurrence of different types of dislocations. EDX compositional analyses reveal that the light grey regions are rich in Nb and Ta whereas the darker ones are enriched in Zr and Ti (Table 1).

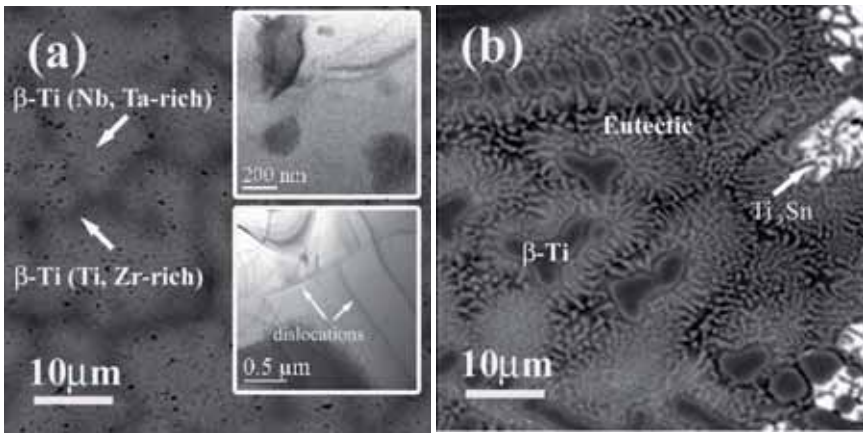

Fig. 1. *SEM micrographs of back-scattered electrons of the (a) Ti-39.3Nb-13.3Zr-10.7Ta and (b) Ti-31.0Fe-9.0Sn alloys. Indicated with arrows in (a) are the two β-phases (with different grey tonality) composing the Ti-39.3Nb-13.3Zr-10.7Ta alloy. The arrow in (b) indicates the presence of Ti_3Sn intermetallic phase. The insets in (a) correspond to TEM images of the Ti-39.3Nb-13.3Zr-10.7Ta alloy indicating the presence of sub-μm grains, together with several types of dislocations.*

Table 1

Chemical composition (wt.%) obtained by EDX nano-probe analysis on different regions of the Ti-31.0Fe-9.0Sn and Ti-44.3Nb-8.7Zr-12.5Ta alloys.

Sample	Phases	Element concentration (wt.%)					
		Ti	Fe	Sn	Nb	Zr	Ta
Ti-39.3Nb-13.3Zr-10.7Ta	**β-Ti(light grey)** **β-Ti (dark grey)**	33.2 43.0	-- --	-- --	45.0 29.9	7.8 22.1	14.0 5.0
Ti-31.0Fe-9.0Sn	**β-Ti (dendrites)** **Ti_3Sn** **Eutectic regions**	66.9 59.7 48.8	25.8 16.7 50.2	7.1 23.6 1.0	-- -- --	-- -- --	-- -- --

The lighter contrast comes mainly from the high Ta content, since the atomic weight of this element (180.95 g $mole^{-1}$) is the largest amongst all the constituent elements of this alloy. In spite of this two-region microstructure, the XRD pattern only shows a few Bragg's peaks corresponding to the β-phase (see Fig. 2). This indicates that both regions consist of β-Ti phases with different amounts of dissolved Zr, Ta and Nb. However, the cell parameters of the light and

dark grey regions are very similar (a ≈ 0.33258 nm), therefore the resulting XRD peaks become overlapped.

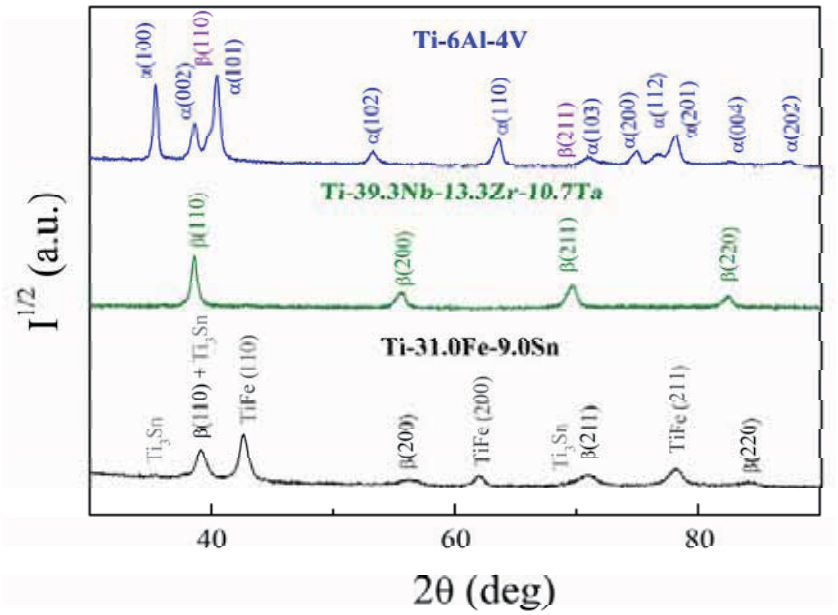

Fig. 2. *X-ray diffraction patterns of the Ti-6Al-4V, Ti-39.3Nb-13.3Zr-10.7Ta and Ti-31.0Fe-9.0Sn alloys. The Miller indices of the XRD peaks corresponding to the α–, β–Ti and cubic TiFe phases composing the alloys, together with small peaks corresponding to the hcp Ti_3Sn phase, are indicated.*

The microstructure of the Ti-31.0Fe-9.0Sn alloy is quite different. In this case, a composite-like morphology is observed. Two types of micrometer-sized dendrites (with dark grey and bright contrast) are embedded in an ultra-fine eutectic matrix. EDX analyses reveal that the bright dendrites contain a high Sn content, whereas the grey ones are rich in Ti. High amounts of Fe are detected in the nanoeutectic matrix (Table 1). Analysis of the XRD pattern (Fig. 2) reveals the presence of mainly two crystallographic phases in this alloy: bcc-Ti (Im3m) (i.e., β-phase) and bcc-TiFe (Pm3m). The β-Ti phase comprises both the grey dendrites and one of the phases of the eutectic matrix, while bcc-TiFe is the other phase in the eutectic matrix [38]. The third phase (corresponding to the brightest dendrites) is hardly detectable by XRD but it presumably corresponds to hexagonal Ti_3Sn phase (P63/mmc) [39,40]. Fig. 2 also shows the XRD pattern of the commercial Ti-6Al-4V alloy, which mainly consists of an α-Ti phase with small amounts of β-Ti phase. Rietveld refinement of the XRD patterns using the MAUD software allows determining the cell parameters, crystallite sizes and microstrains of the different phases. To

properly account for the differences in chemical composition (i.e., cell parameter) and crystallite size, two distinct β-Ti phases were considered in the refinement of the Ti-31.0Fe-9.0Sn XRD patterns (one for the dendrites and the other for the eutectics). Conversely, since the two β-Ti regions in the Ti-39.3Nb-13.3Zr-10.7Ta sample are virtually indistinguishable by XRD, they were both adjusted as a single β-Ti phase. As shown in Table 2, the unit cell parameter for the Ti-39.3Nb-13.3Zr-10.7Ta alloy is slightly larger than the value tabulated for pure bcc Ti (a = 0.33065 nm) [41]. This is probably related to the larger covalent radii of Nb (164 pm), Zr (175 pm) and Ta (170 pm), as compared to Ti (160 pm). An increase of the cell parameter in the β-Ti phase will thus occur if such elements (Nb, Zr or Ta) enter this phase in substitution of Ti atoms. Conversely, the cell parameters of the β-phases in the Ti-31.0Fe-9.0Sn alloy are smaller than the tabulated value, probably because of the small atomic radii of Fe (132 pm) and Sn (139 pm) as compared to Ti. The lattice parameter of the TiFe phase (a = 0.30033) is slightly larger than the value reported for the equiatomic Ti-Fe composition (a = 0.2976 nm) [42], which indicates that the TiFe phase in the eutectic regions is probably enriched in Ti. Also remarkable from Table 2 is that the crystallite sizes in all existing phases fall within the sub-50 nm range. Particularly small crystallite size values are obtained in the Ti-31.0Fe-9.0Sn alloy, in agreement with its rather refined microstructure, as observed by SEM imaging (Fig. 1). The values of microstrains range between $8 \cdot 10^{-4}$ and $5 \cdot 10^{-3}$, being a bit larger in the phases forming the eutectic matrix of the Ti-31.0Fe-9.0Sn alloy.

Table 2

Summary of the structural parameters of the Ti-6Al-4V, Ti-39.3Nb-13.3Zr-10.7Ta and Ti-31.0Fe-9.0Sn alloys (crystallographic phases, lattice parameters, crystallite sizes and microstrains), determined from Rietveld refinements of the XRD patterns.

Sample	Phases	a (nm)	c (nm)	<D> (nm)	$(\varepsilon^{1/2})^2$
Ti-6Al-4V	**α-phase**	0.23144	0.46762	46	0.0008
Ti-39.3Nb-13.3Zr-10.7Ta	**β-phase**	0.33258	--	38	0.0019
Ti-31.0Fe-9.0Sn	**β-phase (Ti, dendrites)** **β-phase (Ti, eutectic)** **β-phase (TiFe,eutectic)**	0.30384 0.32612 0.30033	-- -- --	23 15 20	0.0009 0.0050 0.0031

3.2. Mechanical Properties

Fig. 3 shows representative nanoindentation curves corresponding to the Ti-6Al-4V, Ti-39.3Nb-13.3Zr-10.7Ta and Ti-31.0Fe-9.0Sn alloys.

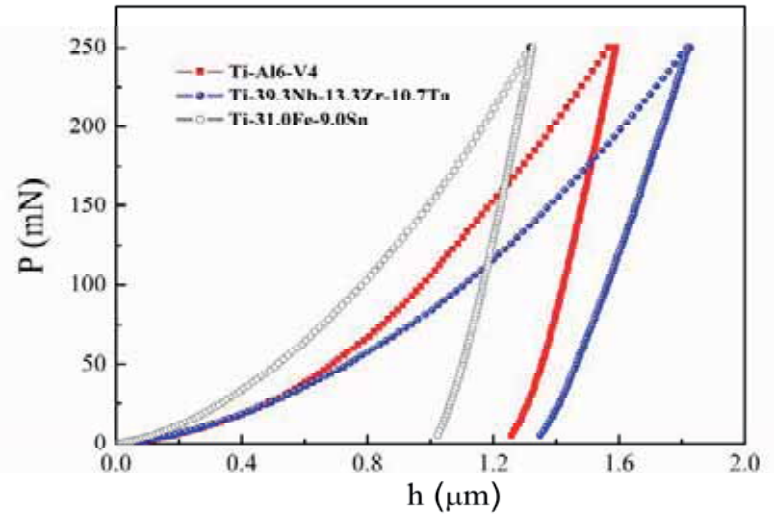

Fig. 3. *Representative load (P) – displacement (h) nanoindentation curves for Ti-6Al-4V, Ti-39.3Nb-13.3Zr-10.7Ta and Ti-31.0Fe-9.0Sn alloys obtained applying a maximum force* P_{max} *= 250 mN.*

The largest value of maximum penetration depth, obtained at the end of the loading segment, is observed for the Ti-39.3Nb-13.3Zr-10.7Ta alloy, indicating that this material possesses the lowest hardness value amongst the three investigated systems. Conversely, the Ti-31.0Fe-9.0Sn alloy is the mechanically hardest one. Furthermore, the initial slope of the unloading indentation segment, i.e., the contact stiffness, is also higher for the Ti-31.0Fe-9.0Sn alloy and lower for the Ti-39.3Nb-13.3Zr-10.7Ta sample, indicating that the former exhibits the largest reduced Young's modulus whereas the latter possesses the lowest one (see Eq. 3). For each sample, the hardness and the reduced Young's modulus have been calculated from an average of 50 indentations performed using a maximum load of 250 mN. Such relatively high value of applied load created indents at the surface of the specimens which are sufficiently large to embrace all the phases/regions composing the investigated alloys (see Fig. 4). When looking at Fig. 4 one can notice that the imprint in the Ti-39.3Nb-13.3Zr-10.7Ta sample is larger than that in the Ti-31.0Fe-9.0Sn one. This is in agreement with the data from the indentation curves (Fig. 3) and confirms that the Ti-31.0Fe-9.0Sn alloy is mechanically harder.

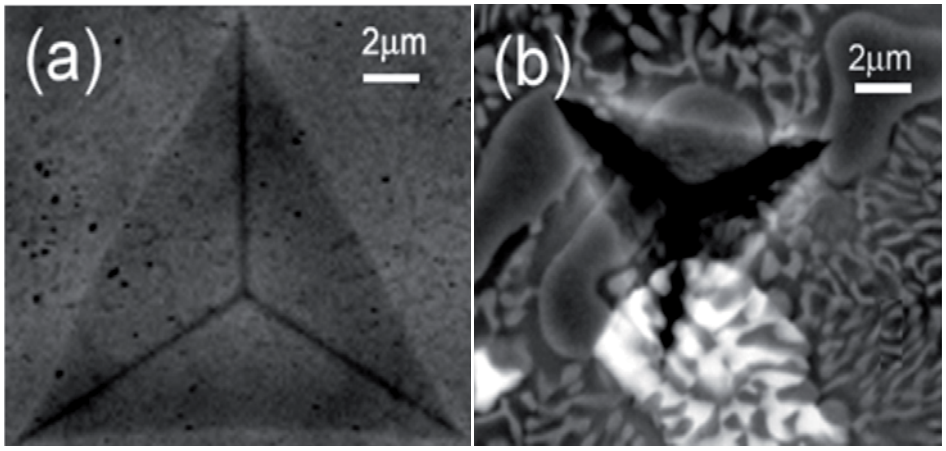

Fig. 4. *SEM images (backscattered electrons) of the Ti-39.3Nb-13.3Zr-10.7Ta and Ti-31.0Fe-9.0Sn alloys after nanoidentation.*

Table 3 lists the values of hardness (H) and reduced Young's modulus (E_r) of the investigated samples, as well as the ratios H/E_r, H^3/E^2_r, U_{el}/U_{tot} (i.e., elastic recovery) and U_{pl}/U_{tot} (i.e., plasticity index). Remarkably, the Ti-31.0Fe-9.0Sn alloy exhibits a rather large hardness (H = 8.9 GPa), i.e. almost twice the value of Ti-44.3Nb-8.7Zr-12.3Ta, although both alloys are composed of phases with similar crystallographic structures (i.e., cubic). It may be argued that solution hardening effects could be responsible for such pronounced difference in hardness between the two β-type alloys. However, the Vickers hardness of Fe is 40% lower than that of Ti, whereas Nb exhibits Vickers hardness about 40% larger than Ti [41]. Hence, in terms of solution hardening, Nb could be expected to induce an increase of strength in β-Ti, whereas Fe would eventually cause mechanical softening. This is opposite to what is experimentally observed. Therefore, the differences in microstructure between the two alloys, rather than solution hardening effects, are likely to be mainly responsible for the observed dissimilar mechanical strength. In fact, TiFe is known to be a hard intermetallic phase [26]. Furthermore, eutectic structures are usually mechanically harder than dendritic ones [43,44]. This is due to the large amount of inter-phase boundaries existing in eutectic regions, which hinder dislocation motion. Moreover, the influence of crystallite size should also be taken into account. The XRD peaks in Ti-31.0Fe-9.0Sn are broader than those in Ti-39.3Nb-13.3Zr-10.7Ta (see Fig. 2), indicating smaller crystallite sizes, particularly in the phases composing the eutectic regions, as shown in Table 2. The Hall-Petch relationship postulates that the hardness increases as $1/\langle D\rangle^{1/2}$ (where $\langle D\rangle$ is the crystallite size). For small crystallite sizes, the role of grain boundaries in disrupting dislocation propagation becomes more and more pronounced, resulting in an increased stress concentration at grain

boundaries due to dislocation pile-up. Thus, higher applied stresses are needed to propagate dislocations through the material, resulting in a larger hardness [45]. The dendrite/matrix boundaries can also cause pile-up of the dislocations generated in the dendrites before they can enter the ultra-fine eutectic matrix, eventually also leading to an increase of hardness [44]. It is worth mentioning that the hardness of Ti-39.3Nb-13.3Zr-10.7Ta is larger than that of "TiOsteum" (i.e., Ti-35Nb-7Zr-5Ta wt.%) [16,46], an alloy which has been investigated to a certain extent because of its rather low Young's modulus (E = 55 GPa).

The Ti-39.3Nb-13.3Zr-10.7Ta alloy exhibits the lowest Young's modulus (E_r = 71 GPa) amongst the three alloys investigated in this work (see Table 3). The commercial Ti-6Al-4V material possesses a Young's modulus in excess of 120 GPa, much larger than the value for Ti-39.3Nb-13.3Zr-10.7Ta (E_r = 71 GPa), probably because of the large percentage of α-phase contained in this alloy. The presence of β-stabilizing elements (such as Nb) in Ti-39.3Nb-13.3Zr-10.7Ta favors the reduction of Young's modulus [8,12,15]. However, following this reasoning, a similarly low value of E_r would be expected for Ti-31.0Fe-9.0Sn, since this alloy is also composed of a large fraction of β-Ti phase. Instead, the large E_r in this particular alloy is probably mainly related to the presence of Fe. The Young's modulus of Fe (E_{Fe} = 211 GPa) is much larger than that of Ti (E_{Ti} = 116 GPa) [41]. Conversely, Nb and Zr exhibit rather low Young's moduli (E_{Nb} = 105 GPa and E_{Zr} = 68 GPa). Hence, not only the microstructure (grain size, morphology) but also the elastic properties of the constituent elements determine the overall Young's modulus of the investigated alloys.

Table 3 also lists the values of H/E_r and H^3/E_r^2 for the different alloys. As expected, due to its large hardness, the Ti-31.0Fe-9.0Sn alloy exhibits the highest H/E_r and H^3/E_r^2 ratios. Furthermore, in spite of its relatively low hardness, the Ti-39.3Nb-13.3Zr-10.7Ta alloy also shows a H/E_r ratio larger than the commercial Ti-6Al-4V alloy. This ratio, related to the elastic strain to failure, has been shown to be a suitable parameter to describe the wear resistance of a given material [22].

Table 3

Summary of the values of hardness (H), reduced Young's modulus (E_r), H/E_r, H^3/E^2_r, U_{el}/U_{tot} and U_{pl}/U_{tot} (where U_{pl}, U_{el} and U_{tot} denote the plastic, elastic and total indentation energies, respectively), corresponding to the Ti-6Al-4V, Ti-39.3Nb-13.3Zr-10.7Ta and Ti-31.0Fe-9.0Sn alloys extracted from the nanoindentation curves.

Sample	H (GPa)	E_r (GPa)	H/E_r	H^3/E_r^2 (GPa)	U_{el}/U_{tot}	U_{pl}/U_{tot}
Ti-6Al-4V	5.0 ± 0.1	121 ± 3	0.041 ± 0.001	0.009 ± 0.001	0.254 ± 0.005	0.746 ± 0.014
Ti-39.3Nb-13.3Zr-10.7Ta	4.4 ± 0.2	71 ± 2	0.062 ± 0.002	0.017 ± 0.003	0.353 ± 0.013	0.647 ± 0.023
Ti-31.0Fe-9.0Sn	8.9 ± 0.3	147 ± 4	0.060 ± 0.001	0.033 ± 0.004	0.342 ± 0.009	0.658 ± 0.018

Similarly, the ratio H^3/E_r^2 (sometimes referred to as the yield pressure [21,47] is also indicative of the wear resistance and is as well larger for the Ti-39.3Nb-13.3Zr-10.7Ta alloy than for Ti-6Al-4V. Our results are in good agreement with friction wear tests at different loads performed in various families of Ti-based alloys immersed in a Ringer's solution, which revealed that the weight loss of Ti-6Al-4V was generally larger than of Ti-Nb-Zr-Ta alloys [48], although other studies showed the opposite trend [49]. Such discrepancies may be ascribed to differences in the microstructure. Although the α-phase is intrinsically harder than the β-phase, the presence of crystallite sizes in the nm-range (as in our case) can lead to reasonable hardness values without affecting too much the Young's modulus, thus resulting in reasonably high H/E_r ratios. In the case of the Ti-31.0Fe-9.0Sn alloy, the existence of a two-phase microstructure (including the presence of eutectic regions containing a hard intermetallic phase) favors the increase of the wear resistance [50].

The elastic recovery and plasticity index, related to the nanoindentation elastic and plastic energies, are also parameters that characterize the mechanical behavior of biomaterials. The elastic recovery, (i.e., U_{el}/U_{tot}), indicates how much energy is released from a material after being loaded. In turn, U_{pl}/U_{tot} is often related to the intrinsic plasticity of a given alloy [51]. As shown in Table 3, although a large hardness value is observed for Ti-31.0Fe-9.0Sn, the highest elastic recovery is obtained for the Ti-39.3Nb-13.3Zr-10.7Ta alloy. The elastic recovery of Ti-6Al-4V is the smallest amongst the investigated alloys, in spite of its intermediate hardness which lies between that of Ti-39.3Nb-13.3Zr-10.7Ta and Ti-31.0Fe-9.0Sn. Actually, it has been shown that a general correlation between H and U_{el}/U_{tot} does not necessarily hold for all materials [47].

Instead, U_{el}/U_{tot} is usually proportional to H/E_r [52,53], a trend which is also observed the present case (Table 3). Concerning the U_{pl}/U_{tot} ratio, the values of the β-Ti alloys are larger than those reported for Ti-Cu-Zr-Pd bulk metallic glasses [53]. The Ti-6Al-4V alloy shows the highest U_{pl}/U_{tot} ratio indicating larger intrinsic plasticity, probably because of the presence of ductile Al. However, typical implants utilized for bone replacement are not subject to pronounced plastic strains. Hence, from a mechanical viewpoint, the β-type alloys investigated here are better in many aspects than commercial Ti-6Al-4V.

3.3. Corrosion behavior

Fig. 5 shows representative potentiodynamic polarization curves of the as-cast Ti-31.0Fe-9.0 Sn and Ti-39.3Nb-13.3Zr-10.7Ta samples, along with that of the commercial Ti-6Al-4V alloy, for the aim of comparison. The corresponding corrosion potential, E_{corr}, the corrosion current density, j_{corr}, and the polarization resistance, R_p, values are listed in Table 4. Both Ti-39.3Nb-13.3Zr-10.7Ta and commercial Ti-6Al-4V alloys show similar E_{corr} values, close to 0 V, in agreement with other works in which the corrosion behavior of Ti-35Nb-7Zr-5Ta in Ringer's solution was assessed [54],but different active-to-passive transitions.

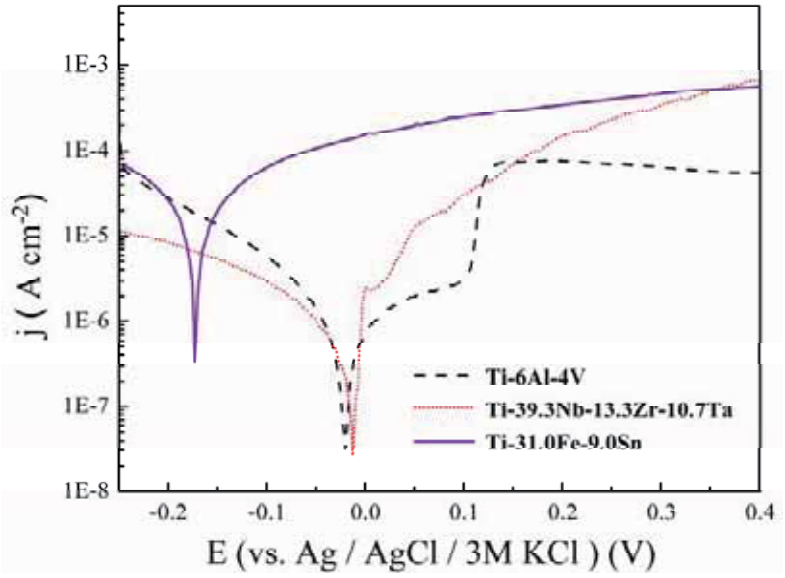

Fig. 5. *Potentiodynamic polarization curves for Ti-6Al-4V, Ti-39.3Nb-13.3Zr-10.7Ta and Ti-31.0Fe-9.0Sn alloys in Hanks's solution electrolyte at a scan rate of 0.1 mV s^{-1}.*

Table 4

Corrosion potential, E_{corr}, corrosion current density, j_{corr}, and polarization resistance, R_p, values obtained from the potentiodynamic polarization tests for the Ti-6Al-4V, Ti-39.3Nb-13.3Zr-10.7Ta and Ti-31.0Fe-9.0Sn alloys, in a simulated body fluid (Hank's solution) at 37.5ºC.

Composition	j_{corr} (Acm^{-2})	E_{corr} (V)	R_p (Ohm)
Ti–6Al–4V	$4.1 \cdot 10^{-7}$	-0.019	$1.8 \cdot 10^{+4}$
Ti-39.3Nb-13.3Zr-10.7Ta	$1.6 \cdot 10^{-6}$	-0.021	$6.5 \cdot 10^{+4}$
Ti-31.0Fe-9.0Sn	$8.7 \cdot 10^{-6}$	-0.175	$1.7 \cdot 10^{+4}$

The j_{corr} value for Ti-39.3Nb-13.3Zr-10.7Ta is slightly higher than that of Ti-6Al-4V due to the higher slope. Interestingly, the R_p of the former is a little bit higher and no clear breakdown is observed in the anodic branch up to 0.4 V, unlike commercial Ti-6Al-4V, which shows an active-to-passive transition at ~0.12 V originating from structural or chemical changes in the passive layer that increases its permeability and ultimately leads to higher current density levels.

Nevertheless, randomly distributed fluctuations can be seen on the potentiodynamic curve of Ti-39.3Nb-13.3Zr-10.7Ta, whose origin is not yet well understood. On the other hand, the Ti-31.0Fe-9.0Sn alloy shows more negative E_{corr} (-0.175 V) and higher j_{corr} values, though passivity breakdown does not occur either. Apart from the composition, which is different, the fact that its average crystallite size is smaller compared to the Ti-39.3Nb-13.3Zr-10.7Ta and Ti-6Al-4V alloys could inherently lead to a poorer corrosion performance due to the larger volume fraction of interfaces [55]. Nevertheless, E_{corr} is more positive than the values of pure iron (-0.542 V vs. Ag|AgCl) [39] and pure titanium (-0.373 V vs Ag|AgCl) [56]. This suggests that not only the composition but also the microstructure plays a key role on the corrosion performance of the material. It should be noted that the corrosion behavior of various Ti-Fe-Sn alloys has been evaluated in different electrolytes with pH in the range 1-13, especially in chloride-containing strong acidic solutions [40], but their behavior in neutral physiological solutions has not been explored yet. The E_{corr} value observed for Ti-31.0Fe-9.0Sn is close to the value for Ti-Fe-Sn alloys with lower Sn content tested in 0.3 M chloride-free borate buffer electrolyte (pH 8.4) (-0.207 V vs. Ag|AgCl). At this point it should be noted that although this material has potential to be used in the biomedical field, an eventual allergenic reaction to this alloy [57] as well as the release, if any, of the metal cations to the bodily fluid warrants an in-depth investigation. Secondary electron (SE) and corresponding backscattered electron (BSE) images of Ti-31.0Fe-

9.0Sn and Ti-39.3Nb-13.3Zr-10.7Ta samples both before and after the corrosion tests are shown in Fig. 6 and 7, respectively. Concerning the Ti-31.0Fe-9.0Sn alloy, a rather unaltered surface was observed at the end of the polarization experiment [Fig. 6 (c) and (d)], featuring a composition close to the nominal one (i.e., before corrosion) (see Table 5). Only a few NaCl particles, coming from waste Hanks' solution, were encountered on the surface [see inset of Fig. 6 (c)]. On the contrary, the surface of the Ti-39.3Nb-13.3Zr-10.7Ta alloy after the corrosion tests showed a larger amount of corrosion products, as evidenced topographically in the SE image and compositionally in the BSE image by the spotty darker areas [Fig. 7(c) and 7(d)].

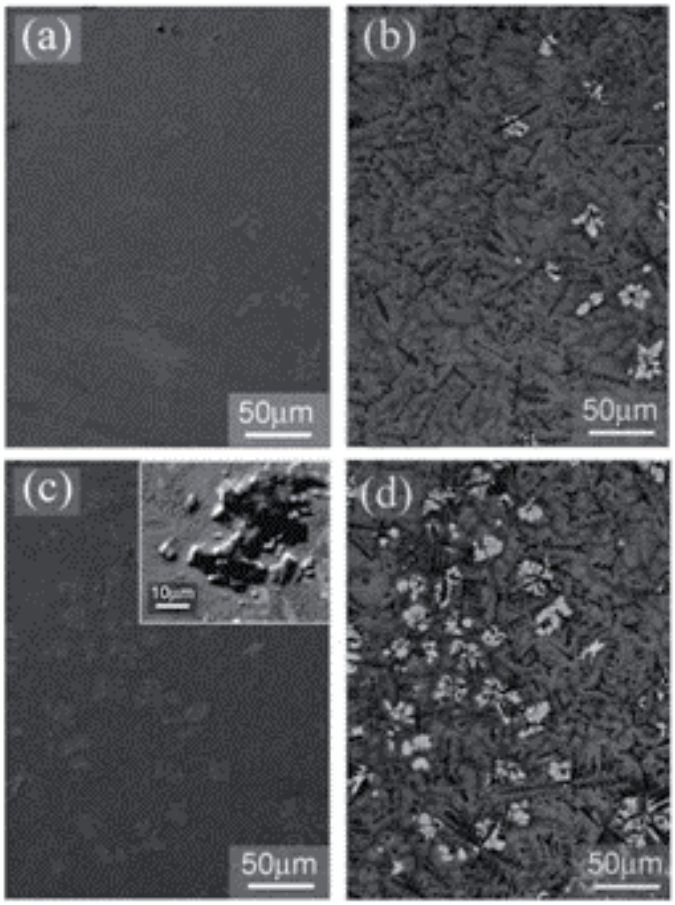

Fig. 6. *SEM images corresponding to the Ti-31.0Fe-9.0Sn alloy, before corrosion [(a) SE and (b) BSE] and after corrosion [(c) SE and (d) BSE]. The inset in (c) corresponds to a particle (corrosion product) deposited at the specimen's surface.*

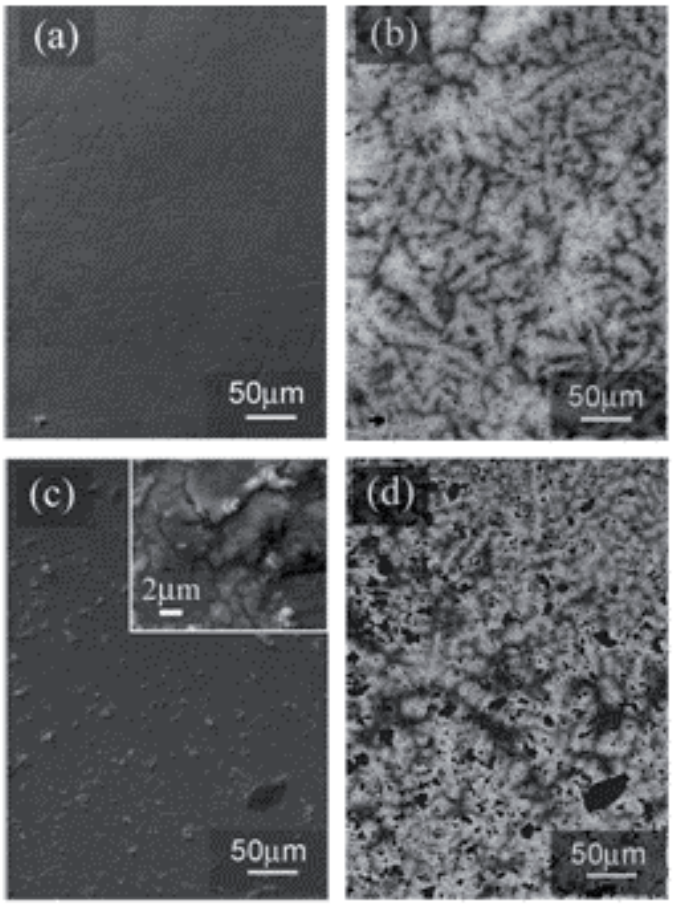

Fig. 7. *SEM images corresponding to the Ti-39.3Nb-13.3Zr-10.7Ta alloy, before corrosion [(a) SE and (b) BSE] and after corrosion [(c) SE and (d) BSE]. The inset in (c) corresponds to a particle (corrosion product) deposited at the specimen's surface.*

Table 5

Chemical composition of the Ti-31.0Fe-9.0Sn alloy surface, obtained by EDX, both before and after corrosion experiments.

	Element concentration (wt.%)					
	Ti	**Fe**	**Sn**	**Na**	**O**	**Cl**
Before corrosion (overall composition, Fig 6a)	60.0	31.0	9.0	-	-	-
After corrosion (from a large region of the surface area - without corrosion products, Fig. 6c)	58.1	33.2	8.7	-	-	-
After corrosion (from a particle deposited on the sample's surface, i.e., corrosion product, Fig. 6c inset)	22.9	19.2	1.3	31.7	2.1	22.7

Table 6

Chemical composition of the Ti-39.3Nb-13.3Zr-10.7Ta alloy surface, obtained by EDX, both before and after corrosion experiments.

	Element concentration (wt.%)							
	Ti	**Nb**	**Zr**	**Ta**	**O**	**P**	**Ca**	**Cl**
Before corrosion (Overall composition, Fig. 7a)	36.7	39.3	13.3	10.7	-	-	-	-
After corrosion (from a large region of the surface area - Fig. 7c)	30.7	35.2	9.9	11.2	16.0	1.2	< 1	< 1
After corrosion (from a particle deposited on the sample's surface, i.e., corrosion product, Fig. 7c inset)	10.7	8.8	23.5	9.7	26.5	< 1	< 1	20.7

The oxygen content was found to be large both locally and globally (Table 6), indicating that an oxide layer has been probably formed on the specimen's surface. Moreover, chlorine was detected in large amounts by EDX-spot analyses in the particles spread on the alloy surface (see inset of Fig. 7(c)).

4. Conclusions

An in-depth comparative study of the microstructure, the mechanical properties and the corrosion behavior in a physiological environment of two different nanostructured β-type Ti-based alloys, synthesized by copper mold casting, as well as the widely used commercial Ti-6Al-4V alloy, has been carried out. While one of the newly developed alloys (Ti-31.0Fe-9.0Sn) is interesting because of its large hardness (H ≈ 9 GPa), the other material (Ti-44.3Nb-8.7Zr-12.3Ta) is appealing because of its low Young's modulus (E_r = 71 GPa). Both alloys exhibit better wear resistance (i.e., larger H/E_r ratios) than commercial Ti-6Al-4V. From the point of view of biocorrosion, none of the new alloys show potential breakdown within the explored potential window (up to 0.4 V), whilst the Ti-6Al-4V does. Both the corrosion potential, E_{corr}, and the corrosion current density, j_{corr}, values exhibited by the Ti-39.3Nb-13.3Zr-10.7Ta alloy are similar to those of commercial Ti-6Al-4V, whereas a shift shit in E_{corr} towards more negative values and increased j_{corr} values are observed for Ti-31.0Fe-9.0Sn, probably due to its smaller average crystallite size. In any case, the surfaces exposed to the bodily fluid do not become particularly damaged. From all these properties, the β-type alloys investigated here are found to be better in many aspects than commercial Ti-6Al-4V. In addition, due to the absence of toxic elements, these materials are well suited for a variety of biomedical purposes.

Acknowledgements

The authors wish to thank the *Servei de Microscòpia* of the *Universitat Autònoma de Barcelona* for the technical assistance. We also acknowledge the Catalan DGR (2009-SGR-1292), the Spanish MICINN (MAT2011-27380-C02-01), the EU (FP7-PEOPLE-2010-ITN-264635, BioTiNet) and the German Science Foundation (SFB-TR79) for financial support. M.D.B. acknowledges partial financial support from an ICREA-Academia Award.

References

[1] B.D. Ratner, et al., Biomaterials Science: an introduction to materials in medicine. Academic Press (1st edition), USA, 1996.

[2] A. Naji, M.F. Harmand, J. Biomed. Mater. Res. Part A, 24 (1990) 861-871.

[3] M. Geetha, et al., Prog. Mater. Sci. 54 (2009) 397-425.

[4] X. Zhao, et al., Mater. Sci. Eng. C 31 (2011) 1436-1444.

[5] M. Atapour, et al., Sci. Eng. C 31 (2011) 885-891.

[6] D.R. Summer, et al., J. Biomech. 31 (1998) 909-917.

[7] M. Niinomi, M. Nakai, Int. J. Biomater. 2011 (2011) 836587.

[8] D.F. Williams, Biomater. 29 (2008) 2941-53.

[9] M. Niinomi, Sci. Technol. Adv. Mater. 4 (2003) 445-454.

[10] S. Rao, et al., J. Biomed. Mater. Eng. 6 (1996) 79-86.

[11] P.R Walker, J. Leblanc, M. Sikorska, Biochem. 28 (1990) 3911-3915.

[12] M. Long, H.J. Rack, Biomater. 19 (1998) 1621-1639.

[13] Y. Song, et al., Mater. Sci. Eng. A 260 (1999) 269-274.

[14] S.J. Li, et al., Wear 257 (2004) 869-876.

[15] Y. Okazaki, S. Rao, Y. Ito, T. Tateishi, Biomater. 19 (1998) 1197-1215.

[16] H.J. Rack, J.I. Qazi, Mater. Sci. Eng. C 26 (2006) 1269-1277.

[17] D.J. Lin, J.H. Chern Lin, C.P. Ju, Biomater. 23 (2002) 1723-1730.

[18] G. He, et al., Nat. Mater. 2 (2003) 33-37.

[19] G. He, et al., Biomaterials 24 (2003) 5115-5120.

[20] J. Sort, et al., Acta Mater. 51 (2003) 6385-6393.

[21] E. Pellicer, et al., Adv. Funct. Mater. 20 (2010) 983-991.

[22] A. Leyland, A. Matthews, Wear 246 (2000) 1-11.

[23] F. Yildiz, A.F. Yetim, A. Alsaran, I. Efeoglu, Wear 267 (2009) 695-701.

[24] Y. Wang, M. Chen, F. Zhou, E. Ma, Nature 419 (2002) 912-915.

[25] K.B. Kim, J. Das , W. Xu, Z.F. Zhang, J. Eckert, Acta Mater. 54 (2006) 3701-3711.

[26] D.V. Louzguine, H. Kato, A. Inoue, J. Alloys Compd. 384 (2004) L1-L3.

[27] J. Das, et al., J. Alloys Compd. 434-435 (2007) 28-31.

[28] L.C. Zhang, et al., J. Phys.: Conf. Series 240 (2010) 012103.

[29] R.A. Young, The Rietveld Method, International Union of Crystallography, Oxford University Press, Oxford, 1995.

[30] J. Sort, et al., Philos. Mag. 83 (2003) 439-455.

[31] W.C. Oliver, G.M. Pharr, J. Mater. Res. 7 (1992) 1564-1583.

[32] G.M. Pharr, W.C. Oliver, J. Mater. Res. 19 (2003) 3-20.

[33] A.C. Fischer-Cripps, Nanoindentation (Ed.: F.F. Ling), Springer, New York, 2004.

[34] Y.W. Bao, W. Wang, Y.C. Zhou, Acta Mater. 52 (2004) 5397-5404.

[35] http://www.metrohm-autolab.com/Applications/.

[36] M. Stern, A.L.Geary, J. Electrochem. Soc. 104 (1957) 56-63.

[37] Goodfellow, code 453–274–50.

[38] N. Van Steenberge, et al., Scripta Mater. 55 (2006) 1087-1090.

[39] E. Zhang, H. Chen, F. Shen, J. Mater. Sci.: Mater. Med. 21 (2010) 2151-2163.

[40] R. Sueptitz, et al., J. Alloys Compd. 503 (2010) 19-24.

[41] http://www.webelements.com/.

[42] R. Ray, B.C. Giessen, N.J. Grant, Metall. Trans. 3 (1972) 627-629.

[43] R.G. Pirich, Metall. Trans. 17 (1986) 1149-1155.

[44] B.B. Sun, et al., Acta Mater. 54 (2006) 1349-1357.

[45] W.F. Smith, J. Hashemi,. Foundations of Materials Science and Engineering (4th ed.), McGraw-Hill, 2006

[46] P.L. Ferrandini, et al., J. Alloys Compd. 433 (2007) 207–210.

[47] J. Musil, et al., Surf. Coat. Technol. 154 (2002) 304-313.

[48] M. Niinomi, J. Mech. Behav, Biomed. Mater. 1 (2008) 30- 42.

[49] I. Cvijović-Alagić, et al., Corros. Sci. 53 (2011) 796-808.

[50] C. Ohkubo, et al., Biomater. 24 (2003) 3377–3381.

[51] Y.V. Milman, J. Phys. D: Appl. Phys. 41 (2008) 074013.

[52] E. Pellicer, et al., Mater. Chem. Phys. 130 (2011) 1380-1386.

[53] J. Fornell, et al., J. Mech. Behav. Biomed. Mater. 4 (2011) 1709-1717.

[54] S. Samuel, et al., J. Biomed. Mater. Res. A 94A (2010) 1251-1256.

[55] C.C. Koch, Nanostructured Materials. Processing, properties and applications, William Andrew Publishing (2nd Edition), New York, 2007.

[56] Y.B. Wang, Y.F. Zheng, Mater. Lett. 63 (2009) 1293-1295.

[57] M. Niinomi, Metall. Mater. Trans. A 33 (2002) 477-486

4.2. Novel Ti-Zr-Hf-Fe Nanostructured Alloy for Biomedical Applications

This article reports on the synthesis and characterization of novel $Ti_{40}Zr_{20}Hf_{20}Fe_{20}$ (at. %) bulk-shape alloy showing a nanocomposite microstructure. Again the Ti-6Al-4V alloy, which is broadly employed in the worldwide medical market, was used for a mechanical and electrochemical comparative study.

$Ti_{40}Zr_{20}Hf_{20}Fe_{20}$ (at. %) alloys were prepared by arc melting, and subsequent Cu mold suction casting techniques. The samples were cast in the form of rods of 2 mm in diameter. Our XRD results reveal that the $Ti_{40}Zr_{20}Hf_{20}Fe_{20}$ (at. %) consists of a mixture of several nanocrystalline phases. The main reflections are ascribed to cubic Hf_2Fe (space group Fd3m, a = 11, 77 Å) and hexagonal Fe_2Zr (space group P63/mmc, a = 5.23 Å; c = 8.37 Å) intermetallic phases as well as to hexagonal α-Ti (space group P63/mmc, a = 3.01 Å; c = 4.53 Å), and cubic β-Ti (space group Im3m, a = 3.42 Å) phases.

The nanoindentation data reveal that the $Ti_{40}Zr_{20}Hf_{20}Fe_{20}$ (at. %) alloy exhibits high hardness (8.7 GPa) and relatively low reduced Young's modulus (104 GPa). These values have been taken as a good indicator of the excellent mechanical behavior of the studied alloy. The Young's modulus obtained by the ultrasonic measurement is also in agreement with nanoindentation tests. It is worth remarking that the hardness and Young's modulus of the $Ti_{40}Zr_{20}Hf_{20}Fe_{20}$ rod-shape alloy are higher and lower, respectively, than those of Ti-6Al-4V (H = 5.0 GPa, E_r = 121 GPa). This can be attributed to the formation of mechanically hard crystalline nano-phases in Ti-Zr-Hf-Fe, which has a key influence on the mechanical performance. Thus the Ti-Zr-Hf-Fe alloy could serve as a permanent biomedical implant, and could be even better suited than the currently used Ti-6Al-4V.

The samples were also tested electrochemically by means of potentiodynamic polarization measurements. The samples were immersed in naturally aerated simulated physiological Hank's balanced salt solution (HBSS) at 37.5 °C. The Ti-Zr-Hf-Fe alloy reveals good corrosion resistance in HBSS ($R_{corr} = 1.4 \times 10^4\ \Omega \cdot cm^2$), as evidenced by the passivation behavior in a wide potential window (−0.197 V) and low corrosion current density ($9.1 \times 10^{-7}\ A \cdot cm^{-2}$). When compared to the commercial Ti-6Al-4V ($R_{corr} = 6.9 \times 10^3\ \Omega \cdot cm^2$), our alloy presents slightly

higher values of polarization resistance and this can be attributed to both the microstructure features and chemical composition of the Ti-Zr-Hf-Fe.

Finally, cytotoxic tests indicate easier adhesion of preosteoblast cells onto the surface of Ti-Zr-Hf-Fe alloy and differentiation into osteoblasts. Extracellular matrix mineralization was similar in osteoblast in contact with the alloy, in the presence of the alloy or in absence of it.

OPEN ACCESS

materials

ISSN 1996-1944

www.mdpi.com/journal/materials

Novel Ti–Zr–Hf–Fe Nanostructured Alloy for Biomedical Applications

Anna Hynowska [1,*], Andreu Blanquer[2], Eva Pellicer [1,*], Jordina Fornell [1], Santiago Suriñach [1], Maria Dolors Baró [1], Sergio González [1], Elena Ibáñez[2], Lleonard Barrios [2], Carme Nogués [2,*] and Jordi Sort [3]

[1] Departament de Física, Facultat de Ciències, Universitat Autònoma de Barcelona, E-08193 Bellaterra, Spain; E-Mails: jordinafornell@gmail.com (J.F.); santiago.surinyach@uab.cat (S.S.); dolors.baro@uab.es (M.D.B); sergiogs10@yahoo.es (S.G.)

[2] Departament de Biologia Cellular, Fisiologia i Immunologia, Universitat Autònoma de Barcelona, E-08193 Bellaterra, Spain; E-Mails: andreublanquer@gmail.com(A.B.); elena.ibanez@uab.cat (E.I.); lleonard.barrios@uab.cat (L.B.)

[3] Institució Catalana de Recerca i Estudis Avançats (ICREA) and Departament de Física, Universitat Autònoma de Barcelona, E-08193 Bellaterra, Spain; E-Mail: jordi.sort@uab.es

* Author to whom correspondence should be addressed; E-Mails: anna.hynowska@campus.uab.cat (A.H.); eva.pellicer@uab.cat (E.P.); carme.nogues@uab.cat (C.N.); Tel.: +34-935-811-401(A.H.); Fax: +34-935-812-155 (A.H.).

Abstract:

The synthesis and characterization of $Ti_{40}Zr_{20}Hf_{20}Fe_{20}$ (at. %) alloy, in the form of rods (ϕ = 2 mm), prepared by arc-melting, and subsequent Cu mold suction casting, is presented. The microstructure, mechanical and corrosion properties, as well as *in vitro* biocompatibility of this alloy, are investigated. This material consists of a mixture of several nanocrystalline phases. It exhibits excellent mechanical behavior, dominated by high strength and relatively low Young's modulus, and also good corrosion resistance, as evidenced by the passive behavior in a wide potential window and the low corrosion current densities values. In terms of biocompatibility, this alloy is not cytotoxic and preosteoblast cells can easily adhere onto its surface and differentiate into osteoblasts.

Keywords: Ti-based alloy; biomaterial; microstructure; mechanical behavior; corrosion performance

1. Introduction

Materials for permanent biomedical implants must be designed in order to guarantee a long lifetime (longevity) of the implant after being inserted into the human body. Metallic alloys present an immense potential for orthopaedic applications, due to their excellent mechanical strength and resilience, which is outstanding in comparison with polymers or ceramics [1]. Permanent implants should contain neither toxic nor allergic elements (e.g. Al, V, Ni, Co) and should possess high corrosion and wear resistances. A good structural and functional connection between living bone and the surface of a load-bearing artificial implant is also essential.

In recent years, Ti-based alloys have gathered special attention in the biomedical field as they show a combination of high strength, reduced stiffness, low density, good biocompatibility and good corrosion resistance, in many cases superior to conventional steel or Co-Cr alloys [2]. Pure Ti and Ti–6Al–4V (composed of a mixture of $\alpha + \beta$ phases) alloys are currently the most widely used structural biomaterials for the replacement of hard tissues in artificial joints. Although pure titanium has acceptable mechanical properties, in most applications Ti is alloyed with small

amounts of aluminium and vanadium, with the aim of stabilizing the β-phase, which exhibits lower Young's modulus than the α-phase. However, the release of V and Al ions to the human body causes long-term health problems, such as peripheral neuropathy, osteomalacia, and Alzheimer diseases [3]. Thus, new Ti-based alloys with low Young's modulus (to ensure good mechanical compatibility with bone) and free from non-biocompatible elements (e.g., Al, V, Ni or Co), are currently required for the next generation of metallic implant materials.

Besides the alloy composition, the microstructure (i.e., grain size and amounts of interphase boundaries) also plays a key role in the resulting physical and chemical properties of synthesized materials. Previously, BMG (bulk metallic glasses) were developed and found to be good candidates fulfilling the requirements of the orthopaedic field. The advancement of BMG led to the discovery of a new nanostructured alloy, which may exhibit even more outstanding properties than BMG and conventional Ti alloys. These nanostructured materials have attracted much interest in the last decade due to their size-dependent (a grain size typically lower than 100 nm) unique mechanical, physical and chemical properties [4]. They can be prepared by a number of different techniques (ball milling and subsequent hot pressing, severe plastic deformation, suction casting, etc.) and the grain size, morphology and composition can be controlled by tuning the processing parameters. In comparison to coarse-grained materials, nanocrystalline alloys show higher strength and hardness at room temperature [5].

Currently, a number of multi-component Ti-based alloys showing nanocrystalline structure and not containing the highly-toxic (Be, Ni, Al, V, Co, Cr etc.), such as Ti-50Ta [6], Ti-Sn-Nb [7], Ti-Mo-Nb [8], Ti-Mo-Zr-Fe, Ti-Nb-Ta-Zr [9, 10] or Ti-Fe-Sn [11], are of special interest for the biomedical field. These alloys constitute so called "second generation biomaterial" [1, 3, 12].

In this paper we focus our attention on the $Ti_{40}Zr_{20}Hf_{20}Fe_{20}$ (at. %) alloys. Samples with this composition had already been prepared but only in ribbon shape (few tens of μm in thickness) and a mixture of amorphous plus nanoscale metastable icosahedral phase, with an average size of 5 nm, was obtained [13]. It was suggested that Fe, due to its high glass-forming ability, could trigger the formation of the amorphous phase also in bulk form or, at least, promote a nanocrystalline structure [13]. Hence, a decrease of the Young's modulus is anticipated in both scenarios. On the one hand, amorphous materials typically exhibit lower Young's modulus than their crystalline counterparts (a behavior termed "elastic softening") [14,15]. On the other hand,

Fe is a β stabilizer element, therefore in Fe-containing nanocrystalline alloys one can expect a lowering of the Young's modulus and a concomitant increase in hardness [16–18]. Moreover, Fe is considered as a suitable element for biodegradable implants and it has been demonstrated to be as high as 80% viable after 4 days in culture with L-929 of [19]. Likewise, the addition of Zr and Hf elements, which belong to the same family as Ti in the periodic table, presumably leads to enhanced mechanical properties, good corrosion resistance and good biocompatibility [20]. The $Ti_{40}Zr_{20}Hf_{20}Fe_{20}$ (at. %) alloy is prepared in the form of rods of 2 mm in diameter. The mechanical and electrochemical corrosion properties are assessed and compared to the commercial Ti-6Al-4V alloy. Standardized in-vitro cytotoxicity assays to evaluate the biocompatibility are also performed. The results reveal the excellent performance of Ti-Zr-Hf-Fe, making this alloy a potential candidate to be used in the biomaterial field.

2. Results and Discussion

2.1. Microstructure

Figure 1 shows the XRD pattern of the $Ti_{40}Zr_{20}Hf_{20}Fe_{20}$as-cast sample. A fully crystalline structure is observed, as noted from the absence of broad halos, typical of amorphous materials. Based on the databases (X'Pert HighScore, FindIt, PCPDFWIN programs), the main reflections of the XRD pattern are ascribed to cubic Hf_2Fe (space group Fd3m , a = 11,77 Å) and hexagonal Fe_2Zr (space group P63/mmc, a = 5.23 Å; c = 8.37 Å) intermetallic phases as well as to hexagonal α-Ti (space group P63/mmc, a = 3.01 Å; c = 4.53 Å) and cubic β-Ti (space group Im3m, a = 3.42 Å) phases, in agreement with previous works [13]. The diffraction peaks are slightly shifted from the tabulated ones. This is usually observed in multicomponent systems where atoms of different species can act as substitutional atoms. For instance, the theoretical cell parameter for β-Ti phase is $a_{th.}$= 3.31 Å which is slightly smaller than the experimental one ($a_{expt.}$ = 3.42 Å). This can be explained by the larger atomic size of Zr and Hf which causes an increment in the lattice parameters.

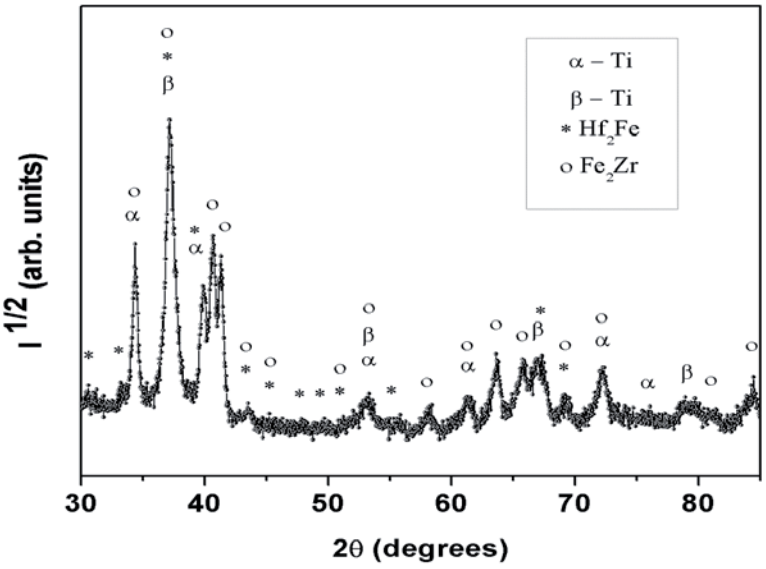

Figure 1. *XRD pattern corresponding to the as–cast $Ti_{40}Zr_{20}Hf_{20}Fe_{20}$ alloy.*

Figure 2 shows secondary (a) and backscattered (b) electron images corresponding to the central part of the cross-section of the rod. Remarkably, a similar microstructure was noticed at the edges of the rods. These materials exhibit a composite-like microstructure, with the presence of at least three different regions that display different brightness (zones A, B and C). Zone A is assigned to micrometer-sized dendrites as shown in Figure 2(a), while zones B and C [insert Figure 2(a)] are the alternated bright and dark structure of the eutectic matrix composed of nanoscale lamellae (width around 100 nm). The varying lamellae geometry is due to different orientations of the eutectic colonies. Hence, upon rapid quenching, the multi-component $Ti_{40}Zr_{20}Hf_{20}Fe_{20}$ liquid underwent an eutectic reaction, forming *in situ* a composite material made of micrometer-sized dendritic (Ti-based solid solution) regions surrounded by an ultra-fine grained eutectic matrix. This kind of microstructure should promote a high strength, in comparison to commercial Ti-6Al-4V alloy [21].

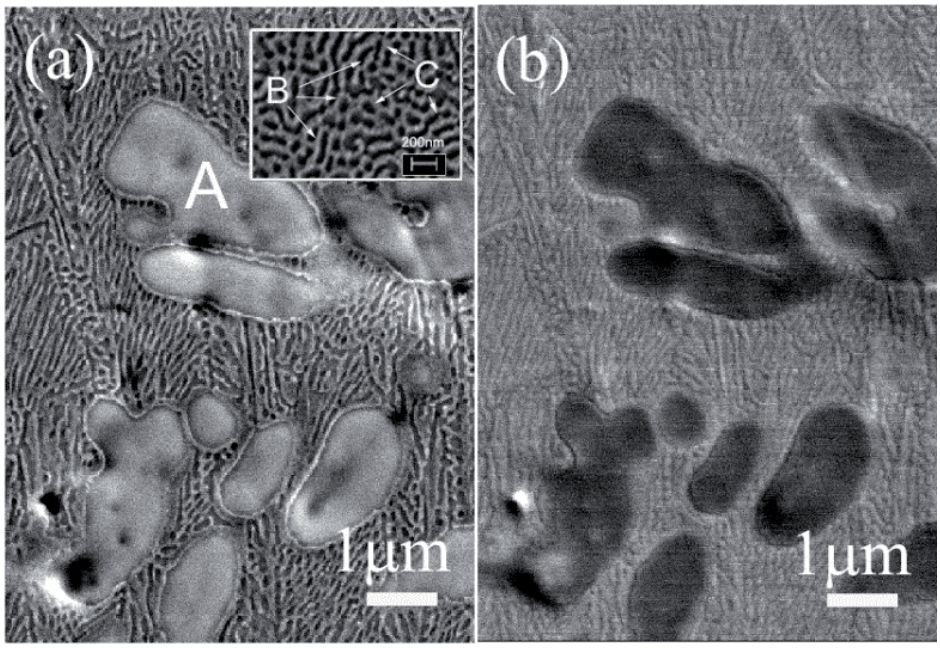

Figure 2. *SEM images of the $Ti_{40}Zr_{20}Hf_{20}Fe_{20}$ alloy taken from the central part of the cross-section area of the rod. Panel* ***(a)*** *is a secondary electrons image and* ***(b)*** *a backscattered electrons image, both showing the coexisting of different zones (A, B and C). Zone A corresponds to large size dendrites, while zones B, C belong to the small lamellae composing the eutectic matrix (2a inset). The size of the inset in* ***(a)*** *is a zoom of 1.2 μm x 0.9 μm.*

Energy dispersive X-ray (EDX) analysis (Figure 3) indicates that Zr and Hf are in a larger amount inside the dendrites, whereas Fe is mainly located in the eutectic matrix. Ti is distributed equally along the selected area of the transverse cross-section of the surface. Based on the compositional analyses and the XRD results, α-Ti and β-Ti with some additional elements in solid solution (partial substitution of Ti for Hf or Zr) could be present in both the dendrites and the eutectic matrix. Fe_2Zr and Hf_2Fe phases are likely to be located in the eutectic matrix, since more Fe is detected in this region.

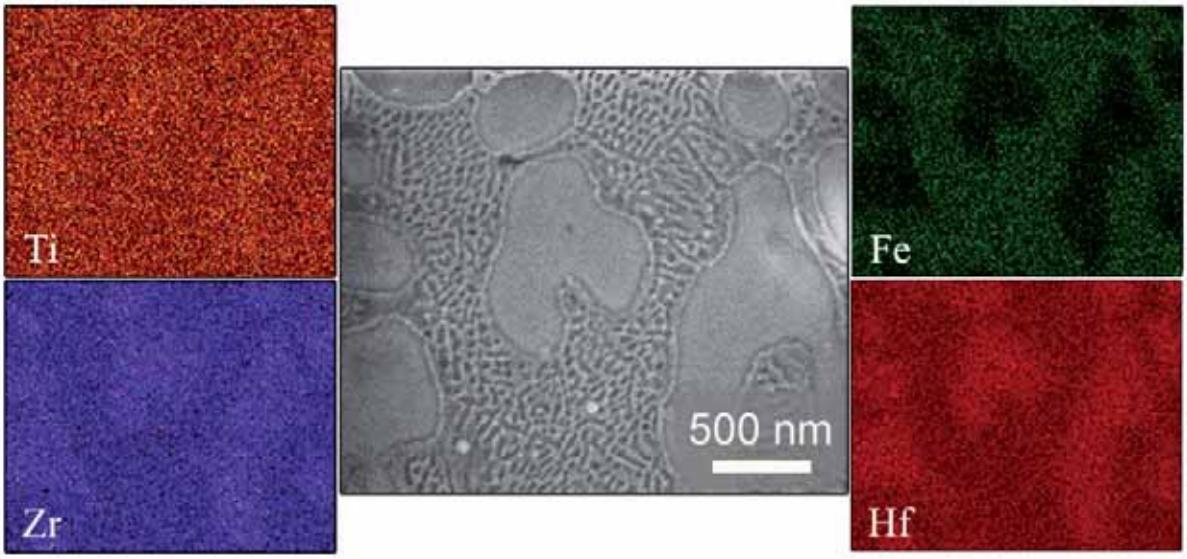

Figure 3. *SEM image of a central region of the $Ti_{40}Zr_{20}Hf_{20}Fe_{20}$ sample, together with the compositional energy dispersive X-ray mappings corresponding to Ti, Zr, Fe and Hf elements.*

2.2. Mechanical properties

Table 1 lists the values of the Poisson's coefficient (ν), Young's modulus (E), shear modulus (G) and bulk modulus (K). The values of Young's and shear modulus for the $Ti_{40}Zr_{20}Hf_{20}Fe_{20}$ are lower than for the commercial Ti-6Al-4V. On the contrary, the values of Poisson's coefficient and bulk modulus are slightly higher compared to the values of commercial alloy. Figure 4 shows representative nanoindentation load-displacement *(P-h)* curves of the $Ti_{40}Zr_{20}Hf_{20}Fe_{20}$ and commercial Ti-6Al-4V alloys, measured up to a maximum load P_{max} = 250 mN. Indentations using such a high load are large enough to embrace all the existing phases (as shown in the inset of Figure 4).

Table 1. *Summary of the elastic properties (υ, E_{Acoust}, G and K denote the Poisson's coefficient, Young's modulus, shear modulus and bulk modulus, respectively) of the as-cast $Ti_{40}Zr_{20}Hf_{20}Fe_{20}$ alloy. Results for the commercial Ti-6Al-4V are shown for comparison purposes.*

Sample	*v*	E_{Acoust} (GPa)	G (GPa)	K (GPa)
$Ti_{40}Zr_{20}Hf_{20}Fe_{20}$	0.359 ± 0.001	102.2 ± 0.3	37.6 ± 0.3	132.3 ± 1.7
Ti-6Al-4V	0.326 ± 0.003	111.5 ± 1.1	42.0 ± 0.4	106.6 ± 1.1

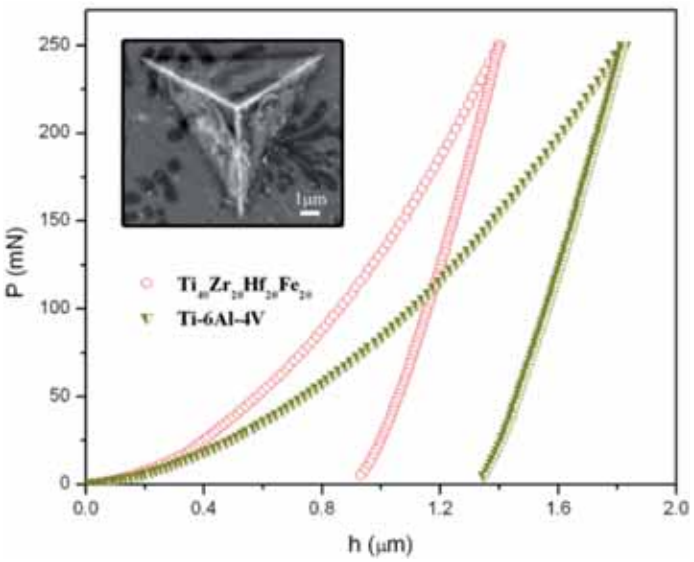

Figure 4. *Load-displacement (P-h) nanoindentation curves of the Ti-6Al-4V and $Ti_{40}Zr_{20}Hf_{20}Fe_{20}$ alloys obtained applying a maximum force P_{Max}=250mN. The inset is a backscattered SEM image showing an indent made close to the centre of the $Ti_{40}Zr_{20}Hf_{20}Fe_{20}$ sample (P_{Max}=250mN).*

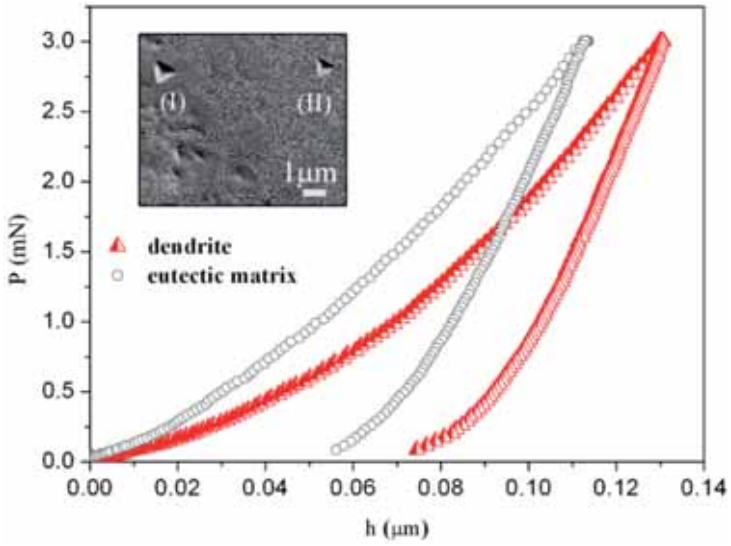

Figure 5. *Load-displacement (P–h) nanoindentation curves for $Ti_{40}Zr_{20}Hf_{20}Fe_{20}$ alloy,corresponding to a dendrite (red curve) and eutectic matrix (grey curve). Shown in the inset is a backscattered SEM image of the indents: (**I**) inside the dendrite and (**II**) inside the eutectic matrix (P_{Max} = 3mN).*

Table 2. *Summary of the values of hardness (H), reduced Young's modulus (E_r), H/E_r, H^3/E^2_r, U_{el}/U_{tot}, and U_{pl}/U_{tot} (where U_{el}, U_{pl} and U_{tot} denote the elastic, plastic and total indentation energies, respectively), corresponding to the Ti–6Al–4V and $Ti_{40}Zr_{20}Hf_{20}Fe_{20}$ alloys extracted from the nanoindentation curves performed with maximum load of 250 mN.*

Sample	H (GPa)	E_r (GPa)	H/E_r	H^3/Er^2 (GPa)	U_{el}/U_{tot}	U_{pl}/U_{tot}
$Ti_{40}Zr_{20}Hf_{20}Fe_{20}$	8.7±0.2	104±3	0.083±0.003	0.060±0.006	0.554±0.019	0.446±0.016
Ti–6Al–4V	5.0±0.1	121±3	0.041±0.001	0.009±0.001	0.254±0.005	0.746±0.014

The $Ti_{40}Zr_{20}Hf_{20}Fe_{20}$ rod-shape alloy is mechanically harder than the Ti-6Al-4V one, as can be deduced from *(P-h)* curve from the larger values of penetration depth of Ti-6Al-4V [22]. The values of hardness of dendrite and eutectic matrix determined using applied load of 3mN are equal to 7.5 GPa and 10.5 GPa, respectively (Figure 5). The average hardness from low-load indentation tests is 9.3 GPa. This is the value calculated for all nanoindentation tests (i.e., from the values of hardness obtained in the dendrites, eutectic matrix and from indentations at the border between dendrites and eutectic regions) (~100 tests). The difference between the hardness at 3 mN (H = 9.3 GPa) and 250 mN (H = 8.7 GPa) is likely due to the indentation size effect (ISE) [23]. The ISE has been ascribed to a variety of factors, such as surface effects [24], friction between the indenter and the sample [25] or, more recently, strain-gradient hardening [26,27]. This latter considers that, as a result of the shear field created by the indenter, the crystal lattice becomes distorted and (extra) geometrically necessary dislocations, besides the statistically stored dislocations, have to be created to account for the large shear strains. For large indentations, the strain variation between two extremes is more gradual and the statistically stored dislocations can easily accommodate the shear stress without the need of geometrically necessary dislocations, thus reducing strain-gradient effects. The eutectic structure is mechanically harder than the dendrites probably because of the smaller grain size and the presence of the intermetallic phases [28,21]. Namely, the large amounts of inter-phase boundaries existing in the eutectic regions hinder dislocation motion and result in increase of strength, an effect known as Hall-Petch [29, 30]. The magnitude of the observed strengthening depends upon structure of the grain boundaries and the degree of misorientation between grains. The higher the applied stress is needed to propagate dislocation, the larger is the resulting hardness value [3,32]. Concerning the reduced Young's modulus, the studied $Ti_{40}Zr_{20}Hf_{20}Fe_{20}$ alloy shows a lower value (104 GPa) than the Ti-6Al-4V alloy (121 GPa), in agreement with acoustic measurements. The difference can be explained by both the relative amount of β phase (i.e., their distinct microstructure) and the

chemical composition. On the one hand, the amount of β phase in the $Ti_{40}Zr_{20}Hf_{20}Fe_{20}$ is higher than in the commercial Ti-6Al-4V [22]. On the other hand, the presence of Hf would lead to a decrease of the Young's modulus. It has been demonstrated that the Young's modulus in quenched Ti-Hf alloys with similar microstructure slightly decreases with an increase in the Hf content [33]. Remarkably, the value of E_r for $Ti_{40}Zr_{20}Hf_{20}Fe_{20}$ is similar to that of $Ti_{40}Cu_{38}Zr_{10}Pd_{12}$ bulk metallic glass (BMG) [34]. Also listed in Table 2 are the ratios H/E_r and H^3/Er^2 for both alloys. These parameters are related to wear resistance and are important to assess the lifetime of the implant. H/E_r stands for the elastic strain to failure [35], while H^3/Er^2 is related to the resistance of a material to plastic deformation in loaded contact. Due to large hardness and relatively low Young's modulus of $Ti_{40}Zr_{20}Hf_{20}Fe_{20}$, the values of H/E_r and H^3/Er^2 are larger than for Ti-6Al-4V. Interestingly, the elastic recovery, U_{el}/U_{tot}, is also higher in the new $Ti_{40}Zr_{20}Hf_{20}Fe_{20}$ alloy, hence this material would be more resistant to impact loading than Ti-6Al-4V.

2.3. Corrosion behavior

As aforementioned, a material intended for implant applications should be free from toxic and allergenic elements and should not be extensively affected by pitting corrosion. For this purpose, interest is laid on designing suitable alloy compositions, microstructures (and crystallite sizes) that are immune in a body fluid environment. Smaller crystallite size typically leads to poorer corrosion performance due to the larger volume fraction of interfaces [36]. The presence of a passive surface layer (typically oxides) on most of the metallic alloys presently used as implants precludes their dissolution when in contact with bodily fluids. The resistance of the passive layer toward the corrosion attack depends on both the alloying elements of the base material and the nature of oxides formed. Ti alloys are widely used in orthopaedic and dental fields because of their combination of excellent corrosion resistance and unique biocompatibility.

Figure 6 shows representative potentiodynamic polarization curves of the $Ti_{40}Zr_{20}Hf_{20}Fe_{20}$ and Ti-6Al-4V alloys. The corresponding corrosion potential, E_{corr}, the corrosion current density, jcorr, and the polarization resistance, R_p, values are listed in Table 3.

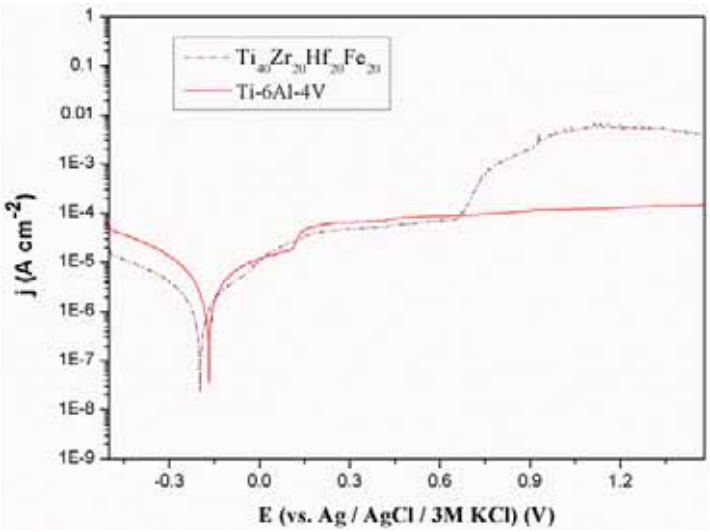

Figure 6. *Polarization curves of the as-cast $Ti_{40}Zr_{20}Hf_{20}Fe_{20}$ and commercial Ti-6Al-4V alloys in naturally aerated Hank's solution at 37.5ºC.*

Table 3. *Summary of the electrochemical parameters obtained for the studied $Ti_{40}Zr_{20}Hf_{20}Fe_{20}$ and commercial Ti–6Al–4V alloys. The values of j_{corr}, E_{corr}, $E_{pit,}$ and R_{corr} denote the corrosion density, the corrosion potential and polarization resistance.*

Sample	j_{corr} (A·cm^{-2})	E_{corr} (V)	R_{corr} (Ω·cm^2)
$Ti_{40}Zr_{20}Hf_{20}Fe_{20}$	9.1×10^{-7}	−0.197	1.4×10^{4}
Ti–6Al–4V	2.1×10^{-6}	−0.168	6.9×10^{3}

Compared to commercial Ti-6Al-4V alloy, the $Ti_{40}Zr_{20}Hf_{20}Fe_{20}$sample exhibits lower j_{corr} and higher R_p values. However, passivity breakdown is observed at 0.7V. This can be attributed to both the microstructural features and chemical composition of the $Ti_{40}Zr_{20}Hf_{20}Fe_{20}$ alloy. For example, Fe-containing alloys typically show passivity breakdown in chloride-containing solutions [37]. Nevertheless, such breakdown occurs beyond the limit (0.6 V vs. Ag/AgCl) typically set for a material to be safely used as a permanent medical implant [38]. Hence, the present alloy still holds promise to be used in the biological field.

2.4. Biological Tests

2.4.1. Cell Viability

The potential cytotoxic effect of $Ti_{40}Zr_{20}Fe_{20}Hf_{20}$ alloy on preosteoblast cultures was analyzed using indirect and direct studies at the same time. After 24 h in culture, no significant differences were observed in the percentages of live cells among the three conditions analyzed, that is, cells adhered to the surface of the alloy (direct studies), to the coverslip in presence of the alloy (indirect studies) and to the coverslip in absence of the alloy (control cells). In all cases, more than 97% of preosteoblasts were alive (direct studies 98.2%, indirect studies 97.1% and control cells 98.1%). These results indicate that the alloy has no toxic effect on preosteoblast cell cultures. Our results are in agreement with other studies which indicated that Zr and Hf are nontoxic elements that can be used as alloying elements [39]. Cations released from the alloy after 24 h are not cytotoxic for cells growing in the presence of the alloy.

2.4.2. Cell Adhesion and Morphology

Cell reaction to a material surface is an important factor to be considered. Preosteoblasts are adherent cells which need to attach to a surface to resume cell cycle and proliferate. Cell morphology and focal contacts are indicatives of cell response to a surface. We demonstrate that preosteblasts can adhere to the surface of the alloy indicating that the mirror-like surface of $Ti_{40}Zr_{20}Fe_{20}Hf_{20}$ is an excellent platform for preosteoblasts to attach to and proliferate.

Figure 7 shows adhesion (a) and morphology (b) of preosteoblasts grown on the top of the alloy. As it can be observed, cells are completely attached to the surface of the alloy by focal contacts at the cell periphery, colocalizing with the extremities of actin filaments (stress fibers), which are well-defined (some of them crossing the cell). Cell adhesion is the first step to occur when cellsare seeded on a surface (alloy orculture plate), as adhesion allows to control the behavior of cells and defines their morphology. No differences in the morphology of preosteoblasts adhered onto the $Ti_{40}Zr_{20}Fe_{20}Hf_{20}$ surface and control coverslips were observed. In both cases, cells exhibited similar polygonal shapes with cytoplasmic extensions and with no specific orientation.

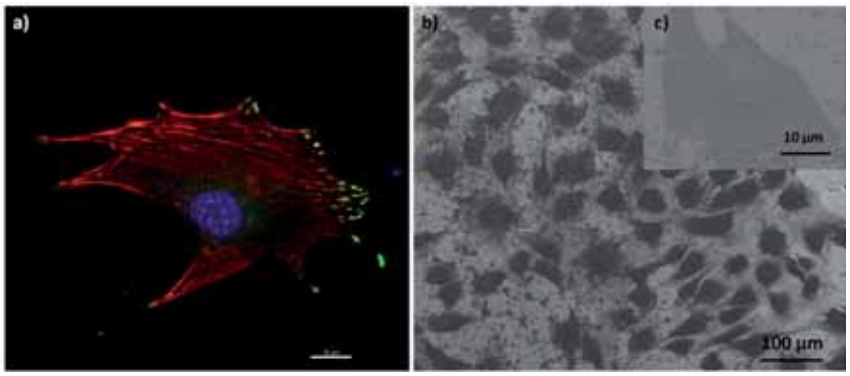

Figure 7. *Preosteoblast adhesion to the surface of $Ti_{40}Zr_{20}Fe_{20}Hf_{20}$ alloy: (**a**) Confocal microscopy image of a preosteoblast showing focal contacts (green), stress fibers (red) crossing the cell, and a nucleus (blue); (**b**) Scanning electron microscopy image showing the polygonal morphology of the preostoblasts (enlarged detail in (**c**).*

2.4.3. Cell Differentiation

For $Ti_{40}Zr_{20}Fe_{20}Hf_{20}$ alloy to be considered a biocompatible material, it must allow cell differentiation to occur. After 14 days in culture with differentiation medium (in presence and absence of the alloy), some nodules of calcium phosphate were detected among the preosteoblasts (Figure 8). After 21 days, a large number of nodules were observed. Extracellular matrix mineralization was similar in osteoblasts in contact with the alloy, in presence of the alloy or in absence of it. Therefore, $Ti_{40}Zr_{20}Fe_{20}Hf_{20}$ alloy allows the differentiation of preostoblasts into osteoblasts.

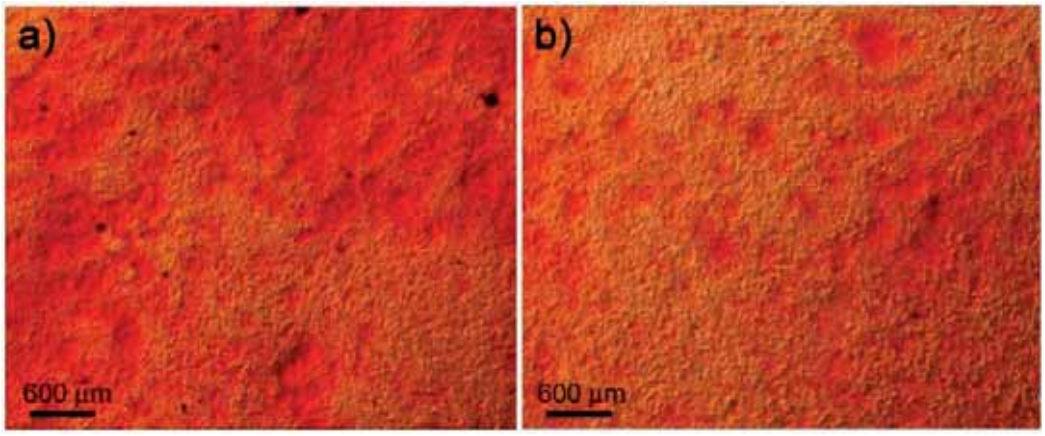

Figure 8. *Mineralization of the extracellular matrix by differentiated osteoblasts after 14 days in culture (**a**) in the presence of the alloy and (**b**) without the alloy. Calcium carbonate can be observed using Alizarin Red S staining (red).*

3. Experimental Section

3.1. Material and sample preparation

$Ti_{40}Zr_{20}Hf_{20}Fe_{20}$ (at. %) master alloy had been prepared by arc melting a mixture of the high purity elements in Ar atmosphere. Subsequently, the master alloy was suction casted into a Cu mold to produce the 2 mm diameter rod.

3.2 Structural characterization

The sample was structurally characterized by X-ray diffraction (XRD), using a Philips X'Pert diffractometer with monochromatic Cu-Kα radiation. The XRD pattern was acquired using a step-scan mode. The 2θ step size was 0.03º and the waiting time per step was selected to be 7s. A scanning electron microscope (SEM - Zeiss Merlin), equipped with an energy dispersive X-ray (EDX) spectrometer was used for microstructure observation and compositional analysis.

3.3 Mechanical behaviour

Nanoindentation experiments were performed on the as-cast sample using a UMIS equipment from Fischer-Cripps laboratories, furnished with a Berkovich pyramidal-shaped indenter tip. The thermal drift was always kept below ± 0.05 nm s^{-1}. Arrays of 50 indentations with applied loads of 250 mN and 3 mN were carried out to probe both the average and local mechanical behaviour and to verify the accuracy of the indentation data. Prior to the nanoindentation tests the specimens were carefully polished to mirror-like appearance using diamond paste. The method of Oliver and Pharr was used to determine the hardness and the reduced Young's modulus [40]. Proper corrections for the contact area (calibrated with a fused quartz specimen), the instrument compliance and initial penetration depth were applied. Finally, the elastic recovery was evaluated as the ratio between the elastic and the total (plastic + elastic) energies during nanoindentation, U_{el}/U_{tot}. These energies were calculated from the nanoindentation experiments as the areas between the unloading curve and the x-axis (U_{el}) and between the loading curve and the x-axis (U_{tot}). The elastic constants were determined using ultrasonic measurements (pulse-echo overlap technique) along with density assessment (Archimedes' method).

3.4 Corrosion characterization

Electrochemical polarization measurements were carried out using a PGSTAT120 Autolab potentiostat/galvanostat (Ecochemie). Prior to the measurements, $Ti_{40}Zr_{20}Hf_{20}Fe_{20}$ (at. %) disks from the rods were cut and carefully ground with emery paper (SiC) up to grit 4000 and further polished with 6, 3 and 1 μm diamond suspension. Subsequently, the samples were degreased in acetone and finally cleaned with distilled water. Electrochemical corrosion experiments were performed in naturally aerated simulated physiological Hank's balanced salt solution (HBSS) at 37.5 °C. The composition of the HBSS solution was: 8.0 g dm^{-3} NaCl + 0.4 g dm^{-3} KCl + 0.04788 g dm^{-3} Na_2HPO_4 + 0.06 g dm^{-3} KH_2PO_4 + 0.185 g dm^{-3} $CaCl_2 \cdot 2H_2O$ + 0.09767 g dm^{-3} $MgSO_4$ + 0.35 g $g \cdot dm^{-3}$ $NaHCO_3$ + 1.0 $g \cdot dm^{-3}$ D-glucose. A typical three-electrode cell configuration was used. The reference electrode consisted of a double junction Ag|AgCl electrode filled with 3M KCl inner solution and 1 M NaCl interchangeable outer solution (E(SHE)= +0.210 V). A platinum foil acted as the counter electrode. Before each polarization scan, the sample was immersed in the electrolyte for 30 min. Afterwards, the potential was swept toward the anodic direction starting from 500 mV below to the open-circuit potential (OCP) at a scan rate of 0.5 $mV \cdot s^{-1}$. The corrosion current density (j_{corr}) values were determined using the Tafel extrapolation method [41]. The mechanical properties and the corrosion behaviour of $Ti_{40}Zr_{20}Hf_{20}Fe_{20}$ alloys were compared with those of commercial Ti–6Al–4V purchased from Goodfellow [42].

3.5. Biological Tests

3.5.1. Cell Culture

MC3T3-E1 mouse preosteoblasts (ATCC) were cultured in α-minimum essential medium (MEMα, Invitrogen) with 10% foetal bovine serum (FBS, Gibco) in standard conditions (at 37°C and 5% CO_2). Alloy disks were glued individually onto a glass coverslip with silicone, introduced into a 4-multiwell culture plate and sterilized under UV light for at least 1 h. Once sterilized, 50.000 preosteoblasts were seeded into each well and cultured in standard conditions for 24 h. For all experiments three groups were analyzed: cells grown on top of the alloy, cells grown on the coverslip in the presence of the alloy and cells grown on the coverslip in absence of the alloy (control culture). All experiments were conducted in triplicate.

3.5.2. Cell Viability Assay

Cytotoxicity was analysed by detecting intracellular esterases activity using the Live/Dead Viability/Cytotoxicity Kit for mammalian cells (Invitrogen), according to the manufacturer's protocol. Images from different regions (alloy disk and coverslip) of each culture sample were captured using an Olympus IX71 inverted microscope equipped with epifluorescence. Data were analyzed for significance using the Fisher's exact test for comparison between groups. Statistically significance was considered when $p < 0.05$.

3.5.3. Scanning Electron Microscope (SEM) Analysis of Cells

Cells were rinsed twice in phosphate buffered saline (PBS), fixed in 4% paraformaldehyde in PBS for 45 min at room temperature (RT) and rinsed twice in PBS. Cell dehydratation was performed in a series of ethanol washes (50%, 70%, 90%, and twice 100%), 7 min each. Finally, samples were dried using hexamethyl disilazane (HMDS; Electron Microscopy Sciences) for 10 min. Samples were mounted on special stubs and analyzed using a SEM (Zeiss Merlin) equipped with energy-dispersive X-ray spectroscopy (EDX) analysis.

3.5.4. Cell Adhesion Analysis

Cell adhesion onto the alloy was determined by the presence of focal contacts. Phalloidin was used to visualize stress fibers (actin filaments) whereas an antibody against vinculin was used to detect the focal contacts. Following the same protocol described for viability studies, 50.000 preosteoblasts were seeded into a well containing an alloy disk glued onto a coverslip. After 24 h of culture, cells were fixed in 4% paraformaldehyde (Sigma) in PBS for 45 min at RT, permeabilized with 0.1% Triton X-100 (Sigma) in PBS for 15 min and blocked for 25 min with 1% PBS-bovine serum albumin (BSA; Sigma) at RT. Samples were then incubated with a mouse anti-vinculin primary antibody (Chemicon) for 60 min at RT and washed with 1% PBS-BSA. Then, samples were incubated with a mixture of Alexa fluor 594-conjugated phalloidin (Invitrogen), Alexa fluor 488 goat anti-mouse IgG1, and Hoechst 33258 (both from Sigma) for 60 min at RT. Finally, samples were washed in 1% PBS-BSA and air dried. Samples were mounted on specific bottom glass dishes (MatTek) using Fluoroprep mounting solution (Biomerieux). Cells were imaged in a confocal laser scanning microscope (Leica SP5). Series of horizontal optical sections were collected at 400 nm intervals and projections were generated with Imaris software (Bitplane).

3.5.5. Cell Differentiation Assay

Preosteoblasts differentiation in the presence of the alloy was analyzed through the detection of calcium deposits, a sign of ECM mineralization. To this aim, 500.000 preosteoblasts were seeded into 35 mm culture dishes containing an alloy disk glued to a coverslip with silicone. After 24 h in culture, MEMα medium was removed and differentiation medium, consisting of MEMα supplemented with 10–8 M dexamethasone, 50 μg/mL ascorbic acid and 8 mM β-glycerophosphate (all from Sigma), was added. Cells were cultured during 14 or 21 days in the presence of the differentiation medium, which was replaced every 3–4 days. Secreted calcium deposits were detected using Alizarin Red S staining. After 14 or 21 days in culture, cells were rinsed in PBS and fixed in 4% paraformaldehyde in PBS for 45 min at RT. Then, cells were washed twice with PBS and incubated with 2% Alizarin Red S (Sigma) for 30 min at RT. Finally, samples were washed with milliQ water and visualized using Olympus IX71 inverted microscope.

4. Conclusions

The synthesis and characterization of $Ti_{40}Zr_{20}Hf_{20}Fe_{20}$ alloy, in form of rods of 2 mm in diameter, by copper mold casting process is reported. Our results reveal that:

(i) The $Ti_{40}Zr_{20}Hf_{20}Fe_{20}$ rod is mechanically harder than Ti–6Al–4V and it shows lower Young's modulus, as determined by nanoindentation tests.

(ii) The $Ti_{40}Zr_{20}Hf_{20}Fe_{20}$ alloy shows good corrosion resistance in HBSS, as evidenced by the passive behavior in a wide potential window and the low corrosion current densities observed. In comparison with commercial Ti–6Al–4V alloy, the $Ti_{40}Zr_{20}Hf_{20}Fe_{20}$ alloy presents slightly larger value of polarization resistance.

(iii) In terms of biocompatibility, the $Ti_{40}Zr_{20}Hf_{20}Fe_{20}$ alloy is not cytotoxic and preosteoblast cells can easily adhere onto its surface and differentiate into osteoblasts.

All abovementioned properties make the $Ti_{40}Zr_{20}Hf_{20}Fe_{20}$ alloy appealing as potential candidate to be used as biomaterial.

Acknowledgments

The authors wish to thank A. Gebert, S. Abdi, M. Calin, S. Donath, J. Eckert and Servei de Microscòpia of the Universitat Autónoma de Barcelona for helpful discussions and for technical support. Funding by the European Commission within the framework of the FP7-ITN network BioTiNet (FP7PEOPLE-2010-ITN-264635). We also acknowledge the Catalan DGR (2009-SGR-1292 and 2009-SGR-282), the Spanish MICINN (MAT2011-27380-C02-01 and TEC2011-29140-C03-03). M.D.B. acknowledges partial financial support from an ICREA-Academia Award.

References

1. Geetha, M.; Singh, A.K.; Asokamani, R.; Gogia, A.K. Ti based biomaterials, the ultimate choice for orthopaedic implants—A review. *Prog. Mater. Sci.* **2009**, *54*, 397–425.
2. Mei, J. Titanium-based Bulk Metallic Glasses: Glass Forming Ability and Mechanical Behavior. Ph.D.Thesis, Joseph Fourier University, Grenoble, France, Northwestern Polytechnical University – Xi'an, China, November, 2009.
3. Niinomi, M. Recent research and development in titanium alloys for biomedical applications and healthcare goods. *Sci. Technol. Adv. Mater.* **2003**, *4*, 445–454.
4. Gleiter, H. Nanoglasses: A new kind of noncrystalline materials. *Beilstein J. Nanotechnol*. **2013**, *4*, 517–533.
5. Suryanarayana, C.; Koch, C.C. Nanocrystalline materials—Current research and future Directions. *Hyperf. Interact.* **2000**, *130*, 5–44.
6. Zhou, Y.L.; Niinomi, M. Microstructures and mechanical properties of Ti–50 mass% Ta alloy for biomedical application. *J. Alloys Compd*. **2008**, *466*, 535–542.
7. Nouri, A.; Hodgson, P.D.; Wen, C.E. Effect of process control agent on the porous structure and mechanical properties of a biomedical Ti–Sn–Nb alloy produced by powder metallurgy. *Acta Biomater.* **2010**, *6*, 1630–1639.
8. Xu, L.J.; Chen, Y.Y.; Liu, Z.G.; Kong, F.T. The microstructure and properties of Ti–Mo–Nb alloys for biomedical application. *J. Alloys Compd*. **2008**, *453*, 320–324.
9. Elias, L.M.; Schneidera, S.G.; Schneidera, S.; Silva, H.M.; Malvisi, F. Microstructural and mechanical characterization of biomedical Ti–Nb–Zr(–Ta) alloys. *Mater. Sci. Eng.* **2006**, *432*, 108–112.
10. Naga, S.; Banerjee, R.; Frasera, H.L. Microstructural evolution and strengthening mechanisms in Ti–Nb–Zr–Ta, Ti–Mo–Zr–Fe and Ti–15Mo biocompatible alloys. *Mater. Sci. Eng.* **2005**, *25*, 357–362.
11. Han, J.H.; Park, D.H.; Bang, C.W.; Yi, S.; Lee, W.H.; Kim, K.B. Sn effect on microstructure and mechanical properties of ultrafine eutectic Ti–Fe–Sn alloys. *J. Alloys Compd*. **2009**, *483*, 44–46.

12. Majumdar, P.; Singh, S.B.; Chakraborty, M.The influence of heat treatment and role of boron on sliding wear behavior of b-type Ti–35Nb–7.2Zr–5.7Ta alloy in dry condition and in simulated body fluids. *J. Mech. Behav. Biomed. Mater.* **2012**, *10*, 1–12.
13. Chen, N.; Louzguine-Luzgin, D.V.; Ranganathan, S.; Inoue, A. Glassy and icosahedral phases in rapidly solidified Ti–Zr–Hf–(Fe, Co or Ni) alloys. *J. Non Cryst. Solids* **2005**, *351*, 2547–2551.
14. Fornell, J.; Suriñach, S.; Baró, M.D.; Sort, J. Unconventional elastic properties, deformation behavior and fracture characteristics of newly developed rare earth bulk metallic glasses. *Intermetallics* **2009**, *17*, 1090–1097.
15. Wang, W.H.; Bai, H.Y.; Luo, J.L.; Wang, R.J.; Jin, D. Supersoftening of transverse phonons in $Zr_{41}Ti_{14}Cu_{12.5}Ni_{10}Be_{22.5}$ bulk metallic glass. *Phys. Rev.* **2000**, *62*, 25–28.
16. Ibrahim, K.; Mhaede, M.; Wagner, L. Effect of annealing temperature on microstructure and mechanical properties of hot swaged cp-Ti produced by investment casting. *J. Mater. Eng. Perform.* **2012**, *21*, 114–118.
17. Sun, F.S.; Cao, C.X.; Kim, S.E.; Lee, Y.T.; Yana, M.G. Mechanism of Beta Stabilizers in a TiAl Alloy. *Metall. Mater. Trans.* **2001**, *32*, 1573–1589.
18. Joshi, V.A. *Titanium Alloys: AnAtlas of Structures and Fracture Features*; CRC Press: Boca Raton, FL, USA, 2006.
19. Liu, B.; Zheng, Y.F. Effects of alloying elements (Mn, Co, Al, W, Sn, B, C and S) on biodegradability and *in vitro* biocompatibility of pure iron. *Acta Biomater*. **2011**, *7*, 1407–1420.
20. Kim, W.G.; Choe, H.C. Nanostructure and corrosion behaviors of nanotube formed Ti–Zr alloy. *Trans. Nonferrous Met. Soc. China* **2009**, *19*, 1005–1008.
21. Sun, B.B.; Sui, M.L.; Wang, Y.M.; He, G.; Eckert, J.; Ma, E. Ultrafine composite microstructure in a bulk Ti alloy for high strength, strain hardening and tensile ductility. *ActaMater.* **2006**, *54*, 1349–1357.
22. Hynowska, A.; Pellicer, E.; Fornell, J.; González, S.; Steenberge, N.; Suriñach, S.; Gebert, A.; Calin, M.; Eckert, J.; Baró, M.D.; Sort, J. Nanostructured β-phase Ti–31.0Fe–9.0Sn and sub-μm structured Ti–39.3Nb–13.3Zr–10.7Ta alloys for biomedical applications: Microstructure benefits on the mechanical and corrosion performances. *Mater. Sci. Eng.* **2012**, *32*, 2418–2425.
23. Manika, I.; Maniks, J. Size effects in micro- and nanoscale indentation. *Acta Mater.* **2006**, *54*, 2049–2056.
24. Gerberich, W.W.; Tymiak, N.I.; Grunlan, J.C.; Horstemeyer, M.F.; Baskes, M.I. Interpretations of indentation size effects. *J. Appl. Mech.* **2002**, *69*, 433–442.
25. Li, H.; Ghosh, A.; Han, Y.N.; Bradt, R.C. The frictional component of the indent of the indentation size effect in low load microhardness testing. *J. Mater. Res.* **1993**, *8*, 1028–1032.
26. Nix, W.D.; Gao, H. Indentation size effects in crystalline materials: A law for strain gradient plasticity. *J. Mech. Phys. Solids* **1998**, *46*, 411–425.

27. Huang, Y.; Qu, S.; Hwang, K.C.; Li, M.; Gao, H. A conventional theory of mechanism-based strain gradient plasticity. *Int. J. Plast.* **2004**, *20*, 753–782.
28. Pirich, R.G. Directional solidification and characterization of near eutectic Sm_2Co_{17}/Co alloys. *Metall. Trans.* **1986**, *17*, 1149–1155.
29. Hertzberg, R.W. *Deformation and Fracture Mechanics of Engineering Materials*; John Wiley & Sons: New York, NY, USA, 1996.
30. Smith, W.F.; Hashemi, J. *Foundations of Materials Science and Engineering*; McGraw-Hill: Boston, MA, USA, 2006.
31. Hall, E.O. The deformation and ageing of mild steel III, Discussion of results. *Proc. Phys. Soc.* **1951**, *64*, 747–753.
32. Petch, N.J. The cleavage strength of polycrystals. *J. Iron Steel Res. Inst.* **1953**, *174*, 25–28.
33. Zhou, Y.L.; Niinomi, M.; Akahori, T. Dynamic Young's modulus and mechanical properties of Ti-Hf alloys. *Mater. Trans.* **2004**, *45*, 1549–1554.
34. Fornell, J.; Steenberge, N.; Varea, A.; Rossinyol, E.; Pellicer, E.; Suriñach, S.; Baró, M.D.; Sort, J. Enhanced mechanical properties and *in vitro in vitro* corrosion behavior of amorphous and devitrified $Ti_{40}Zr_{10}Cu_{38}Pd_{12}$ metallic glass. *J. Mech. Behav. Biomed. Mater.* **2011**, *4*, 1709–1717.
35. Leyland, A.; Matthews, A. On the significance of the H/E ratio in wear control: A nanocomposite coating approach to optimised tribological behaviour. *Wear* **2000**, *246*, 1–11.
36. Koch, C.C. *Nanostructured Materials, Processing, Properties and Applications*; William Andrew publishing: New York, NY, USA, 2007.
37. Ma, F.Y. *Pitting Corrosion*; Intech: New York, NY, USA, 2012.
38. Rosenbloom, S.N.; Corbett, R.A. An assessment of ASTM F 2129 electrochemical testing of small medical implants—Lessons learned. In Proceedings of the NACE Corrosion Conference & Exposition,Nashville, Tennessee, USA, 11-15, March, 2007.
39. Wang, B.L.; Li, L.; Zheng, Y.F. *In vitro* cytotoxicity and hemocompatibility studies of Ti–Nb, Ti–Nb–Zr and Ti–Nb–Hf biomedical shape memory alloys. *Biomed. Mater.* **2010**, *5*, 044102 (7pp).
40. Bao, Y.W.; Wang, W.; Zhou, Y.C. Investigation of the relationship between elastic modulus and hardness based on depth-sensing indentation measurements. *Acta Mater.* **2004**, *52*, 5397–5404.
41. McCafferty, E. Validation of corrosion rates measured by the Tafel extrapolation method. *Corr. Sci.* **2005**, *47*, 3202–3215.
42. http://www.goodfellow.com, code 453–274–50.

4.3. Influence of the irradiation temperature on the surface structure and physical/chemical properties of Ar ion-irradiated bulk metallic glasses

This article tackles the effects of ion irradiation treatments (using Ar ions) on the microstructure, mechanical properties, wettability and corrosion resistance of two types of bulk metallic glasses: Zr-based and Ti-based. Contrary to most previous works in the literature, where ion irradiation is performed only at room temperature (RT), here the surface treatments are performed at RT and also at a temperature close to the glass transition (T_g) and the resulting changes in physical/chemical properties are compared.

The surfaces of both types of metallic bulk alloys ($Ti_{40}Zr_{10}Cu_{38}Pd_{12}$ and $Zr_{55}Cu_{28}Al_{10}Ni_7$) were treated using multiple Ar ion irradiation processes with a maximum energy and fluence of 200 keV and 1×10^{16} ions/cm^2, respectively. Analogous irradiation procedures have been carried out on samples produced at RT (on the as-cast alloys) and at T = 620 K (≈ 0.9 T_g, where T_g denotes the glass transition). For the high-temperature irradiation processes the samples were heated and cooled at 40 K/min and kept at T=620 K for 1 h. The ion damage caused during the cumulative irradiation process was modeled using Monte-Carlo simulations by means of TRIM (Transport of Ion in Matter) software.

The structure, mechanical behavior, wettability and corrosion resistance of the irradiated alloys have been compared with the properties of the as-cast and annealed (T = 620 K) non-irradiated specimens. While ion irradiation at RT does not induce appreciable nanocrystallization of the glassy structure (although it causes a decrease of hardness, Young's modulus and the contact angle, presumably due to the increase of the free volume concentration), evidence for nanocrystallization is obtained on samples ion-irradiated at a temperature close to T_g, hence leading to an increase of hardness, Young's modulus and elastic recovery. Such nanocrystallization occurs as a consequence of the synergistic effects arising from ion irradiation and thermal annealing. In turn, although no clear changes in the corrosion behavior are observed on samples irradiated at RT, electrochemical corrosion tests reveal an improvement of the corrosion resistance after ion irradiation at a temperature close to T_g, particularly for the Ti-based BMG. These results are of practical interest in order to engineer appreciable surface treatments based on ion irradiation, aimed at specific functional applications of bulk metallic glasses.

Influence of the irradiation temperature on the surface structure and physical/chemical properties of Ar ion-irradiated bulk metallic glasses

E. Menéndez [a,*], A. Hynowska [b], J. Fornell [b], S. Suriñach [b], J. Montserrat [c], K. Temst [a], A. Vantomme [a], M.D. Baró [b], E. García-Lecina [d], E. Pellicer [b,*], J. Sort [e,*]

[a]KU Leuven, Instituut voor Kern- en Stralingsfysica, Celestijnenlaan 200 D, 3001 Leuven, Belgium

[b]Departament de Física, Facultat de Ciències, Universitat Autònoma de Barcelona, E-08193 Bellaterra, Spain

[c]Institut de Microelectrònica de Barcelona (IMB-CNM), CSIC, Campus Universitat Autònoma Barcelona, E-08193, Bellaterra, Spain

[d]Surfaces Division, IK4-CIDETEC, Parque Tecnológico de San Sebastián, E-20009 Donostia, Spain

[e]Institució Catalana de Recerca i Estudis Avançats (ICREA) and Departament de Física, Universitat Autònoma de Barcelona, E-08193 Bellaterra, Spain

[*]Corresponding authors: Tel.: +34 935811401; fax: +34 935812155 (J. Sort).

E-mail addresses: Enric.MenendezDalmau@fys.kuleuven.be (E. Menéndez), Eva.Pellicer@uab.cat (E. Pellicer), Jordi.Sort@uab.cat (J. Sort)

ABSTRACT

Surface treatments using multiple Ar ion irradiation processes with a maximum energy and fluence of 200 keV and 1×10^{16} ions/cm^2, respectively, have been performed on two different metallic glasses: $Zr_{55}Cu_{28}Al_{10}Ni_7$ and $Ti_{40}Zr_{10}Cu_{38}Pd_{12}$. Analogous irradiation procedures have been carried out at room temperature (RT) and at T = 620 K (≈ 0.9 T_g, where T_g denotes the glass transition). The structure, mechanical behavior, wettability and corrosion resistance of the irradiated alloys have been compared with the properties of the as-cast and annealed (T = 620 K) non-irradiated specimens. While ion irradiation at RT does not significantly alter the amorphous structure of the alloys, ion irradiation close to T_g promotes decomposition/nanocrystallization. Consequently, the hardness (H) and reduced Young's modulus (E_r) decrease after irradiation at RT but they both increase after irradiation at 620 K. While annealing close to T_g increases the hydrophobicity of the samples, irradiation induces virtually no changes in the contact angle when comparing with the as-cast state. Concerning the corrosion resistance, although not much effect is found after irradiation at RT, an improvement is observed after irradiation at 620 K, particularly for the Ti-based alloy. These results are of practical interest in order to engineer appropriate surface treatments based on ion irradiation, aimed at specific functional applications of bulk metallic glasses.

Keywords: Ion irradiation; Metallic glass; Nanocrystallization; Hardness; Corrosion resistance; Wettability

1. Introduction

Several procedures to physically or chemically treat the surface of functional materials have been implemented over the years with the aim to improve their corrosion resistance, to control friction and wear, to promote the change of a certain physical property (e.g., conductivity, magnetism or reflectivity) [1–5] or to alter the dimensions and/or final appearance of a product (e.g., color, luster or roughness) [6]. These treatments can be classified into two main categories: (i) treatments that involve covering the surface of the material with a coating layer and (ii)

treatments aimed at altering the surface itself, either modifying it entirely or only in some specific regions (i.e., local surface patterning). In the first case, one can distinguish between organic (e.g., paints, laminates or lubricants) and inorganic coatings (e.g., electrodeposited and electroless coatings, conversion coatings, thermal sprayings, hot dippings, etc.). Within the second category, different types of incident particles or beams (e.g., shot peening, laser, flame, electron or ion irradiation) can be used, for example, to enhance the tribological performance of materials or to change their wettability and improve their corrosion behavior. Various methods have been used in the past to enhance the surface mechanical behavior of materials: thermo-chemical treatments to induce case-hardening (i.e., carburizing, chroming, nitriding, etc.); annealing treatments, where microstructural changes are induced by surface heating (e.g., induction, flame, laser, light, electron beam, etc.); and mechanical treatments, where the structural changes are induced by cold working of the surface (e.g., shot peening, deep rolling or shot blasting). In fact, shot penning and ion irradiation treatments can be used to modify the surface of certain materials in a controlled manner through the creation of structural disorder and refinement of the grain size at the top surface [7,8].

In recent years, several works have reported on the effects of ion irradiation on the near-surface morphology of different types of materials. Changes in roughness or porosity have been induced in metals and oxides by employing high energy (≈ MeV) incident ions (N, O or noble gases), sufficiently high fluences (typically > 1×10^{17} ions/cm^2) or directly using heavy ions (e.g., Bi^+) [9–12]. For instance, amorphous sponge-like germanium foams with tunable porosity and nanopore network geometries have been obtained by varying the ion energy, fluence, angle of incidence and target temperature [12]. Conversely, shrinking of pre-existing pores in the near-surface of amorphous metals has been accomplished by low-energy Ar^+ irradiation [13]. Moreover, in some cases, embedded nanofibers or nanowires have also been fabricated using appropriate ion irradiation conditions [14,15].

Among metallic alloys, bulk metallic glasses (BMGs) have attracted interest during the last decades due to their high hardness and yield strain, combined with an easy flow when heated above the glass-transition temperature T_g, thus allowing for thermoplastic molding, similar to polymers [16,17]. BMGs have found applications in sporting goods, medical and electronic devices, and defense and aerospace technologies. However, BMGs suffer from the drawback that they exhibit limited room temperature macroscopic plasticity, compared to polycrystalline metals, due to formation and rapid propagation of a few shear bands [18]. The plasticity in these

materials can be improved by promoting the nucleation and branching of multiple shear bands or by hindering their propagation. This is usually achieved by engineering metallic glass composites in which small nanocrystals are embedded in the glassy matrix. These crystals can be grown *in situ* (i.e., during the casting process) or by annealing treatments in the supercooled liquid region. If the size and shape of these crystals is properly tuned, this can result in a significant enhancement of the compressive plasticity [18]. Besides thermal treatments, application of stress in BMGs has been reported to enhance the atomic mobility (i.e., increasing the amount of free volume) [19,20], eventually also leading to post-synthesis nanocrystallization, if the applied stress is sufficiently high [21,22].

Ion bombardment of crystalline materials can introduce large amounts of structural defects at the surface, eventually leading to amorphization and subsequent worsening of the mechanical properties [23–26]. This process, which usually takes place when the material is subject to high ion fluences and/or irradiation with heavy incident ions, has to be taken into account in materials for structural applications, for example in nuclear reactors. Contrary to crystalline alloys, BMGs can experience radically different microstructural surface effects depending on the ion irradiation conditions. While an increase of the free volume concentration, with the concomitant decrease of hardness, has been observed after ion irradiation at low fluences with low-energy incoming ions [27–29], partial nanocrystallization can occur for sufficiently high fluences and high incident ion energies [30–35]. In this case, an increase of hardness and plasticity is usually reported. Energetic and thermodynamic considerations to establish which irradiation conditions can either promote increase of free volume or nanocrystallization have been recently reported [36].

Suitable thermal annealing treatments can also induce changes in the amount of free volume frozen in the glassy structure of BMGs during the casting and, if the temperature is sufficiently high, crystallization can take place. Annealing at temperatures below T_g typically induces annihilation of free volume [37]. Partial crystallization can occur when the BMG is heated above T_g and full crystallization is observed for temperatures larger than the crystallization temperature T_x. Hence, either annealing or ion irradiation can be used to tune the intrinsic structure of BMGs and, therefore, their physical and chemical properties. However, in most works dealing with ion irradiation of BMGs, the ion bombardment has been performed only at room temperature (RT), without purposely heating the sample during the irradiation process. Hence, the influence of sample temperature during the ion irradiation procedure has remained largely unexplored.

Furthermore, the literature on the effects of ion irradiation (even when it is performed at RT) on the wettability and corrosion behavior of BMGs is rather scarce [38–42].

In this work, ion irradiation treatments (using Ar ions with a maximum energy of 200 keV) are performed at RT and close to T_g on the surface of two BMGs (Zr-based and Ti-based) with the aim of modifying their structure and, thus, enhancing their near-surface mechanical and corrosion performance through tailored irradiation profiles. The effects of the irradiation processes are similar for the two investigated alloys. Ion irradiation at RT does not induce appreciable nanocrystallization of the glassy structure but causes a decrease of hardness, Young's modulus and the contact angle, presumably due to the increase of the free volume concentration. Conversely, evidence for decomposition/nanocrystallization is obtained on samples ion-irradiated at a temperature close to T_g, leading to an increase of hardness, Young's modulus and elastic recovery. While no clear changes in the corrosion behavior are observed on samples irradiated at RT, electrochemical corrosion tests reveal an improvement of the corrosion resistance after ion irradiation at T close to T_g, particularly for the Ti-based BMG.

2. Experimental details

Bulk metallic glass (BMG) alloys with the compositions $Zr_{55}Cu_{28}Al_{10}Ni_7$ and $Ti_{40}Zr_{10}Cu_{38}Pd_{12}$ (at. %) were prepared by arc-melting mixtures of the high purity elements in Ar atmosphere. Rods of 2 mm in diameter were obtained from the melt by copper mold casting. The compositions of the samples were checked by energy-dispersive X-ray (EDX) analysis, using a Zeiss-Merlin scanning electron microscope (SEM), and were found to be homogeneous along and across the rods. Disks of about 250 μm in thickness were cut from the rods and subsequently polished to mirror-like appearance using SiC grinding paper and diamond paste.

The polished BMGs were irradiated with Ar ions using two consecutive irradiation processes (first one at 200 keV followed by another one at 75 keV) aimed at obtaining a significant and homogeneous radiation damage within the upper 100 nm from the surface. The ion damage caused during the cumulative irradiation process was modeled using Monte-Carlo simulations by means of the TRIM (Transport of Ions in Matter) program included in the SRIM (Stopping Range of Ions in Matter) package [43,44]. To avoid irradiation-induced overheating of the sample, the holder was water-cooled in the irradiations carried out at RT. The dpa values are quantified by multiplying the irradiation fluence and the number of target displacements/ (ion·Å) at a certain depth, divided by the atomic density.

The aforementioned two-step irradiation processes were performed both at RT (on the as-cast alloys) and at T= 620 K, which is close to the glass transition, T_g, for both alloys ($T_{g,Ti\text{-}based}$ = 685 K [45], $T_{g,Zr\text{-}based}$ = 702 K [46], i.e., $T \approx 0.9T_g$). For the high-temperature irradiation processes the samples were heated and cooled at 40 K/min and kept at T = 620 K for 1h (the two-step irradiation process, which lasted slightly less than 1h, was performed during the holding temperature segment). For simplicity, the following nomenclature is used in the figures to refer to the different sample states: "as-cast" for non-treated samples, "irradiated RT" for the samples irradiated at RT, "only annealed 620 K" for the samples annealed at T = 620 K, and "irradiated 620 K" for the samples irradiated at T = 620 K.

The samples were structurally characterized by grazing incidence X-ray diffraction (GIXRD), wide angle x-ray scattering (WAXS) and small angle x-ray scattering (SAXS). GIXRD patterns were acquired on a X'pert PRO MRD PANalytical X-ray diffractometer using CuK_α radiation with an incidence angle of the X-ray beam of 1º. WAXS/SAXS measurements were performed at BL11 – NCD beamline at ALBA Synchrotron Light Facility using an incident wavelength of 0.9999 Å. Conversion of the used wavelength into CuK_α (1.54 Å) has been applied for plotting purposes. Surface roughness was characterized by atomic force microscopy (AFM) using a Dual Scope TMC-26 system (Danish Micro Engineering) working in AC mode. A commercial silicon tip (50-100 KHz resonance frequency) was used to scan surface areas of 50 × 50 μm^2 and extract the peak-to-valley distance and the root-mean square (RMS) roughness values.

Nanoindentation experiments were carried out using a UMIS equipment from Fischer-Cripps laboratories equipped with a Berkovich pyramidal-shaped indenter tip. A total of 100 indentations were performed for each sample, in the load control mode, with a maximum applied force of 4 mN. The thermal drift was always kept below ± 0.05 nm/s. The hardness H and reduced Young's modulus values E_r were evaluated at the beginning of the unloading segment, using the method of Oliver and Pharr [47]. Proper corrections for the contact area (calibrated using a reference quartz silica sample), instrument compliance and initial penetration depth were applied. Finally, the elastic recovery was evaluated from the ratio between the elastic and the total (plastic + elastic) energies during nanoindentation U_e/U_{tot}. These energies were calculated from the nanoindentation experiments as the areas between the unloading curve and the displacement axis (U_e) and between the loading segment and the displacement axis (U_{tot}).

The sessile drop technique was employed to assess the wettability of the alloy surfaces, before and after the irradiation processes. Small droplets (1 μl) of Hank's balanced salt solution

(Aldrich) were deposited onto the surfaces of $Ti_{40}Zr_{10}Cu_{38}Pd_{12}$ alloy whereas 5 wt. % NaCl aqueous solution was used for $Zr_{55}Cu_{28}Al_{10}Ni_7$. These media were chosen bearing in mind the potential applicability of these materials for structural applications (eventually in marine environments for the Zr-based alloy [48] and as biomedical implants for the Ti-based alloy [49]). The contact angles were measured with a CAM 200 from Iberlaser at 25 ºC for $Zr_{55}Cu_{28}Al_{10}Ni_7$ (ambient temperature) and at 37 ºC (human body temperature) for $Ti_{40}Zr_{10}Cu_{38}Pd_{12}$.

Electrochemical corrosion experiments were performed in a thermostatized, one-compartment three-electrode cell filled with 50 ml of Hank's solution at 37 ºC (for $Ti_{40}Zr_{10}Cu_{38}Pd_{12}$) and 50 ml of 5 wt. % NaCl for $Zr_{55}Cu_{28}Al_{10}Ni_7$. As aforementioned, the electrolytes were selected according to the potential applications of these alloys. A double junction Ag|AgCl reference electrode was used with 3 M KCl inner solution and 1M NaCl outer solution. A Pt sheet acted as a counter electrode. Initially, the specimens (3.14 mm^2 exposed area) were immersed in the electrolytes to determine the open circuit potential (OCP) for each case. The potential usually became stable after 3 h of immersion. Immediately afterwards, the potential was swept at a rate of 0.1 mV/s from 300 mV below the OCP towards 300 mV above the OCP. The corrosion current density j_{corr} values were determined by extrapolation of the anodic and cathodic Tafel slopes to the corrosion potential E_{corr}.

3. Results and discussion

3.1. Structural characterization

The Monte-Carlo simulations show that the first irradiation step, carried out at an acceleration energy of 200 keV using a fluence of 1×10^{16} ions/cm^2, caused maximum collisional damage at a depth of 50-100 nm, while the second irradiation, performed at 75 keV and a fluence of 5×10^{15} ions/cm^2, induced maximum effects within the upper 10-40 nm (Fig. 1).

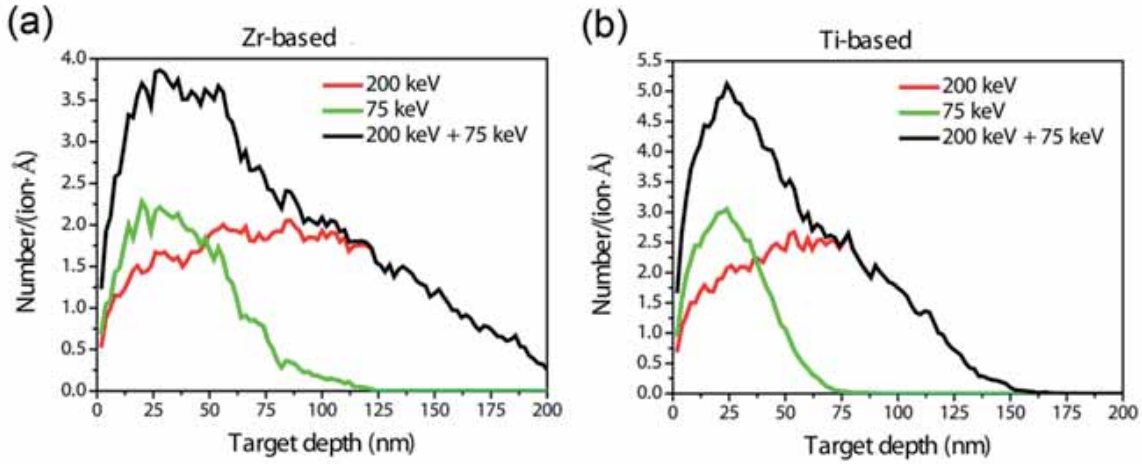

***Fig. 1**. TRIM simulations of the collisional damage distributions (described by the number of target displacements per ion and crossed distance, given in number/ (ion·Å)) in (a) the Zr-based BMG and (b) the Ti-based BMG. The glassy alloys were subject to two consecutive irradiation processes: a first one at 200 keV (fluence of 1×10^{16} ions/cm^2; second one at 75 keV (fluence of 5×10^{15} ions/cm^2).*

The simulations reveal that while a collisional damage of around 29 displacements/ atom (dpa) is induced in the Ti-based alloy within the first top 100 nm, a damage of 22 dpa is induced in the Zr-based BMG. Since the irradiation conditions were the same for the investigated BMGs and both show a similar density (i.e., 6.900 g/cm^3 and 6.755 g/cm^3 for the Ti-based and the Zr-based BMGs, respectively), the differences in the collisional damage are not pronounced. Shown in Fig. 2(a) are the WAXS patterns of the Ti-based alloy in the as-cast state, after ion irradiation at RT, after annealing at T = 620 K and after ion irradiation at 620 K.

The WAXS pattern of the as-cast sample consists of two broad halos with absence of well-defined diffraction peaks, indicating that the as-cast $Ti_{40}Zr_{10}Cu_{38}Pd_{12}$ is amorphous. The same holds for the $Zr_{55}Cu_{28}Al_{10}Ni_7$ alloy (Fig. 3(a)).

Remarkably, no appreciable changes in the WAXS pattern are observed after ion irradiation at RT, neither for the Ti-based nor for the Zr-based BMGs (see also the corresponding GIXRD patterns of Fig. S1). This is opposite to what has been found in other BMGs, where surface crystallization has been occasionally observed after irradiation at RT, particularly when the ion fluence or incident energy were higher than in our case (e.g., 140 keV Heions with fluence of 1.7×10^{17} ions/cm^2 [31,34] or 300 keV Arions with fluence of 3.0×10^{15} [33]) or the incident ions were heavier (e.g., Ga^+ [35], Cu^+ [30] or Ni^+ [32]).

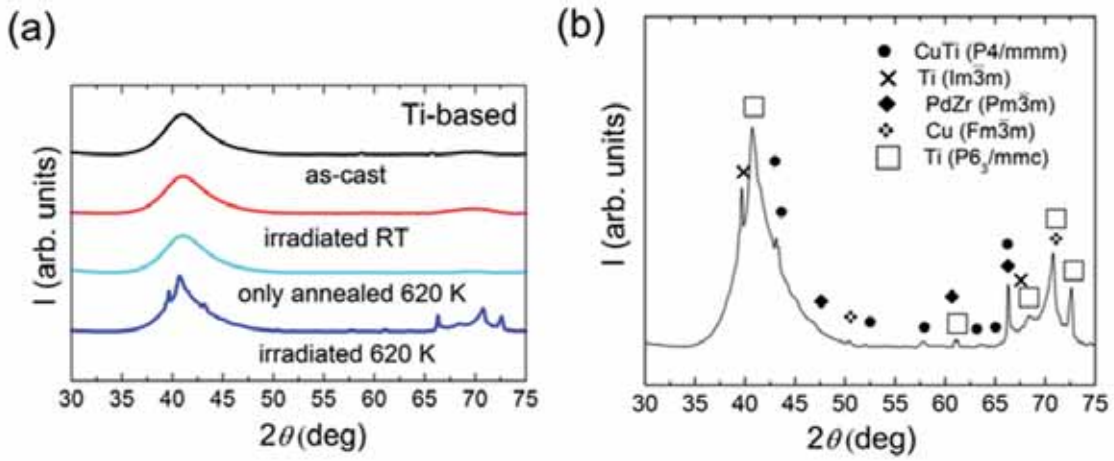

Fig. 2*. (a) WAXS patterns corresponding to the Ti-based metallic glass in the as-cast state, after ion irradiation at room temperature (RT), after annealing at 620 K and after ion irradiation at 620 K and (b) zoomed view of the WAXS pattern for the Ti-based sample ion-irradiated at 620 K.*

Fig. 2(a) and 3(a) also show that $Ti_{40}Zr_{10}Cu_{38}Pd_{12}$ and $Zr_{55}Cu_{28}Al_{10}Ni_7$ remain amorphous after annealing at 620 K, as expected from the thermal stability of glassy materials when heated below T_g. Conversely, a slight decrease of the full width at half height of the amorphous halo located in the 2θ range 35º-50º was observed for $Ti_{40}Zr_{10}Cu_{38}Pd_{12}$ after irradiation at T = 620 K. Actually, discrete narrower peaks can be distinguished superimposed on the amorphous halo for the sample irradiated at 620 K (Fig. 2(b)).

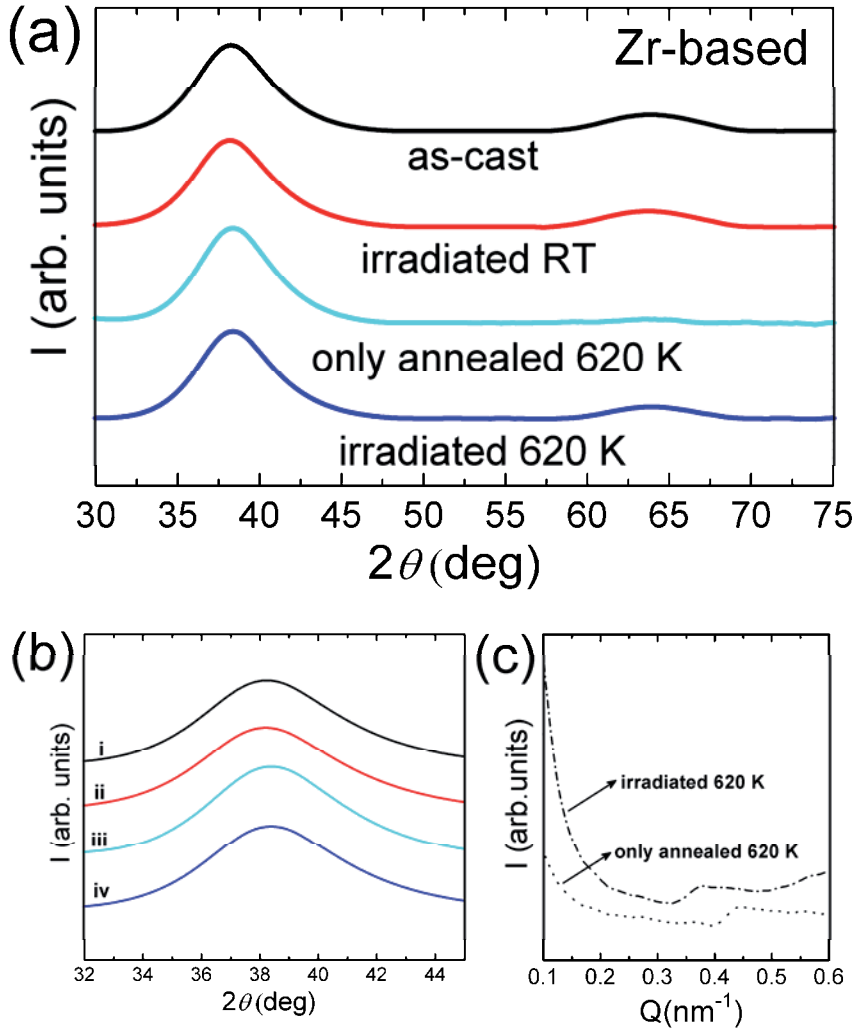

Fig. 3*. (a) WAXS patterns corresponding to the Zr-based metallic glass, (b) detail of the WAXS patterns in angular range corresponding to the main diffraction halo in (i) as-cast state, (ii) after ion irradiation at room temperature (RT), (iii) after annealing at 620 K and (iv) after ion irradiation at 620 K, and (c) SAXS patterns of the Zr-based alloy after annealing at 620 K and after ion irradiation at 620 K*

Several phases (CuTi, Ti, PdZr, and Cu) have been found to match these reflections. This indicates that irradiation close to T_g promotes partial nanocrystallization, even though this temperature is below T_g. Such a decrease of the width of the amorphous hump is not evident for the Zr-based BMG (Fig. 3(b)). In order to gain a deeper knowledge on the eventual structural modifications occurring at surface level, complementary SAXS experiments were conducted for this alloy. Fig. 3(c) shows an interference peak in the SAXS patterns of the Zr-based sample

annealed at 620 K, which slightly shifts toward lower *q* for the sample irradiated at 620 K. Such small shift can be attributed to decomposition stages preceding nanocrystallization, in agreement with [50,51].

AFM images revealed virtually no changes in the surface roughness after annealing and/or irradiation treatments (Fig. S2 and Table S1). Namely, the peak-to-valley surface roughness remained around 20-30 nm (with RMS roughness values of about 2 nm) in all cases.

3.2. Mechanical properties

The results from nanoindentation are shown in Fig. 4. For both BMG families, it is clear that ion irradiation at RT causes an increase of the maximum penetration depth with respect to the as-cast state (i.e., a decrease of hardness). On the contrary, ion irradiation at T = 620 K causes a decrease of the penetration depth (i.e., mechanical hardening) with respect to the as-cast or annealed samples. Similar trends are observed for the reduced Young's modulus. The effect of ion irradiation at RT can be thought to be similar to low-energy shot peening or low-energy laser surface treatments.

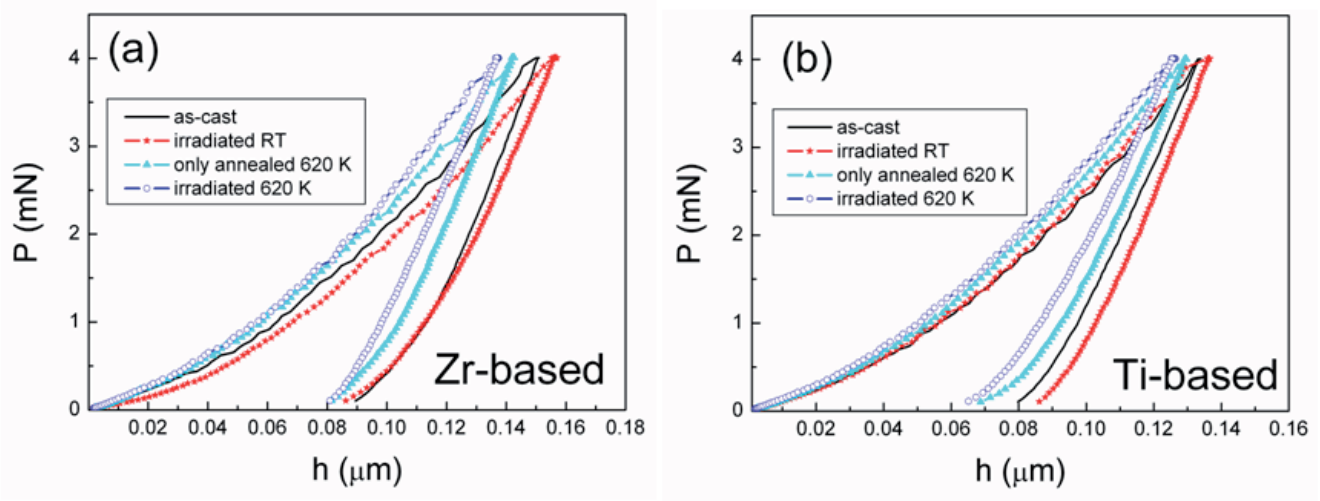

Fig. 4*. Representative nanoindentation curves corresponding to (a) the Zr-based alloy and (b) the Ti-based alloy in the as-cast state, after ion irradiation at room temperature (RT), after annealing at 620 K and after ion irradiation at 620 K.*

In both cases, the mechanical and/or thermal energy causes an increase of the free volume, which enhances atomic mobility and, consequently, reduces hardness and also Young's modulus

[52–54]. Changes in free volume have been also reported in ion irradiated Zr-Ti-Cu-Ni-Be metallic glass [28,29]. In contrast, an increase in the values of H and E_r is observed after annealing at 620 K. This can be ascribed to thermally-induced annihilation of free volume, as has been reported in the literature for metallic glasses annealed at around or below T_g [37]. Partial crystallization of metallic glasses can bring about a further increase of hardness and Young's modulus. In particular, this effect has been reported for both Zr-based [30,33] and Ti-based [45] BMGs. Nevertheless, some embrittlement of the underneath material (i.e., far from the surface) could have been occurred, as shown in BMGs exposed to temperatures close to T_g [55]. From a tribological viewpoint, it is worth mentioning that the wear resistance of a bulk material or a coating not only depends on its hardness (typically harder materials show higher wear resistance) but also on the reciprocal of the Young's modulus. Hence, the elastic strain to failure, which is proportional to H/E_r, turns out to be a suitable parameter to describe the wear resistance of a given material, more than the hardness itself [56]. Our results indicate that although low-energy ion irradiation at RT does not presumably induce changes in the wear resistance, a clear improvement of the H/E_r is observed after ion irradiation close to T_g (Tables 1 and 2).

Table 1*. Summary of the mechanical properties of the Zr-based alloy, assessed by nanoindentation, in the as-cast state, after ion irradiation at room temperature (RT), after annealing at 620 K and after ion irradiation at 620 K. E_r, H, U_e and U_{tot} denote the reduced Young's modulus, the hardness, the elastic and the total indentation energy, respectively.*

	E_r(GPa)	H (GPa)	U_e(nJ)	H/E_r	U_{tot} (nJ)	U_e/U_{tot}
Zr-based as-cast	94.1 ± 0.9	7.52 ± 0.09	0.1021 ± 0.0008	0.0800	0.2377 ±0.0008	0.4297
Zr-based irradiatedRT	82.6 ± 0.5	6.55 ± 0.08	0.107 ± 0.002	0.0793	0.237 ± 0.002	0.4522
Zr-based annealed 620 K	104 ± 3	8.25 ± 0.08	0.1031 ± 0.0004	0.0793	0.224 ± 0.006	0.4598
Zr-based irradiated 620 K	120 ± 1	9.88 ± 0.05	0.104 ± 0.001	0.0822	0.218 ± 0.001	0.4892

Finally, for applications where impact loading can be an issue, the elastic recovery (U_e/U_{tot}) is another interesting mechanical parameter that can be easily extracted from nanoindentation

curves. As shown in Tables 1 and 2, ion irradiation at high temperature (≈ 0.9 T_g) induces an increase of the elastic recovery for both metallic glasses. Such an increase is not so significant after ion irradiation at RT (U_e/U_{tot} actually decreases in the Ti-based alloy after irradiation at RT, when compared to the as-cast state). Although there is no general correlation between hardness and elastic recovery, the values of U_e/U_{tot} have been often reported to be proportional to H/E_r [57,58]. Such a correlation is also roughly observed in the present study.

Table 2*. Summary of the mechanical properties of the Ti-based alloy, assessed by nanoindentation, in the as-cast state, after ion irradiation at room temperature (RT), after annealing at 620 K and after ion irradiation at 620 K. E_r, H, U_e and U_{tot} denote the reduced Young's modulus, the hardness, the elastic and the total indentation energy, respectively.*

	E_r (GPa)	H (GPa)	U_e (nJ)	H/E_r	U_{tot} (nJ)	U_e/U_{tot}
Ti-based as-cast	125 ± 2	10.2 ± 0.2	0.096 ± 0.001	0.0813	0.203 ± 0.001	0.4716
Ti-based irradiated RT	121.4 ± 0.9	9.7 ± 0.1	0.093 ± 0.001	0.0797	0.219 ± 0.002	0.4325
Ti-based annealed 620 K	135 ± 1	11.0 ± 0.3	0.099 ± 0.002	0.0814	0.204 ± 0.002	0.4825
Ti-based irradiated 620 K	141 ± 2	12.1 ± 0.1	0.1073 ± 0.0009	0.0861	0.203 ± 0.003	0.5276

3.3. Wettability

The wettability of a given material is of particular importance since it often determines its corrosion and biofouling performance. Materials with more hydrophobic character are typically more resistant against corrosion. Hence, several surface treatments have been engineered over the years in order to increase the hydrophobicity of different types of materials [59,60]. The wettability can be determined by means of the sessile drop technique, where the contact angle between a liquid droplet and a flat surface of the material of interest is measured. Fig. 5 shows optical microscopy images of Hank's solution droplets deposited onto the surfaces of the as-cast, annealed and ion irradiated $Ti_{40}Zr_{10}Cu_{38}Pd_{12}$ alloys.

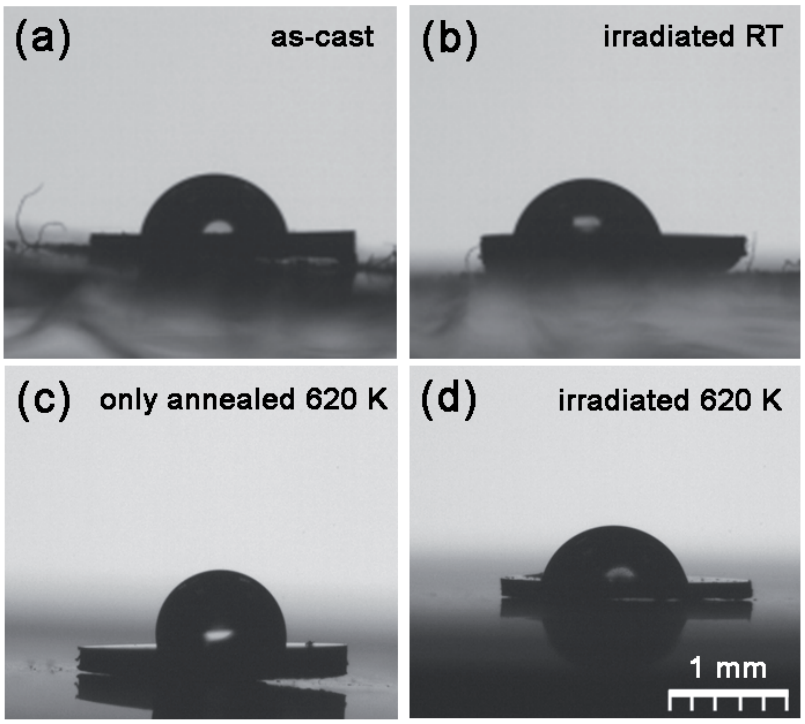

Fig. 5. *Photographs of the as-deposited droplets of Hank's solution onto the surface of the Ti-based alloy in the as-cast state, after ion irradiation at room temperature (RT), after annealing at 620 K and after ion irradiation at 620 K.*

The images reveal that the contact angle is similar in all cases except for the sample annealed at T = 620 K (non-irradiated), where a more hydrophobic character is obtained. The values of contact angle for the different samples investigated in this work are summarized in Table 3. The contact angle decreases slightly after ion irradiation at RT (especially for the Zr-based BMG), it increases significantly after thermal annealing, but it decreases in the samples irradiated at 620 K, approaching the value corresponding to the as-cast state. In a first approximation, if the wetting is non-reactive, the Young's equation can be used to correlate the contact angle with the existing interfacial tensions:

$$\cos\theta = \frac{\sigma_{SV} - \sigma_{SL}}{\sigma_{LV}} \qquad \text{(Eq. 1)}$$

where ρ_{SV}, ρ_{SL} and ρ_{LV} are the interfacial tensions between solid-gas, solid-liquid and liquid-gas phases, respectively [61–64]. Our results indicate that ion irradiation at RT tends to decrease the contact angle; similar to what has been observed after surface laser treatments of metallic glasses

[52]. Since ρ_{LV} depends mainly on the liquid used for the sessile drop experiments, its value can be regarded as constant. Thus, the change in contact angle is attributed to variations in ρ_{SV} and/or ρ_{SL}.

Ion irradiation treatments are likely to induce an increase of free volume in the glassy structure, similar to what has been reported for shot-peened or laser treated metallic glasses [52,53], as well as for amorphous metallic alloys under the action of large shear stresses, where deformation induces a net creation of excess free volume [19,20]. As a result of the increase of the free volume concentration, the atomic mobility is enhanced and ρ_{SV} presumably increases. In turn, when the surface free energy of the solid increases, the attraction between the liquid molecules and the atoms in the solids becomes reinforced, favouring the spreading of the liquid drop on the solid surface, hence decreasing ρ_{SL}. Consequently, the value of $cos\theta$ would turn out to be larger (see Eq. 1), resulting in a lower contact angle [61]. Thermal annealing close to T_g induces structural relaxation of the glassy structure, which brings about a decrease of the free volume concentration. As a result, the contact angle increases mainly because of the increase of $\sigma_{SL.}$ It has also been reported that quite often metallic glasses are more hydrophilic (lower contact angles) than crystalline materials with the same composition [62–64]. It has been argued that since the structure of metallic glasses is metastable, their atomic activity is rather high and this tends to favor the spreading of the liquid drop on the solid surface, hence decreasing ρ_{SL} with respect to the value of the crystalline alloy. In turn, due to the high atomic activity and the presence of not-fully bonded states at the surface of metallic glasses, the value of ρ_{SV} should be higher than for crystalline alloys. In our case, however, a decrease in contact angle after irradiation at T=620 K is observed, in spite of the near-surface decomposition/nanocrystallization evidenced by WAXS (Fig. 2 and 3). This could indicate that surface nanocrystallization, in particular for Ti-based alloy, is only partial and that the effects of thermally-induced annihilation mof free volume on the remaining amorphous matrix are exacerbated due to the high-temperature ion irradiation, thus counterbalancing the effects of nanocrystallization on hydrophobicity.

***Table 3**. Summary of the values of contact angle obtained with 1 μl drop of (a) a 5 wt. % NaCl solution onto the surface of the Zr-based alloy and (b) Hank's solution onto the surface of a Ti-based alloy. The values corresponding to the as-cast state, after ion irradiation at room temperature (RT), after annealing at 620 K and after ion irradiation at 620 K are compared.*

	Contact Angle 1 μl
Zr-based as-cast NaCl 5 wt. % solution	85.0 ± 0.2º
Zr-based irradiated RT NaCl 5 wt. % solution	77.2 ± 0.3º
Zr-based annealed at 620 K NaCl 5 wt. % solution	97.5 ± 0.5º
Zr-based irradiated at 620 K NaCl 5 wt. % solution	84.5 ± 0.5º
Ti-based as-cast Hank's solution	77.4 ± 0.4º
Ti-based irradiated at RT Hank's solution	75.5 ± 0.5º
Ti-based annealed at 620 K Hank's solution	96.1 ± 0.3º
Ti-based irradiated at 620 K Hank's solution	75.2 ± 0.4º

3.4. Corrosion performance

The corrosion performance of the different samples was assessed electrochemically by recording potentiodynamic polarization curves. For the Zr-based alloy, the irradiation does not bring about an improvement of the corrosion resistance in 5 wt% NaCl solution (Fig. 6a). In fact, j_{corr} increases with respect to the as-cast state from 1.2×10^{-5} A/cm^2 to 4.7×10^{-5} A/cm^2 for the sample irradiated at 620 K. Although there is a slight shift of the E_{corr} toward more positive values (ΔE = 27 mV), the change is within the experimental error. It can be observed that this alloy dissolves actively and that the current densities increase rapidly by anodic polarization, similar to what has been observed in other as-cast Zr-based BMGs tested in Cl-containing medium [65]. Only for the samples annealed and irradiated at 620 K, the increase of the current density after E_{corr} is less

sharp but similar values are reached among all samples already at potentials of around 0.4 V. On the contrary, there is an improvement of the corrosion resistance in Hank's solution upon ion irradiation of the surface of Ti-based alloy at 620 K (Fig. 6b). For this alloy, j_{corr} and E_{corr} values for the sample irradiated at RT remain almost the same as for the as-cast state, but the specimens annealed and irradiated at 620 K experience an improvement of the corrosion resistance. A shift in E_{corr} of 40 mV is observed and j_{corr} decreases from 1.3×10^{-5} A/cm^2 (as-cast sample) to 8.8×10^{-6} A/cm^2 and 1.8×10^{-6} A/cm^2 (samples annealed and irradiated at 620 K, respectively). Moreover, the passivity range is enlarged up to 0.65 V. Nevertheless, it should be pointed out that any meaningful comparison between the behaviors of the Zr- and Ti-based alloys is not straightforward since the electrolyte used is different (5 wt. % NaCl vs. Hank's solution). It is conjectured that the protective character of TiO_2 passivation layer typically formed on the surface of Ti-based alloys is enhanced upon ion irradiation. On the contrary, the irradiation of Zr-based alloy might favor surface atom mobility (at least at RT) in a way that triggers even more its active dissolution.

The effects caused by ion irradiation on the corrosion performance of glassy alloys are generally either attributed to chemical modifications of the outmost surface or to structural changes (i.e., nanocrystallization). For example, Jiang et al. observed a clear improvement of the corrosion resistance of a La-based bulk metallic glass in 0.01 M NaCl after implantation of Nb with doses ranging 6×10^{16}-1×10^{17} ions/cm^2 [40]. The authors attributed such improvement to the high passivating ability of the Nb-containing surface layer formed *in situ*; hence, to a chemical modification of the near-surface. The effect of Ar ion bombardment (150 keV, 3×10^{15}-1×10^{17} ions/cm^2) at 77 K on the corrosion properties of Zr-Sn-Fe-Cr BMG in 0.5 M H_2SO_4 was explored by Xiaoyang et al. [41]. The authors observed a different behavior depending on the fluence. At low fluences, E_{corr} shifted toward more cathodic values with respect the as-cast state, whilst at the highest fluences E_{corr} shifted toward more positive values. Simultaneously, the passive current density initially decreased and subsequently increased. Furthermore, j_{corr} did not show any clear pattern with an increase of the fluence. Therefore, it is plausible to assume that the corrosion behavior of irradiated BMGs is strongly dependent on the ion specie, its energy and the fluence used. The corrosion resistance of Ar^+ and Ca^{2+} irradiated $Zr_{46}Cu_{37.636}Al_{8.364}Ag_8$ BMG was evaluated by morphological and compositional analysis of the sample surface after 16 h-immersion in phosphate buffer solution (PBS) [42]. The authors observed a decrease in the density and diameter of pits for the Ar-implanted alloy. However, a study under polarization

conditions was not performed and, hence, the comparison with the Zr-based alloy presented here is not straightforward. Our results on the Ti-based alloy are similar to those reported by Mathur et al. [38,39]. After irradiation of amorphous $Ti_{40}Ni_{60}$ with heavy Ni^{11+} (150 MeV, 1 x 10^{13} ions/cm^2) or N^+ (150 keV, 1×10^{16} ions/cm^2), the authors found that the sample exhibited slightly more positive E_{corr} and lower j_{corr} values compared with the non-irradiated specimen in 1M HNO_3 environment. The decrease of the j_{corr} was attributed to the nanocrystallization-induced irradiation in the case of Ni^{11+}, and to an improvement in the homogeneity and protective character of an oxide film formed on the surface in the case of N^+.

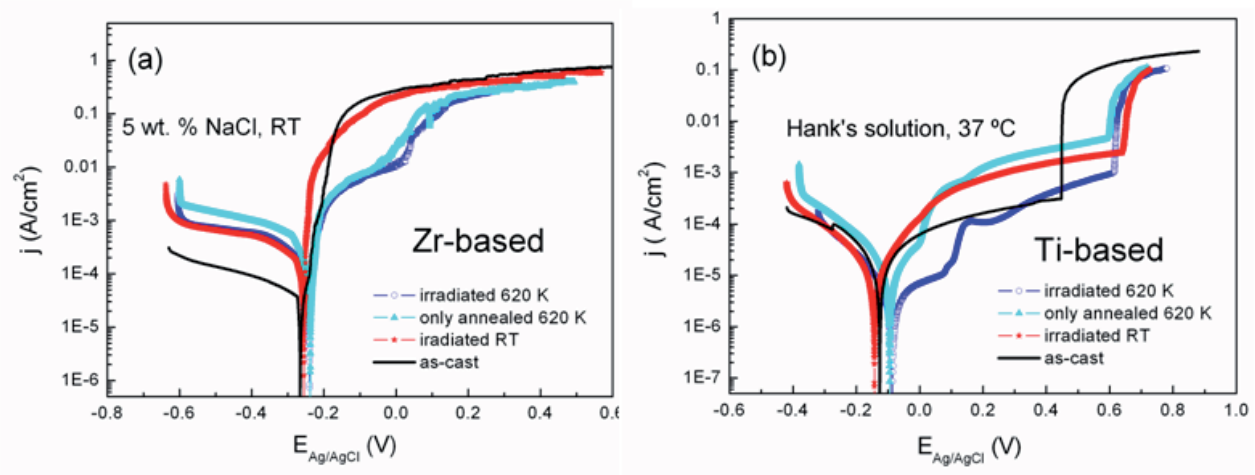

Fig.6. *Representative potentiodynamic polarisation curves corresponding to (a) the Zr-based alloy measured at room temperature using a 5 wt. % NaCl solution and (b) the Ti-based alloy measured at 37 ºC using the Hank's solution, in the as-cast state, after ion irradiation at room temperature (RT), after annealing at 620 K and after ion irradiation at 620 K.*

4. Conclusions

In summary, the combined effects of temperature and ion irradiation damage on the structure and physical/chemical properties (i.e., mechanical behavior, wettability and corrosion performance) of two different metallic glasses have been studied. Our results indicate that for sufficiently low ion fluences and low incident energies, the glassy structure of the as-cast alloys is preserved after irradiation at RT. Conversely, the same mild irradiation conditions applied at a temperature close to T_g induce partial nanocrystallization at the surface of the glassy Ti-based alloy and some decomposition typically occurring before nanocrystallization at the surface of the Zr-based alloy. As a consequence, the changes in mechanical properties observed after irradiation at RT (reduction of hardness and Young's modulus, presumably due to the increase of the free volume

concentration) are opposite to those observed after temperature-assisted ion irradiation processes. In turn, while no improvement of the corrosion performance is observed for the Zr-based alloy, an enhancement is observed after high-temperature irradiation of the Ti-based alloy. Hence, these results indicate that, by tuning both the sample temperature and the irradiation conditions, the properties of the resulting material can be controlled in order to meet specific technological demands, such as mechanical performance.

Acknowledgements

This work was financed by the 2009-SGR-1292 project from the Generalitat de Catalunya, the MAT2011-27380-C02-01 and MAT2011-27380-C02-02 projects from the Spanish Ministerio de Economía y Competitividad (MINECO), the Fund for Scientific Research-Flanders (FWO) and the KU Leuven Concerted Action (GOA/09/006 and GOA/14/007) programs. Part of the work was carried out using the facilities of the ICTS/Clean Room of Micro and Nano-fabrication of the IMB-CNM (CSIC), under the auspices of the GICSERV-6 call (NGG-263 project) funded by MINECO. WAXS/SAXS experiments were performed at BL11–NCD beamline at ALBA Synchrotron Light Facility with the collaboration of ALBA staff. E.M. thanks the FWO for financial support. M.D.B. acknowledges partial financial support from an ICREA-Academia Award. E.P. acknowledges MINECO for the 'Ramon y Cajal' contract (RYC-2012-10839).

REFERENCES

[1] T. Bell, Surf. Eng. 18 (2002) 415–422.

[2] K. Genel, M. Demirkol, M. Çapa, Mater. Sci. Eng., A 279 (2000) 207–216.

[3] E. Menéndez, A. Martinavicius, M. O. Liedke, G. Abrasonis, J. Fassbender, J. Sommerlatte, K. Nielsch, S. Suriñach, M. D. Baró, J. Nogués, J. Sort, Acta Mater. 56 (2008) 4570–4576.

[4] E. Menéndez, J. C. Stinville, C. Tromas, C. Templier, P. Villechaise, J. P. Rivière, M. Drouet, A. Martinavicius, G. Abrasonis, J. Fassbender, M. D. Baró, J. Sort, J. Nogués, Appl. Phys. Lett. 96 (2010) 242509.

[5] E. Menéndez, C. Templier, P. Garcia-Ramirez, J. Santiso, A. Vantomme, K. Temst, J. Nogués, ACS Appl. Mater. Interfaces 5 (2013) 10118–10126.

[6] M. Cartier (ed). Handbook of surface treatments and coatings. Amer Society of Mechanical Engineers ASME Press, New York, US (2003).

[7] N. R. Tao, M. L. Sui, J. Lu, K. Lua, Nanostruct. Mater. 11 (1999) 433–440.

[8] R. S. Averback, R. Benedek, K. L. Merkle, Phys. Rev. B 18 (1978) 4156–4171.

[9] V. Valtchev, E. Balanzat, V. Mavrodinova, I. Díaz, J. El Fallah, J.-M. Goupil, *J. Am. Chem. Soc.*133 (2011) 18950–18956.

[10] P. Romero-Gómez, A. Palmero, T. Ben, J. G. Lozano, S. I. Molina, A. R. González-Elipe, Phys. Rev. B 82 (2010) 115420.

[11] A. G. Pérez-Bergquist, F. U. Naab, Y. Zhang, Nucl. Instrum. Meth. B 269 (2011) 561–565.

[12] L. Bischoff, W. Pilz, B. Schmidt, Appl. Phys. A 104 (2011) 1153–1158.

[13] H. B. George, D. P. Hoogerheide, C. S. Madi, D. C. Bell, J. A. Golovchenko, M. J. Aziz, Appl. Phys. Lett. 96 (2010) 263111.

[14] A. Pérez-Bergquist, S. Zhu, K. Sun, X. Xiang, Y. Zhang, L. Wang, Small 4 (2008) 1119–1124.

[15] Z. Y. Dang, J. Song, S. Azimi, M. B. H. Breese, J. Forneris, E. Vittore, Nucl. Instrum. Meth. B 296 (2013) 32–40.

[16] A. L. Greer, Science 267 (1995) 1947–1953.

[17] W. L. Johnson, MRS Bull. 24 (1999) 42–56.

[18] C. A. Schuh, T. C. Hufnagel, U. Ramamurty, Acta Mater. 55 (2007) 4067–4109.

[19] A. Concustell, J. Sort, G. Alcalá, S. Mato, A. Gebert, J. Eckert, M. D. BaróJ. Mater. Res. 20 (2005) 2719–2725.

[20] J. Fornell, A. Concustell, S. Suriñach , W. H. Li, N. Cuadrado, A. Gebert, M. D. Baró, J. Sort, Int. J. Plasticity 25 (2009) 1540–1559.

[21] J. Das, M. B. Tang, K. B. Kim, R. Theissmann, F. Baier, W. H. Wang, J. Eckert, Phys. Rev. Lett. 94 (2005) 205501.

[22] J. Fornell, E. Rossinyol, S. Suriñach, M. D. Baró, W. H. Li, J. Sort, Scripta Mater. 62 (2010) 13–16.

[23] P. Moine, C. Jaouen, J. Alloys Compd. 194 (1993) 373–380.

[24] A. T. Motta, J. Nucl. Mater. 244 (1997) 227–250.

[25] S. Utsunomiya, L. M. Wang, S. Yudintsev, R. C. Ewing, J. Nucl. Mater. 303 (2002) 177–187.

[26] D. J. Sprouster, R. Giulian, L. L. Araujo, and P. Kluth, B. Johannessen, N. Kirby, K. Nordlund, M. C. Ridgway, Phys. Rev. B 81 (2010) 155414.

[27] J. Carter, E. G. Fu, M. Martin, G. Xie, X. Zhang, Y. Q. Wang, D. Wijesundera, X. M. Wang, W.-K. Chu, L. Shao, Scripta Mater. 61 (2009) 265–268.

[28] R. Raghavan, K. Boopathy, R. Ghisleni, M. A. Pouchon, U. Ramamurty, J. Michler, Scripta Mater. 62 (2010) 462–465.

[29] R. Raghavan, B. Kombaiah, M. Döbeli, R. Erni, U. Ramamurty, J. Michler, Mater. Sci. Eng., A 532 (2012) 407–413.

[30] J. Carter, E. G. Fu, M. Martin, G. Xie, X. Zhang, Y. Q. Wang, D. Wijesundera, X. M. Wang, W.-K. Chu, S. M. McDeavitt, L. Shao, Nucl. Instrum. Meth. B 267 (2009) 2827–2831.

[31] J. Carter, E. G. Fu, G. Bassiri, B. M. Dvorak, N. D. Theodore, G. Xie, D. A. Lucca, M. Martin, M. Hollander, X. Zhang, L. Shao, Nucl. Instrum. Meth. B 267 (2009) 1518–1521.

[32] M. Myers, E. G. Fu, M. Myers, H. Wang, G. Xie, X. Wang, W.-K. Chu, L. Shao, Scripta Mater. 63 (2010) 1045–1048.

[33] W. D. Luo, B. Yang, G. L. Chen, Scripta Mater. 64 (2011) 625–628.

[34] G. Xie, L. Shao, D. V. Louzguine-Luzgin, A. Inoue, Surf. Coat. Technol. 206 (2011) 829–833.

[35] D. J. Magagnosc, R. Ehrbar, G. Kumar, M. R. He, J. Schoers, D. S. Gianola, Sci. Rep. 3 (2013) 1096.

[36] W. Qin, J. A. Szpunar, Y. Umakoshi, Acta Mater. 59 (2011) 2221–2228.

[37] J. Fornell, S. González, E. Rossinyol, S. Suriñach, M.D. Baró, D. V. Louzguine-Luzgin, J. H. Perepezko, J. Sort, A. Inoue, Acta Mater. 58 (2010) 6256–6266.

[38] S. Marthur, R. Vyas, R. Jain, P. Kumar, K. Sachdev, S. K. Sharma, J. Non-Cryst. Solids 357 (2011) 966–969.

[39] S. Marthur, R. Vyas, P. K. Kulriya, K. Asokan, K. Sachdev, S. K. Sharma, J. Alloys Compd. 503 (2010) 192–193.

[40] Q. K. Jiang, C. L. Qin, K. Amiya, S. Nagata, A. Inoue, R. T. Zheng, G. A. Cheng, X. P. Nie, J. Z. Jiang, Intermetallics 16 (2008) 225–229.

[41] L. Xiaoyang, B. Xinde, Z. Chunlan, W. Long, Surf. Coat. Technol. 182 (2004) 138–142.

[42] H. Jia, C. I. Muntele, L. Huang, X. Li, G. Li, T. Zhang, W. He, P. K. Liaw, Intermetallics 41 (2013) 35–43.

[43] J. F. Ziegler, J. P. Biersack, U. Littmark, The Stopping and Range of Ions in Solids; Pergamon Press: New York, 1985.

[44] The TRIM (Transport of Ions in Matter) program is included in the SRIM (Stopping Range of Ions in Matter) package (SRIM-2011). http://srim.org/.

[45] J. Fornell, N. Van Steenberge, A. Varea, E. Rossinyol, E. Pellicer, S. Suriñach, M. D. Baró, J. Sort, J. Mech. Behav. Biomed. Mater. 4 (2011) 1709–1717.

[46] N. Van Steenberge, S. Hóbor, S. Suriñach, A. Zhilyaev, F. Houdellier, F. Mompiou, M. D. Baró, J. Sort, Á. Révész, J. Alloys Compd. 500 (2010) 61–67.

[47] W. C. Oliver, G. M. Pharr, J. Mater. Res., 7 (1992) 1564–1583.

[48] K. Mondal, B. S. Murty, U. K. Chatterjee, Corr. Sci. 48 (2006) 2212–2225.

[49] M. Metikos-Huković, A. Kwokal, J. Piljac, Biomater. 24 (2003) 3765–3775.

[50] X. J. Liu, X. D. Hui, G. L. Chen, M. H. Sun, Intermetallics 16 (2008) 10–15.

[51] J. F. Löffler, W. L. Johnson, Appl. Phys. Lett. 76 (2000) 3394–3396.

[52] J. Fornell, E. Pellicer, E. Garcia-Lecina, D. Nieto, S. Suriñach, M. D. Baró, J. Sort, Appl. Surf. Sci.290 (2014) 188-193.

[53] Y. Zhang, W. H. Wang, A. L. Greer, Nat. Mater. 5 (2006) 857–860.

[54] A. Dubach, R. Raghavan, J. F. Löffler, J. Michler, U. Ramamurty, Scripta Mater. 60 (2009) 567–570.

[55] P. Murali, U. Ramamurty, Acta Mater. 53 (2005) 1467–1478.

[56] A. Leyland, A. Matthews, Wear 246 (2000) 1–11.

[57] Y.-T. Cheng, C.-M. Cheng, Appl. Phys. Lett. 73 (1998) 614–616.

[58] E. Pellicer, S. Pané, K. M. Sivaraman, O. Ergeneman, S. Suriñach, M. D. Baró, B. J. Nelson, J. Sort, Mater. Chem. Phys. 130 (2011) 1380–1386.

[59] X.-M. Li, D. Reinhoudt, M. Crego-Calama, Chem. Soc. Rev. 36 (2007) 1350–1368.

[60] Z. Guo, F. Zhou, J. Hao, W. Liu, J. Am. Chem. Soc. 127 (2005) 15670–15671.

[61] G. F. Ma, H. F. Zhang, H. Li, Z. Q. Hu, J. Alloys Compd. 513 (2012) 273–276.

[62] G. F. Ma, H. F. Zhang, H. Li, Z. Q. Hu, Mater. Lett. 63 (2009) 1605–1607.

[63] P. Shen, J. X. Sun, J. Yang, Y. Qi, Q. C. Jiang, Nanos. Res. Lett. 6 (2011) 318.

[64] E. Pellicer, S. González, A. Blanquer, S. Suriñach, M. D. Baró, L. Barrios, E. Ibáñez, C. Nogués, J. Sort, J. Biomed. Mater. Res. Part A 101 (2013) 502–517.

[65] S. González, E. Pellicer, S. Suriñach, M. D. Baró, E. García-Lecina, J. Sort, Sci. Adv. Mater. 6 (2014) 26-35.

Appendix A. Supplementary material

Supplementary materials associated with this article are provided as follows.

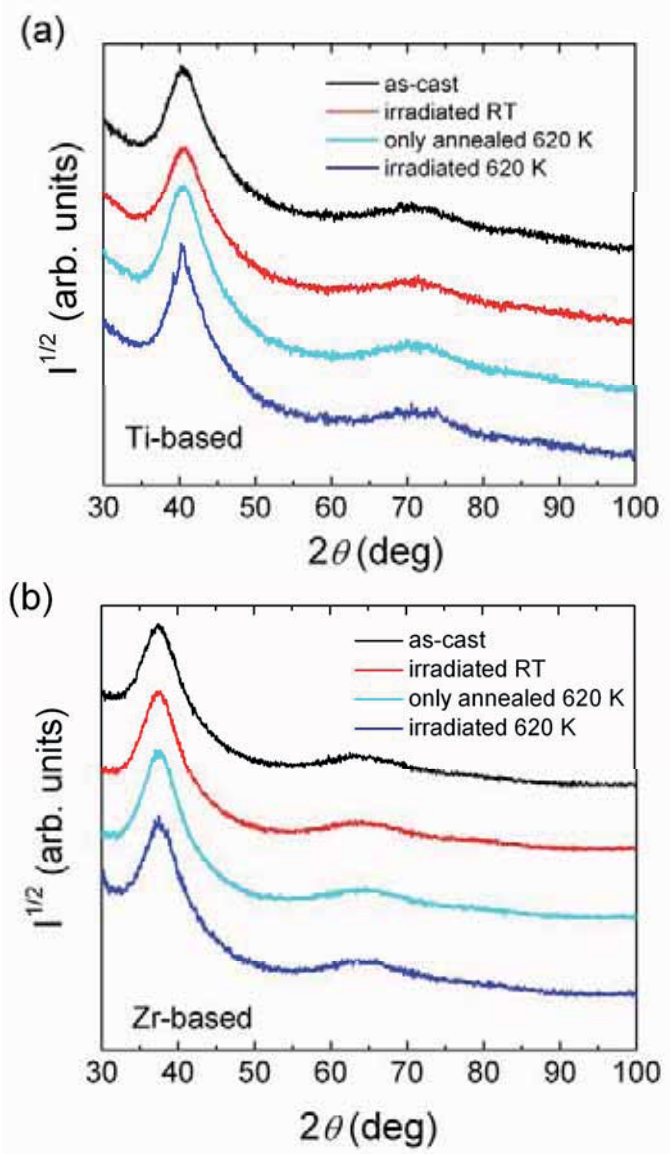

Fig. S1. *X-ray diffraction patterns corresponding to the (a) Ti-based and (b) Zr-based metallic glasses in the as-cast state, after ion irradiation at room temperature (RT), after annealing at 620 K and after ion irradiation at 620 K.*

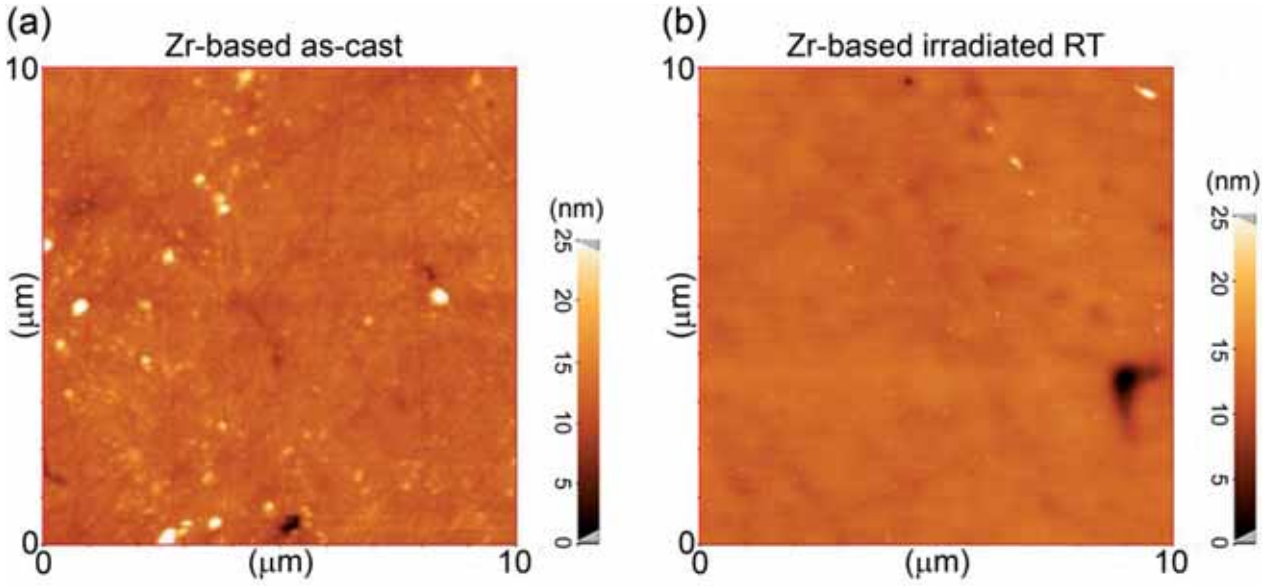

Fig. S2. *AFM images of the surface of Zr-based sample in the (a) as-cast state and (b) after being irradiated at RT.*

Table S1. S_y, S_a and S_q parameters determined from the AFM images shown in Fig. S2.

Sample	$\mathbf{S_y}$ (nm)	$\mathbf{S_a}$ (nm)	$\mathbf{S_q}$ (nm)
Zr-based as-cast	39.2	0.9	1.6
Zr-based irradiated RT	36.3	0.6	1.0

***S_y**: range (it gives the z value range in the assessed area)*
***S_a**: arithmetic mean deviation (it gives the mean of the deviation from the area mean z value)*
***S_q**: root mean square deviation (it gives a measure of the dispersion of the data from the area mean)*

4.4. Nanostructured Ti-Zr-Pd-Si-(Nb) bulk metallic composites: novel biocompatible materials with superior mechanical strength and elastic recovery

This work reports on the synthesis, structural characterization and assessment of the mechanical properties (hardness, elastic recovery and elastic moduli) and biocompatibility of $Ti_{45}Zr_{15}Pd_{35}Si_5$ and $Ti_{45}Zr_{15}Pd_{30}Si_5Nb_5$ bulk nanocomposite alloys, which represent a promising new type of materials suitable for biomedical applications. The properties of these two alloys are compared to commercial Ti-40Nb β-phase alloy. According to XRD, SEM-EDX and TEM studies, both Ti-Zr-Pd-Si-(Nb) alloys show a multi-phase (composite-like) microstructure. The main phase is cubic β-Ti phase (Im3m) but hexagonal α-Ti (P63/mmc), cubic TiPd (Pm3m), cubic PdZr (Fm3m), and hexagonal $(Ti,Zr)_5Si_3$ (P63/mcm) phases are also present.

Both alloys exhibit significantly larger values of hardness (in excess of 10 GPa) and higher wear resistance as compared to commercial Ti-40Nb ($H_{Ti\text{-}40Nb} \approx 2.7$ GPa), while the Young's modulus of $Ti_{45}Zr_{15}Pd_{30}Si_5Nb_5$ is not far from that of Ti-40Nb. This superior mechanical behavior is attributed to the formation of a mixture of mechanically hard nanocrystalline phases, with predominance of the β-Ti phase. Our results also reveal that the replacement of only 5% of Pd with Nb induces significant variations in the relevant mechanical parameters: the Young's modulus decreases from 117 to 85 GPa and the hardness from 14.2 to 10.4 GPa. The combination of large hardness with moderate Young's modulus and high elastic recovery (as determined by nanoindentation), make as-synthesized Ti-Zr-Pd-Si-(Nb) alloys promising new materials for permanent biomedical implants, in some aspects superior to the currently used pure Ti or Ti-40Nb.

Furthermore, the bicompatibility of both alloys (with and without Nb) has also been investigated. Cytotoxicity experiments have included viability tests together with cell morphology observations and analysis of the ability to establish focal contacts cell. The biological tests indicate a large number of live human Saos-2 cells (> 94%) upon culture for 24 h, regardless of the alloy composition (i.e., with or without Nb). It is observed that cells can easily adhere to the surface of the alloys and can thus further differentiate into osteoblasts. For all these reasons, the newly synthesized Ti-Zr-Pd-Si-(Nb) bulky alloys emerge as appealing biomaterials for bone replacement.

Nanostructured Ti-Zr-Pd-Si-(Nb) bulk metallic composites: novel biocompatible materials with superior mechanical strength and elastic recovery

A. Hynowska [1], A. Blanquer [2], E. Pellicer [1,*], J. Fornell [1], S. Suriñach [1], M. D. Baró [1], A. Gebert [3], M. Calin [3], J. Eckert [3,4], C. Nogués [2], E. Ibáñez [2], L. Barrios [2,§], J. Sort [5]

[1]Departament de Física, Universitat Autònoma de Barcelona, E-08193 Bellaterra, Spain

[2]Departament de Biologia Cel·lular, Fisiologia i Immunologia, Universitat Autònoma de Barcelona, E-08193 Bellaterra, Spain

[3]IFW Dresden, P.O. Box 270116, D-01171 Dresden, Germany

[4]TU Dresden, Institute of Materials Science, D-01062 Dresden, Germany

[5]Institució Catalana de Recerca i Estudis Avançats (ICREA) and Departament de Física, Universitat Autònoma de Barcelona, E-08193 Bellaterra, Spain

***** To whom correspondence should be addressed: *Eva.Pellicer@uab.cat, §Lleonard.Barrios@uab.cat

Tel.: +34 935811401; +Fax: +34 935812155.

Abstract:

The microstructure, mechanical behaviour and biocompatibility (cell culture, morphology and cell adhesion) of nanostructured $Ti_{45}Zr_{15}Pd_{35-x}Si_5Nb_x$ with x = 0, 5 (at. %) alloys, synthesized by arc melting and subsequent Cu mould suction casting, in the form of rods with 3 mm in diameter, are investigated. Both Ti-Zr-Pd-Si-(Nb) materials show a multi-phase (composite-like) microstructure. The main phase is cubic β-Ti phase (Im3m) but hexagonal α-Ti (P63/mmc), cubic TiPd (Pm3m), cubic PdZr (Fm3m), and hexagonal $(Ti,Zr)_5Si_3$ (P63/mcm) phases are also present. Nanoindentation experiments show that the $Ti_{45}Zr_{15}Pd_{30}Si_5Nb_5$ sample exhibits lower Young's modulus than $Ti_{45}Zr_{15}Pd_{35}Si_5$. Conversely, $Ti_{45}Zr_{15}Pd_{35}Si_5$ is mechanically harder. Actually, both alloys exhibit larger values of hardness when compared to commercial Ti-40Nb, ($H_{Ti\text{-}Zr\text{-}Pd\text{-}Si} \approx 14$ GPa, $H_{Ti\text{-}Zr\text{-}Pd\text{-}Si\text{-}Nb} \approx 10$ GPa and $H_{Ti\text{-}40Nb} \approx 2.7$ GPa). Concerning the biological behaviour, preliminary results of cell viability performed on several Ti-Zr-Pd-Si-(Nb) discs indicate that the number of live cells is superior to 94% in both cases. The studied Ti-Zr-Pd-Si-(Nb) bulk metallic system is thus interesting for biomedical applications because of the outstanding mechanical properties (relatively low Young's modulus combined with large hardness), together with the excellent biocompatibility.

Keywords: Bioimplant, Ti-based alloy, nanostructured material, mechanical behaviour, biological tests.

INTRODUCTION

Due to the faster population aging, a concern related to the development of suitable materials for bone replacement is continuously arising.[1,2] Specifically, the aim of current investigations is to develop orthopaedic implants that can stand for longer periods of time or even the entire lifetime without failure or need for a revision surgery.[3] These orthopaedic implants must therefore show bio- and mechanical-compatibility with bone. The ideal implant material should not cause any foreign-body inflammatory response, the growth of microorganisms should be suppressed, and it should be non-toxic, non-allergenic and non-carcinogenic.[4] From the mechanical point of view, there are several issues having an impact on the selection of suitable permanent biomaterials. Namely, the candidate material must possess high strength, high hardness, high elastic strain

limit, and relatively low Young's modulus to avoid the occurrence of the so-called stress shielding effect.[5-7] This phenomenon, which occurs when the Young's modulus of the permanent implant differs significantly from the Young's modulus of bone, can ultimately lead to implant loosening. Traditionally, 316L austenitic steel, Co–Cr and Ti alloys have been employed in the biomedical field.[6] Thus, Ti and its alloys have become the most promising engineering materials because they combine high strength with relatively low Young's modulus, reduced stiffness and rather low density (4.5 g/cm^3). In addition, they show good biocompatibility and good corrosion resistance, in many cases superior to those of conventional steel and Co-Cr alloys.[8] So far, the mostly used Ti-based alloys are Ti-6Al-4V (composed of α and β phases) and Ti-40Nb (composed of β phase).[1,5,9-11] Both materials have found applications in many medical devices as biomaterials for orthopaedic implants because of their outstanding mechanical properties.[3] Nevertheless, these alloys face some undesired and unsolved problems. Ti-6Al-4V contains aluminium, which is known to cause certain bone diseases and neurological disorders.[13] and vanadium may become toxic at excessive concentration levels. The toxicity of vanadium is well-known, and can be exacerbated if the implant fractures and undergoes subsequently fretting.[4] Another major concern of Ti-6Al-4V is the mismatch between its Young's modulus (E = 110 – 120 GPa) and that of bone (E = 10 – 30 GPa)[14] that, as aforementioned, can cause implant failure.[15] In spite of the exceedingly low stiffness, Ti-40Nb shows good biocompatibility and possesses lower Young's modulus.[15-19] Therefore, it is of outmost importance to further search for novel bulk Ti-based materials which satisfy: (*i*) chemical composition containing neither toxic nor allergenic elements, and (*ii*) suitable microstructures that promote the targeted mechanical properties. In recent years, bulk metallic glassy alloys based on titanium have been developed.[20] The progress in the design of bulk metallic glasses has also led to progress in the development of new *in situ* formed nano-scale structured materials, which may exhibit even better mechanical performance than bulk metallic glasses and/or traditional commercial Ti-based alloys.[21,22] Considering the biomedical applications, we have focused on the development of new nano/ultrafine-structured Ti-based alloys free of any toxic or allergic elements (e.g. Ni, Cu, Al, V, etc.) and succeeded in finding compositions with superior mechanical properties. Here, the synthesis and characterization of a new Ti-based alloy composition (i.e., $Ti_{45}Zr_{15}Pd_{35-x}Si_5Nb_x$ with x = 0 and 5 at. %) in bulk form is reported. This particular composition (without Nb) had been previously synthesised in the form of melt-spun amorphous ribbons but not in bulk.[23] According to Oak et al. and Inoue, this alloy has the potential to be applied in the biomedical

field as an orthopaedic bone fixation device.[23] In our work, niobium was chosen to partially replace palladium for several reasons. First of all, Nb is much cheaper than Pd and it is a well-known non-toxic and non-allergic element.[24] Besides, addition of Nb promotes the formation of β-phase because it belongs to the β-stabilizer elements. In general, an increase in the amount of β-phase causes a decrease of the Young's modulus, an improvement of the alloy formability and an enhancement of the corrosion resistance.[25] Indeed, β-Ti alloys are better suited for biomedical applications than α-Ti alloys. Finally, it has been reported that Nb can be alloyed to Ti in order to reduce the Young's modulus without compromising the strength.[26,27] Our results reveal that the addition of Nb to $Ti_{45}Zr_{15}Pd_{35-x}Si_5$ brings about a reduction of Young's modulus while preserving reasonably high strength values and not causing detrimental effects on the alloy biocompatibility.

MATERIALS AND METHODS

Master alloys with composition $Ti_{45}Zr_{15}Pd_{35-x}Si_5Nb_x$ (where x = 0 and 5 at. %) were prepared by arc melting a mixture of the highly pure elements (> 99.99% wt. %) under a Ti-gettered Ar atmosphere on a water cooled Cu heart. Rods of 3 mm in diameter were obtained from the melt by suction casting into a Cu mould. The microstructures of as-cast samples were examined using a scanning electron microscope (SEM Zeiss Merlin), equipped with an energy dispersive X-ray detector (EDX, Oxford Instruments, INCA system). The samples were structurally characterised by X-ray diffraction (XRD) (Philips X'Pert diffractometer with monochromatic Cu-K_α radiation). MAUD (Material Analysis Using Diffraction) program based on the Rietveld method was applied to calculate lattice parameters from powder XRD. Transmission electron microscopy (TEM) (JEOL JEM 2011, 200 kV) was used for microstructure observations. Samples for TEM imaging were mechanically pre-thinned to 80 μm and afterwards the thickness was reduced to 30 μm by mechanical dimpling at one side of the samples. Finally, further thinning of the disks was carried out by ion beam milling at 4 keV at an incident angle of 5˚. The elastic properties were evaluated by ultrasonic measurements (pulse-echo overlap technique) along with density assessment (Archimedes' method). The mechanical properties of the as-cast Ti-Zr-Pd-Si-(Nb) alloys were determined by nanoindentation measurements using UMIS equipment from Fischer-Cripps laboratories,[28] equipped with a Berkovich pyramidal-shaped indenter tip. The thermal drift was always kept below ± 0.05 nm s^{-1}. Arrays of 50 and 100 indentations with maximum applied loads of 250 mN and 3 mN, respectively, were carried out to probe both the average and local mechanical behaviour of the samples and to verify the accuracy of the indentation data. Prior to

the nanoindentation tests, the specimens were carefully polished to mirror-like appearance using diamond paste. The method of Oliver and Pharr was used to determine the hardness and the reduced Young's modulus.[29] Finally, the elastic/total indentation energies were also calculated. The total mechanical work done by the indenter during loading, U_{tot}, was calculated from the area enclosed between the loading indentation segment and the displacement axis. This energy is the sum of the elastic, U_{el}, and the plastic, U_{pl}, energies:

$$U_{tot} = U_{el} + U_{pl} \quad (1)$$

where U_{el} is obtained from the area enclosed between the unloading segments and displacement axis.[30-32] The elastic recovery and plasticity index were evaluated from the U_{el}/U_{tot} and U_{pl}/U_{tot} ratios, respectively. The mechanical and elastic properties were compared with those of commercial Ti-40Nb alloy. The biological behavior of $Ti_{45}Zr_{15}Pd_{35-x}Si_5Nb_x$ (x = 0, 5 at. %) alloys were tested in cell culture, analyzing cell viability, morphology and adhesion. Alloy disks were glued individually onto a glass coverslip with silicone (Bayer), introduced into a 4-multiwell culture plate and sterilized under UV light for at least 2 h. Once sterilized, 50,000 cells from the human osteosarcoma cell line Saos-2 (ATCC) were cultured into each well in Dulbecco's modified Eagle medium (Invitrogen) with 10% foetal bovine serum (Gibco) in standard conditions (37°C and 5% CO_2) for 24 h. For all experiments three groups were analyzed: cells grown on top of the alloy disk, cells grown on the coverslip in presence of the alloy and cells grown in absence of the alloy (control culture). All experiments were conducted in triplicate. Cell viability was analysed by Live/Dead Viability/Cytotoxicity Kit for mammalian cells (Invitrogen), according to the manufacturer's protocol. Images from different regions of the alloy disk and its coverslip, and from the control culture were captured using an Olympus IX71 inverted microscope equipped with epifluorescence. A minimum of 200 cells were analyzed per group. Data were analysed for significance using the Fisher's exact test for comparison between groups. Statistical significance was considered when $p < 0.05$. For cell morphology analyses, cultured cells were rinsed twice in phosphate buffered saline (PBS), fixed in 4% paraformaldehyde (Sigma) in PBS for 45 min at room temperature (RT) and rinsed twice in PBS. Cell dehydration was performed in a series of ethanol (50, 70, 90 and twice 100%), 7 min each. Finally, samples were dried using hexamethyl disilazane (HMDS; Electron Microscopy Sciences) for 15 min, mounted on special stubs and analysed using SEM (Zeiss Merlin). Cell adhesion was determined by the presence of focal contacts. Phalloidin was used to visualize actin filaments whereas an antibody against vinculin was used to detect the focal contacts. Cells (50,000) were seeded into a

well containing an alloy and, after 24 h of culture cells were fixed in 4% paraformaldehyde in PBS for 45 min at RT, permeabilised with 0.1% Triton X-100 (Sigma) in PBS for 15 min and blocked for 25 min with 1% PBS-bovine serum albumin (Sigma) at RT. Samples were then incubated with a mouse anti-vinculin primary antibody (Chemicon) for 60 min at RT and washed with 1% PBS-BSA. Next, samples were incubated with a mixture of Alexa fluor 594-conjugated phalloidin (Invitrogen), Alexa fluor 488 goat anti-mouse IgG1 (Sigma) and Hoechst 33258 (Sigma) for 60 min at RT. Finally, samples were washed in 1% PBS-BSA and air dried. Samples were mounted on specific bottom glass dishes (MatTek) using Fluoroprep mounting solution (Biomerieux) and imaged in a confocal laser scanning microscope (Leica SP5).

RESULTS AND DISCUSSION

Microstructure

The XRD patterns of the as-cast (a) $Ti_{45}Zr_{15}Pd_{35}Si_5$ and (b) $Ti_{45}Zr_{15}Pd_{30}Si_5Nb_5$ alloys are shown in Fig. 1. The most intense XRD diffraction peaks belong to the cubic β-Ti phase (Im3m). The remaining peaks indicate the presence of the following phases: hexagonal α-Ti (P63/mmc), cubic TiPd (Pm3m), cubic PdZr (Fm3m), and hexagonal $(Ti,Zr)_5Si_3$ (P63/mcm) phases. Although the α- and β-Ti reflections are partially overlapped, the relative peak intensities do indicate that the β-Ti phase is predominant (cf. JCPDS 44-1288 and 23-1300). Notice also that most of the TiPd reflections are also overlapped with the β-Ti peaks.

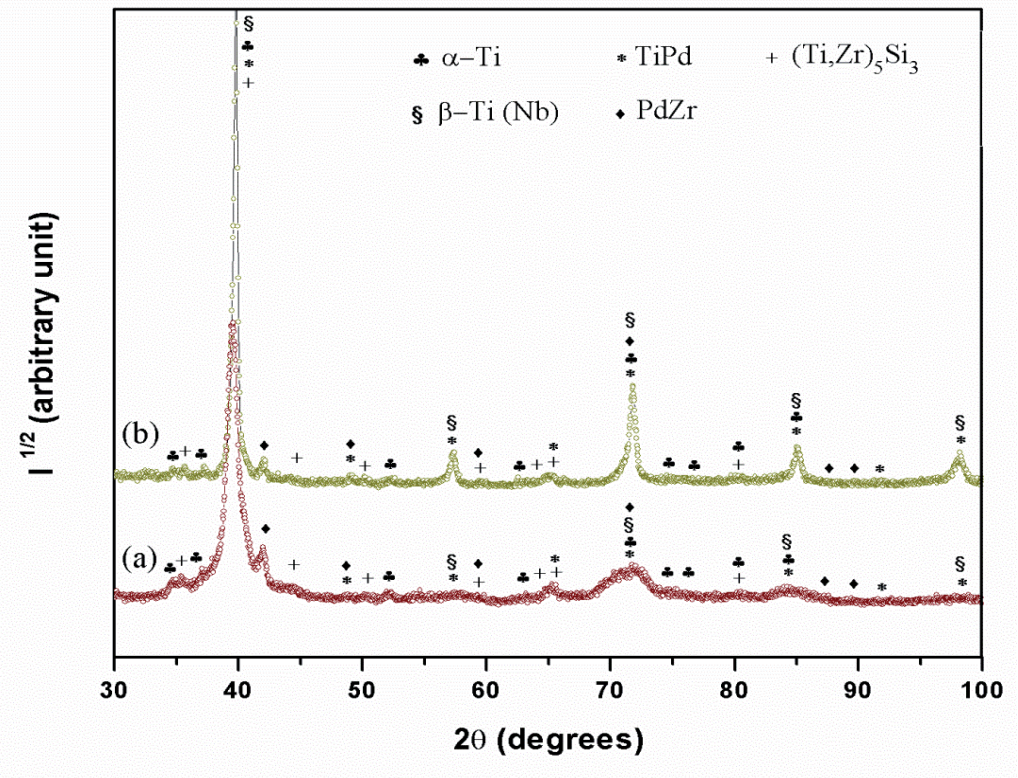

***Fig. 1**. X-ray diffraction patterns (XRD) corresponding to the as-cast (a) $Ti_{45}Zr_{15}Pd_{35}Si_5$ and (b) $Ti_{45}Zr_{15}Pd_{30}Si_5Nb_5$ alloys.*

Nevertheless, the peak located at 2θ = 48.87º which is univocally assigned to the TiPd phase, indicates that its phase amount is rather low. Although both patterns consist of the same phases, the reflections in the diffractogram of $Ti_{45}Zr_{15}Pd_{30}Si_5Nb_5$ are sharper and more intense, particularly those belonging to the β-Ti phase. This suggests the presence of bigger crystals (and lower microstrains) and possibly larger volume fraction of β-Ti. Taking into account the atomic radii of Ti (1.60 Å), Zr (1.75 Å), Pd (1.39 Å), Si (1.11 Å) and Nb (1.65 Å) and their percentages, the following considerations can be done. The tabulated lattice parameter of the β-Ti phase is considerably larger ($a_{tab.}$ = 3.30 Å) than the calculated value ($a_{cal.}$ = 3.212 Å), indicating the probable dissolution of Pd in the β-Ti cubic lattice. Moreover, the tabulated cell parameter of TiPd phases ($a_{tab.}$ = 3.19 Å) is slightly lower than the calculated one ($a_{cal.}$ = 3.22 Å). This difference can be explained by either the presence of substitutional Zr atoms in Ti positions or by slight variations in the stoichiometry (i.e., the concentration of Ti atoms is slightly larger than 1).Fig. 2 shows the SEM images (obtained using backscattered electrons) of the Ti-Zr-Pd-Si-(Nb) alloys. These materials exhibit similar composite-like microstructure with the presence of at least five different phases (see Fi. 3). The images are representative of the microstructure at the centre

of the discs and show four different regions with varying grey scale (from now on A-D), together with eutectic lamellae (from now on E). A zoomed detail of the eutectic matrix is provided as insets of Fig. 2(a, b). No significant differences were observed between $Ti_{45}Zr_{15}Pd_{35}Si_5$ and $Ti_{45}Zr_{15}Pd_{30}Si_5Nb_5$ alloys.

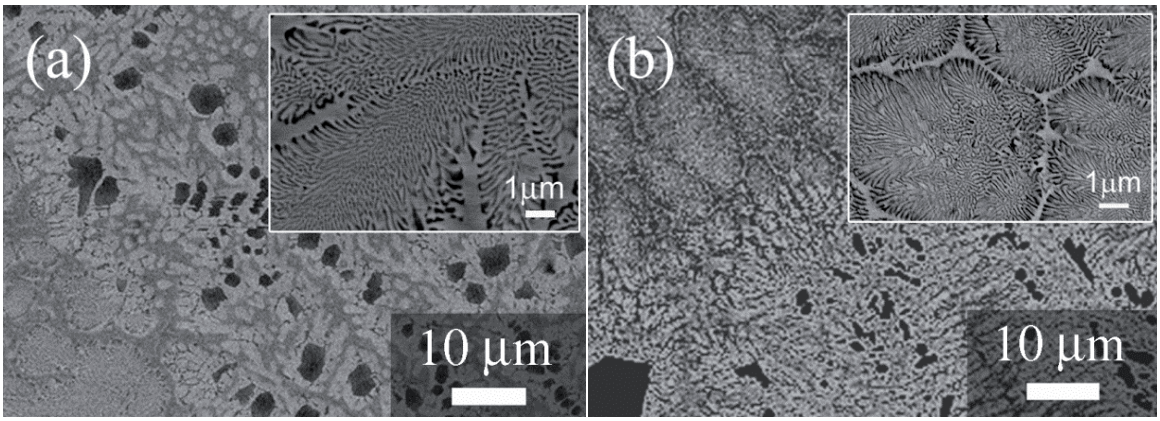

Fig. 2. *Scanning electron microscope (SEM) images (backscattered electrons) of the as-cast (a) $Ti_{45}Zr_{15}Pd_{35}Si_5$ and (b) $Ti_{45}Zr_{15}Pd_{30}Si_5Nb_5$ alloys taken at the centre of the discs. Shown as insets (a, b), are a zoomed detail of eutectic region.*

Energy dispersive x-ray (EDX) mapping analysis was performed on selected zones of the samples to determine the distribution of Ti, Zr, Pd, Si and Nb elements (Fig. 3a-d).

The EDX mapping of Ti-Zr-Pd-Si-(Nb) alloys (Fig. 3(a,c)) indicates that the light grey precipitates (zone A) are rich in palladium, whereas the black precipitates (zone B) are enriched in Zr, Si (and Nb in case of Ti-Zr-Pd-Si-Nb sample) (see Table I).

Ti is almost equally distributed everywhere, although a larger amount was found in the dark grey region (zone C) (Table I). On the other hand, the EDX mapping of eutectic regions in Ti-Zr-Pd-Si-(Nb) alloys (Fig. 3(b, d)) reveals that the interfaces between the eutectic domains (zone D) are rich in Zr, whilst larger amounts of Si (and Nb in case of Ti-Zr-Pd-Si-Nb sample) are concentrated within the eutectic lamellae (zone E). Unfortunately, for this sample, the EDX spot analyses were not conclusive because of its fine microstructure, so that very similar element percentages were observed in both regions, this is, the interfaces between the eutectic domains and eutectic lamellae.

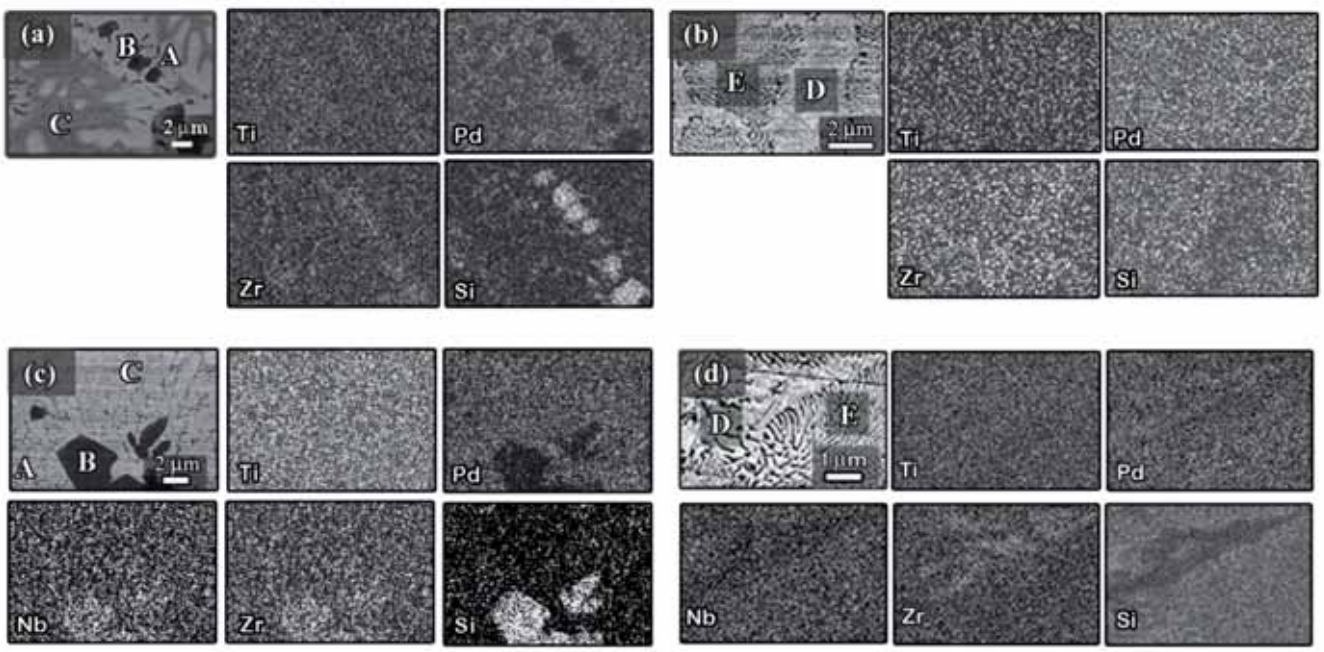

Fig. 3. *SEM (backscattered electrons) images and corresponding energy dispersive x-ray mapping of Ti, Zr, Pd, Si (and Nb) elements in* $Ti_{45}Zr_{15}Pd_{35}Si_5$ *and* $Ti_{45}Zr_{15}Pd_{30}Si_5Nb_5$ *discs taken at central part of the rod showing (a, c) A, B and C regions and (b, d) D, E regions.*

Taking XRD and EDX results of Ti-Zr-Pd-Si-(Nb) system into account, the following considerations can be made. As for the $Ti_{45}Zr_{15}Pd_{35}Si_5$ alloy is concerned, zone A likely corresponds to TiPd phase with Zr in solid solution. This is supported by both the smaller cell parameter of the TiPd phase compared with the tabulated value and the moderate content of Zr determined by EDX (Table I). Besides, zone B could be assigned to $(Ti, Zr)_5Si_3$ phase, whereas the zone C can be mainly linked to α- or β-Ti phases. For the $Ti_{45}Zr_{15}Pd_{30}Si_5Nb_5$ alloy, the zone D could belong to PdZr phase, while the other phases would be forming the surrounding eutectic domains (zone E).

Table I. *Energy dispersive X-ray (EDX) compositional analyses corresponding to the selected areas shown for as-cast $Ti_{45}Zr_{15}Pd_{35}Si_5$ alloy (Figure 3a, b) and $Ti_{45}Zr_{15}Pd_{30}Si_5Nb_5$ (Figure 3c, d). Data estimated with the error of 1-2 %.*

	Element concentration (at. %)								
	Ti-Zr-Pd-Si				**Ti-Zr-Pd-Si-Nb**				
	Ti	**Pd**	**Zr**	**Si**	**Ti**	**Pd**	**Zr**	**Si**	**Nb**
Nominal comp.	45	35	15	5	45	30	15	5	5
Zone(s)	**Fig. 3 (a)**				**Fig. 3 (c)**				
A	40	45	15	< 1	38	40	16	1	5
B	41	9	21	29	33	6	20	31	10
C	49	35	14	1	44	35	16	<1	4
Zone(s)	**Fig. 3 (b)**				**Fig. 3 (d)**				
D	43	32	24	<1	43	33	21	1	2
E	43	36	16	5	40	33	17	5	5

In order to gain deeper insight of the microstructure character of the eutectic region, the Ti-Zr-Pd-Si alloy was analysed by TEM (Fig. 4 (a)-(c)). Fig. 4(a) shows a TEM image of the eutectic lamellae.

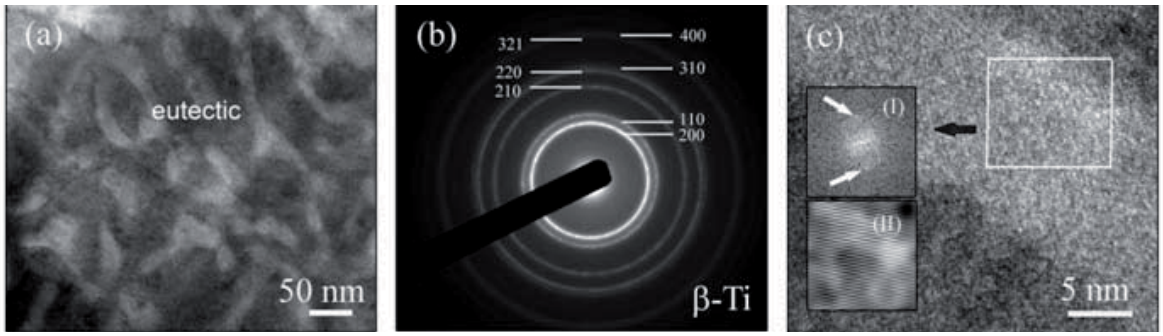

Fig. 4. *(a) Transmission electron micrograph (TEM) of the eutectic matrix in the $Ti_{45}Zr_{15}Pd_{35}Si_5$ alloy, (b) selected area electron diffraction pattern corresponding to the image (a), revealing the existence of β-Ti phase in eutectic matrix. (c) FFT (I) and Fourier filter reconstruction (II) of the crystal shown in the white box, which belongs to α-Ti. The arrows in (I) point to the diffraction spots.*

The selected area electron diffraction (SAED) patterns indicate that the eutectic colonies are composed of alternating Ti lamellae (see light grey lamellae in Fig. 4a and SAED pattern in Fig. 4b) and TiPd (dark grey lamellae in Fig. 4a, SAED pattern not shown). At higher magnification, small crystallites corresponding to α-Ti are also occasionally observed inside the light grey

lamellae (Fig. 4c). The FFT (I) and Fourier filter reconstruction (II) of one of these tiny crystals, belonging to α-Ti, are shown as insets in Fig. 4(c).

Mechanical characterization

Fig. 5 shows representative nanoidentation load-displacement (*P–h*) curves of the $Ti_{45}Zr_{15}Pd_{35}Si_5$, $Ti_{45}Zr_{15}Pd_{30}Si_5Nb_5$ and commercial Ti–40Nb alloys, measured to a maximum load of 250 mN. The Ti-40Nb alloy was used for a comparison aim. Indentations using such a high load are large enough to embrace all the existing phases (A-E), so that the obtained hardness values are representative of the average strength of the alloy. A typical indent made in $Ti_{45}Zr_{15}Pd_{35}Si_5$ is shown as an inset in Fig. 5.

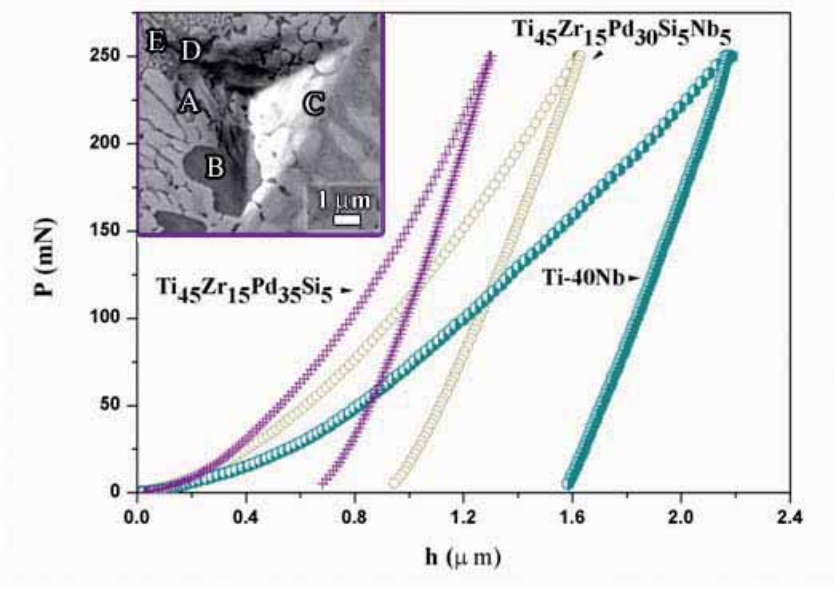

Fig. 5. *Load-displacement (P-h) nanoindentation curves for Ti-40Nb, $Ti_{45}Zr_{15}Pd_{35}Si_5$ and $Ti_{45}Zr_{15}Pd_{30}Si_5Nb_5$ alloys obtained applying a maximum force, ($P_{max.}$ = 250 mN). Shown in the inset is a backscattered SEM image of an indent performed on the $Ti_{45}Zr_{15}Pd_{35}Si_5$ alloy. It can be seen that the indent embraces all existing phases (A-E).*

Table II shows that the addition of Nb decreases the Young's modulus from about 117 GPa to a 85 GPa value, which is just slightly larger than the value of the commercial Ti-40Nb alloy (72 GPa). Ultrasonic measurements were performed to compare the values of Young's modulus with those of nanoindentation tests.

***Table II**. Summary of the mechanical properties (H, E_r, H/E_r, H^3/E^2_r, U_{el}/U_{tot}, and U_{pl}/U_{tot} denote hardness, reduced Young's modulus, elastic, plastic and total indentation energies, respectively), assessed by nanoindentation measurements, corresponding to the $Ti_{45}Zr_{15}Pd_{35}Si_5$, $Ti_{45}Zr_{15}Pd_{30}Si_5Nb_5$ alloys and Ti–40Nb ($F_{max.}$ = 250 mN).*

Sample	H (GPa)	E_r (GPa)	H/E_r	H^3/E_r^2 (GPa)	U_{el}/U_{tot}	U_{pl}/U_{tot}
$Ti_{45}Zr_{15}Pd_{35}Si_5$	14.2 ± 0.5	117 ± 5	0.122 ± 0.005	0.211 ± 0.030	0.586 ± 0.029	0.414 ± 0.021
$Ti_{45}Zr_{15}Pd_{30}Si_5Nb_5$	10.4 ± 0.3	85 ± 2	0.123 ± 0.003	0.156 ± 0.016	0.543 ± 0.017	0.475 ± 0.015
Ti-40Nb	2.7 ± 0.1	72 ± 1	0.038 ± 0.001	0.004 ± 0.001	0.225 ± 0.004	0.775 ± 0.013

Additionally, the other elastic properties values (the Poisson's coefficient (*v*), Young's modulus (*E*), shear modulus (*G*), and bulk modulus (*K*)) were also evaluated (Table III).

***Table III**. Summary of the elastic properties (v, E_{Acoust}, G and K denote the Poisson's coefficient, Young's modulus, shear modulus and bulk modulus, respectively) of the as-cast$Ti_{45}Zr_{15}Pd_{35-x}Si_5Nb_x$ (x=0, 5) alloys. Results for the commercial Ti–40Nb are shown for comparison purposes.*

Sample	*v*	$E_{Acoust.}$ (GPa)	G (GPa)	K (GPa)
$Ti_{45}Zr_{15}Pd_{35}Si_5$	0.405 ± 0.003	100.0 ± 0.1	30.1 ± 0.1	148.6 ± 0.7
$Ti_{45}Zr_{15}Pd_{30}Si_5Nb_5$	0.397 ± 0.001	87.3 ± 0.2	31.3 ± 0.1	139.5 ± 0.2
Ti-40Nb	0.403 ± 0.001	73.8 ± 0.1	26.3 ± 0.1	126.6 ± 0.1

The Young's modulus significantly decreases from 100 GPa for $Ti_{45}Zr_{15}Pd_{35}Si_5$ to 87.3 GPa for $Ti_{45}Zr_{15}Pd_{30}Si_5Nb_5$ alloy, in agreement with nanoindentation data. Besides the elastic modulus, the values of hardness were also determined by nanoindentation tests. Remarkably, both the $Ti_{45}Zr_{15}Pd_{35}Si_5$ and $Ti_{45}Zr_{15}Pd_{30}Si_5Nb_5$ alloys are significantly harder than Ti-40Nb (by a factor 5 and 4, respectively). The $Ti_{45}Zr_{15}Pd_{35}Si_5$ alloy is mechanically harder than the $Ti_{45}Zr_{15}Pd_{30}Si_5Nb_5$ and Ti-40Nb alloys, as can be deduced from (*P*–*h*) curve from the smallest values of penetration depth using force of 250 mN (Fig. 5). It is worth mentioning that the hardness of $Ti_{45}Zr_{15}Pd_{35}Si_5$ and $Ti_{45}Zr_{15}Pd_{30}Si_5Nb_5$ alloys are also larger than that of Ti–39.3Nb–13.3Zr–10.7Ta and Ti–31.0Fe–9.0Sn alloys, which has been previously investigated as suitable material for bone replacement due to its good mechanical properties.[33] Difference in the mechanical response between $Ti_{45}Zr_{15}Pd_{35}Si_5$ and $Ti_{45}Zr_{15}Pd_{30}Si_5Nb_5$ alloys can be explained by the relative fraction of bcc β phase, the chemical composition and the difference in crystal size. In particular, $Ti_{45}Zr_{15}Pd_{30}Si_5Nb_5$ alloy has larger fraction of bcc β phase and larger crystal sizes, resulting in lower hardness than for $Ti_{45}Zr_{15}Pd_{35}Si_5$. In materials with small crystallites, the grain boundaries hinder the dislocation motion and increase the stress concentration and dislocation pile up at the

grain boundaries, ultimately leading to increased hardness.[4] Niobium is considered to be the strongest beta stabilizer, effectively decreasing Young's modulus of titanium alloys.[35] In fact, the Young's modulus of commercial Ti-40Nb, composed only of β-Ti, is the lowest among the examined alloys. According to Abdi et al.,[36] addition of Nb to $(Ti,Zr)_5Si_3$ phase causes a local decrease of E_r as compared to the Nb-free alloy. This is to some extend expected since the Young's modulus of Nb is lower than that of Ti. Listed in Table II are the ratios of H/E_r and H^3/E_r^2 for all investigated alloys. These parameters are associated with wear resistance and are important to estimate the lifetime of the implant. H/E_r indicates the elastic strain to failure[37] while H^3/E_r^2 is related to the resistance of a material to plastic deformation in loaded contact.[38] Due to large hardness and relatively low values of Young's modulus of $Ti_{45}Zr_{15}Pd_{35}Si_5$ and $Ti_{45}Zr_{15}Pd_{30}Si_5Nb_5$, the values of H/E_r and H^3/E_r^2 are almost twice larger than those of Ti-40Nb. In fact, the elastic recovery, U_{el}/U_{tot}, is also higher in the new Ti-Zr-Pd-Si-(Nb) system. Hence, these materials would be more resistant to impact loading than Ti–40Nb.[39] With the aim to study the contribution of the individual phases or regions, to the overall mechanical response, nanoindentation tests applying a maximum load of 3 mN were carried out for $Ti_{45}Zr_{15}Pd_{35}Si_5$ sample.

Table IV. *The mean values of hardness (H) and reduced Young's modulus (E_r) calculated for the indents in different regions in $Ti_{45}Zr_{15}Pd_{35}Si_5$ [see examples in Fig. 6 (a)-(d)]. The mean values of H and E_r are the result of 10 nanoindentation tests in each region.*

Specified area of nanoindents	H (GPa)	E_r (GPa)
Fig 6 (**a**) – light grey precipitates (zone A)	8.9 ± 0.3	104.3 ± 2.1
Fig 6 (**b**) – black precipitates (zone B)	13.7 ± 1.5	135.5 ± 2.6
Fig 6 (**c**) – grey area between the eutectic domains (zone C)	10.1 ± 0.5	122.0 ± 2.8
Fig 6 (**d**) – eutectic lamellae (zone E)	9.7 ± 0.7	109.3 ± 2.6

The mean values of hardness (H) and reduced Young's modulus (E_r) corresponding to the different regions (A-D) are listed in Table IV. SEM images of representative indents on each region are presented in Fig. 6 (a)-(d).

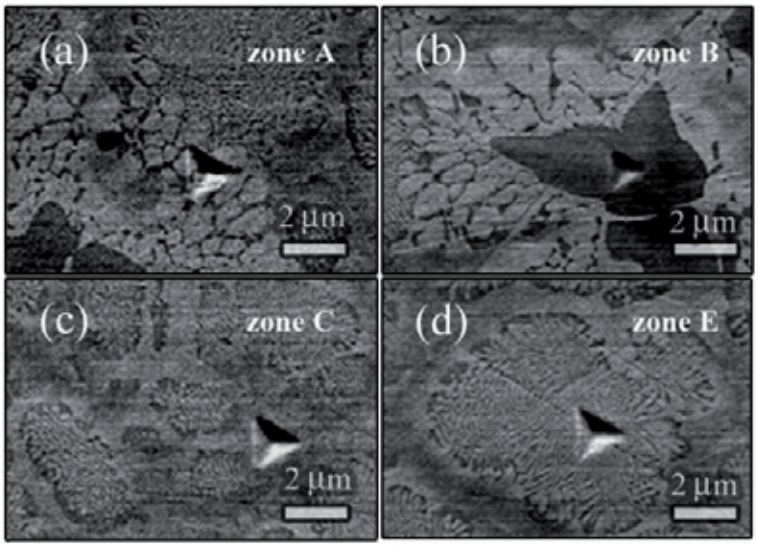

Fig. 6. *Representative SEM (backscattered electrons) images belonging to $Ti_{45}Zr_{15}Pd_{35}Si_5$ composition. Shown in the pictures [(a)-(d)] are the indents inside: (a) the light grey precipitates, (b) black precipitates, (c) grey area between the eutectic domain and (d) the eutectic lamellae, (P_{Max} = 3mN). The size of the imprints on the D regions were larger than the actual size of the region and therefore the corresponding SEM image is not presented.*

The size of indents is different, being that on the zone B (Fig. 6b), the smallest. The values of hardness for the light grey precipitates (Figure 6a), black precipitates (Fig. 6b) grey area between the eutectic domains (Fig. 6c) and eutectic lamellae (Fig. 6d), are equal to 8.9 GPa, 13.7 GPa, 10.1 GPa and 9.7 GPa, respectively (Table IV). The black precipitates are mechanically harder presumably due to the presence of the intermetallic $(Ti,Zr)_5Si_3$ phase. In fact, the hardness of $(Ti, Zr)_5Si_3$ phase has been reported to be 13.7 GPa in Abdi's study.[36] Besides, comparable hardness values were reported by Mitra.[40] Nevertheless, depending on the crystal size the values can slightly vary. For instance, hardness of 12.7 GPa stands for crystal size between 5 to 10 μm, while for smaller crystals (1-2 μm), the hardness values increase up to 17.2 GPa.[40] On the contrary, the hardness of the light grey precipitates (TiPd phase) and eutectic lamellae (phase mixture), are the lowest among all phases (Table IV). Additional consideration can be made on the Young's modulus of white precipitates (TiPd phase) and eutectic lamellae. According to the literature, the calculated Young's modulus of Ti-Pd phase is 80 GPa.[41,42] However, this value increases when it comes to the light grey precipitates region (104 GPa), composed of TiPd phase. This can be explained by the co-existence of α-Ti, which has larger Young's modulus (120 GPa) within this region. Zone C (Fig. 6c) which is composed mainly of α-Ti phase exhibits a Young's

modulus of 120 GPa. On the contrary, the value of the eutectic is found to be experimentally equal to 110 GPa, which can be attributed to the large amounts of inter-phase boundaries existing in the eutectic regions, as a consequence of phase mixture (Fig. 6d).

Biocompatibility

Cultured human Saos-2 cells were distributed randomly onto the metal alloys and coverslips. The percentage of live cells was higher than 94 % in all groups, and no significant differences were observed between the two alloy compositions, or between them and the coverslip and control plate (Fig. 7).

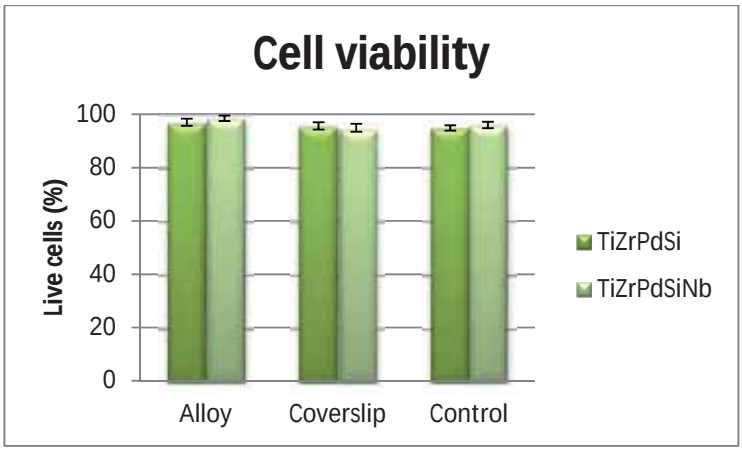

Fig. 7. *Mean percentage of live cells attached to the surface of the tested alloys, their coverslips and in control cultures.*

These results indicate that the addition of Nb to the alloy composition does not cause any cytotoxic effect, in agreement with the observations done by other authors.[43,44] After 24 h of culture, the cells were attached to the surface of $Ti_{45}Zr_{15}Pd_{35}Si_5$ and $Ti_{45}Zr_{15}Pd_{30}Si_5Nb_5$ alloys and of coverslips, and showed a similar morphology under SEM. Cell density was similar in all cultures analysed and in all cases the cells showed a flattened polygonal morphology with nuclei presenting several nucleoli (Fig. 8), an indication of high cellular activity. The actin cytoskeleton structure and its involvement in focal contacts are key to maintain cell adhesion, but also for cell proliferation and differentiation. In this sense, the formation of focal contacts on the surface of the alloy gives information about its biocompatibility.

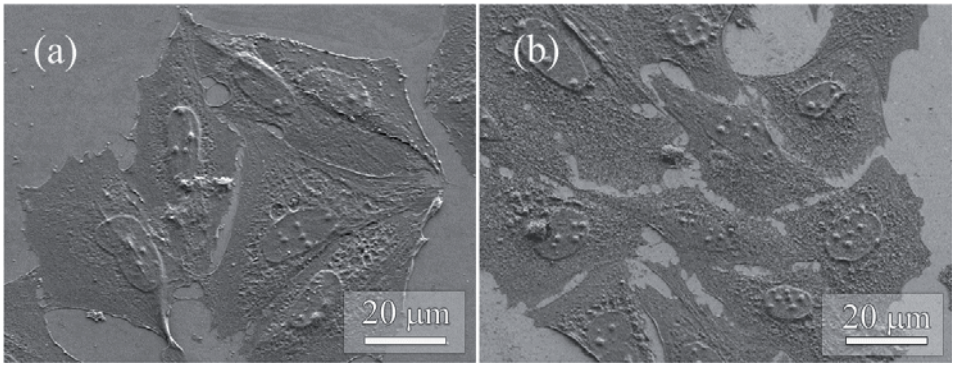

Fig. 8*. SEM images of Saos-2 cells on the surface of alloy disks; (a) $Ti_{45}Zr_{15}Pd_{35}Si_5$ and (b) $Ti_{45}Zr_{15}Pd_{30}Si_5Nb_5$. Flattened cells with polygonal morphologies showing nuclei with several nucleoli can be observed in all cases.*

Focal contact analysis showed that Saos-2 cells were completely adhered to the surface of the two alloyed compositions (Fig. 9) and coverslips. Actin stress fibres were well-defined in all cases, and some of them extended across the cell and ended in focal contacts. The results indicate that $Ti_{45}Zr_{15}Pd_{35}Si_5$ and $Ti_{45}Zr_{15}Pd_{30}Si_5Nb_5$ alloys allow cell adhesion, in agreement with other studies of biocompatible bulk metallic glasses.[45,46]

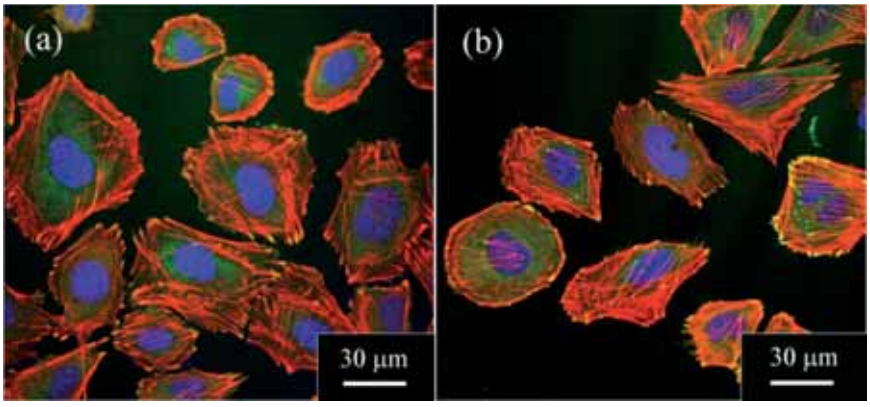

Fig. 9. *Cells adhered on the surface of the alloys. (a) $Ti_{45}Zr_{15}Pd_{35}Si_5$ and (b) $Ti_{45}Zr_{15}Pd_{30}Si_5Nb_5$. Stress fibres (actin; red), focal contacts (vinculin; green) and nuclei (DNA; blue) can be observed.*

Furthermore, the formation of focal contacts on the two alloys suggests that ECM proteins, necessary for cell adhesion, can be adsorbed on the alloy surface.[47]

CONCLUSIONS

The microstructure and mechanical properties of nanostructured $Ti_{45}Zr_{15}Pd_{35-x}Si_5Nb_x$ with x = 0, 5 (at. %) alloys have been investigated and compared to those of commercial Ti-40Nb. Both Ti-Zr-Pd-Si-(Nb) rods show a composite-like microstructure consisting of several phases: a predominant β-Ti and additional phases (TiPd, PdZr, α-Ti and $(Ti, Zr)_5Si_3$ intermetallics) in smaller volume fraction, as identified by XRD, SEM and TEM analyses. In terms of mechanical behaviour, nanoindentation experiments reveal that the $Ti_{45}Zr_{15}Pd_{30}Si_5Nb_5$ alloy exhibits lower Young's modulus and hardness than $Ti_{45}Zr_{15}Pd_{35}Si_5$ ($E_{rTi\text{-}Zr\text{-}Pd\text{-}Si} \approx 117$ GPa and $E_{rTi\text{-}Zr\text{-}Pd\text{-}Si\text{-}Nb} \approx 85$ GPa). This can be explained by the relative amount of β phase in both alloys and the differences in the mean crystal size values. Remarkably, both alloys exhibit larger values of hardness, wear resistance and elastic recovery than commercial Ti-40Nb, ($H_{Ti\text{-}Zr\text{-}Pd\text{-}Si} \approx 14.2$ GPa, $H_{Ti\text{-}Zr\text{-}Pd\text{-}Si\text{-}Nb} \approx 10.4$ GPa and $H_{Ti\text{-}40Nb} \approx 2.7$ GPa. Hence, the newly developed $Ti_{45}Zr_{15}Pd_{35-x}Si_5Nb_x$ alloys with x = 0, 5 (at. %) are interesting for biomedical applications because they combine relatively low Young's modulus (particularly in $Ti_{45}Zr_{15}Pd_{30}Si_5Nb_5$) with large values of hardness. Additionally, the biological compliance with body system (cell culture, cell viability and cell adhesion) of these two alloys was analysed. Preliminary results of cell viability performed on several Ti-Zr-Pd-Si-(Nb) discs indicate that the number of live cells is superior to 94 % in both cases. From these outstanding mechanical properties and the excellent biocompatibility these alloys turn out to have a large potential to be used as permanent implants for bone replacement.

ACKNOWLEDGEMENTS

The authors wish to thank E. Rossinyol, M. Stoica, S. Donath, S. Abdi and Servei de Microscòpia of the Universitat Autònoma de Barcelona for helpful discussions and for technical support. Funding by the European Commission within the framework of the FP7-ITN network BioTiNet (FP7-PEOPLE-2010-ITN-264635). We also acknowledge the Catalan DGR (2014-SGR-1015 and 2014-SGR-524), the Spanish MICINN (MAT2011-27380-C02-01 and TEC2011-29140-C03-03). E.P. is grateful to MINECO for the 'Ramon y Cajal' contract (RYC-2012-10839). M.D.B. acknowledges partial financial support from an ICREA-Academia Award.

REFERENCES

1. Viteri VS, Fuentes E. Titanium and Titanium Alloys as Biomaterials. In: Jürgen Gegner, editor. Tribology – Fundamentals and Advancements, INTECH, InTech: Rijeka, Croatia, Chapter 5. 2013, p.155-181.

2. Liu X, Chu P, Ding C. Surface modification of titanium, titanium alloys, and related materials for biomedical applications. Mater Sci Eng R Reports 2004;47:49–121.

3. Geetha M, Singh AK, Asokamani R, Gogia AK. Ti based biomaterials, the ultimate choice for orthopaedic implants – A review. Prog Mater Sci 2009;54:397–425.

4. Mudali UK, Sridhar TM, Raj B. Corrosion of bio implants. Sadhana 2003;28:601–637.

5. Niinomi M. Mechanical biocompatibilities of titanium alloys for biomedical applications. J Mech Behav Biomed Mater 2008;1:30–42.

6. Long M, Rack HJ. Titanium alloys in total joint replacement – a materials science perspective. Materials 1998;19:1621–1639.

7. Wang Y, Chen M, Zhou F, Ma E. High tensile ductility in a nanostructured metal. Nature 2002;419:912–915.

8. Sivakumar M, Kamechi Mudali U, Rajeswali S. In vitro electrochamical investigations of stainless steel for orthopeadic implants applications. J Mater Eng Perform 1994;3:744–759.

9. Hynowska A, Blanquer A, Pellicer E, Fornell J, Suriñach S, Baró M, González S, Ibáñez E, Barrios L, Nogués C, Sort J. Novel Ti–Zr–Hf–Fe Nanostructured Alloy for Biomedical Applications. Materials 2013;6:4930–4945.

10. Niinomi M, Nakai M, Hieda J. Development of new metallic alloys for biomedical applications. Acta Biomater 2012;8:3888–3903.

11. Raju A. Effect of equal channel angular extrusion on the shape memory property of Ti-Nb Alloys – doctoral thesis. Korea Advanced Institute of Science and Technology; South Korea, 2010.

12. Wills M, Savory J. Aluminium poisoning: dialysis, encephalopathy, osteomalacia, and anaemia. Lancet 1983;2:29–34.

13. Fornell J, González S, Pellicer E, Van Steenberge N, Pérez P, Suriñach S, Baró MD, Sort J. Deformation and fracture behavior of corrosion-resistant, potentially biocompatible, $Ti_{40}Zr_{10}Cu_{38}Pd_{12}$ bulk metallic glass. J Alloys Compd 2012;536:S74–S77.

14. Calin M, Gebert A, Ghinea AC, Gostin PF, Abdi S, Mickel C, Eckert J. Designing biocompatible Ti-based metallic glasses for implant applications. Mater Sci Eng C 2013;33:875–883.

15. Ozaki T, Matsumoto H, Watanabe S, Hanada S. Beta Ti alloys with low Young's modulus. Mater Trans 2004;45:2776–2779.

16. Hao YL, Niinomi M, Kuroda D, Fukunaga K, Zhou YL, Yang R, Suzuki A. Young's modulus and mechanical properties of Ti-29Nb-13Ta-4.6Zr in relation to α′′ martensite. Metall Mater Trans A 2002;33:3137–3144.

17. Kuroda D, Niinomi M, Morinaga M, Kato Y, Yashiro T. Design and mechanical properties of new β type titanium alloys for implant materials. Mater Sci Eng A 1998;243:244–249.

18. Hanada S, Matsumoto H, Watanabe S. Mechanical compatibility of titanium implants in hard tissues. Int Congr Ser 2005;1284:239–247.

19. Ma C, Soejima H, Ishihara S, Amiya K, Nishiyama N, Inoue A. New Ti-Based Bulk Glassy Alloys with High Glass-Forming Ability and Superior Mechanical Properties. Mater Trans 2004;45:3223–7.

20. Wang WH, Dong C, Shek CH. Bulk metallic glasses. Mater Sci Eng R Reports. 2004;44:45–89.

21. He G, Eckert J, Löser W, Schultz L. Novel Ti-base nanostructure-dendrite composite with enhanced plasticity. Nat Mater 2003;2:33–37.

22. Weertman JR, Farkas D, Hemker K, Kung H, Mayo M, Mitra R VSH. Structure and Mechanical Behavior of Bulk Nanocrystalline Materials. Mech Behav Nanostructured Mater. 1999;24:44–53.

23. Oak J-J, Inoue A. Formation, mechanical properties and corrosion resistance of Ti–Pd base glassy alloys. J Non Cryst Solids 2008;354:1828–1832.

24. Li Y, Yang C, Zhao H, Qu S, Li X, Li Y. New developments of Ti-based alloys for biomedical applications. Materials 2014;7:1709–1800.

25. Niinomi M. Recent research and development in titanium alloys for biomedical applications and healthcare goods. Sci Technol Adv Mater 2003;4:445–454.

26. Gabriel SB, Panaino JVP, Santos ID, Araujo LS, Mei PR, Almeida LH, Nunes CA. Characterization of a new beta titanium alloy, Ti–12Mo–3Nb, for biomedical applications. J Alloys Compd 2012;5365:S208–S210.

27. Song Y, Xu DS, Yang R, Li D, Wu WT, Guo ZX. Theoretical study of the effects of alloying elements on the strength and modulus of β-type bio-titanium alloys. Mater Sci Eng A 1999;260:269–274.

28. Fischer-Cripps AC. Nanoindentation; Mechanical Engineering Series. Third. New York: Springer; 2011.

29. Oliver WC, Pharr GM. An improved technique for determing hardness and elastic modulus. J Mater Res 1992;7:1564–1583.

30. Pellicer E, Varea A, Pané S, Nelson BJ, Menéndez E, Estrader M, Suriñach S, Baró MD, Nogués J, Sort J. Nanocrystalline electroplated Cu–Ni: metallic thin films with enhanced mechanical properties and tunable magnetic behavior. Adv Funct Mater 2010;20:983–991.

31. Bao YW, Wang W, Zhou YC. Investigation of the relationship between elastic modulus and hardness based on depth-sensing indentation measurements. Acta Mater 2004;52:5397–5404.

32. Wang WH, Dong C, Shek CH. Bulk metallic glasses. Mater Sci Eng R Reports 2004;44:45–89.

33. Hynowska A, Pellicer E, Fornell J, González S, van Steenberge N, Suriñach S, Gebert A, Calin M, Eckert J, Baró MD, Sort J. Nanostructured β – phase Ti–31.0Fe–9.0Sn and sub – μm structured Ti–39.3Nb–13.3Zr–10.7Ta alloys for biomedical applications: Microstructure benefits on the mechanical and corrosion performances. Mater Sci Eng C 2012;32:2418–2425.

34. Hall EO. The deformation and ageing of mild steel III, Discussion of results. Proc Phys Soc. 1951;64:747–753.

35. Brailovski V, Prokoshkin S, Gauthier M, Inaekyan K, Dubinskiy S, Petrzhik M, Filonov M. Bulk and porous metastable beta Ti–Nb–Zr-(Ta) alloys for biomedical applications. Mater Sci Eng C 2011;31:643–657.

36. Abdi S, Khoshkhoo MS, Shuleshova O, Bönisch M, Calin M, Schultz L, Eckert J, Baró MD, Sort J, Gebert A. Effect of Nb addition on microstructure evolution and nanomechanical properties of a glass-forming Ti–Zr–Si alloy. Intermetallics 2014;46:156–163.

37. Leyland A, Matthews A. On the significance of the H/E ratio in wear control: a nanocomposite coating approach to optimised tribological behaviour. Wear 2000;246:1–11.

38. Musil J, Kunc F, Zeman H, Poláková H. Relationships between hardness, Young's modulus and elastic recovery in hard nanocomposite coatings. Surf Coat Technol 2002;154:304–313.

39. Milman YV. Plasticity characteristic obtained by indentation. J Phys D Appl Phys 2008;41:074013.

40. Mitra R. Microstructure and mechanical behavior of reaction hot – pressed titanium silicide and titanium silicide – based alloys and composites. Metall Mater Trans A 1998;29:1629–1641.

41. Bihlmayer G, Eibler R, Neckel A. Martensitic phase transformation and electronic structure of NiTi and PdTi. Philos Mag Part B 1996;73:511–524.

42. Chen X-Q, Fu CL, Morris JR. The electronic, elastic, and structural properties of Ti–Pd intermetallics and associated hydrides from first principles calculations. Intermetallics 2010;18:998–1006.

43. Miura K, Yamada N, Hanada S, Jung T-K, Itoi E. The bone tissue compatibility of a new Ti-Nb-Sn alloy with a low Young's modulus. Acta Biomater 2011;7:2320–2326.

44. Silva LM, Claro APRA, Donato TAG, Arana-Chavez VE, Moraes JCS, Buzalaf MAR, Grandini CR. Influence of heat treatment and oxygen doping on the mechanical properties and biocompatibility of titanium-niobium binary alloys. Artif Organs 2011;35:516–521.

45. Blanquer A, Pellicer E, Hynowska A, Barrios L, Ibáñez E, Baró MD, Sort J, Nogués C. In vitro biocompatibility assessment of $Ti_{40}Cu_{38}Zr_{10}Pd_{12}$ bulk metallic glass. J Mater Sci Mater Med 2013;25:163–172.

46. Huang L, Cao Z, Meyer HM, Liaw PK, Garlea E, Dunlap JR, Zhang T, He W. Responses of bone-forming cells on pre-immersed Zr-based bulk metallic glasses: Effects of composition and roughness. Acta Biomater 2011;7:395–405.

47. Bacakova L. Modulation of cell adhesion, proliferation and differentiation on materials designed for body implants. Biotechnol Adv 2011;29:739–767.

General Conclusions

Four Ti-based nanostructured alloys with nominal composition, **Ti-44.3Nb-8.7Zr12.3Ta (wt. %)**, **Ti-31.0Fe-9.0Sn (wt. %)**, **$Ti_{40}Zr_{20}Hf_{20}Fe_{20}$ (at. %)**, **$Ti_{45}Zr_{15}Pd_{35-x}Si_5Nb_x$ (x = 0, 5 at. %)**, and one Ti-based BMG, **$Ti_{40}Zr_{10}Cu_{38}Pd_{12}$ (at. %)**, were investigated in this Thesis. These Ti-based materials were chosen due to their potential applications as orthopedic implants. The first part of our study focused on the synthesis and characterization of all these alloys paying special attention to the correlation triangle microstructure-mechanical behavior-biocompatibility. The second part was devoted to ion-irradiation treatment of the bulk metallic glasses (BMGs) as a means to modify the surface properties and therefore increase the biomechanical compatibility of these BMGs. The main outcomes of this work can be summarized as follows:

(I) Novel nanostructured alloys with superior performance have been synthesized by copper mould casting technique.

(II) All studied alloys exhibit better wear resistance than that of commercially used Ti-6Al-4V.

(III) The Ti-Zr-Nb-Ta nanostructured alloy is appealing because of its low Young's modulus (E_r = 71 GPa), whereas the Ti-Fe-Sn system is interesting because of its large hardness (H = 8.9 GPa). Meanwhile Ti-Zr-Pd-Si-Nb alloys possess relatively low Young's modulus (E_r = 85 GPa) and high hardness (H = 10.4 GPa).

(IV) The lowering of Young's modulus and the increase in hardness was achieved through proper combination of β-stabilizer elements (Nb, Ta, Fe and Pd) alloyed with Ti.

(V) Replacement of Pd by Nb is a convenient strategy to decrease the Young's modulus (almost a drop up to 30% in E_r was observed) of the Ti-Zr-Pd-Si system, and also to reduce costs.

(VI) A microstructure consisting of a mixture of nanophases gives rise to large hardness values, as is the case of Ti-Zr-Pd-Si-(Nb) and Ti-Zr-Hf-Fe alloys.

(VII) None of the studied alloys showed extensive corrosion damage when tested electrochemically, although pitting was observed in $Ti_{40}Zr_{10}Cu_{38}Pd_{12}$.

(VIII) In terms of biocompatibility, the $Ti_{40}Zr_{20}Hf_{20}Fe_{20}$ alloy is not cytotoxic and mouse preosteoblast cells can easily adhere onto its surface and differentiate into osteoblasts.

(IX) The number of human osteosarcoma live cells in contact with Ti-Zr-Pd-Si-(Nb) alloys was superior to 94%. This is due, to some extent, to the presence of safe (i.e., non-toxic) elements in the alloys' composition.

(X) The use of ion irradiation combined with annealing treatment seems to be a proper way to induce decomposition/nanocrystallization at surface level in BMGs, which further positively influences their mechanical behavior (E_r and H) and corrosion resistance.

Future Perspectives

Although this Thesis greatly contributes to the progress in the field of nanostructured alloys and BMGs for biomedical applications in several aspects, there is still room to explore.

- The fabrication of porous materials is currently a cutting-edge topic and different approaches have been devised to prepare them (either porous surface materials or metallic foams). However, little is known about nanoporosity induced in Ti-based BMGs. Therefore, fabrication of nanoporous surfaces by electrochemical oxidation (e.g. in NaOH) of Ti-based Ti-Zr-Cu-Pd bulk metallic glass and nanostructured Ti-Zr-Pd-Si-(Nb) alloy appears to be a hot topic which deserves investigation. Also appealing is the development of fully porous metallic foams. The correlation between surface morphology (i.e., pore architecture), mechanical properties and cell adhesion could be studied and hopefully contribute to solve common problems (e.g., implant adhesion) encountered in tissue engineering applications. Furthermore, the overall reduction of the Young's modulus in bulk porous alloys would enhance the biomechanical compatibility between the implant and bone.

- It is known that surface hardening is a suitable means to improve wear resistance, to increase surface strength for load carrying, to induce suitable residual and compressive stresses and to improve fatigue life and/or impact resistance. Recently, researchers have demonstrated an increased interest in laser treatments on polycrystalline materials. With this technique one can adjust the strengthening effect by accurately selecting the working parameters. Moreover, it is not a time-consuming technique and it is a well-established method in the industry. On the other hand, a considerable amount of literature has been published on laser peening. Such studies reported an increase in hardness and better fatigue performance on peened surfaces [207–210]. Changes induced by shot and laser peening have been compared in various studies [207, 211]. The results reveal that laser peening can induce deeper compressive residual stress fields making metallic materials with better fatigue resistance. This method was already applied in the Group to modify the surface of Ti-Zr-Cu-Pd alloy [212]. Therefore, laser treatments could be applied to the surface of Ti-Zr-Cu-Pd alloy in order to compare the surface morphological, structural and mechanical changes with those induced by both ion irradiation and shot peening.

- The further substitution of Pd by higher amount of Nb in Ti_{45}-Zr_{15}-$Pd_{35-x}Si_5$-Nb_x alloys could be tackled in order to reduce production costs and further improve mechanical properties (Young's modulus, strength etc.) and corrosion resistance.

- Compression tests on Ti-Zr-Hf-Fe and Ti-Zr-Pd-Si-(Nb) alloys could be performed in order to complete the overall mechanical characterization and therefore establish if the material meets all the requirements that apply in biomaterials for orthopedic purposes.

- So far, the biocompatibility assays of Ti-Zr-Hf-Fe alloy were conducted using MC3T3-E1 mouse preosteblasts. Additional biological tests using human cells would be worth carrying out, since this alloy is intended to replace human bones.

- Finally, machining strategies of the rod-like specimens into real implant shapes, while avoiding undesirable changes into the materials' properties, should be explored.

REFERENCES

1. Liu, X.; Chu, P.K.; Ding, C. Surface modification of titanium, titanium alloys, and related materials for biomedical applications. *Mater. Sci. Eng. R Reports* **2004**, 47, 49–121.

2. Viteri, V.S.; Fuentes, E. Titanium and Titanium Alloys as Biomaterials. In: *Tribology-Fundamentals and Advancements*; Gegner, J., (Ed.); INTECH: Rijeka, Croatia, **2013**; Chapter 5, pp. 155–181.

3. Hansen, D.C. Metal Corrosion in the Human Body: The ultimate bio-corrosion scenario. *Interface* **2008**, 17, 31–34.

4. Orthoworld. *The Orthopaedic Industry Annual Report*, **2013**, (available at www.orthoworld.com).

5. Geetha, M.; Singh, A.K.; Asokamani, R.; Gogia, A.K. Ti based biomaterials, the ultimate choice for orthopaedic implants – A review. *Prog. Mater. Sci.* **2009**, 54, 397–425.

6. Karimi, S. *Corrosion behavior of metallic bio-implant alloys*. Ph.D Thesis, University of British Columbia, Vancouver, Canada, **2014**.

7. Sivakumar, M.; Rajeswari, S. Investigations of failures in stainless steel orthopeadic implants devices: Pit induced stress corrosion cracking. *J. Mater. Sci.* **1992**, 11, 1039–1042.

8. Silver, F.; Doillon, C. *Biocompatibility: Interactions of Biological and Implantable Materials*, 1st ed.; VCH Publishers Inc.: NY, USA, **1989**.

9. Disegi, J.A; Kennedy, R.L.; Pillar, R., (Eds.). *Cobalt-based alloys for biomedical applications*; ASTM International: PA, USA, **1999**.

10. Jakobsen, S.S. et al. Effects of as-cast and wrought Cobalt-Chrome-Molybdenum and Titanium-Aluminium-Vanadium alloys on cytokine gene expression and protein secretion in J774A.1 macrophages. *Eur. Cell. Mater.* **2007**, 14, 45–55.

11. Berlin, R.M.; Gustavson, L.J; Wang, K.K. Influence of post-processing on the mechanical behavior of investment cast and wrought Co-Cr-Mo alloys. In: *Cobalt-based alloys for biomedical applications*; Disegi, J.A.; Kennedy, R.L.; Pillar, R. (Eds.); ASTM International: PA, USA, **1999**.

12. Dobbs, H.S.; Robbinson, J.L.M. Heat treatment of cast Co-Cr-Mo alloys for orthopeadic implant use. *J. Mater. Sci.* **1983**, 18, 391–401.

13. Hanawa, T. Metal ion release from metal implants. *Mater. Sci. Eng. C* **2004**, 24, 745–752.

14. Revell, P.A., (Ed.). *Joint Replacement Technology*; CRS Press: NY, USA, **2008**.

15. Boyer, R.; Welsch, G.: Colling, E.W. (Eds.). *Materials Properties Handbook: Titanium Alloys*; ASM International: OH, USA, **1994**.

16. Niinomi, M. Mechanical biocompatibilities of titanium alloys for biomedical applications. *J. Mech. Behav. Biomed. Mater.* **2008**, 1, 30–42.

17. Lautenschlager, E.P.; Monaghan, P. Titanium and titanium alloys as dental materials. *Int. Dent. J.* **1993**, 43, 245-253.

18. Caborn, D.N. et al. Biomechanical comparison between BioScrew and titanium alloy interference screws for bone-patellar tendon-bone graft fixation in anterior cruciate ligament reconstruction. *Arthroscopy* **1997**, 13, 229–32.

19. Barbucci, R. *Integrated biomaterials science*; Springer: NY, USA, **2002**.

20. Donachie, M.J. *Titanium: Technical Guide*, 2nd ed.; ASM International: OH, USA, **2000**.

21. Lapman, S. Titanium and Its Alloys for Biomedical Implants. In: *Material for Medical Devices*; Narayan, R. (Ed.); ASM International: OH, USA, **2012**; Vol. 23.

22. Hynowska, A. et al. Nanostructured β-phase Ti–31.0Fe–9.0Sn and sub-μm structured Ti–39.3Nb–13.3Zr–10.7Ta alloys for biomedical applications: Microstructure benefits on the mechanical and corrosion performances. *Mater. Sci. Eng. C* **2012**, 32, 2418–2425.

23. *www.nof.org.*

24. *www.niams.nih.gov/Health_Info/Bone.*

25. *www.nytimes.com/health/guides/disease/osteoporosis.*

26. Solomon, E.P.: Solomon, M.K.; Solomon, K. *Study Guide for Introduction to Human Anatomy and Physiology*, 3rd ed.; Saunders: PA, USA, **2008**.

27. Pronovost, A. *Vitamin D status and bone health in Inuit women 40 years of age and older*. Ph.D Thesis, McGill University, Quebec, Canada, **2009**.

28. LeGeros, R.Z. Calcium Phosphates in Oral Biology and Medicine. *Monogr. Oral Sci.* **1990**, 15, 1–201.

29. Harada, S.; Rodan, G.A. Control of osteoblast function and regulation of bone mass. *Nature* **2003**, 423, 349–355.

30. Bosco, R. et al. Surface Engineering for Bone Implants: A Trend from Passive to Active Surfaces. *Coatings* **2012**, 2, 95–119.

31. *www.ns.umich.edu*

32. Buser, D. et al. Influence of surface characteristics on bone integration of titanium implants. A histomorphometric study in miniature pigs. *J. Biomed. Mater. Res.* **1991**, 7, 889–902.

33. Simmons, C.A.; Valiquette, N.; Pilliar, R.M. Osseointegration of sintered porous-surfaced and plasma spray-coated implants: An animal model study of early postimplantation healing response and mechanical stability. *J. Biomed. Mater. Res.* **1999**, 47, 127–138.

34. Yang, Y.; Tian, J.; Deng, L.; Ong, J.L. Morphological behavior of osteoblast-like cells on surface-modified titanium in vitro. *Biomaterials* **2002**, 23, 1383–1389.

35. Bacakova, L. Modulation of cell adhesion, proliferation and differentiation on materials designed for body implants. *Biotechnol. Adv.* **2011**, 29, 739–767.

36. Anselme, K..; Noel, B. Human osteoblasts adhesion on titanium alloy, stainless steel, glass and plastic substrates with some surface topography. *J. Mater. Sci Mater. Med.* **1999**, 815–819.

37. Okazaki, Y.; Gotoh, E. Metal release from stainless steel, Co–Cr–Mo–Ni–Fe and Ni–Ti alloys in vascular implants. *Corros. Sci.* **2008**, 50, 3429–3438

38. Eisenbarth, E.; Velten, D.; Muller, M.; Thull, R.B. Biocompatibility of β-stabilizing elements of titanium alloys. *Biomaterials* **2004**, 25, 5705–5713.

39. Straface, E. et al. C3-fullero-tris-methanodicarboxylic acid protects epithelial cells from radiation-induced anoikia by influencing cell adhesion ability. *FEBS Lett.* **1999**, 454, 335–340.

40. Chen, C.S. et al. Micropatterned surfaces for control of cell shape, position, and function. *Biotechnol. Prog.* **1998**, 14, 356–363.

41. Ingber, D.E.; Sun, Z.; Betensky, H. Cell shape, cytoskeletal mechanics, and cell cycle control in angiogenesis. *J. Biomech.* **1994**, 7, 1471–1484.

42. Zaidel-Bar, R.; Milo, R.; Kam, Z.; Geiger, B. A paxillin tyrosine phosphorylation switch regulates the assembly and form of cell-matrix adhesions. *J. Cell Sci.* **2007**, 120, 137–148.

43. Wang, Y.B.; Zheng, Y.F.; Wei, S.C.; Li, M. In vitro study on Zr-based bulk metallic glasses as potential biomaterials. *J. Biomed. Mater. Res. B.: Appl. Biomater.* **2011**, 96, 34–46.

44. Williams, D. On the mechanisms of biocompatibility. *Biomaterials* **2008**, 29, 2943–2953.

45. Bar-Cohen, Y.: Zacny, K. (Eds.). *Drilling in Extreme Environments: Penetration and Sampling on Earth and other Planets*; VCH-Wiley: NY, USA, **2009**.

46. Katz, J.L. Anisotropy of Young's modulus of bone. *Nature* **1980**, 283, 106–107.

47. Black, J.: Hastings, G. (Eds.). *Handbook of biomaterials properties*; Chapman & Hall; London, UK, **1998**.

48. Sumner, D.R., et al. Functional adaptation and ingrowth of bone vary as a function of hip implant stiffness. *J. Biomech.* **1998**, 31, 909-917.

49. Niinomi, M.; Nakai, M. Titanium-Based Biomaterials for Preventing Stress Shielding between Implant Devices and Bone. *Int. J. Biomater.* **2011**, 2011, 836587.

50. Dowson, D. New joints for the Millennium: Wear control in total replacement hip joints. *Proc. Inst. Mech. Eng. Part H – J. Eng. Med.* **2001**, 215, 335–358.

51. Affatato, S. (Ed.). *Wear of orthopaedic implants and artificial joints*; Woodhead Publishing Ltd.: Oxford, UK, **2012**.

52. Patterson, S.P.; Daffner, R.H; Gallo, R.A. Electrochemical corrosion of metal implants. *Am. J. Roentgenol.* **2005**, 184, 1219–1222.

53. Kruger, J. Passivity of metals–a materials science perspective. *Int. Mater. Rev.* **1988**, 33, 113–130.

54. Jacobs, J.J.; Gilbert, J.L.; Urban, R.M. Current concepts review: Corrosion of metal orthopaedic implants. *J. Bone Jt. Surg.* **1998**, 80-A (2), 268–284.

55. Jones, D.A. *Principles and prevention of corrosion*, 2nd ed. MacMillan, NY, USA, **1992**.

56. Atkinson, J.R.; Jobbins, B. Properties of engineering materials for use in body. In *Introduction to biomechanics of joint and joint replacement*; Dowson D, Wright V: London, *Mech. Eng. Publ.* **1981**, p. 141–145.

57. Chu, P.K. et al. Plasma-surface modification of biomaterials. *Mat. Sci. Eng. R* **2002**, 36, 143–206.

58. Galeotti, A. et al. Effect of pH on in vitro biocompatibility of orthodontic miniscrew implants. *Prog. Orthod.* **2013**, 14, 15.

59. Standard test method for conducting cyclic potentiodynamic polarization measurements to determine the corrosion susceptibility of small implant devices. ASTM Inc.: F-2129-06: PA, USA, **2006**.

60. Padilla, N.; Bronson, A. Electrochemical characterization of albumin protein on Ti-6Al-4V alloy immersed in a simulated plasma solution. *J. Biomed. Mater. Res. A* **2007**, 81, 531–543.

61. Songür, M. et al. Electrochemical corrosion properties of metal alloys used in orthopaedic implants. *J. Appl. Electrochem.* **2009**, 39, 1259–1265.

62. Puigdomenech, I. *Hydra/Medusa Chemical Equilibrium Database and Plotting Software*; KTH Royal Institute of Technology, Stockholm, Sweden, **2004**.

63. McCafferty, E. *Introduction to Corrosion Science*. Springer, London, UK, **2010**.

64. Hallab, N.J.; Urban, R.M.; Jacobs, J.J. Corrosion and biocompatibility of Orthopedic Implants. In: *Biomaterial in Orthopedics*. Yaszemski, M.Y. et al. (Eds.); CRC Press: NY, USA, **2004**; pp. 63–92.

65. Inoue, A. Hard magnetic bulk amorphous Nd-Fe-Al alloys of 12 mm in diameter made by suction casting. *Mater. Trans.* **1996**, 37, 636–640.

66. Inoue, A. Bulk Nd-Fe-Al amorphous alloys with hard magnetic properties. *Mater. Trans.* **1996**, 37, 99–108.

67. Ashby, M.F.; Greer, A.L. Metallic glasses as structural materials. *Scr. Mater.* **2006**, 54, 321–326.

68. Fornell, J. *Metallic glasses and derived composite materials: a correlation between microstructure and mechanical properties*. Ph.D Thesis, Universitat Autònoma de Barcelona, Bellaterra, Spain, **2012**.

69. Li, J.F., Huang, Z.H., Crystallization of amorphous $Zr_{60}Al_{15}Ni_{15}$ alloy. *Intermetallics* **2007**, 15, 1013–1019.

70. Klement, W.; R.H. Willens. Non-crystalline Structure in Solidified Gold-Silicon Alloys. *Nature* **1960**, 187, 869–870.

71. Duwez, P. Metallic glasses-historical background. In: *Glassy Metals I*. Güntherodt, H.J.; Beck, H., (Eds.); Springer-Verlag: Berlin, Germany, **1981**; pp. 19–23.

72. Suryanarayana, C.; Inoue, A. *Bulk metallic glasses*; CRC Press: NY, USA, **2011**.

73. Nieh, T.G., et al. Plasticity and structural instability in a bulk metallic glass deformed in the supercooled liquid region. *Acta Mater.* **2001**, 49, 2887–2896.

74. Kauzmann, W. The Nature of the Glassy State and the Behavior of Liquids at Low Temperatures. *Chem. Rev.* **1948**, 43, 219–256.

75. Adam, G.; Gibbs, J.H. On the Temperature Dependence of Cooperative Relaxation Properties in Glass-Forming Liquids. *J. Chem. Phys.* **1965**, 43, 139.

76. Turnbull, D. Under what conditions can a glass be formed? *Contemp. Phys.* **1969**, 10, 473.

77. Cohen, M.H.; Turnbull, D. Molecular transport in liquids and glasses. *J. Chem. Phys.* **1980**, 31, 1979.

78. Kalikmanov, I.V. Classical Nucleation Theory. In: *Nucleation Theory*, Springer: London, UK, **2013**; Chapter 3, pp. 17–41

79. Boettinger, W.J.; Perepezco, J.H. Rapidly solidified crystalline alloys. In: *Fundamentals in Rapid Solidification*; Das, S.K.; Kear, B.H.; Adam, C.M., (Eds.); Proc. Symp. On Rapidly Solidified Crystalline alloys, Northeast Regional Meeting of TMS-AIME, NJ, May 1985, The Metallurgical Society of AIME; Warrendale. PA, USA, **1985**.

80. Polk, D. E.; Giessen, B. C. *Metallic glasses*. Gilman, J.J.; Leamy, H.J. (Eds.); ASM International: OH, USA, **1977**.

81. Uhlmann, D.R. A kinetic treatment for glass formation. *J. Non. Cryst. Solids* **1972**, 7, 337.

82. Löffler, J.F.; Schroers, J.; Johnson, W.L. Time–temperature–transformation diagram and microstructures of bulk glass forming $Pd_{40}Cu_{30}Ni_{10}P_{20}$. *Appl. Phys. Lett.* **2000**, 77, 681.

83. Löffler, J.F. Bulk metallic glasses. *Intermetallics* **2003**, 11, 529–540.

84. Yavari, A.R., et al. The effect of fusion volume on the kinetics of formation of metallic glasses by liquid quenching. *J. Chim. Phys. Physico-Chimie Biol.* **1982**, 79, 579.

85. Lu, Z.P.; Liu, C.T. A new glass-forming ability criterion for bulk metallic glasses. *Acta Mater.* **2002**, 50, 3501–3512.

86. Inoue, A. Stabilization of metallic supercooled liquid and bulk amorphous alloys. *Acta Mater.* **2000**, 48, 279–306.

87. Bernal, J.D. Geometry of the Structure of Monatomic Liquids. *Nature* **1960**, 185, 68–70.

88. Polk, D. The structure of glassy metallic alloys. *Acta Metall.* **1972**, 20, 485–491.

89. Gaskell, P.H. A new structural model for amorphous transition metal silicides, borides, phosphides and carbides. *J. Non. Cryst. Solids* **1979**, 32, 207–224.

90. Miracle, D.B.; Egami, T.; Flores, K.M.; Kelton, K.F. Structural Aspects of Metallic Glasses. *MRS Bull.* **2011**, 32, 629–634.

91. Miracle, D.B. A structural model for metallic glasses. *Nat. Mater.* **2004**, 3, 697–702.

92. Miracle, D.B. The efficient cluster packing model – An atomic structural model for metallic glasses. *Acta Mater.* **2006**, 54, 4317.

93. Spaepen, F. A microscopic mechanism for steady state inhomogeneous flow in metallic glasses. *Acta Metall.* **1977**, 25, 407–415.

94. *www.docstoc.com*

95. Russew, K.; Sommer, F. Length and density changes of amorphous $Pd_{40}Cu_{30}Ni_{10}P_{20}$ alloys due to structural relaxation. *J. Non. Cryst. Solids* **2003**, 319, 289–296.

96. Yavari, A.R. et al. Excess free volume in metallic glasses measured by X-ray diffraction. *Acta Mater.* **2005**, 53, 1611–1619.

97. Faupel, F. et al. Diffusion in metallic glasses and supercooled melts. *Rev. Mod. Phys.* **2003**, 75, 237–280.

98. Vaidya, R.U.; Subramanian, K.N. Metallic glass ribbon–reinforced glass–ceramic matrix composites. *J. Mater. Sci.* **1990**, 25, 3291–3296.

99. Vaidya, R.U.; Subramanian, K.N. Metallic glass ribbon–reinforced glass–ceramic matrix composites. *J. Mater. Sci.* **1990**, 25, 3291–3296.

100. Cytron, S.J. A Metallic Glass–Metal Matrix Composite. *J. Mater. Sci. Lett.* **1982**, 1, 211–213.

101. Kato, H. High strength and good ductility of $Zr_{55}Al_{10}Ni_5Cu_{30}$ bulk glass containing ZRC particles. *Scr. Mater.* **2000**, 43, 503–507.

102. Li, J. et al. Synthesis and characterization of particulate reinforced Mg-based bulk metallic glass composites. *Mater. Lett.* **2007**, 61, 2217–2221.

103. Deng, S.T. et al. Metallic glass fiber-reinforced Zr–based bulk metallic glass. *Scr. Mater.* **2011**, 64, 85–88.

104. Flores, K.M.; Johnson, W.L.; Dauskardt, R.H. Fracture and fatigue behavior of a Zr–Ti–Nb ductile phase reinforced bulk metallic glass matrix composite. *Scr. Mater.* **2003**, 49, 1181–1187.

105. Kühn, U.; Eckert, J.; Mattern, N.; Schultz, L. ZrNbCuNiAl bulk metallic glass matrix composites containing dendritic bcc phase precipitates. *Appl. Phys. Lett.* **2002**, 80, 2478.

106. Hays, C.; Kim, C.; Johnson, W. Microstructure controlled shear band pattern formation and enhanced plasticity of bulk metallic glasses containing in situ formed ductile phase dendrite dispersions. *Phys. Rev. Lett.* **2000**, 84, 2901–2904.

107. He, G.; Eckert, J.; Löser, W.; Schultz, L. Novel Ti-base nanostructure-dendrite composite with enhanced plasticity. *Nat. Mater.* **2003**, 2, 33–37.

108. Fornell, J. et al. Enhanced mechanical properties and in vitro corrosion behavior of amorphous and devitrified $Ti_{40}Zr_{10}Cu_{38}Pd_{12}$ metallic glass. *J. Mech. Behav. Biomed. Mater.* **2011**, 4, 1709–1717.

109. Pauly, S. *Phase formation and mechanical properties of metastable Cu-Zr-based alloys*. Ph.D Thesis, Technische Universität Dresden, Dresden, Germany, **2010**.

110. Venkataraman, S. et al. Calorimetric study of the crystallization kinetics of $Cu_{47}Ti_{33}Zr_{11}Ni_8Si_1$ metallic glass. *Phys. Rev. B* **2007**, 75, 104206.

111. Avrami, M. Kinetics of phase change. I General theory. *J. Chem. Phys.* **1939**, 7, 1103–1112.

112. Christian, J.W. *The theory of transformation in metals and alloys (Part I+ II)*, Pregamon Press, Oxford, **2002**.

113. Burke, J. *The kinetics of phase transformations in metals*; Pregamon Press Inc.: NY, USA, **1965**.

114. Louzguine, D.V.; Inoue, A. Crystallization behavior of $Ti_{50}Ni_{25}Cu_{25}$. *J. Mater. Sci.* **2000**, 35, 4159–4164.

115. Fornell, J., et al. Enhanced mechanical properties due to structural changes induced by devitrification in Fe–Co–B–Si–Nb bulk metallic glass. *Acta Mater.* **2010**, 58, 6256–6266.

116. Liu, Y.; Zhou, J.; Hui, D. A strain–gradient plasticity theory of bimodal nanocrystalline materials with composite structure. *Compos. Part B Eng.* **2012**, 43, 249–254.

117. Lu, K. Nanocrystalline metals crystallized from amorphous solids: nanocrystallization, structure, and properties. *Mater. Sci. Eng. R Reports* **1996**, R16, 161–221.

118. Siegel, R.W. Nanostructured materials – mind over matter. *Nanostruct. Mater.* **1993**, 3, 1–18.

119. Mütschele, T. Kirchheim, R. Hydrogen as a probe for the average thickness of a grain boundary. *Scr. Metall.* **1987**, 21, 1101–1104.

120. Suryanarayana, C.; Koch, C.C. Nanocrystalline materials – Current research and future directions. *Hyperfine Interact.* **2000**, 130, 5–44.

121. Gleiter, H. Nanocrystalline materials. *Prog. Mater. Sci.* **1990**, 33, 223–315.

122. Meyers, M.A.; Mishra, A.; Benson, D.J. Mechanical properties of nanocrystalline materials. *Prog. Mater. Sci.* **2006**, 51, 427–556.

123. Inoue, A. Cobalt-based bulk glassy alloy with ultrahigh strength and soft magnetic properties. *Nat. Mater.* **2003**, 2, 661–663.

124. Greer, A.L. Metallic glasses. *Science* **1995**, 267, 1947–1953.

125. Chen, H.S.; Goldstein, M. Anomalous viscoelastic behavior of metallic glasses of Pd–Si–Based alloys. *J. Appl. Phys.* **1972**, 43, 1642.

126. Argon, A.S. Plastic deformation in metallic glasses. *Acta Metal.* **1979**, 27, 47–58.

127. Huang, R.; Suo, Z.; Prevost, J. H.; Nix, W. D. Inhomogeneous deformation in metallic glasses. *J. Mech. Phys. Solids* **2002**, 50, 1011–1027.

128. Dai, L.H.; Yan, M.; Liu, L.F.; Bai, Y.L. Adiabatic shear banding instability in bulk metallic glasses. *Appl. Phys. Lett.* **2005**, 87, 141916.

129. Leamy, H.J.; Chen, H.S. Plastic flow and fracture of metallic glasses. *Mater. Trans.* **1972**, 3, 699.

130. Falk, M.L.; Langer, J.S. Dynamics of viscoplastic deformation in amorphous solids. *Phys. Rev. E* **1998**, 57, 7192.

131. Leamy, H.J., Wang, T.T.; Chen, H.S. Plastic flow and fracture of metallic glasses. *Metall. Trans.* **1972**, 3, 699.

132. Yao, K.F.; Ruan, F.; Yang, Y.Q.; Chen, N. Superductile bulk metallic glass. *Appl. Phys. Lett.* **2006**, 88, 122106.

133. Das, J. et al. "Work-Hardenable" Ductile Bulk Metallic Glass. *Phys. Rev. Lett.* **2005**, 94, 205501.

134. Saida, J.; Setyawan, A.D.; Kato, H.; Inoue, A. Nanoscale multistep shear band formation by deformation-induced nanocrystallization in Zr-Al-Ni-Pd bulk metallic glass. *Appl. Phys. Lett.* **2005**, 87, 151907.

135. Yao, K.F.; Ruan, F.; Yang, Y.Q.; Chen, N. Superductile bulk metallic glass. *Appl. Phys. Lett.* **2006**, 88, 122106.

136. Fornell, J. et al. Yielding and intrinsic plasticity of Ti–Zr–Ni–Cu–Be bulk metallic glass. *Int. J. Plast.* **2009**, 25, 1540–1559.

137. Schuh, C.; Hufnagel, T.; Ramamurty, U. Mechanical behavior of amorphous alloys. *Acta Mater.* **2007**, 55, 4067–4109.

138. Sun, G.Y.; Chen, G.; Liu, C.T.; Chen, G.L. Innovative processing and property improvement of metallic glass based composites. *Scr. Mater.* **2006**, 55, 375–378.

139. Qin, C.L. et al. A novel Cu-based BMG composite with high corrosion resistance and excellent mechanical properties. *Acta Mater.* **2006**, 54, 3713–3719.

140. Lee, S.-W.; Huh, M.-Y.; Fleury, E.; Lee, J.-C. Crystallization-induced plasticity of Cu–Zr containing bulk amorphous alloys. *Acta Mater.* **2006**, 54, 349–355.

141. Chen, M.; Inoue, A.; Zhang, W.; Sakurai, T. Extraordinary Plasticity of Ductile Bulk Metallic Glasses. *Phys. Rev. Lett.* **2006**, 96, 245502.

142. Chokshi, A.H. On the validity of the Hall-Petch relationship in nanocrystalline materials. *Scr. Metall.* **1989**, 23,1679–1683.

143. Zhu, Y.T. Retaining ductility. *Nat. Mater.* **2004**, 4, 351–352.

144. Suryanarayana, C.; Koch, C.C. Nanocrystalline materials – Current research and future directions. *Hyperfine Interact.* **2000**, 130, 5–44.

145. Kou, H. et al. Electrochemical corrosion properties of Zr- and Ti-based bulk metallic glasses. *Trans. Nonferrous Met. Soc. China* **2011**, 21, 552–557.

146. Vishwanadh, B. et al. Effect of Structural Defects, Surface Irregularities, and Quenched-In Defects on Corrosion of Zr-Based Metallic Glasses. *Metall. Mater. Trans. A* **2009**, 40, 1131–1141.

147. Blackburn, M.J.; Malley, D.R. Plasma arc melting of titanium alloys. *Mater. Des.* **1993**, 14, 19.

148. Morita, A. et al. Alloying titanium and tantalum by cold crucible levitation melting (CCLM) furnace. *Mater. Sci. Eng. A* **2000**, 280, 208.

149. Liu, L.; Li, Y.; Wang, F. Electrochemical Corrosion Behavior of Nanocrystalline Materials – a Review. *J. Mater. Sci. Technol.* **2010**, 26, 1–14.

150. Yu, B.; Woo, P.; Erb, U. Corrosion behaviour of nanocrystalline copper foil in sodium hydroxide solution. *Scr. Mater.* **2007**, 56, 353–356.

151. Lopez-Hirata, V.M.; Arce-Estrada, E.M.; Postal, A. Characterization of Co-Cu mechanical alloys by linear sweep voltammetry. *Electrochim. Acta* **1997**, 42, 61–65.

152. Vinogradov, A.; Mimaki, T.; Hashimoto, S. On the corrosion behaviour of ultra-fine grain copper. *Scr. Mater.* **1999**, 3, 319–326.

153. Duan, G.; et al. Lightweight Ti-based bulk metallic glasses excluding late transition metals. *Scr. Mater.* **2008**, 58, 465–468.

154. Tanner, L.E.; Ray, R. Physical properties of $Ti_{50}Be_{40}Zr_{10}$ glass. *Scrip. Metall.* **1977**, 11, 783–789.

155. Polk, D.E., Calka, A., Giessen, B.C. The preparation and thermal and mechanical properties of new titanium rich metallic glasses. *Acta Metall.* **1978**, 26,1097–1103.

156. Zhang, T.; Inoue, A.; Masumoto, T. The effect of atomic size on the stability of the supercooled liquid for amorphous (Ti,Zr,Hf)65Ni25Al10 and (Ti,Zr,Hf)65Cu25Al10 alloys. *Mater. Lett.* **1993**, 15, 379–382.

157. Inoue, A., et al. Ti-based amorphous alloys with a wide supercooled liquid region. *Mater. Lett.* **1994**, 19, 131–135.

158. Peker, A J. W. US Patent 5, **1994**, p. 344.

159. Zhang, T.; Inoue, A. Preparation of Ti-Cu-Ni-Si-B amorphous alloys with a large supercooled liquid region. *Mater. Trans.* **1999**, 40, 301–306.

160. Kim, J-J, Choi, Y.; Suresh, S.; Argon, A. Nanocrystallization during nanoindentation of a bulk amorphous metal alloy at room temperature. *Science* **2002**, 295, 654–657.

161. Kim, Y.C. et al. Role of nanometer-scale quasicrystals in improving the mechanical behavior of Ti-based bulk metallic glasses. *Appl. Phys. Lett.* **2003**, 83, 3093.

162. Kim, Y.C.; Kim, W.T.; Kim, D.H. A development of Ti-based bulk metallic glass. *Mater. Sci. Eng. A* **2004**, 375-377, 127–135.

163. Qin, F.X.; Wang, X.M.; Inoue, A. Effect of annealing on microstructure and mechanical property of a Ti–Zr–Cu–Pd bulk metallic glass. *Intermetallics* **2007**, 15, 1337–1342.

164. He, G.; et al. Nanostructured Ti-based multi-component alloys with potential for biomedical applications. *Biomaterials* **2003**, 24, 5115–5120.

165. Zhang, Y.; Lim, C.T.; Ramakrishna, S.; Huang, Z.-M. Recent development of polymer nanofibers for biomedical and biotechnological applications. *J. Mater. Sci. Mater. Med.* **2005**, 16, 933–946.

166. Nouri, A; Hodgson, P.D.; Wen, C.E. Effect of process control agent on the porous structure and mechanical properties of a biomedical Ti-Sn-Nb alloy produced by powder metallurgy. *Acta Biomater.* **2010**, 6, 1630–1639.

167. Xu, L.J.; Chen, Y.Y.; Liu, Z.G.; Kong, F.T. The microstructure and properties of Ti–Mo–Nb alloys for biomedical application. *J. Alloys Compd.* **2008**, 453, 320–324.

168. Elias, L.M. et al. Microstructural and mechanical characterization of biomedical Ti–Nb–Zr(–Ta) alloys. *Mater. Sci. Eng. A* **2006**, 432, 108–112.

169. Han, J.H.; et al. Sn effect on microstructure and mechanical properties of ultrafine eutectic Ti–Fe–Sn alloys. *J. Alloys Compd.* **2009**, 483, 44–46.

170. Niinomi, M. Recent research and development in titanium alloys for biomedical applications and healthcare goods. *Sci. Technol. Adv. Mater.* **2003**, 4, 445–454.

171. Cartier, M. *Handbook of surface treatment and coatings*; ASME Press: NY, USA, **2003**.

172. Tao, N.R.; Sui, M.L.; Lu, J.; Lua, K. Surface nanocrystallization of iron induced by ultrasonic shot peening. *Nanostruct. Mater.* **1999**, 11, 433–440.

173. Averback, R.S.; Benedek, R.; Merkle, K.L. Ion-irradiation studies of the damage function of copper and silver *Phys. Rev. B* **1978**, 18, 4156–4171.

174. Valtchev,V.et at. High energy ion irradiation-induced ordered macropores in zeolite crystals. *J. Am. Chem. Soc.* **2011**, 133, 18950–18956.

175. Romero-Gómez, P.A. et al. *Phys. Rev. B* **2010**, 82, 115420.

176. Pérez-Bergquist, A.G.; Naab, F.U.; Zhang, Y. Etch-free formation of porous silicon by high-energy ion irradiation. *Nucl. Instrum. Meth.* B **2011**, 269, 561–565.

177. Bischoff, L.; Pilz, W.; Schmidt, B. Amorphous solid foam structures on germanium by heavy ion irradiation. *Appl. Phys. A* **2011**,104, 1153–1158.

178. George, H.B. et al. Ion-sculpting of nanopores in amorphous metals, semiconductors, and insulators. *Appl. Phys. Lett.* **2010**, 96, 263111.

179. Pérez-Bergquist, A., et al. Embedded nanofibers induced by high-energy ion irradiation of bulk GaSb. *Small* **2008**, 4, 1119–1124.

180. Dang,Z.Y. et al.On the formation of silicon wires produced by high-energy ion irradiation. *Nucl. Instrum. Meth. B* **2013**,296, 32–40.

181. Schuh, C.A.; Lund, A.C; Nieh, T.G. New regime of homogeneous flow in the deformation map of metallic glasses: Elevated temperature nanoindentation experiments and mechanistic modeling. *Acta Mater.* **2004**, 52, 5879-5891.

182. Concustell,A.et al. Plastic deformation and mechanical softening of $Pd_{40}Cu_{30}Ni_{10}P_{20}$ bulk metallic glass during nanoindentation. *J. Mater. Res.* **2005**, 20, 2719–2725.

183. Fornell, J. et al.Yielding and intrinsic plasticity of Ti-Zr-Ni-Cu-Be bulk metallic glass. *Int. J. Plasticity* **2009**, 25, 1540–1559.

184. Das, J. et al. "Work-hardenable" ductile bulk metallic glass. *Phys. Rev. Lett.* **2005**, 94 , 205501.

185. Fornell, J. et al. Enhanced mechanical properties in a Zr-based metallic glass caused by deformation-induced nanocrystallization. *Scripta Mater.* **2010**, 62, 13–16.

186. Moine, P.; Jaouen, C. Ion beam induced amorphization in the intermetallic compounds NiTi and NiAl. *J. Alloys Compd*. **1993**, 194, 373–380.

187. Motta, A.T. Amorphization of intermetallic compounds under irradiation - A review. *J. Nucl. Mater.* **1997**, 244, 227–250.

188. Utsunomiya, S.; Wang, L.M.; Yudintsev, S.; Ewing, R.C. Ion irradiation-induced amorphization and nano-crystal formation in garnets. *J. Nucl. Mater.* **2002**, 303, 177–187.

189. Sprouster, D.J. et al. Ion-irradiation-induced amorphization of cobalt nanoparticles. *Phys. Rev. B* **2010**, 81, 155414.

190. Carter, J. et al. Effects of Cu ion irradiation in $Cu_{50}Zr_{45}Ti_5$ metallic glass. *Scripta Mater*. **2009**, 61, 265–268.

191. Raghavan, R. Ion irradiation enhances the mechanical performance of metallic glasses. *Scripta Mater.* **2010**, 62, 462–465.

192. Raghavan, R. et al. Nanoindentation response of an ion irradiated Zr-based bulk metallic glass. *Mater. Sci.* Eng. A **2012**, 532, 407–413.

193. Carter, J. et al. Ion irradiation induced nanocrystal formation in amorphous $Zr_{55}Cu_{30}Al_{10}Ni_5$ alloy. *Nucl. Instrum. Meth. B* **2009**, 267, 2827–2831.

194. Carter, J. Effects of ion irradiation in metallic glasses. *Nucl. Instrum. Meth. B* **2009**, 267, 1518–1521.

195. Myers, M. et al. An experimental and modeling study on the role of damage cascade formation in nanocrystalization of ion-irradiated $Ni_{52.5}Nb_{10}Zr_{15}Ti_{15}Pt_{7.5}$ metallic glass. *Scripta Mater.* **2010**, 63, 1045–1048.

196. Luo, W.D.; Yang, B.; Chen, G.L. Effect of Ar^+ ion irradiation on the microstructure and properties of Zr-Cu-Fe-Al bulk metallic glass. *Scripta Mater.* **2011**, 64, 625–628.

197. Xie, G.; Shao, L.; Louzguine-Luzgin, D.V.; Inoue, A. He ion irradiation induced nanocrystallization in $Cu_{50}Zr_{45}Ti_5$ glassy alloy. *Surf. Coat. Technol.* **2011**, 206, 829–833.

198. Magagnosc, D.J. et al. Tunable tensile ductility in metallic glasses. *Sci. Rep.* **2013**, 3, 1096.

199. Qin, W.; Szpunar, J.A.; Umakoshi, Y. Electron or ion irradiation-induced phase-change mechanism between amorphous and crystalline state. *Acta Mater.* **2011**, 59, 2221–2228.

200. *www.arcastinc.com*

201. Dave, K. Permanent mold cast copper alloys: Provide opportunities for conversion success. *Modern Cast.* **1998**, 88, 43–45.

202. Lutterotti, L.; Scardi, P. Simultaneous structure and size-strain refinement by the Rietveld method. J. *Appl. Crystall.* **1990**, 23, 246–252.

203. Lutterotti, L.; Gialanella, S. X-ray diffraction characterization of heavily deformed metallic specimens. *Acta Mater.* **1998**, 46, 101–110.

204. Bontempi, E. et al. Glancing-incidence X-ray diffraction of Ag nanoparticles in gold lustre decoration of Italian Renaissance pottery. *Appl. Phys. A* **2006**, 83, 543–546.

205. Oliver, W.C.; Pharr, G.M. An improved technique for determining hardness and elastic modulus using load and displacement sensing indentation experiments. *J. Mater. Res.* **1992**, 7, 1564–1583.

206. Oliver, W.C.; Pharr, G.M. Measurement of hardness and elastic modulus by instrumented indentation: Advances in understanding and refinements to methodology. *J. Mater. Res.* **2004**, 19, 3–20.

207. Gao, Y.K. Improvement of fatigue property in 7050–T7451 aluminum alloy by laser peening and shot peening. *Mater. Sci. Eng. A* **2011**, 528, 3823–3828.

208. Nagase, T.; Umakoshi, Y. Electron irradiation induced crystallization of the amorphous. *Sci. Technol. Adv. Mater.* **2004**, 57, 57–67.

209. Sathyajith, S.; Kalainathan, S.; Swaroop, S. Optics & Laser Technology Laser peening without coating on aluminum alloy Al-6061-T6 using low energy Nd: YAG laser. *Opt. Laser Technol.* **2013**, 45, 389–394.

210. Sathyajith, S.; Kalainathan, S. Effect of laser shot peening on precipitation hardened aluminum alloy 6061-T6 using low energy laser. *Opt. Lasers Eng.* **2012**, 50, 345–348.

211. Hatamleh, O. A comprehensive investigation on the effects of laser and shot peening on fatigue crack growth in friction stir welded AA 2195 joints. *Int. J. Fatigue* **2009**, 31, 974–988.

212. González, S., et al. Influence of the shot-peening intensity on the structure and near-surface mechanical properties of $Ti_{40}Zr_{10}Cu_{38}Pd_{12}$ bulk metallic glass. *Appl. Phys. Letters* **2013**, 103, 211907.

Publications

1. **Hynowska**, **A**.; Pellicer, E.; Fornell, J.; González, S.; Van Steenberge, N.; Suriñach, S.; Eckert, J.; Baró, M.D.; Sort, J. Nanostructured β-phase Ti-31.0Fe-9.0Sn and sub-μm structured Ti-39.3Nb-13.3Zr-10.7Ta alloys for biomedical applications: Microstructure benefits on the mechanical and corrosion performances. *Mat. Sci. Eng. C* **2012**, 8, 2418–2425.

2. **Hynowska**, **A.**; Blanquer, A.; Pellicer, E.; Fornell, J.; González, S.; Suriñach, S.; Baró, M.D.; Ibáñez, E.; Barrios, L.; Nogués, C.; Sort, J. Novel Ti–Zr–Hf–Fe Nanostructured Alloy for Biomedical Applications. *Materials* **2013**, 6, 4930–4945.

3. Blanquer, A.; Pellicer, E.; **Hynowska, A.**; Barrios, L.; Ibáñez, E.; Baró, M.D.; Sort, J.; Nogués, C. In vitro biocompatibility assessment of $Ti_{40}Cu_{38}Zr_{10}Pd_{12}$ bulk metallic glass. *J. Mater. Sci.: Mater. Med.* **2014**, 25, 163–172.

4. Menéndez, E.; **Hynowska, A.**; Fornell, J.; Suriñach, S.; Montserrat, J.; Temst, K.; Vantome, A.; Baró, M.D.; García-Lecina, E.; Pellicer, E.; Sort, J. Influence of the irradiation temperature on the surface microstructure and physical/chemical properties of Ar ion-irradiated bulk metallic glasses. *J. Alloys Compd.* **2014**, 610, 118–125.

5. **Hynowska, A.**; Blanquer, A.; Pellicer, E.; Fornell, J.; Suriñach, S.; Baró, M.D.; Gebert, A.; Calin, M.; Eckert, J.; Nogués, C.; Ibáñez, E.; Barrios, L.; Sort, J. Superior mechanical behaviour and excellent biocompatibility of novel nanostructured Ti-Zr-Pd-Si-(Nb) bulk metallic alloys: attractive materials for biomedical applications. *J. Biomed. Mater. Res. B (submitted).*